DEVELOPMENT OF X-RAY DIFFRACTION IMAGING TECHNIQUES FOR THE QUASI IN SITU CHARACTERIZATION OF CRYSTAL DEFECTS

Zur Erlangung des akademischen Grades eines

DOKTORS DER NATURWISSENSCHAFTEN (Dr. rer. nat.)

von der KIT-Fakultät für Physik des
Karlsruher Instituts für Technologie (KIT)

angenommene

DISSERTATION

von

DIPL. PHYS. SIMON BODE
geboren in Gießen

Tag der mündlichen Prüfung: 12. November 2021

Referent: Prof. Dr. Tilo Baumbach
Korreferent: Prof. Dr. Andreas Danilewsky

Dipl. Phys. Simon Bode: *Development of X-Ray Diffraction Imaging Techniques for the Quasi In Situ Characterization of Crystal Defects,* von der Fakultät für Physik des Karlsruher Instituts für Technologie (KIT) angenommene Dissertation, 2022

ABSTRACT

Focusing on methodological development, this work revises the theoretical foundations of X-ray Diffraction Laminography (XDL) aiming for a profound understanding of the combined topographic and laminogprahic principles, especially for the three-dimensional (3D) imaging of dislocation arrangements and their evolution. XDL so far has enabled non-destructive 3D imaging of crystal defects in monocrystalline samples, in particular for technologically relevant sizes like typical industrial wafers. The capabilities have successfully been demonstrated by characterizing *static* dislocation arrangements in silicon, capturing volumes of several mm^3 with an estimated spatial resolution of 3 to 5 µm. Driven by the demands of modern micro-electronic technology, this work aims to enable quasi *in situ* imaging of defect dynamics and advance the technique towards routine application.
In this regard, simulations provide a more quantitative understanding of the image formation mechanism and related methodological properties, like intrinsic resolution limits, enabling the development of approaches for enhancing the spatial resolution and optimizing the 3D reconstruction. Eventually, this will result in new techniques to determine important parameters, like e.g. the Center of Rotation (CoR), and result in a significant reduction of the required projections. Beyond the geometrical arrangement, additional information about dislocation properties, like Burgers vectors (BVs), becomes accessible directly via the 3D image provided by XDL.
By deriving specifications from these theoretical considerations, an instrumentation fulfilling the specific mechanical requirements of 3D X-ray diffraction imaging will be commissioned and characterized. The methodological progress accomplished within this work, encompassing substantial improvements regarding measurement, data processing and analysis, finally enables the quasi *in situ* characterization of defect dynamics in 3D. The new capabilities of XDL are successfully demonstrated by feasibility studies and application oriented examples, like the visualization of slip band formation in mechanical damaged silicon during thermo-mechanical treatment.

ZUSAMMENFASSUNG

Mit einem Fokus auf Methodenentwicklung untersucht diese Arbeit das theoretische Fundament von *X-Ray Diffraction Laminography* (XDL) mit dem Ziel ein tieferes Verständnis der kombinierten topographischen und laminografischen Prinzipien zu schaffen, insbesondere bzgl. der dreidimensionalen (3D) Bildgebung von Versetzungsstrukturen und ihrer Entwicklung. XDL hat bisher die zerstörungsfreie 3D Bildgebung von Kristalldefekten in Einkristallen ermöglicht und ist speziell geeignet für technologisch relevante Probengrößen, wie z.B. die von industriellen Wafern. Die Einsatzmöglichkeiten wurden mit der Charakterisierung von *statischen* Arrangements von Versetzungen in Silizium erfolgreich demonstriert. Dabei wurden Kristallvolumen von mehreren mm^3 mit einer räumlichen Auflösung von 3 bis 5 µm abgebildet. Im Hinblick auf die steigenden Anforderungen von Technologien im Bereich der Mikroelektronik zielt diese Arbeit darauf ab, die quasi *in situ* Bildgebung von Defektdynamiken zu ermöglichen und die routinemäßige Anwendung von XDL voranzutreiben.
In diesem Zusammenhang stellen Simulationen und deren Analyse ein quantitativeres Verständnis der Kontrastformation und den damit verbundenen methodischen Eigenschaften, wie intrinsichen Grenzen des Auflösungsvermögens, bereit. Auf dieser Basis werden neue Ansätze entwickelt, um die räumliche Auflösung zu verfeinern und die 3D Rekonstruktion zu optimieren. Es werden neue Techniken bereit gestellt, um wichtige Parameter wie das Rotationszentrum (CoR) zu bestimmen und die benötigte Anzahl von Projektion bedeutend zu reduzieren. Über das rein geometrische Arrangement hinaus werden zusätzliche Information über die Versetzungen, wie z.B. über ihre Burgersvektoren (BVs), direkt durch das von XDL bereitgestellte 3D Bild zugänglich.
Anhand Spezifikationen, abgeleitet von diesen theoretischen Betrachtungen, wird eine dedizierte Instrumentierung in Betrieb genommen und charakterisiert, die die besonderen mechanischen Anforderungen von auf Röntgenbeugung basierenden 3D Bildgebungsverfahren erfüllt. Der methodische Fortschritt, der im Rahmen dieser Arbeit erzielt wird, resultiert in substanziellen Verbesserungen hinsichtlich Messung, Datenverarbeitung und Datenanalyse und ermöglicht schließlich die quasi *in situ* Charakterisierung von Defektdynamiken in 3D. Das neue Einsatzvermögen von XDL wird erfolgreich in Machbarkeitsstudien und anwendungsbezogenen Beispielen wie der Visualisierung von *Slip Band* Formationen in mechanisch beschädigtem Silizium während einer thermomechanischen Behandlung demonstriert.

CONTENTS

1 INTRODUCTION

Single crystals, due to their optical and electrical properties, play a crucial role in modern technology. Many monocrystalline semiconductors are industrially used in technical applications, especially in micro-electronics, with the most prominent example today being silicon. Due to the ongoing further miniaturization, imperfections like inhomogeneous strain or crystal defects like point-defects (e.g. impurities or vacancies), stacking faults, or dislocations become increasingly relevant and represent important topics of ongoing research [1]. Due to their impact on material properties and because they can be induced during industrial processing, also to previously dislocation-free crystals, dislocations may have crucial effects on the performance and yield of manufactured devices. Therefore, a deeper understanding of these defects and their dynamical behavior under external forces is crucial for avoiding dislocation emergence during growth and processing of monocrystalline semiconductors.
In this regard, imaging techniques represent indispensable tools for the detection and characterization of such defects. X-ray Diffraction Laminography (XDL) recently enabled capturing the three-dimensional (3D) dislocation structure in monocrystalline samples of industrially relevant size, non-destructively [2]. The work presented aims for a refinement of this approach by providing a deeper understanding of the methodology, enhancing related instrumentation, thereby enabling routine application and ultimately extending XDL's capabilities towards the quasi *in situ* imaging of dislocation dynamics.

1.1 EFFECTS OF DISLOCATIONS

Silicon is the most widely used substrate in semiconductor device manufacturing. Substrate flatness is key for technologies build on nm-scale and tolerances for structuring critical elements, e.g., in the case of finFET transistors, decreased to 1 nm [3]. Due to continuous improvement of growth techniques achieved over the last decades, silicon (and other materials) can nowadays be grown dislocation-free. However, dislocations remain a crucial concern, since handling during industrial manufacturing may introduce mechanical damage (scratches and microcracks) to the wafer surface. Afterwards, further treatment during, e.g., CMOS-processing may lead to dislocation nucleation and propagation driven by thermal forces during annealing procedures. Dislocations may extend into previously dislocation-free regions of the crystal volume on the mm-scale and beyond forming complex ar-

rangements, which may lead to slip band formation [4] and warpage [5]. Furthermore, each dislocation reaching the crystal surface results in an atomic (i.e., on nm-scale) step on that surface. Therefore, the defect structure within a bulk or wafer may also degrade the flatness of specimen and hereby the quality as a substrate.
Next to gallium nitride, gallium arsenide is the most important material for high-frequency and opto-electronic applications, where inhomogeneous properties stemming from defects may degrade device yield and performance considerably [6]. It also draws more and more attention as a sensor material, e.g., for high-Z single-photon counting X-ray detectors [7–9], alongside cadmium telloride [10, 11]. Growth, in particular when aiming for large ingots to satisfy industrial demands, and application of materials like GaAs, GaN, and CdTe up to this day face dislocation related challenges [6].
Aluminum nitride is another noteworthy material, which is used as a substrate for UVC emitting devices based on compressively strained $Al_xGa_{1-x}N$ layers aiming for high quantum efficiencies. While progress was possible by the availability of Physical Vapor Transport (PVT) grown AlN substrates, the avoidance of dislocation multiplication during the seed process is crucial for increasing the PVT-AlN crystal's diameter to commercially viable sizes [12, 13].
PVT grown SiC - which will also serve as test material within this work - presently is considered a new material for high performance power devices, which makes the understanding of defect generation during growth, e.g., of basal plane dislocations, [14–16], or micropipes [17], essential.
In summary, the overcoming of dislocation related challenges in crystal growth and semiconductor device manufacturing is of high application oriented scientific and direct industrial interest and requires a deep understanding of defect properties and their behavior and dynamics under external driving forces.

1.2 IMAGING DISLOCATIONS

Although a dislocation's core structure is determined by displacements of atoms on atomic scale, strain and distortions induced to the crystal lattice extend into the bulk volume to ranges on the µm-scale. These lattice distortions lead to a local variation of diffraction conditions, which can be utilized to create image contrast. This fundamental mechanism is exploited by Transmission Electron Microscopy (TEM) as well as X-ray topography, which also represent the two most widely used approaches for the imaging of dislocations. Despite this similarity, the two techniques are highly complementary, motivating a brief summary of their properties and the most impactful developments.

The first detection of individual dislocations by TEM was achieved in 1956 [18, 19]. In 1969 *weak-beam* contrast was introduced to TEM in order to enhance the achievable spatial resolution: A monochromatic beam is used for the targeted excitation of regions with lattice distortions in the vicinity of the dislocation core. This enabled capturing the image of a dislocations with a width of $\sim$ 1.5 nm [20], providing information about the defect structure in unprecedented resolution. With many observations indicating the 3D nature of dislocation structures and the significance of elastic anisotropy, first approaches to recover the 3D information, relied on stereoscopic principles [21, 22]. Developments of suited instrumentation providing the necessary level of precision did take until the early 2000's to enable tomographic approaches to reconstruct the 3D structure of dislocation arrangements from two-dimensional (2D) TEM *quasi*-projections [23]. In 2006, electron tomography was used for the 3D imaging of dislocations and a resolution of $\sim$ 5 nm was achieved [24, 25]. Only recently, dislocations have been imaged in 3D also with resolution on atomic scale by using *high angle annular dark-field scanning* TEM or *HAADF-STEM* [26, 27].
Summarizing, TEM allows for high resolution on the nm-scale and below, however, the strong interaction between electrons and matter (i.e., the sample) also leads to a restriction to particularly thin samples with short path lengths through the material (in the range of 1 µm or below, e.g., for measuring the threading dislocation density in germanium [28]). Sample preparation for TEM is extensive and complicated to a level where it constitutes its own field of research with highly impactful developments, like e.g., the focused ion beam - or *FIB* - method [29, 30]. As a consequence, for the case of crystals of industrially relevant sizes like wafers, which would have to be devided into much smaller specimen, the method has to be considered as destructive. Furthermore, high resolution and small sample sizes in turn limit the size of the capturable crystal volume (typically $\sim$ µm^3). Therefore, TEM requires high dislocation densities ($\sim 10^6/\text{cm}^2$) in order to record a dislocation within the Field of View (FoV) with a reasonable probability.

Starting with the first visual evidence provided in 1931 [31] and the first detection of individual dislocations by X-ray experiments following in 1957 [32, 33], the foundation for developing a variety of methods was laid out.
Regarding X-ray topography based approaches, the availability of synchrotron sources, offering unprecedented beam properties, opened up a field of scientific and technological applications [34–36]: Due to the weaker interaction of X-rays (in comparisson to electrons) with matter, samples can be of considerable thickness ($\sim$ mm), making the techniques applicable to industrially relevant samples. Long-range defect features can be captured, e.g., strain and dislocation structures in wafers of up to 300 mm in diameter [37]. Furthermore, the de-

velopment of Rocking Curve Imaging (RCI) allowed strain analysis, studies on lattice tilts and dislocation distributions and their Burgers vectors (BVs) with µm resolution [38–41]. Using weak-beam conditions reduced the line width of a dislocation image to a few µm [42], while the minimum distance between two features still allowing separation could be reduced to about 10 µm in 2D. Spatial resolution has been further enhanced, especially in the recent years by placing an objective lense in the diffracted beam, an approach known as *X-ray dark-field microscopy*. This allows mapping strain fields, lattice tilts, the evolution of subgrains and also strain fields around individual dislocation with a resolution of 100 to 200 nm [43, 44].
With stereography giving first 3D impressions, so-called *section topography* enabled the extraction of 3D information: A slender X-ray beam is used to capture depth information by imaging cross sections of the sample, enabling the construction of a *quasi* 3D image by stacking up the acquired slices, [32, 45]. Nowadays, this technique is routinely used for the imaging of dislocation structures by translating the sample between image acquisition about 15 µm with typical beam width and height of up to 10 mm and about 15 µm, respectively [46].
The first *topo-tomographic* approaches were developed in 2001 [47]. In the recent years, the newly developed XDL enabled imaging dislocation structures in 3D with 3 to 5 µm resolution, while capturing extensions on a mm-scale in typical industrial silicon wafers. This first application allowed tracing individual dislocation lines within arrangements [2] and due to the non-destructive nature of the method, the information could later be correlated with results from X-ray White Beam Topography (XWBT) and circular polarized visible light differential interference contrast microscopy to yield a comprehensive characterization including the BV distribution and linking the dislocations in the bulk to corresponding surface steps [48, 49].

1.3 OBJECTIVES AND OUTLINE

Recently, the high potential of XDL, in particular for the 3D characterization of industrially relevant samples, has exemplarily been demonstrated by studying dislocations at the onset of slip band formation in silicon wafers. However, only one snap shot during the process could be provided, even though particularly the dynamics and their relation to the involved driving forces are of high scientific and industrial interest. Of course, similar questions also arise for other materials, like GaAs.
Motivated and driven by these demands, in order to achieve routine applicability of XDL, and notably extend its capabilities towards the imaging of dynamical processes, this work aims on key advancements in the following fields:

- A deeper understanding of XDL's methodology, in particular of the topographic contrast formation mechanism
- The realization of a dedicated instrumentation for sample manipulation
- The optimization of data processing and in particular data analysis
- Demonstration of the enhanced Capabilities in feasibility studies

With regard to the first two objectives, a theoretical framework will be utilized to perform simulations of the image formation mechanism and investigate the topographic projection acquisition, the laminographic reconstruction, and the interplay of the two. Concluding from the evaluation of these theoretical analysis, the mechanic requirements regarding stability and precision in motion for an instrument for μ-diffraction imaging will be derived. In particular, the setup will have to fulfill the high demands in both, translational and angular space, stemming from the topographic *and* laminographic aspects combined by XDL.
Continuing, selected reconstruction techniques will be tested with a focus on their suitability for the specific properties of XDL contrast, aiming to decrease the number of projections required for a successful reconstruction. Hereby accomplishing a significant speedup of the measurement procedure, the here presented work aims for enabling the 3D imaging of dislocation evolution with a sufficient resolution of the dynamic processes in a *quasi in situ* fashion, providing a number of snap shots of the emerging dislocation structure during sample treatments typical for industrial semiconductor manufacturing.
A major challenge in this context is stemming from the contrast formation: XDL utilizes a monochromatic X-ray beam to excite lattice distortions in the vicinity of the dislocation core and it has been shown that the crystal region fulfilling the local Bragg condition is view direction dependent. Consequently, the 3D object function one tries to recover from 2D projections becomes view direction dependent itself, which violates requirements for the application of reconstruction techniques. Furthermore, it complicates conventional procedures to determine important parameters for the reconstruction, like e.g., the Center of Rotation (CoR), i.e., the position of the rotation axis. Therefore, concepts and techniques will be developed, that in combination with suited measurement schemes will allow a further optimization of reconstruction parameters. In addition, this work aims to open new routes for the exploitation of contrast properties in order to enhance the spatial resolution of the resulting 3D image and give access to additional information about dislocation properties, like e.g., their BV, directly via XDL data.

Finally, the enhancements and the extended capabilities of XDL accomplished within the frame of this work, will be demonstrated at application relevant examples.

Part I

THEORY

2 X-RAY DIFFRACTION LAMINOGRAPHY

The three-dimensional (3D) imaging of dislocation by means of X-ray Diffraction Laminography (XDL) encompasses concepts from different fields: The X-ray topography based contrast formation combines X-ray physics with elements from solid state physics and crystallography and the subsequent 3D reconstruction relies on techniques known from Computerized Tomography (CT), or more precisely, the generalized case of computed laminography, which will be in more detail discussed later in this chapter. The purpose of this chapter is to introduce these basic concepts and their interplay in the case of XDL. While Chapter 3 will be dedicated in more detail to the basic properties of dislocations, Chapter 4 to the theory of X-ray diffraction, and Chapter 5 to a suited theoretical framework for the simulation of the contrast formation mechanism, respectively, the next section will start with the description of approaches for the 3D reconstruction. This is meaningful since it allows us to introduce important terminology for later reference, to emphasize the challenges related to the recovery of a 3D dislocation structure, and lay out the basis for the selection of suited reconstruction methods covered in Chapter 8. Later on, Section 2.2 will already touch on approaches to apply the laminographic concepts to diffraction contrast, summarizing the findings presented in [49].

2.1 COMPUTERIZED TOMOGRAPHY

In general, tomography is a technique for the cross-sectional imaging of an object. In a broader sense, "tomography" (deriving from ancient greek for "slice writing") can refer to any technique which enables displaying a two-dimensional (2D) cross-section of a 3D object.
However, nowadays we refer to a method that enables imaging the internal structure of an object, without the need to cut it, i.e., one can ascribe a non-destructive nature to tomography, of course only as long as the object is resilient to the amount of radiation that it is exposed to. A prominent example with revolutionary impact first in medicine and later in technical applications is CT, which was developed for medical imaging applications in the 1960s and 1970s [50–52], with G. M. Hounsfield receiving the Nobel prize in 1972 and sharing it with Allan Cormack. In the field of material science, especially utilizing X-ray radiation from synchrotron sources extended the capabilities to 3D microstructural imaging of a variety of specimen [53]. This is due to the advances synchrotron sources provide over laboratory systems, e.g., high photon flux leading to higher spatial resolution with similar

exposure times, monochromatic radiation, and coherence properties.

2.1.1 *The Radon-Transform*

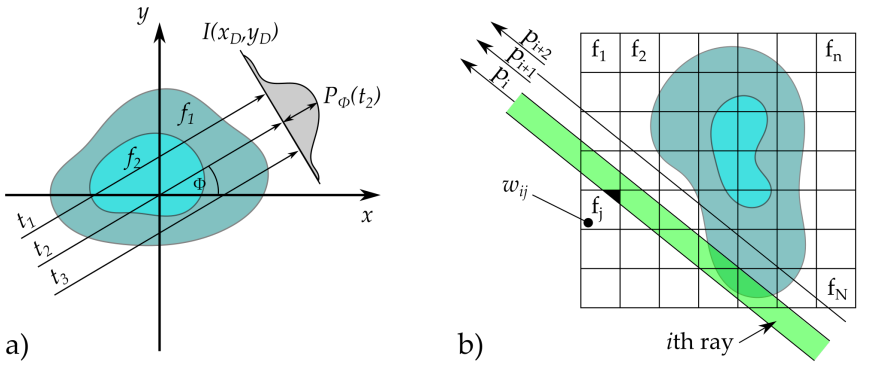

Figure 2.1: a) A 2D object consisting of two materials. Assuming parallel rays and this only to be a cross-section, the 3D case could be imagined consisting of several cross-sections on top of each other, as indicated by the two dimensional intensity profile $I(x_D, y_D)$, where the y_D-axis would be oriented normal to the image plane. b) 2D illustration of an object function $f(x,y)$ in a grid of N cells $f_1, ..., f_N$. The ith ray is determining the ith ray-sum p_i via the weighting factors w_{ij}. Exemplarily shown is w_{ij}, the contribution of the jth cell to the ith ray-sum. It is given by the ratio of the area of the black triangle to the area of the complete cell.

To illustrate the basic mechanisms of CT, here a 2D-object defined by an *object function* $f(x,y)$ is assumed. For the case of parallel rays this may be considered as a cross section of a 3D object with an object function $f(x,y,z)$. The object described by $f(x,y)$ consists of two different materials, which differently interact with the probe radiation resulting in $f(x,y) = f_1$ in the outer and $f(x,y) = f_2$ in the inner material as shown in Fig. 2.1a. As an illustrative example we could consider two materials with different absorption properties regarding X-ray radiation (i.e., the utilization of absorption contrast), given by the attenuation coefficients μ_1 and μ_2. The 2D beam profile can then be recorded by a film or a digital detector after the rays have been transmitted through the sample. The intensity profile $I(x_D, y_D)$ - where x_D and y_D are the Cartesian coordinates on the detector plane - can then be written as

$$I(x_D, y_z) = I_0(x_D, y_z) \mathrm{e}^{-\int_l \mathrm{d}l f_z(x,y)} \tag{2.1}$$

with incoming intensity I_0 and spatial dependent attenuation coefficient $\mu(\boldsymbol{r})$, which shapes the intensity profile according to the ray path

$\boldsymbol{l}$. (The index z again indicates how the case for an 3D object can for parallel rays be seen as an ensemble of such measurements. It will be omitted from now on.) This is the well-known Beer-Lambert law [54] and can also be considered a *contrast function*. The exponent represents a line integral and by parameterizing the line via (ϕ, t) we obtain the so-called Radon transform $P_\phi(t)$ of the funtion $f(x, y)$

$$P_\phi(t) = \int_{\boldsymbol{l}(\phi,t)} f(x,y)\mathrm{d}\boldsymbol{l}, \tag{2.2}$$

which can be rewritten with the δ-distribution as

$$P_\phi(t) = \int_{-\infty}^{\infty}\int_{-\infty}^{\infty} f(x,y)\delta(x\cos\phi + y\sin\phi - t)\mathrm{d}x\mathrm{d}y \tag{2.3}$$

and in connection with the Beer-Lambert law 2.1 and a so-called *flat-field* correction can be expressed by

$$P_\phi(t) = \int_{\boldsymbol{l}(\phi,t)} f(x,y)\mathrm{d}\boldsymbol{l} = -\log\frac{I(x_D)}{I_0(x_D)}. \tag{2.4}$$

A collection of these line integrals, e.g., forming an image on the detector, yields a *projection* along a certain view angle ϕ, i.e., a set of measurements of integrated values of some parameter of the object. In the simplest case the individual rays of one measurement, i.e., in one projection, follow parallel paths through the object as it is the case in Fig. 2.1a.
The inversion of the Radon-transform, i.e., the recovering of the 3D information about the object from a set of 2D projections constitutes the Filtered Backprojection (FBP), one of many so-called reconstruction methods.

2.1.2 *Object Reconstruction*

Based on the very basic description of image formation for CT we will now briefly illustrate two approaches to reconstruct an image of the object from a set of acquired projections.

2.1.2.1 *Filtered Back-Projection*

Due to its extreme accuracy yielding high quality reconstructions and the possibility of fast implementation, e.g., by making use of fast Fourier transforms, FBP is one of the best known and most widely used reconstruction algorithms. It has also been utilized successfully to obtain the 3D information from XDL data sets in [2] and [48]. Therefore, the utilization of FBP will serve as a guiding principle for the

considerations in Chapter 8. We will here give a brief description of the procedure for later reference and a basic understanding of the reconstruction problem itself. First the Fourier slice theorem will be introduced and throughout the consideration a beam geometry of parallel rays will be assumed, which is often an appropriate approximation regarding suited synchrotron sources.
For a realistic (and therefore finite) object in N-dimensional (ND) space, we may presume square integrability of its object function $f(\boldsymbol{r})$, i.e.,

$$\int_{-\infty}^{\infty} |f(\boldsymbol{r})|^2 \mathrm{d}\boldsymbol{r} < \infty. \tag{2.5}$$

Thus, we can write the Fourier transform and the inverse Fourier transform as

$$F(\boldsymbol{k}) = \int_{-\infty}^{\infty} \mathrm{d}\boldsymbol{r} f(\boldsymbol{r}) \mathrm{e}^{-\mathrm{i}2\pi \boldsymbol{r}\boldsymbol{k}} \tag{2.6a}$$

$$f(\boldsymbol{r}) = \int_{-\infty}^{\infty} \mathrm{d}\boldsymbol{k} F(\boldsymbol{k}) \mathrm{e}^{\mathrm{i}2\pi \boldsymbol{r}\boldsymbol{k}} \tag{2.6b}$$

with the ND coordinate vectors in real and Fourier space $\boldsymbol{r}$ and $\boldsymbol{k}$, respectively. A projection of the object function $f(\boldsymbol{r})$ along one dimension $\boldsymbol{i}$ on a (N-1D) submanifold is then expressed by the Radon transform [55] as

$$P_{\boldsymbol{l}}(\boldsymbol{u}) = \int_{-\infty}^{\infty} \mathrm{d}s f(\boldsymbol{u} + s\boldsymbol{l}), \tag{2.7}$$

where we can select $r_i = r_1$ and thus $\boldsymbol{l} = \boldsymbol{e}_1$ without limiting generality. The $\boldsymbol{l}$- or rather $\boldsymbol{e}_1$-indepentend subset $\boldsymbol{u}$ is then given by

$$\boldsymbol{u} = (u_2, ..., u_N) = \sum_{j=2}^{N} u_j \boldsymbol{e}_j, \tag{2.8}$$

which obviously fulfills $\boldsymbol{e}_1 \cdot \boldsymbol{e}_j = 0 \; \forall \; j$. The (N-1D) hyperplane in Fourier space can then be written as

$$F(\boldsymbol{k})|_{k_1=0} = \int_{-\infty}^{\infty} \mathrm{d}r_2 ... \mathrm{d}r_N \left(\int_{-\infty}^{\infty} f(\boldsymbol{r}) \mathrm{d}r_1 \right) \mathrm{e}^{-\mathrm{i}2\pi \sum_{j=2}^{N} k_j r_j}, \tag{2.9}$$

$$F(\boldsymbol{k})|_{k_1=0} = \int_{-\infty}^{\infty} \mathrm{d}r_2 ... \mathrm{d}r_N \Big(P_{\boldsymbol{l}=\lambda \boldsymbol{e}_1}(\boldsymbol{u}) \Big) \mathrm{e}^{-\mathrm{i}2\pi \sum_{j=2}^{N} k_j r_j}. \tag{2.10}$$

This is known as the *Fourier slice theorem*, since a 2D projection of a 3D object allows the calculation of a 2D slice through the 3D Fourier transform $F(\boldsymbol{k})$ of the object function, i.e., a *slice* of $F(\boldsymbol{k})$. With the definition of a matrix $R_{\boldsymbol{e}_j}(\phi)$ performing a rotation of angle ϕ around a unit vector $\boldsymbol{e}_j \perp \boldsymbol{e}_1$ we may perform the calculation for different view directions. It can be shown, that assuming an infinite number of projections is taken, each for a different angle $\phi_i \neq \phi_j + n\pi \; \forall \; i \neq j$ and $n \in \mathbb{Z}$, the Fourier transform $F(\boldsymbol{k})$ would be known at all positions $\boldsymbol{k}$ in Fourier space and thus the object function $f(\boldsymbol{r})$ could be recovered by the inverse Fourier transformation 2.6b. However, since only the acquisition of a finite set of projections is realistic, one has to acknowledge, that the *slices* intersect in the origin and therefore the sampling of the Fourier space becomes less dense with increasing distance from the origin. Often times a weighting factor is applied for compensation, i.e., one uses a *filtered* Fourier transforms of the projections. The derivation of such a filter for regular CT in the 2D-case and for a geometry of parallel beams is straight forward [56].

2.1.2.2 *Algebraic Reconstruction Techniques*

In contrast to FBP, image reconstruction by Algebraic Reconstruction Techniques (ART) is carried out completely in real space. In general this approach is simpler than transform based methods. However, it usually requires a lot larger amount of computational memory, furthermore, implementations of algebraic methods are also inferior to transformation based techniques regarding speed and accuracy. On the other hand, if computational power, memory, and time is available, they usually produce better results for data sets with only few projections. Since the performance of selected ARTs will be addressed in Chapter 8, at this point the basic approach will be briefly illustrated at the example of a 2D image reconstruction, basically following the description of the Kaczmarz approach [57] given in [56].
Assuming an object encompassing a total of N cells and defined by an object function $f(x, y)$ the ray-sum p_i of the ith ray is given by

$$\sum_{j=1}^{N} w_{ij} f_j = p_i, \qquad i = 1, 2, ..., M \tag{2.11}$$

where M is the total number of rays in all projections and w_{ij} is the weighting factor equal to the area in the jth cell illuminated by ith ray, i.e., the contribution of the jth cell to the ray-sum p_i, also see Fig. 2.1b. Note, that rays here are defined not as thin lines but as broad stripes. Rewriting Eq. 2.11 for illustration purposes we obtain:

$$\begin{aligned} w_{11}f_1 + w_{12}f_2 + \cdots + w_{1N}f_N &= p_1 \\ w_{21}f_1 + w_{22}f_2 + \cdots + w_{2N}f_N &= p_2 \\ \vdots \qquad\qquad\qquad\qquad &= \vdots \\ w_{M1}f_1 + w_{M2}f_2 + \cdots + w_{MN}f_N &= p_M. \end{aligned} \tag{2.12}$$

Note, that each line in Eq. 2.12 may be written in the form

$$\boldsymbol{w}_i \cdot \boldsymbol{f} = p_i \tag{2.13}$$

with $\boldsymbol{w}_i = (w_{i1}, w_{i1}, ..., w_{iN})$. Thus, Eq. 2.13 can be interpretated as a hyperplane in ND space where the correct reconstruction image corresponds to a single point, which would be given by the intersection of all hyperplanes given by the lines of 2.12. After some geometrical considerations and calculation steps one obtains the iterative formula

$$\boldsymbol{f}^i = \boldsymbol{f}^{i-1} - \frac{\left(\boldsymbol{f}^{i-1} \cdot \boldsymbol{w}_i - p_i\right)}{\boldsymbol{w}_i \cdot \boldsymbol{w}_i} \boldsymbol{w}_i. \tag{2.14}$$

The computation starts with an initial guess for the solution, which is successively projected onto the hyperplanes in Eq. 2.12 to yield $\boldsymbol{f}^M$. The next iteration then starts by projecting $\boldsymbol{f}^M$ onto the first line in Eq. 2.12 and so on.
For faster computation, approximations could be used, e.g., for the weighting factor w_{ij}. Orthogonalization schemes to be applied to Eq. 2.12 were proposed to increase the speed of convergence [58]. With the continuously increasing capabilities of GPUs over the last years the improvement of reconstruction algorithms is further advancing, [59, 60]. Again it is important to note, that this section's purpose is not a detailed description of ARTs or their implementation. The intend of presenting this basic principles is rather to illustrate two major take-aways: First of all, in this basic description of ARTs the value of each cell f_j is changed with every projection onto the next hyperplane. Secondly, one finds that this kind of reconstruction techniques allow for a straight-forward incorporation of *a priori* knowledge: For example, the assumption could be made, that there are no negative values in the reconstruction image. Furthermore, one might know that the structure to be reconstructed only occupies certain regions of the volume while great parts are empty. Therefore, the corresponding cells in $\boldsymbol{f}$ could be confined to zero throughout the computation.

2.2 LAMINOGRAPHY AND DIFFRACTION CONTRAST

Laminography refers to a generalization of the above discussed tomography, allowing an inclination of the rotation axis with respect to the

beam direction about an angle θ, as shown in Fig. 2.2a. Throughout this thesis, we will refer to θ as the *laminographic tilt angle* not to be confused with the *tomographic rotational angle* ϕ, with the corresponding axes being denoted as $\boldsymbol{\Theta}$ and $\boldsymbol{\Phi}$, respectively. Together these angles define the view direction. Nevertheless, for easier readability and due to the fact that θ is often fixed or only subject to minor variations during a measurement ($\sim 10^{-3\circ}$), the view direction of the 2D image will often be only denoted by ϕ.
Utilizing synchrotron radiation laminography has been proven to be very well suited for the investigation of flat specimen [61, 62]. Theoretical frameworks for reconstruction have been developed and are available for routine application [63]. Furthermore, phase contrast based approaches have been applied and 3D imaging of structures and compositions in laterally extended objects on the nm-scale has been realized [64, 65]. Commonly, methods of this kind are summarized under the umbrella term *synchrotron radiation computed laminography*.
The laid out groundwork becomes important with the transition from absorption contrast (assumed in the previous sections) to diffraction contrast. Combining diffraction contrast with a tomographic approach requires the Bragg condition to be fulfilled during the sample rotation for the acquisition of images from different view directions. In other words, the tomographic rotation axis $\boldsymbol{\Phi}$ has to be aligned parallel to a selected reciprocal lattice vector: $\boldsymbol{\Phi} \parallel \boldsymbol{h}_{hkl}$. Therefore, the laminographic tilt angle equals the Bragg angle: $\theta = \theta_B$. Two geometries enable this diffraction based approach: so-called Bragg-reflection geometry (BRG), where the sample, e.g., a wafer is mounted similarly to the regular laminographic geometry, see Fig. 2.2b. And Laue-transmission geometry (LTG) where the sample is mounted upright and then tilted, the selected reciprocal lattice vector $\boldsymbol{h}_{hkl}$ is then parallel to the sample surface, not the surface normal, see Fig. 2.2c.

Although, an incoming X-ray beam $\boldsymbol{k}_0$ changes its direction when diffracted at a crystal volume by $2\theta_B$ to $\boldsymbol{k}_h$, the diffracted X-rays may be extended to obtain a virtual straight ray path $\boldsymbol{k}_0'$ that is equivalent to the one in the laminographic case as illustrated in Frame 2.2a by the dotted lines. This means, that independent of the sample shape or dimensions the reconstruction problem of data sets obtained by employing diffraction contrast is always of a more general laminographic nature due to the tilt of the rotation axis about θ_B.
Another important aspect of laminography is that in contrast to tomography (i.e., the special case of $\theta = 0^\circ$) it is not possible to cover the whole Fourier space. A detailed investigation of the Fourier space coverage in dependence of the laminographic tilt angle θ and the accessible acquisition interval (e.g., if a full rotation of 360° is unfeasible or even prohibited by the sample geometry - this case is usually referred to as limited angle laminography) can be found in [49]. Eventually, the information provided by a single 130°-acquisition interval has

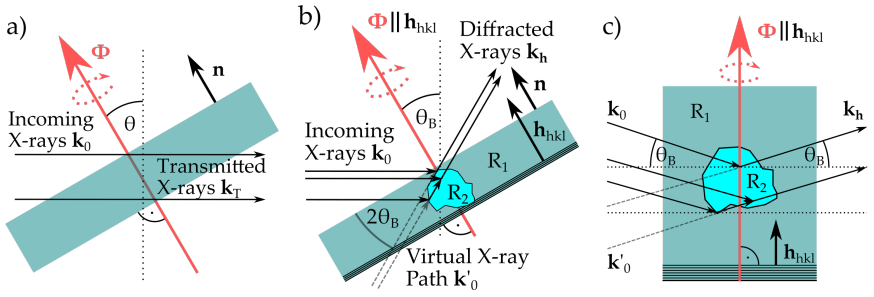

Figure 2.2: a) Laminography of a laterally extended sample. If, e.g., absorption contrast is exploited the X-rays follow straight lines but they are still tilted with respect to the rotation axis $\mathbf{\Phi}$ by angle θ. b) Direct transition to *diffraction laminography* for $\theta = \theta_B$, with θ_B being the Bragg angle. This measurement geometry is also referred to as BRG. c) Tomography approach utilizing diffraction contrast. Making use of virtual beams $\boldsymbol{k}_0'$ one can assume undiffracted beams, i.e., beams that follow a straight line, but are tilted towards the rotation axis by the Bragg angle θ_B. This measurement geometry is also referred to as LTG.

proven to be sufficient to reconstruct the 3D structure of dislocation arrangements via FBP in silicon in previous studies.

2.2.1 *Object Function and Contrast Function for Diffraction Contrast*

In the first section of this chapter the object function - later referred to as $f(\boldsymbol{r})$ - was given by the absorption coefficient, which may vary in an object due to its composition of different materials. To clearly illustrate the basic challenges regarding diffraction contrast, a definition of the object function and the contrast function for projection acquisition is meaningful. The object function simply represents a localized property of the object. In the example given above this is the attenuation factor. The contrast function then describes how this object property is mapped onto a detector to create a 2D projection image. Thus, in the context of Section 2.1 the contrast function would be given by the equivalent Eqs. 2.1, 2.2, 2.3, or 2.4. These represent the *projection criteria*, which is a requirement for tomographic or laminographic reconstruction to be applicable.
To extend the considerations to diffraction contrast one may assume a local reflectivity $R(\boldsymbol{r})$ as an object function. Under the assumption that intensities of the reflected rays add up incoherently along $\boldsymbol{k_h}(\phi) = \boldsymbol{l}(\phi)$, the intensity profile can again be written as a line integral:

$$I(x_D, y_D) = \int_{\boldsymbol{k}_h(\phi)} \mathrm{d}l\, I_0 R(\boldsymbol{r}) = I_0 \int_{\boldsymbol{l}(\phi)} \mathrm{d}l(\boldsymbol{r}) R(\boldsymbol{r}) = P_\phi^R(x_D, y_D). \quad (2.15)$$

With an homogeneous illumination that can be expressed via a constant factor I_0 the measured intensity distribution on the detector can be interpreted as projection of the reflectivity $R(\boldsymbol{r})$ along the direction of the reflected - or diffracted - X-rays $\boldsymbol{k_h}(\phi)$ or $\boldsymbol{l}(\phi)$. This makes use of the concepts of virtual rays to avoid the description of a change of directions from $\boldsymbol{k}_0$ to $\boldsymbol{k_h}$. Hence, one can interpret Eq. 2.15 as the contrast function for diffraction contrast, which in connection with the object function $R(\boldsymbol{r})$ fulfills the projection criteria. However, so far an additional absorption by the material has been neglected. Following [49] this can be respected by defining an *effective* local reflectivity $\tilde{R}(\boldsymbol{r})$ as

$$\tilde{R}(\boldsymbol{r},\phi) = R(\boldsymbol{r})\mathrm{e}^{-\mu_0(l_0(\boldsymbol{r},\phi)+l_{\boldsymbol{h}}(\boldsymbol{r},\phi)} \tag{2.16}$$

where $l_0(\boldsymbol{r},\phi)$ and $l_{\boldsymbol{h}}(\boldsymbol{r},\phi)$ denote the path length of the incident beam through the material until reaching the reflecting volume at $\boldsymbol{r}$ and the path length starting from this volume to the sample's surface on the way to the detector, respectively. This is illustrated in Fig. 2.2c. Apart from sample shapes that have an cylindrical symmetry with respect to the selected reciprocal lattice vector $\boldsymbol{h}_{hkl}$ (and therefore with respect to $\boldsymbol{\Phi}$) this obviously introduces an intrinsic ϕ-dependence to the projected intensities which can be written as

$$\tilde{P}^{\tilde{R}}(x_D, y_D, \phi) = I_0 \int_{l_{\boldsymbol{h}}(x_D,y_D,\phi)} \mathrm{d}l\tilde{R}(\boldsymbol{r},\phi). \tag{2.17}$$

The dependence on the view angle consequently means, that images acquired from different view angles, each show projections of a different object, which can mathematically not be described by the Radon transform. Therefore, in principle, reconstruction techniques based on this approach have to be ruled out. However, for simple sample geometries (like e.g., flat and laterally extended with a homogeneous thickness, like wafers) the effects of absorption on the projection images can easily be corrected afterwards, where in LTG basically all rays constituting one projection have to pass the same path length through the material.

2.2.2 *Imaging Dislocations by X-ray Diffraction Laminography*

The presented approach to define the local reflectivity $R(\boldsymbol{r})$ may be feasible for some cases, if absorption can be neglected or its effects can be corrected afterwards. In the case of imaging dislocations by means of XDL, however, a monochromatized X-ray beam is diffracted by deformations of the crystal lattice in the vicinity of dislocations, while aiming for the undistorted dislocation-free crystal matrix remaining unexcited. This is also referred to as *weak-beam* contrast and enhances

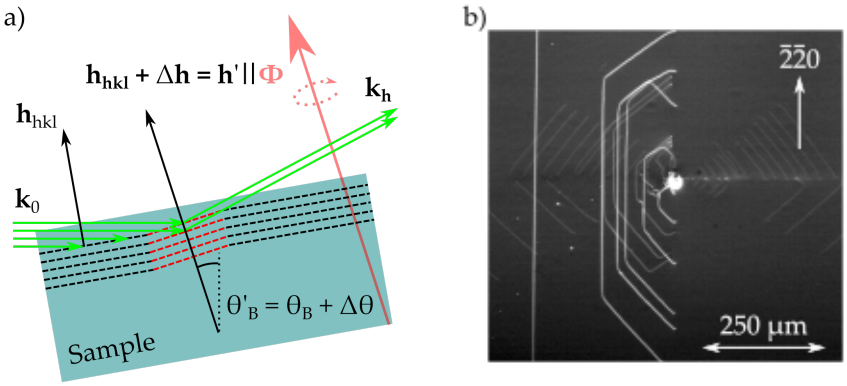

Figure 2.3: a) Illustration of weak-beam contrast created by distortions in a crystal lattice. The black dotted lines represent a set of lattice planes *hkl*, while the distortions, which correspond to the local lattice vector $\boldsymbol{h}' = \boldsymbol{h}_{hkl} + \Delta\boldsymbol{h}$, are colored in red. $\boldsymbol{h}'$ is now sensitive to radiation impinging from an angle $\theta'_B = \theta_B + \Delta\theta$, note, how X-rays hitting the undistorted lattice are not diffracted since here the Bragg condition is not fulfilled. b) Exemplary XDL projection image of a dislocation structure in silicon. The image was acquired in LTG at an energy of 25 keV exploiting the $\bar{2}\bar{2}0$-reflex. The sample was tilted by 0.003° out of the Bragg peak, i.e., the weak-beam paramater was set to $\Delta\theta = 0.003°$.

spatial resolution since it usually prevents dynamical features to dominate the image formation and enables a kinematic description of the diffraction process at distorted crystal regions, also see Section 4.3. This is accomplished by introducing a slight deviation to the tilt angle θ, the so-called *Bragg deviation* or *weak-beam parameter* $\Delta\theta$:

$$\theta'_B = \theta_B + \Delta\theta. \tag{2.18}$$

For the case of silicon a suited deviation is in the magnitude of $\Delta\theta \sim 10^{-3\circ}$. It is intuitively clear, that this means that the reflectivity is not only depending on the view direction ϕ but also on the lattice distortion or the strain in the crystal lattice and thereby on the specific properties of the dislocation itself. Where regular tomography and laminography assume a local and scalar object function, for the case of XDL the object function and its interplay with the contrast function to create a 2D image that could be deemed as a projection is much more complicated and - strictly speaking - can not be described via line integrals. For instance, a reasonable choice for the object function is given by the displacement field $\boldsymbol{u}(\boldsymbol{r})$, describing the lattice distortions close to a dislocation. This choice would represent an inherent object property that does not change. But considering, how this property is mapped or projected onto a detector, e.g., by making use of the *effective misorientation* $\delta(\boldsymbol{r})$, one finds that the excited crystal volume fulfilling the local Bragg condition for Eq. 2.18 is depending on the selected

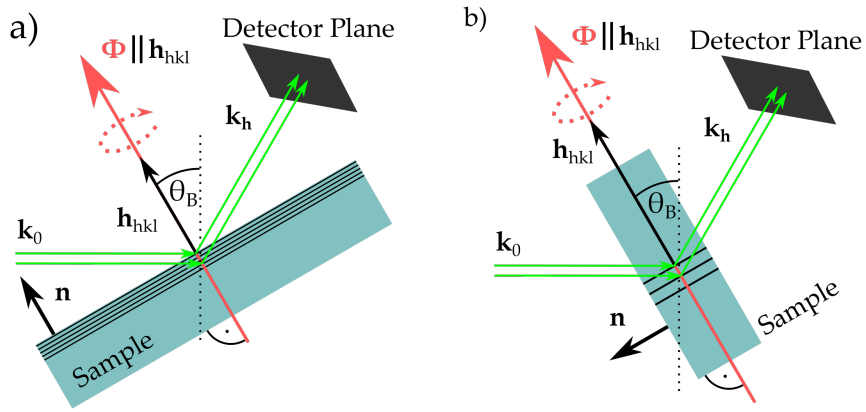

Figure 2.4: Schematic view of two possible measurement geometries typical for XDL data acquisition: a) BRG enabling a full rotation about the tomographic rotation axis $\boldsymbol{\Phi}$. b) LTG is limited for laterally extended wafer shapes, since image recording with the diffraction plane oriented parallel to the sample's lateral extension is not feasible, resulting in limited angle laminography.

reciprocal lattice vector $\boldsymbol{h}_{hkl}$, $\boldsymbol{k}_{\boldsymbol{h}}$ (view direction and energy of the X-ray beam), and the Burgers vector (BV) $\boldsymbol{b}$ describing the dislocation's properties, which will be discussed in more detail in the next chapter. The considerations in Chapter 5 will show that while varying the view angle ϕ the illuminated crystal volume circles around the dislocation core and is localized in a distance of a few µm, resulting in the resolution limit in the magnitude of several µm as stated in [2, 48, 49].

2.3 COMPARISON OF MEASUREMENT GEOMETRIES

Two favorable measurement geometries, that enable the exploitation of crystal reflexes whose respective reciprocal lattice vectors are oriented in line with certain directions of a laterally extended sample geometry, were already mentioned above:

In BRG the sample is placed flat on the sample table and tilted towards the incoming X-ray beam to reach Bragg condition for a reciprocal lattice vector $\boldsymbol{h}_{hkl}$, which is oriented parallel to the sample surface normal $\boldsymbol{n}$ and coincides with the tomographic rotation axis $\boldsymbol{\Phi}$, see Fig. 2.4a.

Another possible sample position is referred to as LTG, where the sample is placed upright on the table. Here, the selected reciprocal lattice vector $\boldsymbol{h}_{hkl}$ is oriented perpendicular to the sample surface normal $\boldsymbol{n}$ and again coincides with the tomographic rotation axis $\boldsymbol{\Phi}$, compare Fig. 2.4b.

Naturally, both geometries come with specific advantages and disadvantages. Obviously, BRG provides access to the whole angular range of 360° for the tomographic rotation angle ϕ, since the sample shape

provides rotational symmetry with respect to the $\mathbf{\Phi}$-axis (at least if we restrict the consideration to a round-shaped region of the sample containing the whole illuminated crystal volume). LTG, however, leads to difficulties approaching tomographic angles of $\phi = \pm 90°$, since in these cases the X-ray beam would have to follow a path through the whole lateral extension of the sample. ($\phi = 0°$ usually refers to the case where the surface normal $\boldsymbol{n}$ is parallel to the diffraction plane.) Consequently, the image acquisition for LTG will from now on be considered as restricted to two wedges each with an angular range of 130° evenly distributed around the surface normal of the sample's front- and rear-side, respectively, see Fig. 2.5c. Additionally, we may note that in BRG the path length through the material is constant with changing view angle ϕ, but depends on the depth in which the diffracting crystal volume is located within the wafer. In LTG on the other hand, the path length is strongly dependent on ϕ but the same for every ray contributing to a single projection, since it does not depend on the localization of the diffracting region within the sample volume. At first glance, full accessible angular range and view direction independent X-ray path lengths may suggest that BRG is preferable. But, with typical Bragg-angles during XDL-scans ranging from 4 to 10°, path lengths in BRG turn out significantly longer than in LTG, if the diffracting dislocation structure is not located close to the sample surface. The ratio of diffracted and incoming intensity over rotational angle ϕ is shown in Fig. 2.5a. The calculations simulated diffraction at the 004-reflex in BRG and diffraction at the $\overline{2}\overline{2}0$-reflex in LTG for silicon, both cases assuming an X-ray-beam energy of 25 keV resulting in Bragg angles of $\theta_B^{BRG} = 10.523°$ and $\theta_B^{LTG} = 7.420°$. Sample and measurement geometries are illustrated in frames in 2.5b and 2.5c.

Since the direction dependent attenuation in LTG can be compensated rather well with a simple division of the acquired images by the respective attenuation factors, Fig. 2.5a already shows the advantages of LTG. Especially, since in BRG features in different depth will create image contrast by X-rays with significantly varying path lengths through the material. This image property is not easily compensated and may lead to various problems during data processing. Furthermore, previous studies showed that BRG is more sensitive to surface features, which overshadow the underlying dislocation structure. Although a 3D reconstruction is still possible, this is a strong argument for employing LTG for XDL-projection acquisition, especially when aiming to significantly reduce the required number of projections.
Due to these reasons, LTG allows the acquisition of XDL data that yields 3D reconstructions of higher quality. Therefore, this work will strongly focus on XDL's application in LTG. It has even turned out that the result is improved further by only using images from one of the two 130°-wedges as input, if one assumes a local reflectivity $R(\boldsymbol{r})$ and neglects its $\boldsymbol{k_h}$-dependence. However, considerations presented later

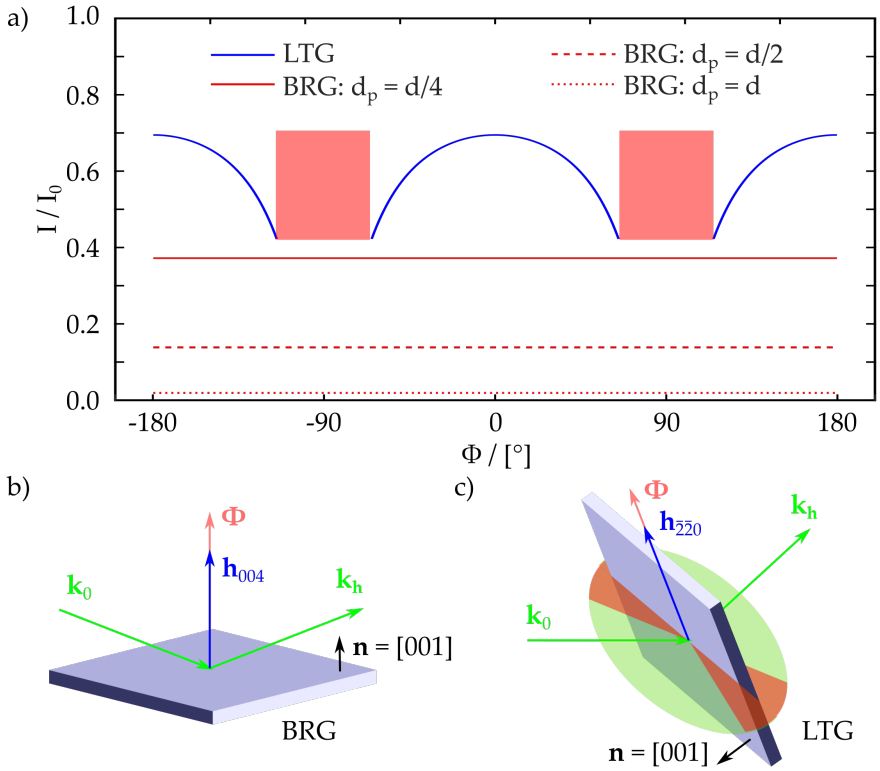

Figure 2.5: a) Calculated X-ray attenuation for LTG and BRG in comparison for a silicon wafer with a thickness of d =750 µm and a surface normal parallel to the crystal direction [001]. For BRG - illustrated in b) - the constant attenuation is plotted for three different penetrations depths d_p. For the last case only roughly 2% of the incoming intensity leave the material. The gaps (light red areas) in the case of LTG - illustrated in c) - result from the restriction to two wedge-like measurement intervals of 130° each, this is also illustrated in frame c): Accessible ranges are shown in green, unaccessible ranges in red. Here, the 0°-degree direction is assigned to the case were the diffraction plane is parallel to the plane spanned by rotation axis $\boldsymbol{\Phi}$ and surface normal $\boldsymbol{n}$ of the sample.

in Chapter 6 of this thesis will strongly support the incorporation of both acquisition intervals. Nevertheless, it is noteworthy, that BRG is more suited for other applications, such as so-called Multi-Azimuth Rocking Curve Imaging (MARCI), e.g. for the mapping of strain around an indent-like damage, which is typically located close to the sample surface.

From this point on throughout this work - if not explicitly declared otherwise - measurements in LTG, as illustrated in more detail in Fig. 2.6, will be assumed. Here, the laboratory coordinate system Σ_L is determined by the incoming X-ray beam defining the $\boldsymbol{y}_L$-axis and the vertical $\boldsymbol{z}_L$-axis. The sample coordinate system Σ_S emerges from Σ_L by rotation about the laminographic tilt axis $\boldsymbol{\Theta}$ which is parallel to $\boldsymbol{x}_L$ and

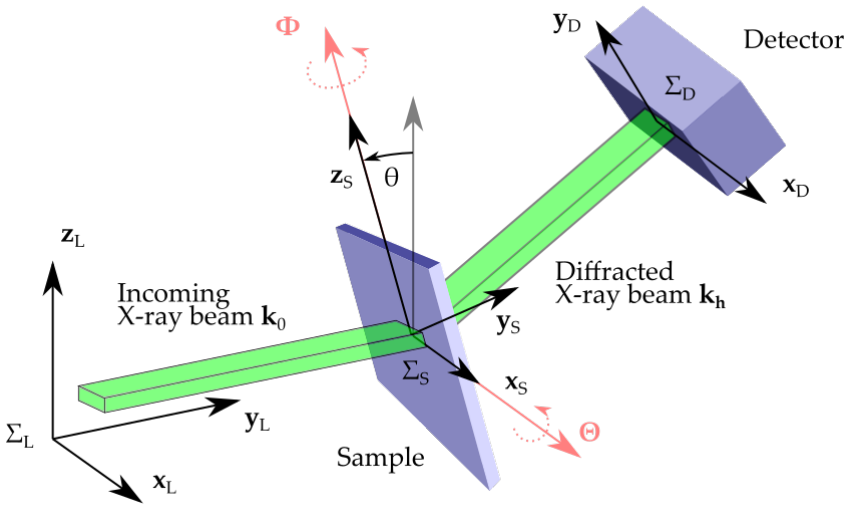

Figure 2.6: Schematic view of a typical XDL measurement, showing the laboratory coordinate system Σ_L, the sample coordinate system Σ_S which emerges from Σ_L by a rotation θ about the x-axis, and the 2D detector coordinate system Σ_D. In shallow red the relevant rotation axes $\boldsymbol{\Theta}$ and $\boldsymbol{\Phi}$ are indicated.

centered in the illuminated crystal volume. The tomographic rotation axis $\boldsymbol{\Phi}$ is aligned parallel to the selected reciprocal lattice vector $\boldsymbol{h}_{hkl}$ with $hkl = \overline{2}\overline{2}0$ if not declared otherwise. (Note, that $hkl = \overline{2}\overline{2}0$ is chosen over $hkl = 220$ for easier comparison to data and results in ongoing and from earlier studies, in particular the ones presented in [2, 48, 49]. More details can be found in Appendix H.) Furthermore, we will assume a detector tilted by $2\theta_B$, so that the diffracted X-ray beam hits the detector plane perpendicularly.

2.4 SUMMARY

Technically speaking, tomography and its generalization laminography require a localized sample property, that can be expressed by a scalar function, the object function. The contrast function then describes the image formation by projecting this property via line integrals onto the detector plane. When utilizing diffraction contrast an object function can be formulated but the interplay with the contrast function becomes view direction dependent. In addition, the image formation follows physical principles of X-ray diffraction, involving non-local and non-linear properties and concepts and thus represents a much more complex problem than projecting, e.g., absorption properties onto the detector plane. Therefore the projection criteria is violated, i.e., reconstruction techniques are not applicable by default.
Furthermore, this combination of laminography and topography results in complex requirements regarding instrumentation used for sample manipulation during a measurement. Laminography requires

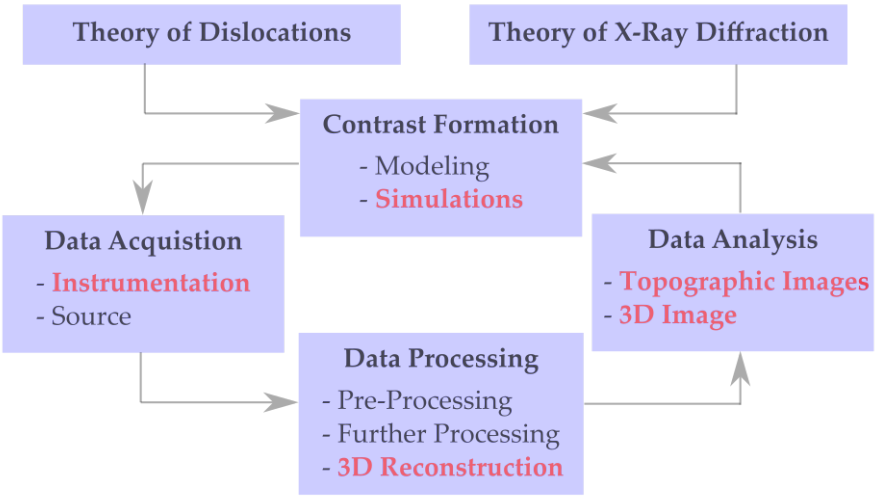

Figure 2.7: Schematic overview illustrating the connections of theoretical background to the different steps in the workflow of the development continuation of XDL. The foci of the here presented work are highlighted in red.

a high precision of motion in real space, while topography - especially if a monochromatic beam is applied to create weak-beam contrast - needs a high resolution in reciprocal space.
In the following chapters the theoretical basis for a framework enabling the simulation of the contrast formation will be laid out. Simulations will then be utilized to determine the specifications of a dedicated instrumentation and select suited 3D reconstruction techniques with a high level of resilience against the inconsistencies inherent in XDL data. Furthermore, based on this simulations concepts will be developed and applied to approximate an object function that describes the position of the dislocation core rather than the lattice distortions that locally fulfill the Bragg condition and contribute to the contrast formation. Retrieving the dislocation core position has the advantages, that it is independent of view direction, dislocation properties, and measurement parameters like the weak-beam parameter $\Delta\theta$. Fig. 2.7 illustrates the interplay of the theoretical, instrumentational and laminographic (i.e., the reconstruction problem) aspects of XDL.

To end this chapter, some important measurement routines and a data processing technique will briefly be described for later reference:

XDL SCAN The acquisition of topographic weak-beam images from different view directions within a certain angular range turning about the tomographic rotation axis $\mathbf{\Phi}$. In this work these topographs will be referred to as XDL *projections*, *quasi projections*, or just *projections*.

ROCKING SCAN The acquisition of topographic images with a monochromatic beam, while the laminographic tilt angle θ is varied in a step-wise manner to sample the rocking curve at a given position ϕ.

MULTI-AZIMUTH ROCKING CURVE IMAGING MARCI refers to the acquisition of rocking scans from different view directions within a certain angular range turning about the tomographic rotation axis $\mathbf{\Phi}$.

VIRTUAL WEAK BEAM Although, Virtual Weak-Beam (VWB) has not been developed in the frame of this thesis, it is utilized for certain reconstructions. A rocking scan enables extracting the rocking curve in every single detector pixel; by certain processing steps a virtual projection for a selected weak-beam parameter can be computed pixel-wise from this information. The approach is currently under development, but has already proven very useful for selected application cases.

3

PROPERTIES OF DISLOCATIONS

Perfect crystals do not - or only to some extend, e.g., in a confined region of a bulk - exist in reality. The regular periodic atom arrangement is disturbed by defects, which may be classified into *point*, *line*, *planar*, or *volume* defects. Point defects can again be devided into *intrinsic* defects, like vacancies or self-interstitial atoms, and *extrinsic* defects, like impurities, which can again be devided into two types: *substitutional* and *interstitial*, where a regular atom of the lattice is replaced by an impurity atom or the impurity is inserted between regular lattice atoms, respectively, analogous to the intrinsic point defects. Planar defects are stacking faults, grain boundaries and twin boundaries. The surface of a crystal is also considered a planar defect, since the translational symmetry ends at this boundary and thus any real crystal is not defect-free. Voids or precipitates are volume defects [69]. Line defects are also referred to as dislocations and they are the key subject to defect imaging by means of X-ray Diffraction Laminography (XDL) within the frame of this work.
Although the atomic displacement is in the magnitude of the lattice constant (in the case of silicon $\sim 10^{-10}$m) the distortions in the crystal lattice - resulting in so-called *strain* - reach much further ($\sim 10^{-6}$m, i.e., their reach is on the µm scale). Lattice deformations in the vicinity of dislocations may alter the material properties significantly: This ranges from electronic properties (already mentioned in Chapter 1) affecting, e.g., battery performance [66] over radiation resistance to mechanical strength. In fact, historically a broad range of theories and models were developed around the topic of dislocations, e.g., dissociated [67] and circumstances leading to sessile dislocations [68] had been suggested, explaining nearly any result in plastic deformation before techniques were available to proof them or observe the nature and effects of dislocations directly under a microscope [23]. For later reference, especially in connection to the theoretical considerations in Chapter 5, in this chapter basic properties of dislocation and their description will be introduced, basically following [69]. Note, that the discussion will be restricted to *perfect* dislocations, since *partial* dislocations have not been observed by XDL yet. Therefore, considerations regarding partial dislocations would be entirely theoretical and not be verifiable by comparison with measurement data.

3.1 SCREW AND EDGE DISLOCATIONS

Dislocations constitute an irregularity within the crystal lattice, which may be described as following an imaginary line. In the following the direction of this line will be denoted by the vector $\boldsymbol{l}$, also see Fig. 3.1. There are two major types of dislocations: *edge* dislocations and *screw* dislocations. The easier example are the so-called *edge* dislocations where the displacement of atoms basically occurs within a lattice plane and the line-like character stems from a re-occurrence of the same irregularity at the corresponding position in the parallel lattice planes. Thus, the misplacement is perpendicular to the line direction $\boldsymbol{l}$. *Screw* dislocations on the other hand describe a spiral misplacement continuing periodically in adjacent lattice planes. The geometrical displacement of atoms characterizing dislocations can be expressed via the so-called Burgers vector (BV) $\boldsymbol{b}$ with its length being denoted by $|\boldsymbol{b}| = b$, [69–71]. To construct the BV one may utilize the most useful definition of a dislocation: the Burgers circuit. The Burgers circuit describes a closed atom-to-atom path. If the same path-steps are performed in a perfect reference lattice and the path is not closed, the original path encloses one or more dislocations. The BV $\boldsymbol{b}$ is then given by the path from finishing to staring point. A clear definition can be given by relying on the right-hand/finish-start - or short RH/FS - convention [72], which connects the sign of the BV $\boldsymbol{b}$ to the sign of the selected line direction $\boldsymbol{l}$: If the sign of $\boldsymbol{l}$ is changed, the sign of $\boldsymbol{b}$ changes accordingly. This is illustrated in Fig. 3.1 for the case of a pure edge (Frames 3.1a and 3.1b) and a pure screw dislocation (Frames 3.1c and 3.1d).

Fig. 3.1 leads to following conclusions for the two basic types of dislocations:

- In the case of a pure edge dislocation the BV is always directed perpendicular to the line direction: $\boldsymbol{b} \perp \boldsymbol{l} \Rightarrow \boldsymbol{b} \cdot \boldsymbol{l} = 0$.
- For a pure screw dislocation the BV is always parallel or antipralel to the line direction: $\boldsymbol{b} \parallel \pm\boldsymbol{l}$.

In reality, next to the two basic dislocation types often mixtures occure, that contain an edge- and a screw-part, b_s and b_e, respectively, which are then given by:

$$b_e = |\boldsymbol{l} \times (\boldsymbol{b} \times \boldsymbol{l})| \tag{3.1}$$

$$b_s = \boldsymbol{b} \cdot \boldsymbol{l}. \tag{3.2}$$

For the case of a face-centered cubic structure - like in a broader sense diamond or silicon - the shortest lattice vectors are $\langle 001 \rangle$ and $\frac{1}{2}\langle 110 \rangle$. Since the energy of a dislocation (screw, edge, and mixed) is proportional to b^2, with

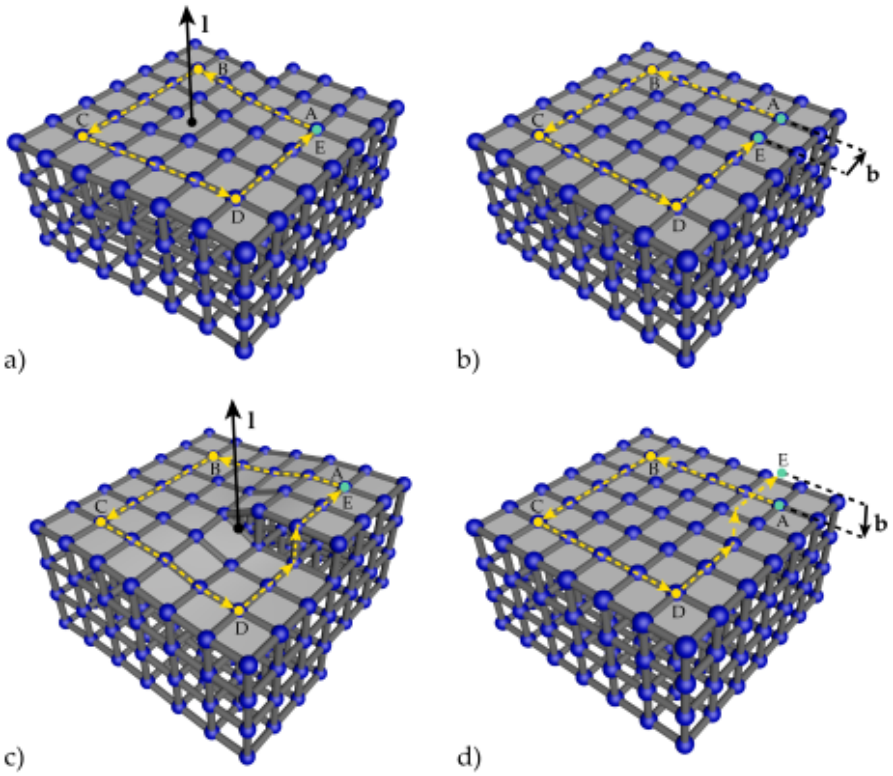

Figure 3.1: Illustrations of the two basic dislocation types: a) Edge dislocation in a simple cubic crystal lattice with right handed Burgers circuit (yellow) and line direction $\boldsymbol{l}$. b) Burgers circuit from a) mapped to a perfect crystal lattice with resulting BV $\boldsymbol{b}$. c) Illustration of a screw dislocation similar to a). d) Burgers circuit corresponding to c) and resulting BV $\boldsymbol{b}$ for a screw dislocation. (Illustration taken from [49] with permission of the author.)

$$\text{Perfect}\left(\boldsymbol{b}=\frac{1}{2}\langle 110\rangle\right): b^2=\frac{a^2}{4}\left(1^2+1^2+0\right)=\frac{a^2}{2} \tag{3.3}$$

this means $E \sim a^2/2$ for the BVs with directions $\langle 110\rangle$ and $E \sim a^2$ for $\langle 001\rangle$ directions, respectively. This makes dislocations with a BV described by Eq. 3.3 the energetically most favourable case, explaining why dislocations of this kind are present far more often and dislocations with $\boldsymbol{b} \in a\langle 001\rangle$ are only rarely observed, [69]. Furthermore, dislocations of this kind will leave behind a perfect crystal after propagation through a certain volume, since $\frac{1}{2}\langle 110\rangle$ is a translational vector of the lattice, making them *perfect* dislocations. These circumstances justify further confining the considerations presented in this work to BVs in the $\langle 110\rangle$ directions.

3.2 DISPLACEMENT FIELD OF A DISLOCATION

Of special importance for the considerations in Chapter 5 regarding the contrast formation due to excitation of the lattice distortions in the vicinity of a dislocation is the displacement field $\boldsymbol{u}(\boldsymbol{r}) = [u_x(\boldsymbol{r}), u_y(\boldsymbol{r}), u_z(\boldsymbol{r})]$. It describes the displacement of a point (or atom) in a strained body from its position in the unstrained body via

$$\boldsymbol{r}' = \boldsymbol{r} + \boldsymbol{u}(\boldsymbol{r}). \tag{3.4}$$

Assuming linear elasticity and isotropic properties of the material, $\boldsymbol{u}(\boldsymbol{r})$ for an infinitely long, straight dislocation can be written in Cartesian coordinates as [70]:

$$u_x(\boldsymbol{r}) = \frac{b_e}{2\pi}\left[\arctan\left(\frac{y}{x}\right) + \frac{xy}{2(1-\nu)(x^2+y^2)}\right] \tag{3.5a}$$

$$u_y(\boldsymbol{r}) = \frac{-b_e}{8\pi(1-\nu)}\left[2(1-2\nu)\ln\left(\frac{\sqrt{x^2+y^2}}{r_0}\right) + \frac{x^2-y^2}{x^2+y^2}\right] \tag{3.5b}$$

$$u_z(\boldsymbol{r}) = \frac{b_s}{2\pi}\arctan\left(\frac{y}{x}\right) \tag{3.5c}$$

Here, ν denotes the material's *Poisson's ratio*, while $\boldsymbol{r} = (x, y, z)$. It is important to note, that the coordinate system has been defined by choosing $\boldsymbol{b}_s = (\boldsymbol{b}\cdot\boldsymbol{l})\cdot\boldsymbol{e}_z \parallel \boldsymbol{e}_z$, and $\boldsymbol{b}_e = |\boldsymbol{l}\times(\boldsymbol{b}\times\boldsymbol{l})|\cdot\boldsymbol{e}_x \parallel \boldsymbol{e}_x$, while $\boldsymbol{e}_y$ follows the definition of a right handed Cartesian coordinate system: $\boldsymbol{e}_y = \boldsymbol{e}_z \times \boldsymbol{e}_x$.
Investigating Eqs. 3.5, it becomes clear that this approximation is in agreement with the properties given in Section 3.1 and the displacement stemming from an edge dislocation is confined to a plane normal to the dislocation line direction $\boldsymbol{l}$, while a screw dislocation only displaces the atoms in $z-$ or $l-$direction and the (x, y)-position is preserved.

3.3 DISLOCATIONS AND PLASTIC DEFORMATION

In order to emphasize why and how dislocations may significantly impact material properties, this section will illustrate basic elements of the theory of dislocations, like their origin and the movement of dislocations by glide, slip and related steps on a sufficiently flat surface already mentioned in Chapter 1.
Intrinsic dislocations - generated already during the growth process - predominantly stem from high temperature gradients, impurities can nowadays be avoided in most cases. Furthermore, imperfect seed crystals will lead to dislocations affecting the crystal matrix and lattice

mismatches between growth crystal and substrate may be compensated by the occurance of dislocations. Origins like these are referred to as *heterogeneous* nucleation. *Homogeneous* nucleation within perfect crystal volumes is also possible, although it requires stresses in the GPa-range. These conditions can be introduced by mechanical loads applied to small areas, which experimentally can be realized by means of controlled nano-indentation or accidently in industrial processes by handling. Another important mechanism, that generally requires less energy, is dislocation *multiplication*, e.g. from so-called *Frank-Read* sources. These are able to generate multiple dislocation loops if certain requirements of continuously applied shear stress are met. In this thesis dislocations of this type will be referred to as *extrinsic* dislocations, i.e., dislocations that emerge only after the growth process of the crystal is completed. Due to energetical reasons such dislocations in perfect crystal volumes only exist in closed loops or - as more prominent in the applications presented later in this work - the end points of the dislocation lines intersect with the crystal surface.
Assuming a nearly perfect surface, which is often realizable for semiconductor wafers by cutting and a subsequent polishing procedure, Frame c) in Fig. 3.1 indicates how dislocations lead to steps on the surface except for the special case of a pure edge dislocation directed parallel to the surface normal $\boldsymbol{n}$ meaning $\boldsymbol{b} \parallel \boldsymbol{l} \parallel \boldsymbol{n}$ as shown in Frame 3.1a. The height of these surface steps ΔH is given by

$$\Delta H = \boldsymbol{b} \cdot \boldsymbol{n} \tag{3.6}$$

if $|\boldsymbol{n}| = 1$, which follows from straight forward geometrical considerations.
Although Frame 3.1c is a schematic depiction of a static displacement, it also serves as a good illustration for a dynamical deformation process, so-called *slip*: The crystal volumes surrounding point D and E may be considered as displaced with respect to each other, whereas the crystal parts surrounding B and C are not displaced. The magnitude of the displacement is $b = |\boldsymbol{b}|$ and the direction of slip is necessarily always parallel to the BV $\boldsymbol{b}$. Dislocations, therefore, may be regarded as the elementary, quantized carriers of plastic deformation. Slip occurs when many dislocations move or *glide*. Dislocations that are able to glide (driven by external stress) do this in so-called glide planes, which are defined by $\boldsymbol{b}$ and $\boldsymbol{l}$. For diamond- and related structures this results in $\{111\}$ planes. Often the glide planes are the closest packed lattice planes in the crystal and the respective glide directions are given by the closest packed directions in these glide planes, i.e., the shortest lattice vectors in these glide planes. Pairs of glide planes and glide directions are referred to as glide systems [69], for which the notation $\{hkl\}\langle uvw\rangle$ will be used. Here, the glide planes are denoted first in the curved brackets and the glide directions are second. For face-centered

cubic crystals like silicon the slip often occurs in the $\{111\}\langle 110\rangle$ slip system.

Unarguably, dislocations, plastic deformation and related surface steps introduce a variety of challenges to the fabrication of high performance devices. Especially, since steps on the surface will pile up if the corresponding dislocations have the same BV and glide on the same or nearby (on an atomic scale) parallel glide planes, which is typical as application cases in later chapters of this thesis will show and which was already reported in [48, 49]. The dynamics contributing to plastic deformations are closely related to the dynamics of dislocations and do not only involve movement of already existing dislocations but also the generation of new defects. Although basic models have existed for several decades, a detailed description of the physical mechanisms enabling reliable quantitative calculations is still a topic of present research [73]. This again underlines the aspiration to combine the current capabilities of XDL with the ability of capturing dynamical processes in a quasi *in situ* fashion.

4

THEORY OF X-RAY DIFFRACTION

This chapter will present the fundamental concepts of X-ray diffraction to lay a basis for the contrast formation processes enabling topographic image acquisition and thereby X-ray Diffraction Laminography (XDL).

4.1 FUNDAMENTAL EQUATION OF X-RAY DIFFRACTION

Following the standard derivation found in a variety of textbooks, one may start from the Maxwell Equations of classical electrodynamics in their differential form and written out in the SI unit system

$$\nabla \cdot \boldsymbol{D} = \rho_f \qquad \text{Gauss's Law} \tag{4.1a}$$

$$\nabla \cdot \boldsymbol{B} = 0 \qquad \text{Gauss's Law of Magnetism} \tag{4.1b}$$

$$\nabla \times \boldsymbol{E} = -\frac{\partial \boldsymbol{B}}{\partial t} \qquad \text{Faraday's Law of Induction} \tag{4.1c}$$

$$\nabla \times \boldsymbol{H} = \boldsymbol{j}_f + \frac{\partial \boldsymbol{D}}{\partial t} \qquad \text{Ampère's Circuital Law} \tag{4.1d}$$

with $\boldsymbol{D}$ denoting the electric displacement field, free electric charge density ρ_f, magnetic induction $\boldsymbol{B}$, electric field $\boldsymbol{E}$, magnetic field $\boldsymbol{H}$, and electric current density $\boldsymbol{j}$. With the material equations

$$\boldsymbol{D} = \epsilon\epsilon_0\boldsymbol{E} \tag{4.2a}$$

$$\boldsymbol{B} = \mu\mu_0\boldsymbol{H} \tag{4.2b}$$

$$\boldsymbol{j} = \sigma\boldsymbol{E} \tag{4.2c}$$

with the dielectric permittivity of material and vacuum, ϵ and ϵ_0, respectively, which connect to the susceptibility χ via

$$\epsilon\epsilon_0 = \epsilon_0(1+\chi), \tag{4.3}$$

the magnetic permeability (of free space) $\mu_{(0)}$ and the electric conductivity tensor σ, now the assumption of no free charge carriers and currents, i.e. $\rho_f = 0$ and $\boldsymbol{j}_f = \boldsymbol{0}$, in a non-magnetic material is made, $\mu \approx 1$. By applying a rotation from the left hand side to Eq. 4.1c and using Eq. 4.1d in combination with the material relations 4.2 we obtain

$$\left(\epsilon(\boldsymbol{r})\epsilon_0\mu_0\frac{\partial^2}{\partial t^2} - \Delta\right)\boldsymbol{E}(\boldsymbol{r},t) + \nabla\left(\nabla \cdot \boldsymbol{E}(\boldsymbol{r},t)\right) = 0. \tag{4.4}$$

By inserting a time-harmonic wave $\boldsymbol{E}(\boldsymbol{r},t) = \boldsymbol{E}(\boldsymbol{r})\mathrm{e}^{-\mathrm{i}\omega t}$ and making use of Eq. 4.3 with a frequency dependent susceptibility and $k = \omega/c$ for the wave vector k one obtains the *fundamental equation of X-ray diffraction* [74, 75]:

$$(\Delta + K^2)\boldsymbol{E}(\boldsymbol{r},\omega) = \nabla(\nabla \cdot \boldsymbol{E}(\boldsymbol{r},\omega)) - K^2\chi(\boldsymbol{r},\omega)\boldsymbol{E}(\boldsymbol{r},\omega) \tag{4.5}$$

which by using the definition $\hat{\boldsymbol{V}}\boldsymbol{E}(\boldsymbol{r}) = \nabla(\nabla \cdot \boldsymbol{E}(\boldsymbol{r})) - K^2\chi(\boldsymbol{r})\boldsymbol{E}(\boldsymbol{r})$ can be rewritten as a *Helmholtz equation*:

$$(\Delta + K^2)\boldsymbol{E}(\boldsymbol{r}) = \hat{\boldsymbol{V}}(\boldsymbol{r})\boldsymbol{E}(\boldsymbol{r}). \tag{4.6}$$

A formal solution of Eq. 4.6 can be found with the Green function method in the form

$$\boldsymbol{E}(\boldsymbol{r}) = \boldsymbol{E}_0(\boldsymbol{r}) + \int \mathrm{d}^3r' G_0(\boldsymbol{r} - \boldsymbol{r}')\hat{\boldsymbol{V}}(\boldsymbol{r}')\boldsymbol{E}(\boldsymbol{r}') \tag{4.7}$$

where $\boldsymbol{E}_0(\boldsymbol{r})$ is the solution to the homogeneous part of Eq. 4.6 and $G_0(\boldsymbol{r} - \boldsymbol{r}')$ is the Green function satisfying

$$(\Delta + K^2)G_0(\boldsymbol{r} - \boldsymbol{r}') = \delta^3(\boldsymbol{r} - \boldsymbol{r}') \tag{4.8}$$

with $\delta^3(\boldsymbol{r})$ denoting the three-dimensional (3D) δ-distribution [76].

4.2 X-RAY DIFFRACTION BY CRYSTALS

The interaction of X-ray radiation represented by the electric field $\boldsymbol{E}$ in Eq. 4.6 is described via susceptibility χ, which in its Fourier decomposition can be written as

$$\chi(\boldsymbol{r}) = \sum_{\boldsymbol{h}} \chi_{\boldsymbol{h}} \mathrm{e}^{\mathrm{i}\boldsymbol{h}\boldsymbol{r}} \tag{4.9}$$

with reciprocal lattice vectors $\boldsymbol{h}$ given by

$$\boldsymbol{h} = h\boldsymbol{b}_1 + k\boldsymbol{b}_2 + l\boldsymbol{b}_3 \tag{4.10}$$

where $\boldsymbol{b}_i$ with $i = 1, 2, 3$ are the unit vectors of the reciprocal lattice fulfilling the well-known relation

$$\boldsymbol{a}_i \cdot \boldsymbol{b}_j = 2\pi\delta_{ij} \tag{4.11}$$

with the unit vectors of the crystal lattice $\boldsymbol{a}_i$ with $i = 1, 2, 3$ (here, the definition according to solid state physics was chosen; in crystallography the definition is equivalent but excluding the factor 2π). The

susceptibility as given in Eq. 4.9 assumes a perfect, infinitely large crystal. With regard to dislocation imaging by means of X-ray diffraction, now crystal deformation described by the displacement field $\boldsymbol{u}(\boldsymbol{r})$ may be introduced, representing the displacement of an atom at position $\boldsymbol{r}$ with original position $\boldsymbol{r}_0$ in the undisturbed or perfect reference lattice, as already introduced in section 3.2. Therefore, the continuous function $\boldsymbol{u}(\boldsymbol{r})$ is given by

$$\boldsymbol{u}(\boldsymbol{r}) = \boldsymbol{r} - \boldsymbol{r}_0. \tag{4.12}$$

With the approximation

$$\chi'(\boldsymbol{r}) \approx \chi(\boldsymbol{r}_0) = \chi(\boldsymbol{r} - \boldsymbol{u}(\boldsymbol{r})) \tag{4.13}$$

one assumes, that the electric susceptibility of the deformed crystal lattice at point $\boldsymbol{r}$ is the same as the perfect crystal's susceptibility at $\boldsymbol{r}_0$, where $\boldsymbol{r}$ had been before the deformation. In other words: The electron density distribution is only shifted but not altered. The assumption is valid as long as the core electron wavefunctions of the displaced atoms do not overlap and valence and conduction electrons only make a minor contribution to the overall scattering, which is often a good approximation for most crystals. It is generally fulfilled if

$$\frac{\partial u_i}{\partial x_j} \ll 1 \; \forall \; i, j \tag{4.14}$$

which then leads to the following form of the susceptibility of the deformed crystal expressed by its Fourier expansion:

$$\chi'(\boldsymbol{r}) = \sum_{\boldsymbol{h}} \chi_{\boldsymbol{h}} \mathrm{e}^{\mathrm{i}\boldsymbol{h}\cdot(\boldsymbol{r}-\boldsymbol{u}(\boldsymbol{r}))}. \tag{4.15}$$

With the local reciprocal lattice vector written as

$$\boldsymbol{h}'(\boldsymbol{r}) = \nabla(\boldsymbol{h}\cdot(\boldsymbol{r} - \boldsymbol{u}(\boldsymbol{r})) = \boldsymbol{h} - \nabla(\boldsymbol{h}\cdot\boldsymbol{u}(\boldsymbol{r})) \tag{4.16}$$

and under the condition that $\boldsymbol{h}'$ is depending so weekly on $\boldsymbol{r}$ that

$$\boldsymbol{h}'(\boldsymbol{r}) \approx \nabla(\boldsymbol{h}'(\boldsymbol{r})\cdot\boldsymbol{r}) = \nabla(S_{\boldsymbol{h}}(\boldsymbol{r})) \tag{4.17}$$

an *eikonal-like* function $S_{\boldsymbol{h}}(\boldsymbol{r})$ may be defined and we may write the Fourier expansion in Eq. 4.15 as

$$\chi'(\boldsymbol{r}) = \sum_{\boldsymbol{h}} \chi_{\boldsymbol{h}} \mathrm{e}^{\mathrm{i}\boldsymbol{h}'(\boldsymbol{r})\cdot\boldsymbol{r}}. \tag{4.18}$$

To now formally solve the fundamental equation of X-ray diffraction in the form given by Eq. 4.5 with the susceptibility in Eq. 4.18, the concept of Bloch waves, well-known in solid state physics, may be used

$$\boldsymbol{E}(\boldsymbol{r}) = \sum_{\boldsymbol{h}} \boldsymbol{E}'_{\boldsymbol{h}} \mathrm{e}^{\mathrm{i}\boldsymbol{k}'_{\boldsymbol{h}}\boldsymbol{r}} \tag{4.19}$$

$$\text{where} \quad \boldsymbol{k}'_h = \boldsymbol{k}_0 + \boldsymbol{h}'(\boldsymbol{r}). \tag{4.20}$$

This results in:

$$\begin{aligned} 0 = \sum_m \Big[& 4K^2 \boldsymbol{E}'_m(\boldsymbol{r}) - 4\boldsymbol{k}'^{\,2}_m(\boldsymbol{r}) \boldsymbol{E}'_{m[\perp \boldsymbol{k}'_m]}(\boldsymbol{r}) \\ & + 4K^2 \sum_n \chi_{m-n} \boldsymbol{E}'_n(\boldsymbol{r}) + 4\mathrm{i} \left(\boldsymbol{k}'_m \nabla\right) \boldsymbol{E}'_m(\boldsymbol{r}) \\ & + 2\mathrm{i} \boldsymbol{E}'_m(\boldsymbol{r}) \nabla \boldsymbol{k}'_m + \Delta \boldsymbol{E}'_m(\boldsymbol{r}) \\ & - 2 \left(\mathrm{i}\boldsymbol{k}'_m \nabla \boldsymbol{E}'_m(\boldsymbol{r}) + \mathrm{i}\nabla \left(\boldsymbol{k}'_m \boldsymbol{E}'_m(\boldsymbol{r})\right)\right) \\ & - \nabla \left(\nabla \boldsymbol{E}'_m\right) \Big] \mathrm{e}^{\mathrm{i}\boldsymbol{k}'_m(\boldsymbol{r})\boldsymbol{r}}. \end{aligned} \tag{4.21}$$

$\boldsymbol{E}'_{m[\perp \boldsymbol{k}'_m]}$ denotes the part of $\boldsymbol{E}'_m$ perpendicular to $\boldsymbol{k}'_m$ and due to the small difference between the two, $\boldsymbol{E}'_{m[\perp \boldsymbol{k}'_m]}$ can be replaced by $\boldsymbol{E}'_m$, which is a very good approximation because of the refractive index being almost one for sufficient X-ray energies. To solve Eq. 4.21 in all points $\boldsymbol{r}$ in the crystal, the terms in the brackets must vanish leading to

$$\begin{aligned} 0 = & 4 \left[K^2 \boldsymbol{E}'_m(\boldsymbol{r}) - \boldsymbol{k}'^{\,2}_m(\boldsymbol{r}) \boldsymbol{E}'_m + K^2 \sum_n \chi_{m-n} \boldsymbol{E}'_n \right] \\ & + 4\mathrm{i} \left(\boldsymbol{k}'_m \nabla\right) \boldsymbol{E}'_m(\boldsymbol{r}) + 2\mathrm{i} \boldsymbol{E}'_m \nabla \boldsymbol{k}'_m + \Delta \boldsymbol{E}'_m(\boldsymbol{r}) \\ & - 2\mathrm{i} \left[\boldsymbol{k}'_m \left(\nabla \boldsymbol{E}_m\right) + \nabla \left(\boldsymbol{k}'_m \boldsymbol{E}_m\right)\right] - \nabla \left(\nabla \boldsymbol{E}'_m\right). \end{aligned} \tag{4.22}$$

This set of equations now allows to draw conclusions in different levels of approximation as presented in [77] and also in [49], which served as guidelines for this section. In particular, they concern X-ray diffraction by perfect crystals and crystals with weak, moderate and strong deformations. Only the results given for strongly deformed crystals will be briefly summarized here, since these include the introduction of the effective misorientation which will play an important role and be derived in another way in Chapter 5 following [49].

For *strong deformations* in a crystal [77] mentions a wave optical theory based ansatz which relies on the equations

$$\begin{aligned} 0 =& \pi K^2 \left(\frac{\boldsymbol{k}_m'^{\,2}(\boldsymbol{r}) - K^2(1+\chi_0)}{K^2} \boldsymbol{E}_m'(\boldsymbol{r}) - \sum_{n \neq m} \chi_{m-n} \boldsymbol{E}_n'(\boldsymbol{r}) \right) \\ & - \mathrm{i} \left(\boldsymbol{k}_m' \nabla \right) \boldsymbol{E}_m'(\boldsymbol{r}) \quad \forall\ m. \end{aligned} \tag{4.23}$$

Now it is possible to derive the *Takagi equations of wave optics* [78] by assuming that only two points in the reciprocal lattice are excited and the main contributions arise from $m = 0$ and $m = h$, yielding

$$\frac{\partial E_0'(x_0, x_h)}{\partial x_0} = \mathrm{i}\pi K \left(\chi_{\bar{h}} C E_{\boldsymbol{h}}'(x_0, x_h) - 2\delta_0' E_0'(x_0, x_h) \right) \tag{4.24a}$$

$$\frac{\partial E_0'(x_0, x_h)}{\partial x_h} = \mathrm{i}\pi K \left(\chi_h C E_{\boldsymbol{0}}'(x_0, x_h) - 2\delta_0' E_{\boldsymbol{h}}'(x_0, x_h) \right) \tag{4.24b}$$

where $\partial / \partial x_{0,h}$ denotes the directional derivatives

$$\frac{1'}{k_{0,h}} (\boldsymbol{k}_{0,h}'(\boldsymbol{r}) \nabla) \tag{4.25}$$

in the direction of the vectors $\boldsymbol{k}_{0,h}'$. The parameters $\delta_{0,h}'$ are given by

$$\delta_m' = \frac{k_m'^2 - K^2(1+\chi_0)}{2K^2} \tag{4.26}$$

$$\approx -\left[\Delta\theta - \Delta\theta_B - \delta\theta(\boldsymbol{r}) \right] \sin(2\theta_B) \tag{4.27}$$

where $\Delta\theta$ represents the angular deviation from the kinematical Bragg condition and

$$\Delta\theta_B = -\frac{\chi_0 \left(1 - \frac{\cos(\Psi_h)}{\cos(\Psi_0)} \right)}{2 \sin(2\theta_B)} \tag{4.28}$$

is the shift of the Bragg angle due to refraction, with $\Psi_{0,h}$ being the angle of the incoming and diffracted waves and the surface normal of the crystal, respectively. The *effective misorientation* $\delta\theta(\boldsymbol{r})$ connects the deformation of the diffracting lattice planes to a local shift in the Bragg angle θ_B of an undistorted reference lattice. It is expressed by

$$\delta(\boldsymbol{r}) = \frac{1}{K \sin(2\theta_B)} \frac{\partial}{\partial x_h} \left[\boldsymbol{h} \cdot \boldsymbol{u}(\boldsymbol{r}) \right]. \tag{4.29}$$

The effective misorientation and its derivative - the strain gradient $\partial / \partial x_h \delta\theta(\boldsymbol{r})$ - control the influence of the lattice deformation on the diffraction and are therefore of major importance for the following

chapters. This is why the expression 4.29 will be derived in a different way in Chapter 5 as presented in [49]. The range of applicability for this approach can be defined via the conditions [79]

$$\left| \frac{\partial^2 u_k}{\partial x_i \partial x_j} \right| \ll K \left| \chi_h \right| \tag{4.30}$$

with $i, j, k = 1, 2, 3$ in addition to Eq. 4.14. An equivalent condition refers to a slow variation of the amplitudes of the electric field $\boldsymbol{E}'_m(\boldsymbol{r})$ on a length L which is in the magnitude of 50 nm [80]. Since this length is well below the resolution limit of X-ray topography (typically about 1 µm) the condition holds and the approximation describes dynamical effects of X-ray diffraction by crystals with deformations like they are present in the vicinity of a dislocation core.

4.3 FRAUNHOFER APPROXIMATION AND KINEMATIC X-RAY DIFFRACTION

In cases where the distance from the sample to the detector D is much larger than the extension of the scattering potential $\chi(\boldsymbol{r}')$ itself, meaning $|\boldsymbol{r}'| \ll |\boldsymbol{r}| \approx D$, the scattering potential may be treated as a point source emitting a spherical wave front. This is the so-called *Fraunhofer* or *far-field approximation* which is valid for scattering potentials within in the first Fresnel zone given by $L_\nu = \sqrt{\lambda d}$, resulting in, e.g., 1.5 µm for 30 keV and a distance d of 5 cm. Making use of the Fraunhofer approximation a solution to the inhomogeneous Helmholtz equation 4.6 for $\hat{\boldsymbol{V}} = \delta(\boldsymbol{r} - \boldsymbol{r}')$ is given by

$$G_0(\boldsymbol{r} - \boldsymbol{r}') = -\frac{1}{4\pi} \frac{\mathrm{e}^{\mathrm{i}K|\boldsymbol{r}-\boldsymbol{r}'|}}{|\boldsymbol{r} - \boldsymbol{r}'|} \tag{4.31}$$

and may be rewritten as

$$G_0(\boldsymbol{r} - \boldsymbol{r}') \approx G_0^{FH}(\boldsymbol{r} - \boldsymbol{r}') = -\frac{1}{4\pi} \frac{\mathrm{e}^{\mathrm{i}Kd}}{d} \mathrm{e}^{-\mathrm{i}\boldsymbol{k}_s \boldsymbol{r}'} \tag{4.32}$$

where $\boldsymbol{k}_s = K\boldsymbol{r}/r$ is the wave vector of the scattered signal. Furthermore, as often done in quantum mechanics one may introduce the scattering operator

$$\hat{\boldsymbol{T}} = \hat{\boldsymbol{V}} + \hat{\boldsymbol{V}}\hat{\boldsymbol{G}}_0\hat{\boldsymbol{V}} + \hat{\boldsymbol{V}}\hat{\boldsymbol{G}}_0\hat{\boldsymbol{V}}\hat{\boldsymbol{G}}_0\hat{\boldsymbol{V}} + ... \tag{4.33}$$

and the formal solution of Eq. 4.6 given by Eq. 4.7 can be expressed by

$$\boldsymbol{E}(\boldsymbol{r}) = \boldsymbol{E}_0(\boldsymbol{r}) + \int \mathrm{d}^3 r' G_0(\boldsymbol{r} - \boldsymbol{r}') \hat{\boldsymbol{T}} \boldsymbol{E}_0(\boldsymbol{r}'). \tag{4.34}$$

In the Fraunhofer approximation with Eq. 4.32 this results in

$$\boldsymbol{E}(\boldsymbol{r}) = \mathrm{e}^{\mathrm{i}\boldsymbol{k}_0\boldsymbol{r}} - \frac{1}{4\pi}\frac{\mathrm{e}^{\mathrm{i}Kr}}{r}\int \mathrm{d}^3r'\hat{\boldsymbol{T}}(\boldsymbol{r}')\mathrm{e}^{-\mathrm{i}(\boldsymbol{k}_s-\boldsymbol{k}_0)\boldsymbol{r}'}. \tag{4.35}$$

The advantage of this formulation is, that it in principle allows solving the problem up to any desired order but if and how fast convergence is reached is always depending on the specific scattering potential.

For further simplification we here introduce the *First Born* or *kinematic approximation*, which is often applied to describe the diffraction by small crystal regions within a greater *mosaic*-like crystal. This can be considered similar to the case of dislocation imaging in the weak-beam regime. Due to the intended angular deviation from the Bragg condition $\Delta\theta$ introduced in Chapter 2 in Eq. 2.18 great parts of the crystal volume remain unexcited, with only distorted parts of the lattice close to dislocation cores contributing to diffraction. These regions represent small crystal volumes fulfilling the Bragg condition embedded in a large matrix. Mathematically, the kinetic approximation is simply a truncation of the scattering operator $\hat{\boldsymbol{T}}$ after the first order:

$$\hat{\boldsymbol{T}}_{\mathrm{kin}} = \hat{\boldsymbol{V}}. \tag{4.36}$$

With the definition of $\hat{\boldsymbol{V}}\boldsymbol{E}(\boldsymbol{r}) = \nabla(\nabla\cdot\boldsymbol{E}(\boldsymbol{r})) - K^2\chi(\boldsymbol{r})\boldsymbol{E}(\boldsymbol{r})$ the scattering potential can be simplified by neglecting all polarization effects (i.e., $\nabla(\nabla\cdot\boldsymbol{E}_0(\boldsymbol{r})) = 0$), resulting in

$$\hat{\boldsymbol{V}} = -K^2\chi(\boldsymbol{r}). \tag{4.37}$$

Hereby, the components of the electric field become decoupled. The physical assumption is that only single-scattering events contribute and any multi-scattering events are excluded. For the case of a σ-polarized electric field, combining the Fraunhofer and the kinematic approximation, i.e., Eq. 4.35 and Eq. 4.37, for describing diffraction by sufficiently small crystals in the far field will yield

$$\begin{aligned}\boldsymbol{E}(\boldsymbol{r}) &= \boldsymbol{E}_0(\boldsymbol{r}) + \boldsymbol{E}_S(\boldsymbol{r})\\ &= \mathrm{e}^{\mathrm{i}\boldsymbol{k}_0\boldsymbol{r}} - \frac{K^2}{4\pi}\frac{\mathrm{e}^{\mathrm{i}Kr}}{r}\int \mathrm{d}^3r'\chi(\boldsymbol{r}')\mathrm{e}^{-\mathrm{i}\boldsymbol{Q}\boldsymbol{r}'}.\end{aligned} \tag{4.38}$$

To account for the small size of the crystallite again the susceptibility may be expressed by its Fourier expansion - since the 3D periodicity is preserved - and be combined with a shape function $G(\boldsymbol{r})$, which is 1 inside the crystal volume and 0 outside of the crystal volume.

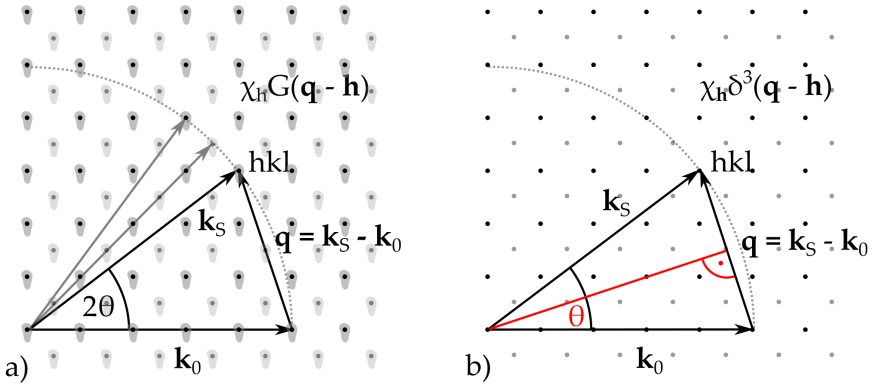

Figure 4.1: a) Ewald sphere for a small crystal. b) Ewald sphere for an infinite crystal.

Following the convolution theorem the multiplication in real space leads to a convolution in reciprocal space:

$$\chi(\boldsymbol{r}) = \chi_\infty(\boldsymbol{r})G(\boldsymbol{r}) = \int \mathrm{d}^3q \sum_{\boldsymbol{h}} \chi_{\boldsymbol{h}} \tilde{G}(\boldsymbol{q}-\boldsymbol{h}) \mathrm{e}^{\mathrm{i}\boldsymbol{q}\boldsymbol{r}}, \tag{4.39}$$

where $\chi_\infty(\boldsymbol{r})$ denotes the susceptibility of an infinite crystal and $\tilde{G}(\boldsymbol{q})$ represents the Fourier transform of the shape function $G(\boldsymbol{r})$. This now enables the derivation of the *scattering amplitude for kinematical diffraction by small crystals*:

$$E_S(r) = -\frac{K^2}{4\pi}\frac{\mathrm{e}^{\mathrm{i}Kr}}{r} \sum_{\boldsymbol{h}} \chi_{\boldsymbol{h}} \tilde{G}(\boldsymbol{q}-\boldsymbol{h}). \tag{4.40}$$

An infinitely extended crystal would be described by $G(\boldsymbol{r}) = 1 \; \forall \; \boldsymbol{r}$ - and therefore $\tilde{G}(\boldsymbol{q}-\boldsymbol{h}) \to \delta^3(\boldsymbol{q}-\boldsymbol{h})$ - and lead to sharp points in the reciprocal lattice, where any spatial confinement or boundary condition would result in an increasingly strong smearing of the reciprocal lattice points with decreasing crystal size. This is indicated in Fig. 4.1, where the *Ewald construction* is used to illustrate the condition for diffraction. With $\boldsymbol{q} = \boldsymbol{k}_{\boldsymbol{h}} - \boldsymbol{k}_0$ only certain reciprocal lattice points, which intersect with the *Ewald sphere* with radius $|\boldsymbol{k}_0|$, are able to contribute to the signal. This illustration also allows for an easy geometrical derivation of *Bragg's Law* as

$$\sin\theta_B = \frac{|\boldsymbol{h}_{hkl}|}{|\boldsymbol{k}_0|} = \frac{\lambda}{2d_{hkl}} \tag{4.41}$$

where the wavelength is given by the well-known relation $\lambda = 2\pi/|\boldsymbol{k}_0|$ and $d_{hkl} = 2\pi/|\boldsymbol{h}_{hkl}|$ is the distance between the *hkl* lattice planes.

4.4 DISCUSSION

The wave optical ansatz for diffraction by a crystal with strong deformations given by Eq. 4.23 has proven to yield good results for the simulation of rocking curves and topographic images. However, the equations have to be solved numerically. Furthermore, the physical interpretation is not as straight forward as in geometrical theories. Apart from that, the wave optical ansatz describes image formation by linking the observable contrast to lattice deformations in a non-linear and non-local way, which contradicts the projection criteria and therefore raise questions on the applicability of the reconstruction techniques, introduced in Chapter 2.

With image acquisition being performed in the weak-beam regime, i.e., by the targeted excitation of lattice distortions with a monochromatic beam while the undisturbed crystal matrix remains mainly unexcited, one can describe the contrast formation based on the theory of kinematic diffraction and dynamical effects can be neglected.

Despite the accurate description of topographic image formation, i.e., the *forward* problem, by wave optical approaches, kinematical theories are better in agreement with the requirements for tomographic and laminographic reconstruction procedures, i.e., the *backward* problem. Therefore, in the next chapter the derivation of a ray tracing model will be presented, which assumes that the excited crystal volumes are consisting of *small enough* crystallites along the dislocation line and diffract kinematically.

The Fraunhofer approximation has to be applied carefully, since depending on the specific distance from detector to sample images might be recorded in the vicinity of the first Fresnel zone. However, the approach has been solidified by the first successful applications of XDL and has so far shown good agreement of simulations and measurement.

5

MODELING DISLOCATION CONTRAST FORMATION IN WEAK-BEAM

In this chapter, the theoretical background for a geometrical ray tracing approach will be presented. For a general description of the topographic image contrast formation one would rely on the dynamical theories presented in the previous chapter. Therefore, the Takagi equations would have to be solved. This has been done by suitable numeric integration and the results have shown agreement with the experimental findings [81, 82]. However, since interpretations on this basis are difficult, here, another approach, that allows an easier investigation of the parameter space, will be introduced, closely following [49]. Ray tracing has been broadly utilized as an approach for simulations regarding X-ray topography [83–85] and within this work, it will be used to perform simulations of X-ray Diffraction Laminography (XDL) projections, which then will undergo a subsequent three-dimensional (3D) reconstruction in Chapter 6.

Based on full dynamical theory (i.e., the Takagi Equations), a topograhic image can be decomposed into three main contributing parts, [35, 75]. Without going too much into detail, here only a brief description will be given: (i) The *dynamical image* of a dislocation in a topograph shows a blurred white line. It can be understood as a shadow cast of the incoming X-ray beam along the propagation direction of the wavefield impinging on the dislocation. Far from the dislocation core strain bends the wavefield, while closer to the dislocation core so-called *interbranch scattering* is dominant. (ii) The *direct image* is created by reflection of the direct beam by more distorted areas close to the dislocation core. For high absorption the dynamical image dominates (typically $\mu L > 6$, with the linear absorption coefficient μ and path length through the material L), while the direct image mainly contributes for values of μL up to 2 or 3. (iii) The *intermediary image* is created by interference between interbranch scattered waves and the original ones. It has been first described experimentally and theoretically in [86]. The direct image acquired under weak-beam conditions comes closest to fulfilling the projection requirement. It has explained the width of dislocation images in topographs observed during experiments [42]. It also represents the contribution to the topograph the following considerations will focus on.

In summary, the derivation of the theoretical framework for contrast formation of a dislocation in a XDL projection will follow the following scheme: The displacement field $\boldsymbol{u}(\boldsymbol{r})$, given by Eq. 3.5, will be used to describe the dislocation, i.e. incorporating the assumptions of linear

elasticity theory and isotropic properties of the material, leading to a local reciprocal lattice vector $\boldsymbol{h}'$. Since XDL employs a monochromatized X-ray beam, an angular excitation interval will be defined for the resulting effective misorientation $\delta(\boldsymbol{r})$ introduced already in Section 4.2. Making use of the *mosaic* model, the diffracting volumes are small enough to diffract only kinematically, so that dynamical effects can be neglected. The image on the detector plane will then be computed by ray tracing of parallel rays.

5.1 DEFORMATION IN A CRYSTAL LATTICE

Next to the previously introduced description of the local reciprocal lattice vector $\boldsymbol{h}'$ via the displacement field $\boldsymbol{u}(\boldsymbol{r})$ and an eikonal function $S_h(\boldsymbol{r})$ in Eq. 4.17 of Section 4.2, the here presented derivation will be based on the local lattice tilts $\omega_x(\boldsymbol{r})$ and $\omega_y(\boldsymbol{r})$ and the local lattice strain $[\Delta d/d]\,(\boldsymbol{r})$. Again an undistorted reference lattice will be used to define these local properties, for which $\omega_x(\boldsymbol{r}) = \omega_y(\boldsymbol{r}) = 0°$ and the interplanar spacing will be given by $d(\boldsymbol{r}) = d_{hkl}$. With the definition of a coordinate system as shown in Fig. 5.3, i.e., a positive value of $\omega_{x,y}$ indicates a tilt towards the respective axis while the reciprocal lattice vector of the reference lattice is parallel to the z-axis, $\boldsymbol{h}^0 \parallel \hat{\boldsymbol{e}}_z$, one easily finds the relations

$$\frac{h_x}{h_z} = \tan(\omega_x) \tag{5.1}$$

$$\frac{h_y}{h_z} = \tan(\omega_y), \tag{5.2}$$

see Fig. 5.1b. Exploiting the definition of the reciprocal lattice vector given in Eqs. 4.10 and 4.11, one can derive the connection between the interplanar spacing d and the reciprocal lattice vector itself as

$$|\boldsymbol{h}| = \frac{2\pi}{d}, \tag{5.3}$$

which allows to express the local reciprocal lattice via a normalization factor and the direction shown in Fig. 5.3 as

$$\boldsymbol{h}(\boldsymbol{r}) = \frac{2\pi}{d(\boldsymbol{r})\sqrt{\tan^2(\omega_x(\boldsymbol{r})) + \tan^2(\omega_y(\boldsymbol{r})) + 1}} \begin{pmatrix} \tan(\omega_x(\boldsymbol{r})) \\ \tan(\omega_x(\boldsymbol{r})) \\ 1 \end{pmatrix}. \tag{5.4}$$

It is noteworthy, that so far this approach is not limited by any level of distortion. Now resuming to the considerations regarding an eikonal function as introduced in section 4.2 one can write

$$\begin{aligned}\boldsymbol{h}'(\boldsymbol{r}) &= \nabla(S_{\boldsymbol{h}}(\boldsymbol{r})) = \nabla(\boldsymbol{h}(\boldsymbol{r}-\boldsymbol{u}(\boldsymbol{r}))\\ &= \boldsymbol{h} - \nabla(\boldsymbol{h}\cdot\boldsymbol{u}(\boldsymbol{r})),\end{aligned} \tag{5.5}$$

which with the definition $\Delta\boldsymbol{h}(\boldsymbol{r}) = \boldsymbol{h}'(\boldsymbol{r}) - \boldsymbol{h}$ yields

$$\Delta\boldsymbol{h}(\boldsymbol{r}) = -\nabla(\boldsymbol{h}\cdot\boldsymbol{u}(\boldsymbol{r})). \tag{5.6}$$

Assuming sufficiently small deviations of the tilts and strain with respect to the reference lattice, with this the relations to the displacement field $\boldsymbol{u}(\boldsymbol{r})$ are

$$\begin{aligned}\omega_x(\boldsymbol{r}) &\approx -\partial_x u_z(\boldsymbol{r})\\ \omega_y(\boldsymbol{r}) &\approx -\partial_y u_z(\boldsymbol{r})\\ \frac{\Delta d}{d^0}(\boldsymbol{r}) &\approx +\partial_z u_z(\boldsymbol{r}).\end{aligned} \tag{5.7}$$

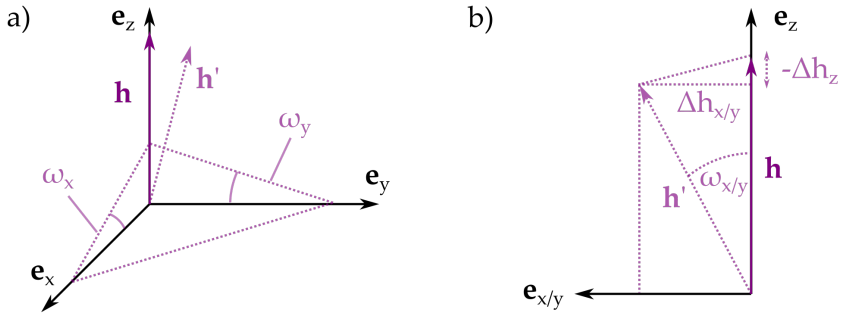

Figure 5.1: a) Local reciprocal lattice vector and reference lattice. b) View direction perpendicular to the xz- or yz-plane, respectively.

5.2 GEOMETRICAL RAY TRACING

To derive the geometrical ray tracing model one considers the case where only one point *hkl* in the local reciprocal space of the discrete sample lattice is taken into account. Obviously, the contribution to the diffraction signal of an infinitesimally small crystal volume is only possible if the Bragg condition 4.41 is fulfilled. The diffracted ray's direction is then given by $\boldsymbol{k}_{\boldsymbol{h}}$ and the signal detected by the detector occurs at the intersection point of $\boldsymbol{k}_{\boldsymbol{h}}$ with the detector plane. In the following the analytical considerations will be restricted to the case of a parallel incident beam and perpendicular orientation of the detector plane with respect to $\boldsymbol{k}_{\boldsymbol{h}}$, which practically means a tilt of the

detector about 2θ in comparison to a regular tomographic alignment. The image is then given by the incoherent superposition of all rays diffracted by crystallite points in the sample in Bragg condition.

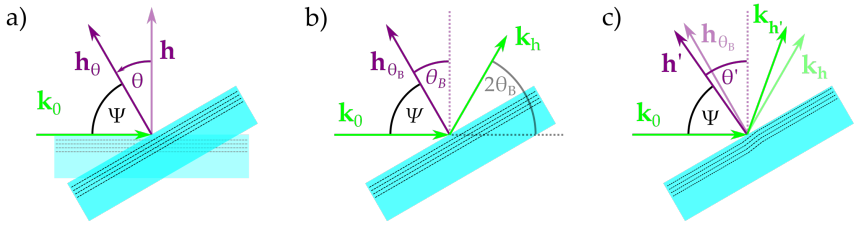

Figure 5.2: a) A rotation or tilt is performed to transition from a tomographic into a laminographic configuration with $\theta \neq 0$. b) Diffraction in Bragg condition. The wave vector of the diffracted ray $\boldsymbol{k_h}$ results from rotation of $\boldsymbol{k}_0$ about $\boldsymbol{\Theta}$ by $2\theta_B$. c) A small distortion is introduced by $\boldsymbol{h}'$ resulting in the diffracted wave vector $\boldsymbol{k}_{\boldsymbol{h}'}$.

5.2.1 *The Case of an Undistorted Lattice*

As a preliminary step the case of a perfect reference lattice will be briefly discussed by starting off with the reciprocal lattice vector being oriented perpendicular to the incident beam, i.e. $\boldsymbol{k}_0 \perp \boldsymbol{h}$. By means of XDL this represents the special case of $\theta = 0$, where laminography transitions into regular tomography. In order to exploit diffraction contrast the sample is tilted about a rotation axis $\boldsymbol{\Theta}$ perpendicular to $\boldsymbol{k}_0$ and $\boldsymbol{h}$, i.e.

$$\hat{\boldsymbol{e}}_{\boldsymbol{\Theta}} = \frac{\boldsymbol{h} \times \boldsymbol{k}_0}{|\boldsymbol{h} \times \boldsymbol{k}_0|}, \tag{5.8}$$

also see Fig. 5.2a.
Relying on the laboratory coordinate system illustrated in Fig. 2.6 and without loss of generality we can select $\hat{\boldsymbol{e}}_{\boldsymbol{\Theta}}$ to be parallel to the x-axis. The selected reciprocal lattice vector tilted by θ is given by

$$\boldsymbol{h}_\theta = R_{\boldsymbol{\Theta}}(\theta)\boldsymbol{h} \tag{5.9}$$

with

$$R_{\boldsymbol{\Theta}}(\theta) = \begin{pmatrix} 1 & 0 & 0 \\ 0 & \cos(\theta) & -\sin(\theta) \\ 0 & \sin(\theta) & \cos(\theta) \end{pmatrix}. \tag{5.10}$$

Making use of the conservation of the wave vector, i.e. $|\boldsymbol{k}_0| = |\boldsymbol{k}_h| = k$, also compare Fig. 5.2b, and the well-known definition of the scalar product in 3D space one finds

$$\cos(\Psi) = -\frac{\boldsymbol{k}_0 \cdot \boldsymbol{h}_\theta}{k\,|\boldsymbol{h}_\theta|}. \tag{5.11}$$

Rewriting Bragg's Law from Eq. 4.41 as

$$\sin(\theta_B) = \frac{\lambda}{2d} = \frac{1}{2}\frac{2\pi}{k}\frac{|\boldsymbol{h}_{\theta_B}|}{2\pi} = \frac{|\boldsymbol{h}_{\theta_B}|}{2k} \tag{5.12}$$

and exploiting common trigonometrical relations for the case $90° - \Psi = \theta = \theta_B$ this yields

$$\frac{\boldsymbol{k}_0 \cdot \boldsymbol{h}_\theta}{|\boldsymbol{h}_\theta|^2} = -\frac{1}{2}. \tag{5.13}$$

Obviously, Eq. 5.13 represents a general requirement for diffraction since the Bragg condition itself is incorporated. To finish the considerations for the perfect lattice, calculating the direction of $\boldsymbol{k_h}$, i.e., the direction in which the image is projected onto the detector plane, yields

$$\boldsymbol{k_h} = k\begin{pmatrix}0\\1\\0\end{pmatrix} + h\begin{pmatrix}0\\-\sin(\theta)\\\cos(\theta)\end{pmatrix} = k\begin{pmatrix}0\\-\cos(2\theta)\\\sin(2\theta)\end{pmatrix}, \tag{5.14}$$

where the Laue condition already given in Eq. 4.20 and here denoted as

$$\boldsymbol{k_h} = \boldsymbol{k}_0 + \boldsymbol{h}_\theta, \tag{5.15}$$

was used.

5.2.2 *Distorted Lattice*

Now the transition from the perfect reference lattice to the distorted lattice, as it is present, e.g., in the vicinity of a dislocation, see Fig. 5.2c, has to be performed. The focus lies on determining the angular shift in the Bragg peak

$$\Delta\theta = \theta'_B - \theta_B, \tag{5.16}$$

where θ'_B denotes the Bragg angle of the distorted lattice. Additionally, the direction of diffracted rays is of interest, or the deviation in direction with respect to Eq. 5.14. The computations can be found in popular textbooks like [75], however, the derivation in [49] is closer

connected to XDL in an illustrative manner and allows a preparation for an approach used for the characterization of a dedicated instrument for 3D X-ray diffraction imaging presented in Chapter 7.
Considering a local reciprocal lattice vector of a distorted lattice in the form

$$\boldsymbol{h}' = \boldsymbol{h} + \Delta\boldsymbol{h} = \begin{pmatrix} \Delta h_x \\ \Delta h_y \\ h_z + \Delta h_z \end{pmatrix} = \begin{pmatrix} h'_x \\ h'_y \\ h'_z \end{pmatrix} \tag{5.17}$$

as introduced in Section 5.1 one may insert it into the important condition 5.13 to yield

$$h'_z \sin(\theta'_B) - h'_y \cos(\theta'_B) = \frac{|\boldsymbol{h}'|^2}{2k}. \tag{5.18}$$

Analogous to Eq. 5.13 for the perfect reference lattice, Eq. 5.18 represents a condition for fulfilled Bragg condition for the distorted lattice. A solution can found to be

$$\theta'_B = 2\arctan\left[\frac{2kh'_z \pm \sqrt{4k^2\left({h'_y}^2 + {h'_z}^2\right) - h'^4}}{h'^4 - 2kh'_y}\right], \tag{5.19}$$

where $h' = |\boldsymbol{h}'|$, the absolute value of the local reciprocal lattice vector. There exists no solutions for θ'_B if $4k^2({h'_y}^2 + {h'_z}^2) < h'^4$, i.e., in this case diffraction is not possible. In real space this would mean that the wave length λ of the incident radiation is simply to large with respect to the interplanar distance d, i.e., $\lambda/d > 2$.
To approximate Eq. 5.19 a Taylor expansion with respect to $\Delta h_{x,y,z}/h$ can be performed and truncated after the terms of second order

$$\begin{aligned}\theta'_B = \theta &+ \frac{\Delta h_y}{h} + \tan(\theta_B)\frac{\Delta h_z}{h} \\ &+ \frac{1}{2}\tan(\theta_B)\left(\frac{\Delta h_y}{h}\right)^2 + \tan(\theta_B)\left(\frac{\Delta h_x}{h}\right)^2 \\ &+ \frac{1}{2}\tan^3(\theta_B)\left(\frac{\Delta h_z}{h}\right)^2 - \frac{\Delta h_y \Delta h_z}{h^2} \\ &+ \mathcal{O}^3\left(\frac{\Delta h_x}{h}, \frac{\Delta h_y}{h}, \frac{\Delta h_z}{h}\right).\end{aligned} \tag{5.20}$$

Restricting the considerations only to the first line of Eq. 5.20, i.e., the first (and zero-) order, one finds that for small distortions a transition similar to Eq. 5.1 may be performed in the form

$$\begin{aligned}\frac{\Delta h_x}{h} &\to \omega_x \\ \frac{\Delta h_x}{h} &\to \omega_y \\ \frac{\Delta h_z}{h} &\to \frac{\Delta d}{d},\end{aligned} \tag{5.21}$$

which then yields:

$$\Delta\theta_b = \theta' - \theta_B \approx \omega_y - \tan(\theta_B)\frac{\Delta d}{d}. \tag{5.22}$$

This result can also be obtained by plugging the local reciprocal lattice vector 5.4 into Eq. 5.19 and applying a Taylor expansion with respect to ω_x, ω_y, and $\Delta d/d$ as shown in [49]. The straight forward interpretation of this result is simple: ω_y is an additional tilt in the diffraction plane, i.e. a constant added to the tilt angle θ. $\Delta d/d$ represents a change in interplanar spacing of the distorted lattice and therefore changes the Bragg angle θ_B for a certain X-ray energy of the crystallite itself. Often the linear approximation given by Eq. 5.22 is called the crystal lattice's local *effective misorientation*, [35, 75, 77], but usually in literature it is found with the opposite sign as

$$\delta(\boldsymbol{r}) = -\Delta\theta_B(\boldsymbol{r}). \tag{5.23}$$

In the here presented case, according to Eq. 5.16 the effective misorientation represents the angular deviation induced by deformation in the lattice to reach Bragg condition, i.e. the Bragg angle for a given deformation has to be corrected by $\Delta\theta_B = -\delta\theta$. From here on, the effective misorientation will be expressed in its most general form already introduced in Eq. 4.29 in Section 4.2. Therefore, one may use relation 5.7 in Eq. 5.23 with expression 5.22

$$\begin{aligned}\delta &= -\omega_y + \tan(\theta_B)\frac{\Delta d}{d} \\ &= \partial_y u_z + \tan(\theta_B)\partial_z u_z \\ &= \frac{1}{h}\left(\partial_y + \tan(\theta_B)\partial_z\right)\left(h\hat{\boldsymbol{e}}_z \cdot \boldsymbol{u}\right).\end{aligned} \tag{5.24}$$

With the diffracted wave vector defined in the crystal coordinate system of the perfect reference lattice, where $\boldsymbol{h} \parallel \hat{\boldsymbol{e}}_z^{\text{Cryst}}$ and the y-axis is lying in the diffraction plane spanned by $\boldsymbol{h}$ and the incident wave vector $\boldsymbol{k}_0$, given by

$$\boldsymbol{k}_{\boldsymbol{h}} = \frac{k}{\sqrt{1+\tan(\theta_B)}}\begin{pmatrix}0\\1\\\tan(\theta_B)\end{pmatrix} \tag{5.25}$$

Eq. 5.24 can be written as

$$\delta(\boldsymbol{r}) = \frac{1}{hk\cos(\theta_B)} \boldsymbol{k_h} \cdot \nabla \left(\boldsymbol{h} \cdot \boldsymbol{u}(\boldsymbol{r}) \right). \tag{5.26}$$

Making use of Bragg's Law in the form of Eq. 5.12 this yields

$$\delta(\boldsymbol{r}) = \frac{1}{k\sin(2\theta_B)} \frac{\partial}{\partial x_{\boldsymbol{h}}} \left(\boldsymbol{h} \cdot \boldsymbol{u}(\boldsymbol{r}) \right) \tag{5.27}$$

where $\partial/\partial x_{\boldsymbol{h}}$ was used to denote the directional derivative along the direction of the diffracted wave vector $\boldsymbol{k_h}$. With Eq. 5.26 we have casted the effective misorientation in its most general form, identical to Eq. 4.29, and independent of the chosen coordinate system.

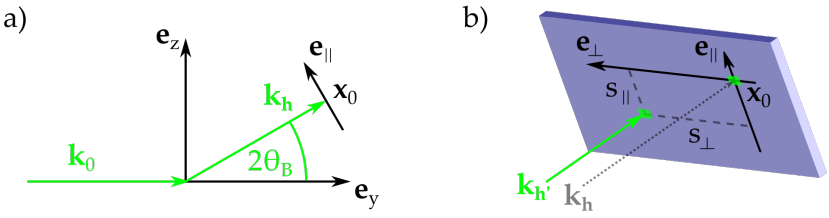

Figure 5.3: a) Detector alignment. b) Signal peak deviation with respect to a ray diffracted by an undistorted crystal.

In order to complete the considerations regarding the geometrical ray tracing for image formation, now the directional deviation of the diffracted ray $\boldsymbol{k_{h'}}$ with respect to the case for the undistorted lattice has to be investigated. The following gives a summary of the presentation given in [49]. By inserting the local reciprocal lattice vector from Eq. 5.17 into the Laue condition 5.15 one obtains

$$\boldsymbol{k_{h'}} = \begin{pmatrix} h'_x \\ k + h'_y\cos(\theta_B) - h'_z\sin(\theta_B) \\ h'_y\sin(\theta_B) + h'_z\cos(\theta_B) \end{pmatrix} \tag{5.28}$$

$$= \begin{pmatrix} h'_x \\ k - \frac{h'^2}{2k} \\ \mp\sqrt{h'^2 - \frac{h'^4}{4k^2} - h'^2_x} \end{pmatrix} \tag{5.29}$$

where in the second line Eq. 5.18 was used for the y-component and the z-component was rewritten with the conservation of the wave vector $|\boldsymbol{k}_0| = |\boldsymbol{k_{h'}}| = k$. The position of the detected signal on the detector plane can then be found as the solution of

$$\nu \boldsymbol{k}_{\boldsymbol{h}'} = \boldsymbol{x}^{\mathrm{ref}} + s_{\perp}\boldsymbol{e}_{\perp} + s_{\parallel}\boldsymbol{e}_{\parallel} \tag{5.30}$$

where $\boldsymbol{x}^{\mathrm{ref}}$ represents the point of signal detection on the detector for the undistorted reference lattice and $\boldsymbol{e}_{\perp}$ and $\boldsymbol{e}_{\parallel}$ are the unit vectors of the detector plane, perpendicular and parallel to the diffraction plane, respectively:

$$\boldsymbol{x}^{\mathrm{ref}} = D\begin{pmatrix} 0 \\ \cos(2\theta_B) \\ \sin(2\theta_B) \end{pmatrix},\ \boldsymbol{e}_{\perp} = \begin{pmatrix} 1 \\ 0 \\ 0 \end{pmatrix},\ \boldsymbol{e}_{\parallel} = \begin{pmatrix} 0 \\ -\sin(2\theta_B) \\ \cos(2\theta_B) \end{pmatrix}. \tag{5.31}$$

The parameters $s_{\perp}$ and $s_{\parallel}$ then directly represent the signal shift on the detector. Note, that the here presented computation is referring to the case of a detector plane tilted by 2θ, i.e., the diffracted rays hit the detector plane perpendicularly, since this was the chosen geometry for all simulations and most of the measurement data presented in this thesis. (The data from previous measurements already published in [2, 48] was recorded with an untilted detector. In the frame of this thesis it will later serve as a reference point.) The solutions to the system of linear equations 5.30 are given by

$$s_{\perp} = D\frac{k_x}{k_z\sin(2\theta_B) + k_y\cos 2\theta_B} \tag{5.32}$$

$$s_{\parallel} = D\left[\frac{k_z}{k_z\sin(2\theta_B)\cos(2\theta_B) + k_y\cos^2(2\theta_B)} - \tan(2\theta_B)\right]. \tag{5.33}$$

Again derivation of two alternative expressions is possible: one with dependence on $\Delta h_{x,y,z}$ by inserting Eq. 5.28 into the solutions 5.32 and 5.33, and another depending on the tilt angles ω_x and ω_y and on the strain $\Delta d/d$ by making additional use of Eq. 5.4. Here, the Taylor expansion of the latter with respect to ω_x, ω_y, and $\Delta d/d$ up to second order is presented:

$$s_{\perp} = 2D\sin(\theta_B)\left[\omega_x - \omega_x\frac{\Delta d}{d}\right] + \mathcal{O}^3\left(\omega_x, \omega_y, \Delta d/d\right) \tag{5.34}$$

$$\begin{aligned} s_{\parallel} = {} & 2D\tan(\theta_B)\left[-\frac{\Delta d}{d} - \frac{1}{2}\cos(2\theta_B)\omega_x^2\right. \\ & \left. + \frac{1+\cos^2(\theta_B)}{2\cos^2(\theta_B)}\left(\frac{\Delta d}{d}\right)^2\right] + \mathcal{O}^3\left(\omega_x, \omega_y, \Delta d/d\right) \end{aligned} \tag{5.35}$$

This allows to connect an estimate for the spatial resolution of XDL to the tilt of the distorted lattice, which will become relevant in Chapter 11. In this regard, the lattice tilt is then given by the Bragg deviation $\Delta\theta$. We will here use only the first order terms,

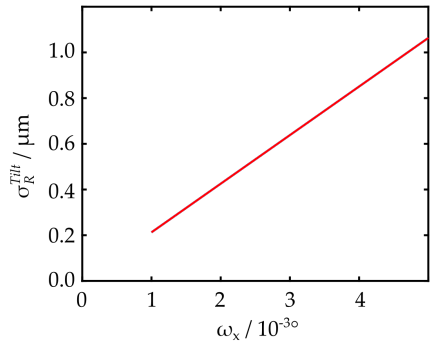

Figure 5.4: Influence of lattice tilt parameter ω_x on spatial resolution for a sample-detector distance of $D = 5$ cm and a Bragg angle of $\theta_B = 7°$.

$$\sigma_R^{\text{Tilt}}(\omega_x) = 2D\sin(\theta_B)\omega_x \tag{5.36}$$

$$\sigma_R^{\text{Strain}}\left(\frac{\Delta d}{d}\right) = -2D\tan(\theta_B)\frac{\Delta d}{d}, \tag{5.37}$$

and first concentrate on the σ_R^{Tilt}, since according to linear elasticity theory under isotropic conditions the introduced relation

$$\frac{\Delta d}{d} \approx -\partial_z u_z = 0. \tag{5.38}$$

Fig. 5.4 shows that for typical experimental conditions (sample-detector distance $D = 5$ cm, Bragg angle $\theta_B = 7°$) σ_R^{Tilt} yields approximately 0.5 µm, which is comparable to the typical effective pixel size of XDL projections (ranging from a minimum of 0.36 to 1.0 µm). Appendix A presents an additional approximation to estimate the strain $\Delta d/d$. With top values of $\Delta d/d = 7.0\times10^{-5}$ this will introduce smaller effects to the signal deviation than the lattice tilt, except for pure edge dislocations (compare Fig. A.2). This approximation indicates, that for small sample-detector distances of approximately $D \approx 5$ cm these effects are similar to the image resolution and therefore neglectable, if the effective pixel size does not decrease below 0.36 µm.

5.3 EFFECTIVE MISORIENTATION

In order to enable suitable simulations of XDL projections via a ray tracing approach (and later perform a 3D reconstructions of such simulated data sets), it is now meaningful to derive a suited expression of the effective misorientation $\delta(\boldsymbol{r})$. In practical terms, it will allow calculating the angular tilt of the lattice in a plane perpendicular to the dislocation line. Again the given presentation summarizes the more

detailed presentation of [49], with a focus on practical application. As a first step, we define the local reflectivity as

$$R_\delta(\boldsymbol{r}) = \begin{cases} 1 & \text{if } \delta_{\min} \leqslant \delta(\boldsymbol{r}) \leqslant \delta_{\max} \\ 0 & \text{else,} \end{cases} \tag{5.39}$$

meaning that any weighting on the contribution to diffraction of a particular region due to its misorientation is neglected. A crystal volume at position $\boldsymbol{r}$ with a certain orientation is either diffracting to the full extend or not at all. Keeping in mind the expressions 5.26 or 5.27 for the effective misorientation, it becomes obvious that due to the dependence on the wave vector $\boldsymbol{k_h}$, $\delta(\boldsymbol{r})$ is depending on the tomographic rotation angle ϕ and the laminographic tilt angle θ, i.e., the view direction. Therefore, these important measurement parameters are already involved. Under the assumption that factors blurring the image, like the effects on spatial resolution $\sigma_R^{\text{Tilt/Strain}}$ and the distance between dislocation core and diffracting crystal volume are not too large in comparison to the detector pixel size the recorded image can then be interpreted as an projection of the local reflectivity $R_\delta(\boldsymbol{r})$ onto the detector plane.
The following calculation will be performed in the dislocation coordinate system, meaning that the dislocation line $\boldsymbol{l}$ defines the direction of the z-axis $\hat{\boldsymbol{e}}_z$, and therefore $\boldsymbol{b}_s$, the screw component of the Burgers vector (BV), is also parallel to $\hat{\boldsymbol{e}}_z$, while the edge component $\boldsymbol{b}_e$ is defining the x-axis. (Of course this means, that for a true screw dislocation, $\boldsymbol{b} = \boldsymbol{b}_s$, the choice of $\hat{\boldsymbol{e}}_x$ is arbitrary as long as $\hat{\boldsymbol{e}}_x \perp \hat{\boldsymbol{e}}_z$ is fulfilled.) For easier notation we introduce the normalized BV components

$$B_s = \frac{b_s}{b} \quad \text{and} \quad B_e = \frac{b_e}{b} \tag{5.40}$$

as well as the normalized reciprocal lattice vector

$$\boldsymbol{H} = \frac{1}{h}\boldsymbol{h}. \tag{5.41}$$

Furthermore the calculations will be carried out in cylindrical coordinates. For position and wave vector this means

$$\boldsymbol{r} = r \begin{pmatrix} \cos\psi \\ \sin\psi \\ x_3/r \end{pmatrix}, \quad \boldsymbol{k}_{\boldsymbol{h}}^0 = k_{\boldsymbol{h}}^\perp \begin{pmatrix} \cos\alpha \\ \sin\alpha \\ k_{\boldsymbol{h}}^\parallel / k_{\boldsymbol{h}}^\perp \end{pmatrix}, \tag{5.42}$$

where $r^\perp$ and $k_{\boldsymbol{h}}^\perp$ denote the components of $\boldsymbol{r}$ and $\boldsymbol{k_h}$ perpendicular to $\hat{\boldsymbol{e}}_z$ and ψ and α denote the angles between $r^\perp$ and $k_{\boldsymbol{h}}^\perp$ and the x-Axis

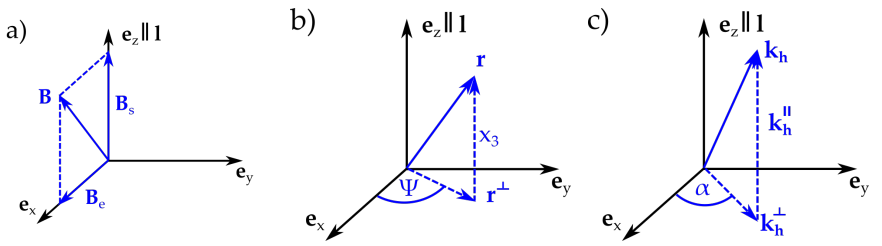

Figure 5.5: a) The dislocation coordinate system defined by the line direction $\boldsymbol{l}$ and the edge component of the (normalized) BV $\boldsymbol{B}_e$. b) Illustration of the position vector $\boldsymbol{r}$ in cylindrical coordinates. c) The representation of the wave vector of the diffracted wave $\boldsymbol{k_h}$ in the dislocation coordinate system.

$\hat{\boldsymbol{e}}_x$, respectively, also see Fig. 5.5. Using this notation, one needs to insert the derivations of the displacement field $\boldsymbol{u}(\boldsymbol{r})$ (which are written out in Appendix A) into Eq. 5.27. After some rearrangements one then obtains the effective misorientation in the form:

$$\begin{aligned}\delta(\boldsymbol{r}) = &-\frac{b}{2\pi\cos(\theta_B)}\frac{k_h^{\perp}}{k}\frac{\sin(\psi-\alpha)}{r}\\ &\times\left[B_e H_1\left(1+\frac{\cos(2\psi)}{2(1-\nu)}\right)+B_s H_3\right.\\ &\left.+\frac{B_e H_2}{2(1-\nu)}\Big((1-\nu)\cot(\psi-\alpha)+\sin(2\psi)\Big)\right].\end{aligned} \tag{5.43}$$

5.4 SYMMETRY CONSIDERATIONS

Before finishing this chapter with considering the size of the excited volume, some important symmetry properties of the effective misorientation $\delta(\boldsymbol{r})$ and therefore the defined local reflectivity $R_\delta(\boldsymbol{r})$ will be considered. These will lay an important basis for approaches presented in the following chapters of this work and help understand the evaluation of simulated data sets in the next chapter. First of all, one finds for the displacement field in Eq. 3.5

$$\boldsymbol{u}(\boldsymbol{b}) = -\boldsymbol{u}(-\boldsymbol{b}) \tag{5.44}$$

and

$$\boldsymbol{u}(-\boldsymbol{r}) = \boldsymbol{u}(\boldsymbol{r}) \pm \begin{pmatrix} b_e/2 \\ 0 \\ b_s/2 \end{pmatrix}, \tag{5.45}$$

meaning that the displacement field is described by an odd function with respect to the BV $\boldsymbol{b}$ and an even function with respect to the

position $\boldsymbol{r}$, respectively. With parity flipping to the opposite after differentiation this results in

$$(\nabla \boldsymbol{u})(-\boldsymbol{r}) = -(\nabla \boldsymbol{u})(\boldsymbol{r}), \quad \text{and} \tag{5.46}$$

$$\delta(\boldsymbol{b}, \boldsymbol{r}) = -\delta(-\boldsymbol{b}, \boldsymbol{r}) = -\delta(\boldsymbol{b}, -\boldsymbol{r}) = \delta(-\boldsymbol{b}, -\boldsymbol{r}). \tag{5.47}$$

This directly translates to the local reflectivity as

$$R_\delta(\boldsymbol{b}, \boldsymbol{r}) = R_{-\delta}(-\boldsymbol{b}, \boldsymbol{r}) = R_{-\delta}(\boldsymbol{b}, -\boldsymbol{r}) = R_\delta(-\boldsymbol{b}, -\boldsymbol{r}). \tag{5.48}$$

A slightly more detailed discussion to these findings can be found in [49]. Here, an additional aspect regarding the view direction defined by the wave vector $\boldsymbol{k_h}$ needs to be highlighted for later reference: Considering the special case of tomography, i.e., the laminographic tilt angle being $\theta = 0°$, hypothetically an additional symmetry property regarding the sign or direction of the diffracted wave vector $\boldsymbol{k}_h$ would be valid. Of course, this is unrealizable for diffraction based imaging approaches. However, with utilized X-ray energies (usually between 20 and 40 keV for silicon) and the selected reflexes and in line with the motivation to obtain high Fourier space coverage, the resulting Bragg angles usually are in a range between 2° to 8°. This means that the disturbance of this symmetry is expected to be rather weak and a *quasi*-symmetry should remain noticeable. With the general form of the effective misorientation in Eq. 5.26 one finds that changing the view direction ϕ by 180° should approximately result in a flip in the sign of $\delta(\boldsymbol{r})$, i.e.

$$\delta_{\boldsymbol{k_h}}(\boldsymbol{b}, \boldsymbol{r}) \approx -\delta_{-\boldsymbol{k_h}}(\boldsymbol{b}, \boldsymbol{r}) \tag{5.49}$$

and since $\delta \to -\delta$ corresponds to the transformations of $\delta_{\text{min}} \to -\delta_{\text{max}}$ and $\delta_{\text{max}} \to -\delta_{\text{min}}$, this consequently means - within the frame of this theoretical approach: During an XDL-measurement the rotation of the tomographic axis $\boldsymbol{\Phi}$ by 180° is expected to be not equal but similar to changing the sign of the selected Bragg deviation and therefore varying the laminographic tilt angle from $\theta = \theta_B + \Delta\theta$ to $\theta = \theta_B - \Delta\theta$. More precisely, although the line of contrast of a dislocation will change its orientation and position in the topograph according to the new view direction, the localization and size of the excited volume in the crystal will be similar to the case where the sign of $\Delta\theta$ is switched and the view direction remains unchanged. This is further illustrated on the basis of binary maps of the local reflectivity R_δ in Appendix B.

5.5 EXCITED VOLUME PER LINE LENGTH

In the last section of this chapter the excited Volume per line length V_δ will be introduced via the definition

$$V_\delta = \int_{r_\parallel = \text{const}} \mathrm{d}\boldsymbol{r}_\perp R_\delta(\boldsymbol{r}). \tag{5.50}$$

The integration variable $\boldsymbol{r}_\perp$ denotes the component of the position $\boldsymbol{r}$ perpendicular to the line direction $\boldsymbol{l}$ of the dislocation, while $\boldsymbol{r}_\parallel$ represents the parallel part. A well sketched out derivation is given in [49], here only results important for later discussions - especially for the investigation of suited reconstruction algorithms in Chapter 8 - will be presented. The final expression can be written as

$$\begin{aligned} V_\delta =& \frac{1}{32\pi\cos^2(\theta_B)} b^2 \left(\frac{k^\perp_{\boldsymbol{h}}}{k}\right)^2 \left|\frac{1}{\delta^2_{min}} - \frac{\sigma}{\delta^2_{max}}\right| \\ &\times \Big[N_3 \Big(B_e H_1\Big)^2 + N_4 \Big(B_e H_2\Big)^2 \\ &+ 4 B_e B_s H_1 H_3 + 2\Big(B_s H_3\Big)^2 \\ &+ 2B_e \Big(N_5 B_e H_2^2 - N_1 B_e H_1^2 - N_1 B_s H_1 H_3\Big)\cos 2\alpha \\ &- 2B_e \Big(N_6 B_e H_1 H_2 + N_1 B_s H_2 H_3\Big)\sin 2\alpha \Big], \end{aligned} \tag{5.51}$$

where the following notation was introduced:

$$N_1 = 1/\left(2\left(1-\nu\right)\right) \tag{5.52a}$$
$$N_2 = 1 - 2\nu \tag{5.52b}$$
$$N_3 = 2 + N_1^2 \tag{5.52c}$$
$$N_4 = N_1^2\left(1 + 2N_2^2\right) \tag{5.52d}$$
$$N_5 = N_1^2 N_2 \tag{5.52e}$$
$$N_6 = N_1 + N_5, \tag{5.52f}$$

with ν again being Poisson's ratio of the material. For further simplification Eq. 5.51 can be rewritten with suited factors C_1, C_2, and C_3 (given in line 2 and 3, line 4, and line 5 in Eq. 5.51, respectively) as

$$\begin{aligned} V_\delta =& b^2 \left(\frac{k^\perp_{\boldsymbol{h}}}{k}\right)^2 \left|\frac{1}{\delta^2_{min}} - \frac{\sigma}{\delta^2_{max}}\right| \\ &\times \Big(C_1 + C_2\cos 2\alpha + C_3 \sin 2\alpha\Big). \end{aligned} \tag{5.53}$$

The parameter $\sigma = \pm 1$ and defines whether the full excitation or the weak-beam regime is selected, which would set $\sigma = -1$ or $\sigma = 1$, respectively. Obviously, the latter case is of higher importance in the frame of this work. The angle α again denotes the angle between $\boldsymbol{k}^\perp_{\boldsymbol{h}}$

and the x-axis $\hat{e}_x$ of the dislocation coordinate system, i.e., $\boldsymbol{b}_e$ if $\boldsymbol{b}_e \neq 0$. Before ending this chapter, some properties of Eq. 5.51, that are already mentioned in [49], will be repeated here due to their importance for the further considerations:

- The excited volume per line length V_δ is quadratically depending on the BV length b, i.e., $V_\delta \propto b^2$. In addition, the dependence only shows terms of order $\mathcal{O}^2(B_e, B_s)$, meaning that V_δ is invariant with respect to a change in the BV-sign, i. e., under changes $\pm\boldsymbol{b}$, which is in agreement with the symmetry considerations in Section 5.4.

- For $|\delta_{\min}|, |\delta_{\max}| \to 0$ the size of V_δ increases strongly, which consequently would result in higher intensity. However, we need to restrict small values from the consideration, since it would result in excitation of less distorted or even undistorted regions in the crystal and therefore blur the dislocation image.

- Eq. 5.51 reveals that for the case of a pure screw dislocation $V_\delta \sim (B_s H_3)^2$, which leads to the known extinction rule for screw dislocations [35]:

$$\boldsymbol{h} \cdot \boldsymbol{b} = 0. \tag{5.54}$$

  For a pure edge dislocation a similar effect occurs if $B_e H_1 = B_e H_2 = 0$, which is the case for $\boldsymbol{h} \parallel \boldsymbol{l}$. So for edge dislocations we obtain an additional condition to Eq. 5.54 for the extinction rule [35]:

$$\boldsymbol{h} \cdot (\boldsymbol{b} \times \boldsymbol{l}) = 0. \tag{5.55}$$

- Eq. 5.53 may be devided in factors that (i) depend solely on the measurement geometry, i.e. on the configuration of $\boldsymbol{k_h}$ and $\boldsymbol{l}$ (first line of Eq. 5.53); and (ii) the configuration of $\boldsymbol{k_h}$ and $\boldsymbol{l}$ and the BV combined (second line of Eq. 5.53). Case (i) is represented by the term $\left(k_{\boldsymbol{h}}^{\perp}/k\right)^2 = \sin^2\eta$, if η is the angle between $\boldsymbol{k_h}$ and $\boldsymbol{l}$. Therefore, $V_\delta \propto \sin^2\eta$, which results in $V_\delta = 0 = \sin^2\eta$ for $\eta = 0$, i.e., $\boldsymbol{l} \parallel \boldsymbol{k_h}$, which leads to an *additional extinction rule* for XDL, which can be written as $|\boldsymbol{k_h} \times \boldsymbol{l}| = 0$.

The simulations and their evaluation in the next chapter will serve as demonstrations and illustrate the consequences these properties have on the detected dislocation image and the 3D reconstruction of an ensemble of projections composed of those images.

Part II

METHOD DEVELOPMENT

6

SIMULATING X-RAY DIFFRACTION LAMINOGRAPHY

The last chapters laid out the fundamental concepts of X-ray Diffraction Laminography (XDL), the basic properties of dislocations, and different approaches to describe X-ray diffraction by crystals. A suited theoretical framework to simulate the topographic image formation mechanism exploited to record XDL *quasi* projections was presented. In this chapter we will now use the previous considerations - especially those in the preceding Chapter 5 - to simulate XDL projections and investigate the influence of different parameters, ranging from dislocation properties to X-ray beam characteristics. Therefore, we will slightly anticipate Chapter 8 to get a first impression, how this affects the three-dimensional (3D) reconstruction of such simulated data sets. The aim is to make predictions, that help selecting suitable beamlines and scanning parameters, which will define the specifications for the X-ray diffraction instrumentation presented in Chapter 7. Furthermore, so far the application of XDL has brought to light some characteristics of the technique that are not yet fully understood. For example, it turned out that the quality of 3D reconstructions performed on data from silicon wafers improved, when projections from only one of the measurement intervals accessible in Laue-transmission geometry (LTG) were used as input, as opposed to using data from both intervals or data from scans in Bragg-reflection geometry (BRG). (Note, that in BRG there are no angular limitations regarding the tomographic angle ϕ, however, LTG has been identified as the favorable measurement geometry for capturing 3D structures within the wafer for the reasons given in Chapter 2 and [49]).
With the new insight provided by the following considerations important concepts will be developed and discussed, that build the basis for enhancements of XDL presented in Chapters 9, 10, and 11.

6.1 CALCULATION AND RECONSTRUCTION OF A SIMULATED PROJECTION ENSEMBLE

As a starting point, the effective misorientation $\delta(\boldsymbol{r})$ in a plane perpendicular to the line direction $\boldsymbol{l}$ of a dislocation with Burgers vector (BV) $\boldsymbol{b}$ will be calculated via Eq. 5.43. This two-dimensional (2D) field will then be binarized according to Eq. 5.39, to determine the contributing area, which corresponds to the excited volume per line length V_δ. For an easier investigation of the effects of $\delta_{\min}$ and $\delta_{\max}$, a re-definition of the local reflectivity will be used, resulting in the form

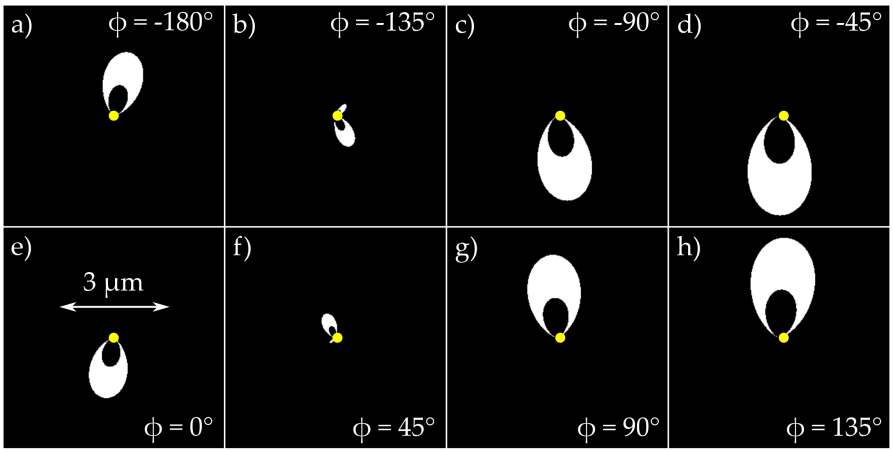

Figure 6.1: 2D plots of the local reflectivity $R_\delta(\boldsymbol{r})$, obtained by binarizing $\delta(\boldsymbol{r})$ for a dislocation with line direction $\boldsymbol{l} = [10\bar{1}]$ and BV $\boldsymbol{b} = a/2\,[011]$ with a, the lattice constant of silicon. The calculation simulated different view directions ϕ for a $\overline{2}20$-reflection with an X-ray energy of 25 keV, a Bragg deviation $\Delta\theta$ =0.002° and δ =0.0007°. The diffracting areas in the vicinity of a dislocation core (indicated by the yellow dots) are shown in white.

$$R_\delta(\boldsymbol{r}) = \begin{cases} 1 & \text{if } -(\Delta\theta + \delta) \leqslant \delta(\boldsymbol{r}) \leqslant -(\Delta\theta - \delta) \\ 0 & \text{else.} \end{cases} \tag{6.1}$$

This is due to relation 5.23 and can be understood as a transition from a material property focused misorientation interval defined by $\delta_{\text{min,max}}$ to a diffraction focused parameter defining the additional tilt to achieve weak-beam conditions. It is now meaningful to introduce the notations $\Delta\theta$ for the *weak-beam deviation* or the *weak-beam parameter* and δ for the *angular acceptance parameter* or the *angular excitation interval*. Note, that distributing the angular range, that contributes to the image formation, symmetrically around the deviation from the Bragg peak is in principle in line with approximations presented in Appendix C. One then obtains binary *maps* for the local reflectivity as shown in Fig. 6.1 for different view angles ϕ. The dislocation core is here always positioned in the center of the respective 2D-plot, indicated by a yellow dot. Note, that the images in each column seem almost like in plane rotations of each other by 180°. The *quasi* symmetry regarding the view direction, i.e. ϕ, seems to be fulfilled to a high degree for a Bragg angle of $\theta_B = 7.42°$, as discussed in Section 5.4.

The corresponding set of projections is shown in Fig. 6.2. It is clearly visible how the simulated detector images from opposite view directions ϕ appear mirrored at first glance, but also how the brighter and darker stripes that constitute the image of the dislocation line switch from top to bottom (and vice versa) with half a full rotation.

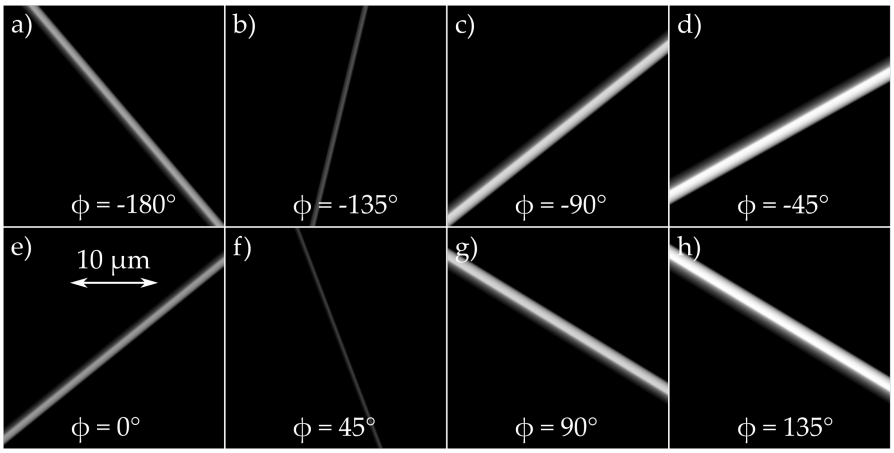

Figure 6.2: Simulated projection images directly calculated from the binary plots of the local reflectivity $R_\delta(\boldsymbol{r})$ in Fig. 6.1 via geometrical ray tracing. The detector pixel size was set to 0.125 µm, to make the structure of the dislocation line image clearly visible. This demonstrates the view direction dependence of the defined local reflectivity $R_\delta(\boldsymbol{r})$, in particular by fluctuating intensities and varying line width.

This is of course completely in line with the observations made with regard to the binary reflectivity maps described above.

If now a Simultaneous Iterative Reconstruction Technique (SIRT) (a description is given in section 8.2.1 and the choice is reasoned in Section 8.4) is applied to the simulated set of projections one obtains a first 3D-reconstruction of this artificial data. Fig. 6.3 shows cross sections, or so-called *slices*, perpendicular to the tomographic rotation axis $\boldsymbol{\Phi} \parallel \boldsymbol{h}_{\overline{2}\overline{2}0}$; the crystal directions parallel to the image edges are given in Frame 6.3b. Note, that throughout this thesis by *cross sections* or *slices* we refer to cross sections of a reconstruction volume perpendicular to the tomographic rotation axis $\boldsymbol{\Phi}$, which is always oriented parallel to the reciprocal lattice vector corresponding to the $\overline{2}\overline{2}0$-reflex, $\boldsymbol{\Phi} \parallel \boldsymbol{h}_{\overline{2}\overline{2}0}$, if not explicitly stated otherwise. (An explanation for this particular choice instead of selecting the 220-reflex is given in Appendix H).

The result in Frame 6.3a was obtained from a set of 36 projections equidistantly distributed over a full rotation of 360°, which would be only possible for samples that show a rather square- or circle-shaped cross section perpendicular to the selected reciprocal lattice vector. With the angular limitations regarding laterally extended samples in mind, Frame 6.3b and 6.3c show two slices obtained from ensembles of projections covering 130°-wedges, one centered around the normal of the front-, the other centered around the normal of the rear-side of the sample, respectively. Note, that here the data sets corresponding to the two measurement intervals were reconstructed separately. Again the rotational step width was set to $\Delta\phi$ =10°, leading to 14 projec-

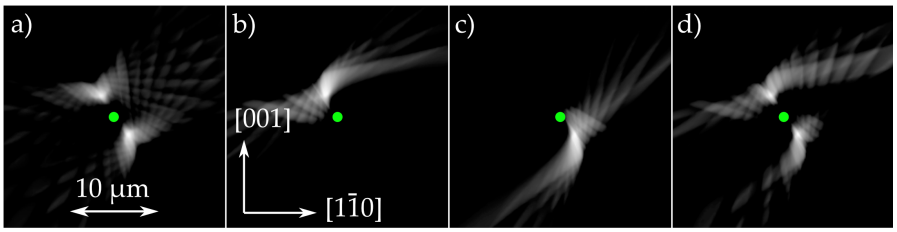

Figure 6.3: Cross sections perpendicular to the rotation axis $\mathbf{\Phi}$ and the reciprocal lattice vector $\boldsymbol{h}_{\bar{2}\bar{2}0}$ through the 3D reconstruction volume, obtained by applying SIRT, see section 8.2.1. a) Obtained from 36 projections covering the full circular range, i.e. 360°. b) Obtained from 14 projections within the interval [-65°,65°], if for $\phi = 0°$ $\boldsymbol{k}_{\boldsymbol{h}}$ lies in the plane spanned by the sample surface normal [001] facing the detector and $\boldsymbol{h}_{\bar{2}\bar{2}0}$. c) Same as b) but for the interval [115°,245°]. d) Both acquisition intervals combined were used as input for the reconstruction. To wedges of 50° each have not been covered.

tions per acquisition interval, since both, starting- and end-point, i.e., ϕ_{Start} and $\phi_{\text{End}} = \phi_{\text{Start}}+130°$, were acquisition positions. In contrast to Frame 6.3b and 6.3c that correspond to the respective measurement intervals reconstructed separately, Frame 6.3d shows a cross section of a reconstruction were both projection ensembles from both intervals were used as input. Compared to 6.3a no projection images from the two *unaccessible* angular segments of 50° each (marked red in Fig. 6.4) were used as input.

Interestingly enough, although the reconstruction in Frame 6.3a used the highest amount of input information, the result's quality is not significantly superior. The higher number of projections used provides a less blurred image of the dislocation features. However, the full rotation covers view directions from which the dislocation image in the projection is very bright and these are opposing each other, compare Fig. 6.2. Connected to the flipping of dark and bright stripes in the projections and the rotation of V_δ in the binary maps in Fig. 6.1 we obtain *two* separate intensity maxima indicating the localization of the dislocation. Consequently, the diffracting volume is migrating around the dislocation core with the tomographic rotation and reaches its maximum size for two ϕ-positions (approximately for $\phi_1^{V_\delta^{\max}} \approx$ -45° and $\phi_2^{V_\delta^{\max}} \approx 135°$, see Fig. 6.1 and 6.2). This is an important observation explaining why in the first application of XDL only incorporating projections from one interval yielded the better result: Especially with noise present the two features can easily merge or overlap with other reconstructed lines, creating an image that suggests lower quality than the reconstruction of a single projection ensemble.
This has further consequences for handling measurement data: Firstly, the position of the rotation axis is not accessible by conventional

(sinogram-based) techniques (also see Chapter 10). Additionally, the images can contain considerable noise or artifacts, or both, and the line blurring might be stronger due to effects neglected in the derivation of the theoretical framework. These factors might lead to the two features merging into one blurred region further degrading the achievable spatial resolution. More difficulties might arise from contrast fluctuations in the projections due to inhomogeneities in the beam profile. One part of the reconstructed volume might show one broad feature, while other slices display two separate features, that could be misinterpreted as two individual dislocations.
This first simulation explains and showcases why the merging of projection data from two acquisition intervals or the reconstruction from projections covering the full range of 360°, e.g., obtained in BRG or from samples with a suited geometry, always seemed to yield results of lower quality than for the case of reconstructions that only used information from one interval as input. Although, this outcome of two reconstruction features per dislocation stood nearby considering the the properties of the effective misorientation $\delta(\boldsymbol{r})$, that were already shown and investigated in [49], the reconstruction provides confirmation, new insight, and possibilities to improve the capabilities of XDL as will be shown in the later chapters of this thesis.

6.2 VARIATION OF PARAMETERS

Based on the conclusions from the last section, considerations will from now on be restricted to reconstructions, that only involve one acquisition interval. Investigations will however concern approaches that assume availability of data from both 130°-wedges that are then reconstructed separately. To analyze and visualize the results simultaneously, one reconstruction will be substracted from the other to obtain the *compounded* or *composed* volume $V_{\mathrm{Comp}}^{\mathrm{Rec}}$:

$$V_{\mathrm{Comp}}^{\mathrm{Rec}} = V_{I_1}^{\mathrm{Rec}} - V_{I_2}^{\mathrm{Rec}}. \tag{6.2}$$

Here, $V_{I_1}^{\mathrm{Rec}}$ and $V_{I_2}^{\mathrm{Rec}}$ denote the reconstruction volumes obtained by using projections from measurement interval I_1 and I_2, respectively. If not specifically noted otherwise, $\phi = 0°$ refers to a configuration where the sample surface with the surface normal parallel to the crystal direction [001] faces the detector and is orientated parallel to the diffraction plane. Intervals I_1 and I_2 are then given by $\phi \in$ [-65°,65°] and $\phi \in$ [115°,245°], respectively. Since the background, i.e., the space not in vicinity of a few µm of a dislocation, is empty or zero, features stemming from different reconstructions will be represented by opposite signs. Therefore, in the following figures gray will represent an empty background, while brighter and darker areas represent features originating from $V_{I_1}^{\mathrm{Rec}}$ and $V_{I_2}^{\mathrm{Rec}}$, respectively. This

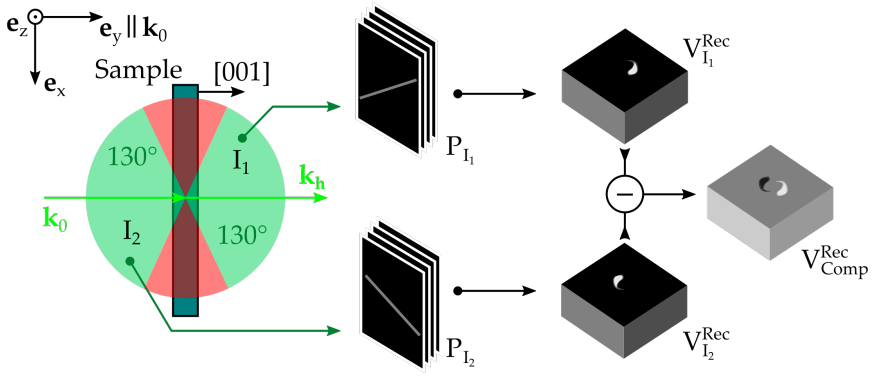

Figure 6.4: Illustration of the XDL-workflow for laterally extended samples: Projection ensembles P_{I_1} and P_{I_2} are acquired in the two accessible wedge-shaped angular ranges, denoted by I_1 and I_2, on the front- and the rear-side, respectively, while the sample is rotated about an axis perpendicular to the illustration plane. Note, that usually we define the interval as I_1, in which the [001] surface normal of the crystal is facing the detector, if the sample is in the center position of the interval. The sets of projections P_{I_1} and P_{I_2} are then reconstructed separately to obtain the reconstruction volumes $V_{I_1}^{\mathrm{Rec}}$ and $V_{I_2}^{\mathrm{Rec}}$, which are then merged via subtraction to yield the composed volume $V_{\mathrm{Comp}}^{\mathrm{Rec}}$. Note, that the inclination of the sample towards the incoming X-ray beam by θ is neglected in this schematic drawing for the sake of simplicity.

scheme is illustrated in Fig. 6.4 and will be referred to as the 2 *Interval Measurement Scheme*.

6.2.1 *Dislocation Properties*

An obvious first attempt is to consider dislocations with different properties, i.e., different line directions $\boldsymbol{l}$ and BV $\boldsymbol{b}$, and how these affect the reconstruction. It shows that within the presented theoretical framework only the configuration of both plays a role and it is sufficient to investigate different BVs for three cases of the line direction: (i) $\boldsymbol{l}$ being (anti-)parallel to the selected reflex, i.e., $\pm\boldsymbol{l} \parallel \boldsymbol{h}_{hkl}$. (ii) $\boldsymbol{l}$ being perpendicular to the selected reflex, i.e., $\boldsymbol{l} \perp \boldsymbol{h}_{hkl}$. (iii) Any other configuration. Since dislocation segments fulfilling condition (ii) are hardly visible in 3D reconstruction images and often have to be inserted between ending points of line segments by educated guessing, cases (i) and (iii) represent the focus of the further analysis.

The consideration will be further limited to so-called *perfect* dislocations as mentioned in Section 3.1. This leaves six possible orientations. Note, that a change in the sign of the BV would here only switch the distributions of bright and dark features, while a switch in the sign of the line direction $\boldsymbol{l}$ would simultaneously switch the sign of the BV, following the definition of the BV presented in Section 3.1 as in [72].

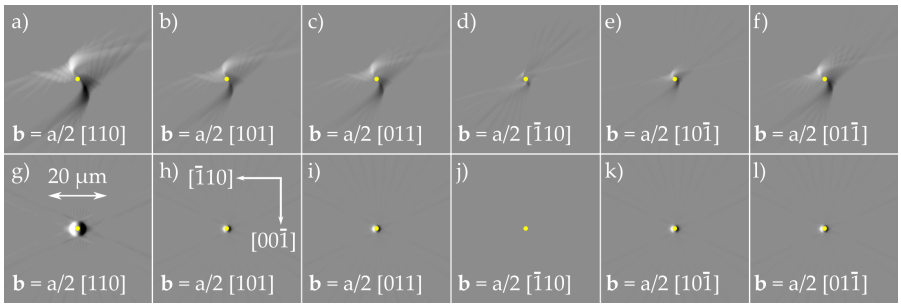

Figure 6.5: Cross sections of the reconstruction volumes perpendicular to the tomographic rotation axis and therefore also perpendicular to the selected reflex $[\overline{2}\overline{2}0]$. The upper row - frames a)-f) - show features stemming from a dislocation with line direction $\boldsymbol{l} = [10\overline{1}]$, while frames g)-l) correspond to $\boldsymbol{l} = [110]$, i.e., $\pm\boldsymbol{l} \parallel \boldsymbol{h}_{hkl} \parallel \boldsymbol{\Phi}$. Shown are the six possible BVs. The X-ray energy was set to 25 keV. The Bragg deviation $\Delta\theta$ =0.002° and the diffraction interval parameter δ =0.0007°.

The resulting reconstruction features in an exemplary slice of $V_{\text{Comp}}^{\text{Rec}}$ are shown in Fig. 6.5 for $\boldsymbol{l} = [10\overline{1}]$ (case (iii), first row) and $\boldsymbol{l} = [110]$ (case (i), second row). The first observation to make is, that line directions that are neither parallel or perpendicular to the reflex create a much more complex reconstruction image. The features show a point-like symmetry with respect to the dislocation core (which again is positioned in the center of each image and here indicated by the yellow dots for better visibility), while they also extend much further into the volume. The largest extension is found in Frame 6.5a for $\boldsymbol{b} = a/2[110]$, i.e., a mixed dislocation ($b_s \neq 0 \neq b_e$), where the peaks of intensity are each distanced about 3.2 to 4.0 µm to the center. For the pure screw dislocation in Frame 6.5e (with $\boldsymbol{b} = a/2[10\overline{1}]$) on the other hand the indicated dislocation positions are very close to the dislocation core, approximately 1.7 µm. Similar distances are obtained for $\boldsymbol{b} = a/2[\overline{1}10]$, although the features stemming from this dislocation in Frame 6.5d seem weaker. This is intuitively clear: Considering the properties of the displacement field $\boldsymbol{u}(\boldsymbol{r})$, see Eq. 3.5, we expect BVs (anti-)parallel to the selected reciprocal lattice vector $\boldsymbol{h}_{hkl}$ to create distortions the topographic image formation is most sensitive to. On the contrary, dislocations with $\boldsymbol{b} = \pm a/2[\overline{1}10] \perp \boldsymbol{h}_{\overline{2}\overline{2}0}$ should only lead to weak contrast, if not vanish completely if additionally $\boldsymbol{l} \parallel \boldsymbol{h}_{hkl}$, as it is the case in Frame 6.5j (due to the well-known extinction rule). Note, that for simplicity these distances are measured in the displayed plane and that the shortest distance from the reconstruction feature to the dislocation core can be calculated by simple methods of linear algebra, see appendix D. With this, the shortest distances of the features to the dislocation core change to 3.2 to 4.9 µm for $\boldsymbol{b} = a/2[110]$, while the changes for $\boldsymbol{b} = a/2[10\overline{1}]$ and $\boldsymbol{b} = a/2[\overline{1}10]$ are already below the pixel size (0.25 µm). This results are in good agreement with the

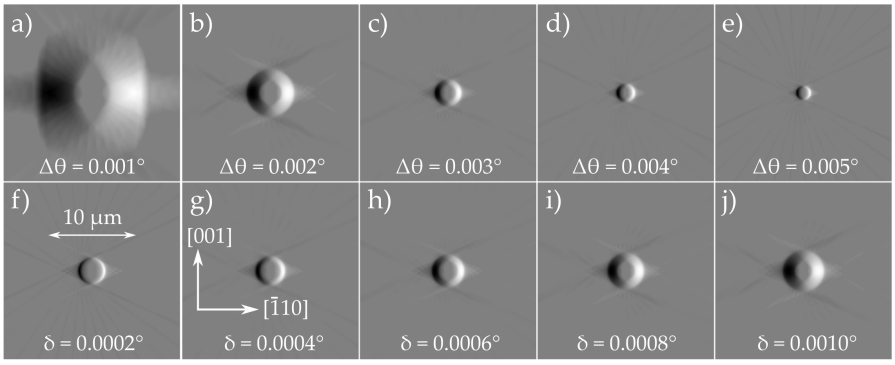

Figure 6.6: Cross sections through several reconstruction volumes. All features stem from a pure screw dislocation with line direction $\boldsymbol{l} = [110] \parallel \boldsymbol{b} = a/2[110] \parallel -\boldsymbol{h}_{[\overline{2}\overline{2}0]}$. Frames a) - e) show the obtained results for varying values of the weak-beam parameter $\Delta\theta$, while δ is fixed at 0.0007°. In frames f) - j) the angular acceptance interval size defined by δ is varied, for a constant $\Delta\theta = 0.0025°$. The X-ray beam energy is set to 25 keV.

estimated spatial resolution limit of XDL of 3-5 µm given in [2, 48, 49]. For segments (anti-)parallel to the selected reciprocal lattice vector (second row in Fig. 6.5) we obtain deviations from 1 (Frames 6.5h, 6.5i, 6.5k, 6.5l) to 2.0 (Frame 6.5j) µm - in this case the in-plane distance is equal to the shortest distance.
From this, we may conclude, that the spatial resolution of XDL is degraded by different line directions and different BVs to a different extend. Predominantly, the mixed dislocation segments (with $b_s \neq 0 \neq b_e$), that are neither parallel nor perpendicular to the selected reflex, have the worst effect on the accuracy of the method.

6.2.2 *Experimental Parameters*

While the specific properties of the dislocations under investigation can not be changed, experimental parameters like X-ray energy and the Bragg deviation $\Delta\theta$ are usually selectable (depending on the range of the monochromator and the used setup). The range of the diffraction interval, defined by $\delta_{\max}$, $\delta_{\min}$ or 2δ is depending on certain characteristics of the beamline, like source-to-sample distance, source size, as well as the monochromator, see Appendix C. When investigating a silicon sample, usually energies between 20 and 40 keV are employed and since there is no significant change between e.g. 25 and 40 keV regarding the outcome of simulations, the focus will be put on the easily adjustable Bragg deviation $\Delta\theta$ and the beamline specific diffraction interval parameter δ.

A dislocation line with the following properties is a meaningful choice: $\boldsymbol{l} = [110] \parallel -\boldsymbol{h}_{[\overline{2}\overline{2}0]} \parallel \boldsymbol{b} = a/2[110]$. The choice of the spatial orientation defined by $\boldsymbol{l}$ will simplify the interpretation while the

selection of $\boldsymbol{b}$ will maximize the negative effects of the contrast formation for the reconstruction. The upper five frames of Fig. 6.6 show how the reconstructed features approach the dislocation core with increasing $\Delta\theta$ and therefore improve the resulting spatial resolution of the measurement, while δ is fixed at 0.0007°. This outcome is to expected, because the further the incidence angle of the beam deviates from the corresponding Bragg angle of the undistorted lattice, the more sensitive one becomes to the strongly distorted areas close to the dislocation core. In Frame 6.6a on the other hand, the deviation is so small, that larger regions with very little distortion are illuminated, i.e., contrast is created further away from the dislocation core. At the same time one has to pay attention to the fact that the diffracting volume becomes smaller and smaller with increasing $\Delta\theta$ and although the simulation still indicates clear visibility at values of $\Delta\theta = 0.005°$, reality has shown that the signal is hardly visible if the laminographic tilt angle is moved so far out on a flank of the rocking curve. During the application of XDL the selection of a suited Bragg deviation $\Delta\theta$ becomes a compromise between the width and the visibility of a dislocation line in the topograph. To enable careful adjustment the sample manipulation has to be performed with high angular precision, preferably with a step size of about 0.0001°. This will also serve as a specification for the dedicated instrumentation, which is subject to the next chapter. (Although, alignment of silicon samples has been performed with step sizes of approximately 0.00025°, other applications might require higher resolution.)
For Frames 6.6f to 6.6j the angular acceptance range 2δ was varied from $[0.0004°, 0.0008°, ..., 0.0020°]$ for a fixed $\Delta\theta = 0.0025°$. Again, the effect - a broadening of the features - is intuitively clear, due to the diffracting area growing with δ. However, it is more important that the broadening effect in this range is rather weak, since this increases the number of potential beamlines that could be used for successful application of XDL.

6.3 CONTRAST INTENSITY OF DISLOCATION LINES

As a last part of this chapter the expressions for the excited volume per line length 5.53 will be used to approximate the intensity of the image contrast stemming from a dislocation detected on the detector plane. Therefore, we make the assumption that the intensity is proportional to the excited volume

$$I \propto V_\delta, \tag{6.3}$$

which is commonly used, when a mosaic model is applied [42, 47, 87]. The effect the excited volume has on an acquired projection is already demonstrated in Fig. 6.1 and 6.2. The white area, i.e. V_δ,

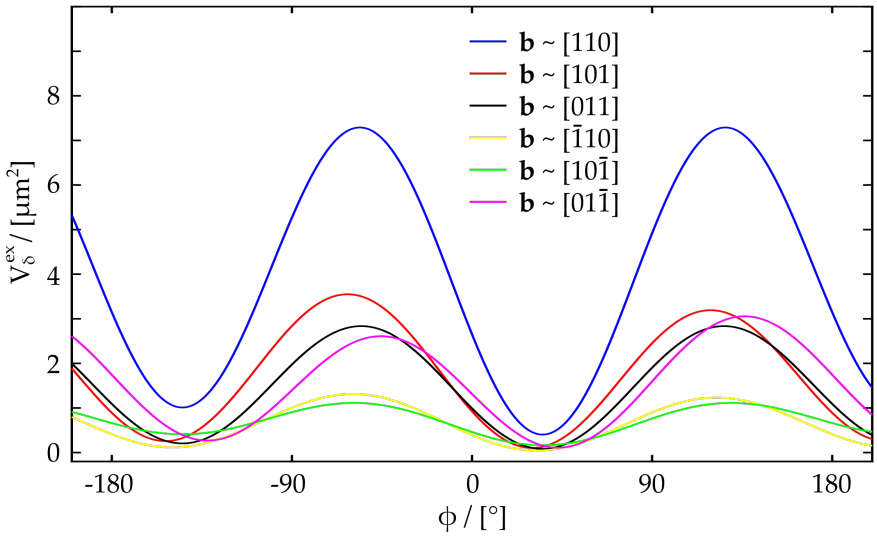

Figure 6.7: Excited Volume per line length over tomographic angle ϕ, based on Eq. 5.51. The calculation was performed for an X-ray energy of 25 keV and line direction of $\boldsymbol{l} = [10\bar{1}]$ for the six relevant BV configurations of perfect dislocations.

in frames 6.1b and 6.1f results in thin lines of considerably weaker contrast in the corresponding frames of Fig. 6.2, than e.g. Frames 6.1d and 6.1h.

Looking at the excited volume per line length and its dependence on the tomographic angle ϕ, i.e., the view direction, from another perspective, Fig. 6.7 shows plots of $V_\delta(\phi)$ for the same BV-configurations, that were used to obtain the reconstruction slices in Fig. 6.5. Here, Eq. 5.51 was evaluated, the line direction was set to $\boldsymbol{l} = [10\bar{1}]$ as in Fig. 6.1 and moreover all other parameters were kept constant (i.e., $E = 25$ keV; $\Delta\theta = 0.002°$, $\delta = 0.0007°$). One observes that intensity minima and maxima occur at similar view directions, and therefore the BV-dependence seems to only have a major influence on the overall intensity and not on its progression over ϕ. To strengthen this assumption one can now separately investigate the purely geometrical contribution $v_1(\boldsymbol{k})$ and the factors depending on the BV-components B_e and B_s denoted as $v_2(B_e, B_s, \alpha)$, according to equation 5.53 given by

$$v_1(\boldsymbol{k}) = \left(\frac{k_{\boldsymbol{h}}^{\perp}}{k}\right)^2 \tag{6.4}$$

$$v_2(B_e, B_s, \alpha) = C_1 + C_2 \cos\alpha + C_3 \sin\alpha. \tag{6.5}$$

Fig. 6.8 shows how the position of the minima and maxima of intensity - or more precisely of the excited volume per line length - is predominately determined by the line direction which manifests in $v_1(\boldsymbol{k})$, see Fig. 6.8a. The BV-dependent part shows a rather similar progression over ϕ for all relevant BV-configurations. This is a rather

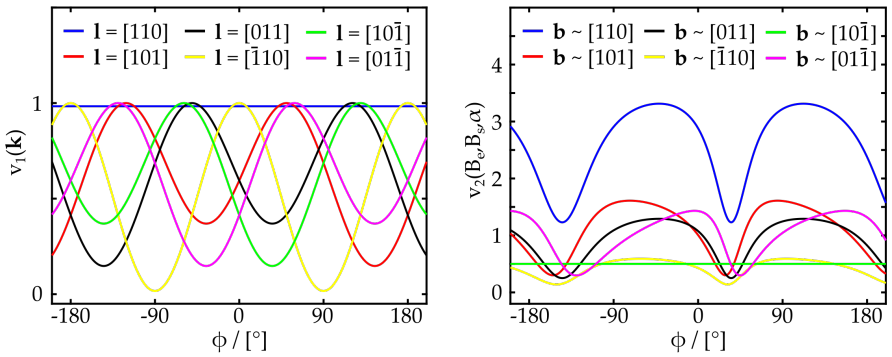

Figure 6.8: Separation of Eq. 5.53 into the *geometrical* part a), only depending on the measurement configuration, i.e., the relative arrangement of $\boldsymbol{k_h}$ and dislocation line direction $\boldsymbol{l}$, and the contribution depending on the BV b). The parameters are the same as in Fig. 6.7.

unfortunate outcome, since the intensity profile seems to indicate the line direction $\boldsymbol{l}$ much stronger, than the BV. However, the line direction of a dislocation segment can easily be extracted from the appearance in certain projection images (and of course from a reconstruction volume), while determining the BV in the conventional way via X-ray White Beam Topography (XWBT) is much more laborious. We will revisit the question, to which degree the BV-distribution can be derived from XDL measurement data without the need for additional measurements in Chapter 12 of this work.

7 REALIZATION OF DEDICATED INSTRUMENTATION

This chapter will address the instrumentational aspects of X-ray Diffraction Laminography (XDL) and novel X-ray diffraction imaging techniques in more detail. Since synchrotron radiation is utilized, one relies on the equipment of suited beamlines to realize the beam properties required for image acquisition (e.g. a monochromator). In many cases these beamlines may also provide adequate detector systems and sometimes even the possibility to tilt the detector by $2\theta_B$ to align the detector plane perpendicular to the diffracted X-ray beam – this e.g., was the case at ID15A and ID19 at the European Synchrotron Radiation Facility (ESRF). For these reasons the focus will exclusively be put on sample alignment and positioning during a measurement.
In this regard, the sample needs to be mounted on a rotation axis, which can be tilted towards or away from the incoming beam. While the precision regarding the position of the rotation axis is not crucial and requirements are usually fulfilled by air-bearing rotary stages, its stability with respect to tilt (i.e., its angular error) is. Furthermore, the selected reciprocal lattice vector needs to be aligned parallel to the rotation axis, another step that demands for careful positioning. The requirements for high accuracy of angular motion (overall angular stability below 0.001°), stem from exploiting diffraction contrast in weak-beam mode and the connected challenges, see Chapter 6. Furthermore, translational motion of the sample with respect to the rotation axis for Region of Interest (ROI) selection needs to be enabled. Preferably a sub-µm resolution in translation should be realized to achieve spatial resolutions below ($\sim$ 0.1 µm) the intrinsic limit of 3-5 µm. The accuracy in direct space becomes even more crucial when aiming at an improvement of XDL's spatial resolution down to 1-3 µm, as drawn out in the later chapters of this thesis.
Although, laminography has been utilized for many scientific and industrial applications [88–92], it is still not as widely used as the special case of tomography. While tomographic setups are commonly available at specialized end stations, sample manipulator systems allowing a tilt of the rotation axis with respect to the incoming beam direction are rather rare. In addition, laminography stations designed for applications using absorption or phase contrast might not provide the angular precision requirements for diffraction imaging in weak-beam.
Concluding, the aim is the realization of a light (weighting up to 30 to 40 kg) and mobile sample manipulator system to enable an easy integration into beamline infrastructure, while at the same time providing

the necessary precision in direct and angular space.
It is important to stress that the required degrees of freedom and the sequential arrangement of the motors enabling them influence each other. In other words, changing the conceptual design of the manipulator system might increase or decrease the number of relevant degrees of freedom and the number of stages involved in the compilation. Therefore, and for easier understanding, first, a conceptual design, representing a meaningful compromise of flexibility, stability, and precision, will be presented. Based on this approach, the required degrees of freedom will be outlined and the precision requirements will be derived based on basic knowledge, prior experience and the simulations in Chapter 6. Following these considerations, the selected devices and their compilation will be presented. Section 7.4 will address a possible approach to characterize the sample manipulator and measurement data will allow estimating the limitations regarding motion precision and stability of the system. Finally, the obtained results will be discussed and the current state of the system will be presented.

7.1 CONCEPTUAL DESIGN

In a first attempt, leading industrial manufacturers were contacted and asked to propose solutions for a sample manipulator system suited for the specific demands of laminographic diffraction imaging. Negotiations did not lead to satisfying results, the proposed realizations would have either been too heavy (in the magnitude of 100 to 1000 kg) and too large in their spatial extension, or otherwise it could not be guaranteed that the precision requirements were met. Therefore, a compilation of several suited devices (in the following also called *motors* or *stages*) based on the "topo-tomographic" setup presented in [47] was proposed. Similar systems were also used for the measurements in [2, 48, 49], indicating that the realization of suited instrumentation for diffraction-based laminographic approaches is possible. The basic idea is placing a goniometer in the bottom (for tilting into Bragg condition), followed by rotary stage in the middle (for changing the view direction during a scan) and additional stages on top to manipulate the sample with respect to the rotation axis, also see Fig. 7.1.

7.1.1 *Degrees of Freedom*

Based on the proposed stack of devices the necessary degrees of freedom the instrument needs to provide will be summarized. Here, the system will be divided into (i) a *sample stack* or *sample manipulator* and (ii) the *base-structure*. The sample stack comprises all motors active during a measurement, e.g., during a XDL-scan. The base structure on the other hand only enables the alignment of the sample stack itself with respect to the incoming beam. In the best case scenario

this sample stack alignment only has to be performed once in the beginning of a measurement campaign.

7.1.1.1 *Sample Manipulator*

Revisiting Fig. 2.6 in Section 2.3 two rotational degrees of freedom, that need to be provided by the sample stack, become obvious at first glance:

- the laminographic tilt axis $\mathbf{\Theta}$,
- and the tomographic rotation axis $\mathbf{\Phi}$.

It is important to note, that Fig. 2.6 already illustrates that the ROI of the crystal volume needs to coincide not only with the impingement point of the incoming X-ray beam but also with the center of rotation of the laminographic tilt $\mathbf{\Theta}$. In the following this will often be referred to as the *Pivot point*. Assuming this was not the case, the illuminated crystal volume would change with variation of θ, making the device unsuited for Rocking Curve Imaging (RCI), where the sample is *rocked*, i.e., θ is varied - often in a stepwise manner - e.g., in order to detect strain in the sample or measure local tilts due to lattice distortions with 1 μm^2 resolution [38, 39, 93, 94]. Consequently, additional degrees of freedom need to be added to be able to translate the sample with respect to the Pivot point for ROI-selection. Note, that this should also enable alignment of the sample with respect to the tomographic rotation axis $\mathbf{\Phi}$, since by careful stacking of the individual components we anticipate the Pivot point to be located on axis $\mathbf{\Phi}$. Furthermore, a procedure that is referred to as *sample fine alignment* has to be performed after placing the crystal region of interest in the pivot point. This basically means small inclinations of the sample (usually below 5° depending on the sample mounting and possible miscut) to achieve parallel orientation of the selected reciprocal lattice vector and the tomographic rotation axis, i.e., $\boldsymbol{h}_{hkl} \parallel \mathbf{\Phi}$, ensuring that the Bragg condition is fulfilled for all view directions in the accessible angular range of ϕ. This adds five necessary degrees of freedom:

- three translational degrees of freedom x_S, y_S, and z_S in the sample coordinate system as illustrated in Fig. 2.6 for ROI selection and positioning the sample with respect to the tomographic rotation axis
- and two rotations ω_x, ω_y for the inclination of the sample to align $\boldsymbol{h}_{hkl} \parallel \mathbf{\Phi}$. (Note, that the third rotation ω_z is in principal only introducing an offset to ϕ, since $\mathbf{\Phi} \parallel \hat{\boldsymbol{z}}_S$, and therefore, a rotational degree of freedom ω_z to rotate about $\hat{\boldsymbol{z}}_S$ is unnecessary.)

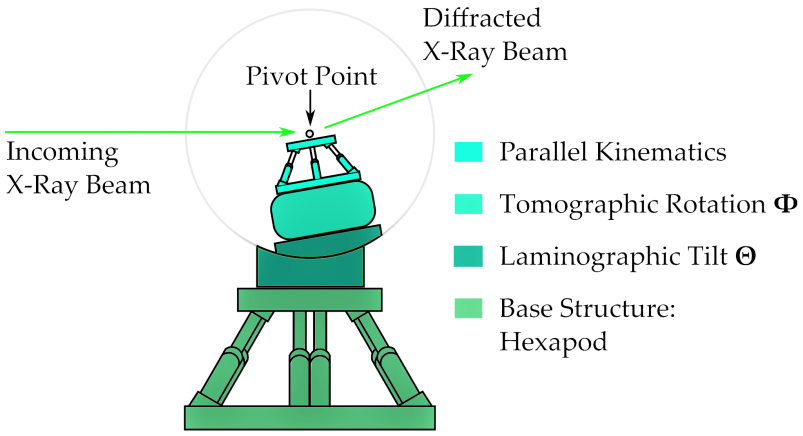

Figure 7.1: Schematic view of the proposed sample manipulator system. The different components are shown in different colors for clear distinguishability. The gray circle indicates the rotary or tilt motion of goniometer $\boldsymbol{\Theta}$ with the Pivot point, i.e., the Center of Rotation (CoR), in the middle.

7.1.1.2 *Base structure*

Continuing with the base structure, aligning the laminographic tilt axis $\boldsymbol{\Theta}$ parallel to the normal of the diffraction plane $\boldsymbol{n}_{E_D}$, $\boldsymbol{\Theta} \parallel \boldsymbol{n}_{E_D}$, needs to be enabled. In principle, this requires three rotational degrees of freedom in the laboratory coordinate system $\theta^L_{x,y,z}$. Furthermore, we need to be able to place the Pivot point of the goniometer (and therefore the tomographic rotation axis $\boldsymbol{\Phi}$) in the incoming beam via two translations x_L and z_L. As shown in Fig. 2.6, the laboratory coordinate system is defined by the vertical z_L-axis and the x_L-axis being oriented perpendicular to the incoming X-rays, i.e., $\hat{\boldsymbol{x}}_L \perp \boldsymbol{k}_0 \perp \hat{\boldsymbol{z}}_L \perp \hat{\boldsymbol{x}}_L$. A third translation $y_L \parallel \boldsymbol{k}_0$ is not strictly required, however it might prove to be convenient to place the sample closer to the detector.
It is noteworthy, that many beamlines provide instrumentation capable of performing the steps necessary for the sample stack alignment. For instance, a tomography table with µm resolution often represents a sufficient base structure. Since such equipment is usually aligned with respect to the incoming beam with a high level of precision, the rotation axis alone enables configuring $\boldsymbol{\theta} \parallel \boldsymbol{n}_{E_D}$. As an example the sample manipulator was mounted on top of a medium resolution tomography table at ID19 at the ESRF, Grenoble, France. For more examples see Appendix E where the instrumentation is shown integrated into four different beamline environments.

7.1.2 *Proposed Compilation of Sample Stack and Base Structure*

The last section has shown, that in addition to the two obvious degrees of freedom we require - namely laminographic tilt $\boldsymbol{\Theta}$ and tomographic

rotation $\mathbf{\Phi}$ - we need a variety of translations and rotations to successfully acquire images from different view directions exploiting diffraction contrasts.
The proposed solution - in more detail - employs a cradle-like goniometer to tilt an air-bearing rotation axis (as it is often used for tomographic data acquisition) towards the beam. Instead of small goniometers on top of the rotation axis, the utilization of piezo motor driven parallel kinematics to enable ROI-selection and sample fine alignment seems more convenient. Parallel kinematics usually provide six degrees of freedom (three translational and three rotational), making them a suitable solution to the challenging problem of enabling complex motion while occupying only limited space and keeping the overall system lightweight. Since also the base structure should provide six degrees of freedom in the ideal case a hexapod with a load capacity of up to approximately 50 kg and sufficient specifications regarding motion accuracy represents an optimal solution. A schematic view of the proposed conceptional design is shown in Fig. 7.1.
Of course, a solution relying on a cradle-like tilting device is strictly limited in the angular range of θ from about -15° to +15°. This directly limits the reflexes and energies that may be selected for image acquisition. However, so far, only 220- and 004-reflexes (or their negative counterparts) have been exploited by means of XDL and by suited energy settings tilt angles remained under 10°. Furthermore, tilt stages relying on this concepts promise high stability.

7.2 PRECISION REQUIREMENTS

Based on experimental experience, it turns out that a system compiled of the selected devices presented in the next section provides sufficient long-term stability and the required resolution in translational space. Concluding from the simulations in Chapter 6 the resolution limit is approximately 0.5 to 1 µm (This is only possible for certain configurations of line direction $\boldsymbol{l}$ and Burgers vector (BV) $\boldsymbol{b}$, see Section 6.2). Furthermore, the minimal incremental motion the parallel kinematics are capable of are significantly below the order of magnitude of µm. It would need expensive, time-consuming and challenging characterization methods to determine the true limits in translational stability and motion of the system. Performing this task seems unreasonable, since, for the time being, it would even be impossible to perceive motion errors in this regard with detector systems commonly used for XDL or Multi-Azimuth Rocking Curve Imaging (MARCI) data acquisition. Their effective pixel size ranges from 0.36 to 0.96 µm resulting in image resolution limits of at least 0.72 to 1.92 µm. Consequently, at least for the initial purpose of the device, laid out in this work, the requirements regarding motion and stability in direct space can be considered to be fulfilled. If in the future the field of applications of the

instrument expands or a lower effective pixel size and thereby higher image resolution is realized, such a characterization might become necessary, of course.
In contrast, the overall angular stability during tomographic rotation is a way more serious concern. First applications have revealed that fine alignment procedures and data acquisition become increasingly challenging and time intensive, if angular errors become too significant. Image contrast properties formated in the weak-beam regime change within the µrad range ($\sim 10^{-4\circ}$) of tilt angle θ. Furthermore, the simulations in Chapter 5 have shown how the crystal volume that fulfills the Bragg condition changes its localization with alterations of the weak-beam parameter $\Delta\theta$. Since the contrast features approach the dislocation core with increasing $\Delta\theta$ leading to less significant inconsistencies in the three-dimensional (3D) reconstruction problem, high values of $\Delta\theta$ seem desirable. At the time, the size of the excited crystal volume decreases with increasing $\Delta\theta$ if other parameters (e.g., angular acceptance δ) remain constant and therefore contrast gets weaker, see Fig. 6.6. Those two factors have to be balanced out by a careful adjustment of the deviation from the Bragg peak of the undistorted crystal lattice, which in turn requires high resolution in angular motion. Therefore, the minimal incremental movement of the laminographic tilt axis should be in the magnitude of $10^{-4\circ}$. In order to minimize time-consuming rocking scans for re-calibration of the selected weak-beam condition, firstly, a nearly perfect fine alignment ($\boldsymbol{\Phi} \parallel \boldsymbol{h}_{hkl}$) has to be enabled and, secondly, the system needs to be stable enough in angular space to maintain this condition during rotation about $\boldsymbol{\Phi}$. Anticipating projection acquisition without intermediate re-alignment procedures, the angular error or *wobble* should stay bellow $10^{-3\circ}$, otherwise the regions contributing to the signal would expand to far into the crystal or vanish completely.

7.3 COMPILATION OF SUITED DEVICES

According to the previous discussions, available devices on the open market were carefully considered and finally a set of stages was compiled and commissioned. These motors will now be briefly described from top to bottom:

7.3.1 *Parallel Kinematics*

For the sample fine alignment and selection of the ROI a SpaceFab Q-Motion 845 by PI GmbH & Co. KG was chosen. The tripod-like device provides six degrees of freedom and in *zero*-position it has a height of 77 mm, weighting 1.9 kg.

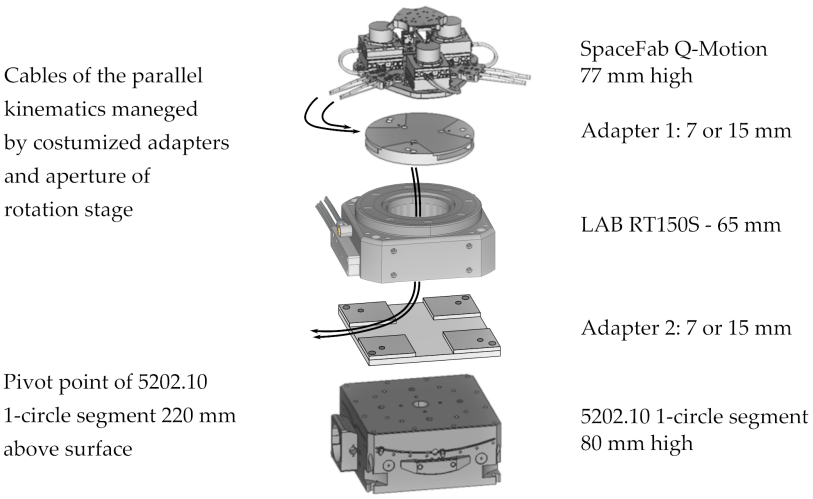

Figure 7.2: Technical drawing of the sample manipulator system compiled from three individual devices and two adapter plates. The six cables attached to the *SpaceFab* (parallel kinematics) are guided through the adapter plates and the aperture of the rotary stage to avoid entanglement.

7.3.2 *Tomographic Rotation: Air-Bearing Rotary Stages*

As mentioned above, smooth and stable motion, i.e., a low angular error or so-called *wobble*, is crucial for successful measurements. Therefore, only air-bearing rotary stages are taken into consideration. The RT150S by Leuven Air-Bearings offers a solution with very little build-up in height and a large aperture, which can be used for managing the cables of the parallel kinematics.

7.3.3 *Laminographic Tilt: Goniometer*

In order to perform high-precision angular motion of the upper part of the sample manipulator (comprised of parallel kinematics and rotary stage), as e.g., required during rocking scans, a 1-circle segment with a 1:20 gear by Huber Diffraktionstechnik GmbH & Co. KG was selected.

Compiling the selected components enables samples of up to 100 mm in diameter for circular shaped or edge length for square shaped wafers to be placed with the Pivot point coinciding with the center of the sample. More detailed information about the specifications of the individual devices can be found in Appendix E.

7.4 CHARACTERIZATION

During the first successful XDL-measurements intermediate rocking scans were performed almost every 3.5° in ϕ, to re-calibrate the weak-beam condition and assure suited contrast conditions. More precisely, during image recording in a 130° acquisition interval (resulting from the restrictions for laterally extended samples in Laue-transmission geometry (LTG) mentioned in Section 2.3) a total of 35 rocking scans were performed for re-alignment purposes. Assuming 2 seconds exposure time and sampling the rocking curve with 50 steps, this already leads to $2 \times 50 \times 35$ s = 3500 sec $\approx$ 1 h in additional acquisition time per interval, which may easily double, due to the motor movement of θ between the individual steps in effective measurement duration. The development of a dedicated instrumentation aims at maintaining suited weak-beam conditions during a full rotation of the tomographic rotation axis $\mathbf{\Phi}$. Other aspects that influence the overall stability of the setup are the stability of the parallel kinematics on top and of the goniometer underneath. Here, the assumption is made that the sample holder provides sufficient stability, while the stress it introduces to the ROI in the sample remains weak enough to record images following a rocking curve only altered by the dislocation arrangement under investigation.

7.4.1 *Theoretical Background*

To be able to investigate the overall angular stability of the setup, one may consider the θ_B-variation for a case in which the fine alignment $\mathbf{\Phi} \parallel \boldsymbol{h}_{hkl}$ is not perfectly achieved. Starting with a selected reciprocal lattice vector

$$\boldsymbol{h}_{hkl} = \begin{pmatrix} h_x^0 \\ h_y^0 \\ h_z^0 \end{pmatrix} \tag{7.1}$$

.

and rotating this vector about the tomographic rotation axis $\mathbf{\Phi}$ via

$$\boldsymbol{R}_{\mathbf{\Phi}}(\phi) = \begin{pmatrix} \cos(\phi) & -\sin(\phi) & 0 \\ \sin(\phi) & \cos(\phi) & 0 \\ 0 & 0 & 1 \end{pmatrix} \tag{7.2}$$

one obtains:

$$\boldsymbol{R}_{\boldsymbol{\Phi}}(\phi)\boldsymbol{h}_{hkl} = \begin{pmatrix} \cos(\phi) & -\sin(\phi) & 0 \\ \sin(\phi) & \cos(\phi) & 0 \\ 0 & 0 & 1 \end{pmatrix} \begin{pmatrix} h_x^0 \\ h_y^0 \\ h_z^0 \end{pmatrix}$$
$$= \begin{pmatrix} \cos(\phi)h_x^0 - \sin(\phi)h_y^0 \\ \sin(\phi)h_x^0 + \cos(\phi)h_y^0 \\ h_z^0 \end{pmatrix} = \begin{pmatrix} h_x(\phi) \\ h_y(\phi) \\ h_z^0 \end{pmatrix}. \tag{7.3}$$

Note, that hereby $h_{x,y}(\phi)$ can be expressed as

$$h_x(\phi) = h\left[\cos(\phi)\tan(\omega_x) - \sin(\phi)\tan(\omega_y)\right], \tag{7.4}$$
$$h_x(\phi) = h\left[\cos(\phi)\tan(\omega_x) - \sin(\phi)\tan(\omega_y)\right], \tag{7.5}$$

where $h_{x,y}^0 = h\tan(\omega_{x,y})$ was used, with $\omega_{x,y}$ defining the inclination of the reciprocal lattice vector with respect to the rotation axis $\boldsymbol{\Phi}$ as shown in Fig. 5.1a. Inserting this into Eq. 5.19 one obtains

$$\theta_B = 2\arctan\left[\frac{2kh_z^0 \pm \sqrt{4k^2\left[h_x^2(\phi) + (h_z^0)^2\right] - h^4}}{h^2 - 2kh_x(\phi)}\right] + \theta_0. \tag{7.6}$$

where $h_z^0 = \sqrt{h^2 - (h_x^0)^2 - (h_y^0)^2}$ can be used to express the Bragg angle θ_B as a function of the view direction given by ϕ and the two inclination parameters ω_x and ω_y as

$$\theta_B(\phi, \omega_x, \omega_y, \theta_0) =$$
$$2\arctan\left[\frac{1}{h^2 - 2kh_x(\phi)}\left(2k\sqrt{h^2 - (h_x^0)^2 - (h_y^0)^2}\right.\right.$$
$$\left.\left. \pm \sqrt{4k^2\left[h^2 - h_y^2(\phi)\right] - h^4}\right)\right] + \theta_0. \tag{7.7}$$

Here, an offset θ_0, has been included, which might result from a tilt of either the whole instrumentation with respect to the incidence beam by the underlying base-structure or deviations stemming from the adapter plates.

7.4.2 *Experimental Outline*

The sample manipulator system can now be tested by mounting a sample in Bragg-reflection geometry (BRG) in the Pivot point of the tilt goniometer and using a monochromatic beam to scan a set of rocking scans for different ϕ during a full rotation of the tomographic rotation axis. The scans can then be analyzed and the Bragg peak θ_B

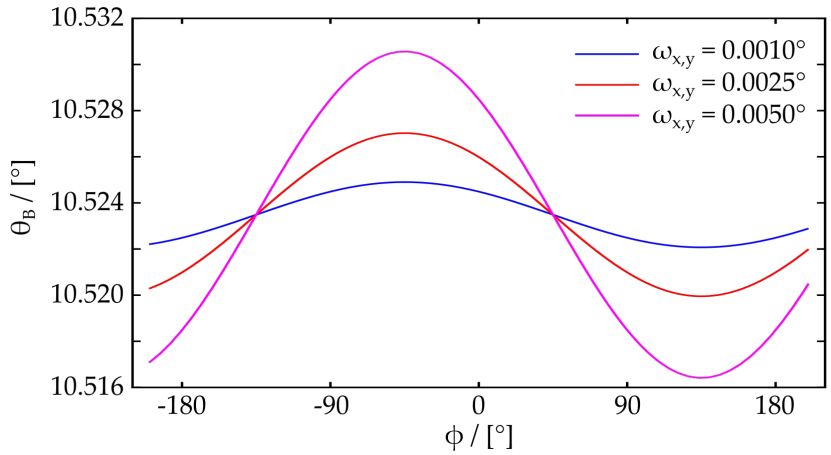

Figure 7.3: Plot of Eq. 7.7, showing the Bragg angle θ_B in dependence of the tomographic rotation angle ϕ for a mis-aligned reciprocal lattice vector. Both mis-alignment parameters, ω_x and ω_x, are set to the same value for each plot. The offset $\theta_0 = 0°$ and the calculations were carried out for an X-ray energy of $E_{X-Ray} = 25.0$ keV being diffracted by the 004 crystal planes of a silicon sample.

can be extracted in a specific ROI, either the center of rotation on the sample surface, i.e., the intersection point of the sample surface and the rotation axis $\mathbf{\Phi}$, or a region with this point in the middle. This will ensure that the measured signal is not distorted by inhomogeneities, like e.g., strain in the sample, since always the same crystal volume is diffracting and possible deviations will be compensated due to the alignment of $\boldsymbol{h}_{hkl}$ with respect to $\mathbf{\Phi}$.
In order to determine the center of rotation on the sample surface and therefore in the Field of View (FoV), a needle can be fixed on the sample with the tip touching the sample surface. It is advisable to acquire a set of 5 to 10 images from different view directions to determine the center of rotation in advance: The positions of the needle tip in the FoV can then be extracted and used to fit an ellipse. The center of rotation is then given by the center of the ellipse. Afterwards the needle should be removed before starting the actual measurement, since it may shadow the incoming or the diffracted beam and thereby influence the contrast stemming from the ROI. To show the effect we here quickly forward to Fig. 7.5, which shows two pairs of rocking scans acquired before and after a rotation about 360°. This of course means, that the angular position ϕ is actually the same and thus the found Bragg peaks should not deviate. In Frames 7.5a and 7.5b the ROI was illuminated without disturbance, while frames 7.5c and 7.5d show measurements where the center of rotation was shadowed by the needle. Although, the determination of the resulting positions θ_{max} is possible for the data in 7.5c and 7.5d and the found error is in the magnitude of $10^{-4\circ}$, which actually represents the resolution limit of the 1-circle segment 5020.10, we observe a sharp decline in

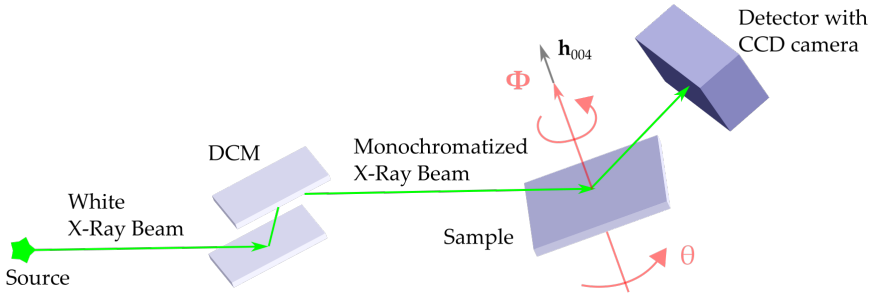

Figure 7.4: Experimental setup utilizing a double crystal monochromator for characterization measurements at ID19, ESRF, Grenoble, France.

counts. Additionally we obtain a better agreement for the scans shown in frames 7.5a and 7.5b:

$$\Delta\theta^{a,b}_{-200^\circ,160^\circ} = |11.1712^\circ - 11.1711^\circ| = 1 \times 10^{-4\circ} \tag{7.8}$$

$$\Delta\theta^{c,d}_{-160^\circ,200^\circ} = |11.1718^\circ - 11.1715^\circ| = 3 \times 10^{-4\circ}. \tag{7.9}$$

Several of the these stability measurements were performed at different end stations. Here tests performed at the ID19 beamline at the ESRF, Grenoble, France, will be of major interest:
At ID19 a Si-111 Double Crystal Monochromator (DCM) was utilized. The energy of the monochromatized beam was set to 23.567 keV. A CCD detector system with an effective pixel size of 0.96 µm was used to record the intensity profile of the beam diffracted by a silicon sample, here exploiting the 004-reflex ($\boldsymbol{h}_{hkl} = \boldsymbol{h}_{004}$) oriented parallel to the surface normal of the sample, see Fig. 7.4. Note, that the experimental conditions provided at ID19 are particularly well suited for this kind of X-ray diffraction imaging techniques. The first application of XDL, [2, 48] have also been conducted at this beamline.

7.4.3 *Measurement Evaluation*

After the determination of the center of rotation, the counts in detector pixels closest to the found position can be analyzed. In the following, the peak positions of the rocking curves were determined by applying a Gaussian fit and extracting the maximum position $b = \theta_{\max}$ of the fitted function

$$g(\theta) = a\mathrm{e}^{-\left(\frac{\theta-b}{c}\right)^2}, \tag{7.10}$$

as shown in Fig. 7.5. One hereby obtains a set of peak positions $\theta_{\max,i}$ - one for every view angle ϕ_i. This allows plotting the Bragg peak as a function of the view direction, i.e., $\theta_B(\phi)$, according to Eq. 7.7.

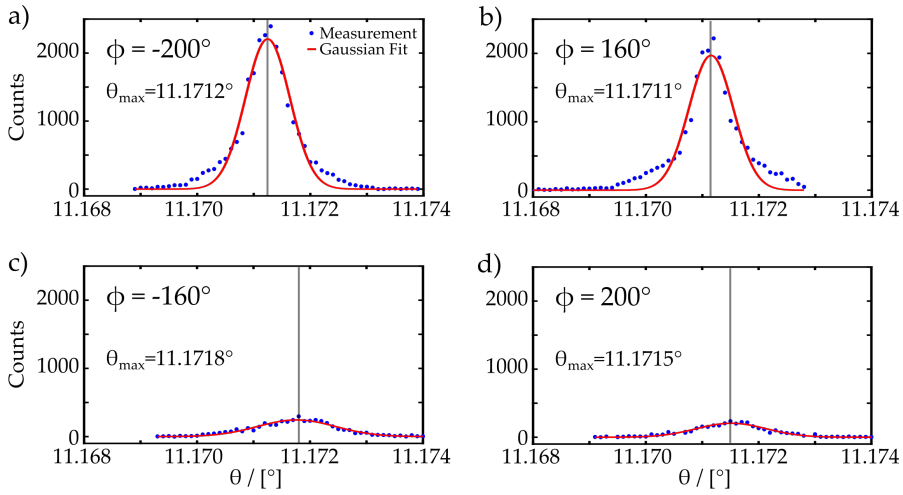

Figure 7.5: Rocking curves measured (blue dots) at ID19, ESRF, Grenoble, France, with the parameters mentioned in Section 7.4.2. A Gaussian function (red line) was fitted to the data to determine the respective maximum positions θ_{max}, which are indicated by the gray lines. The decline in counts in frames c) and d) results from the needle shadowing the beam at the ROI. Note, that these rocking scans were performed during a complete stability measurement of 41 rocking scans with a step size $\Delta\phi = 10°$ in the tomographic rotation, i.e., a total *overlap* of five rocking scans, acquired at the same ϕ-position but after a rotation of 360° and approximately a complete scan duration of 2 to 3 hours in between. This also proves the long-term stability of the instrument for typical measurement durations.

The maximum deviation between the measured Bragg angle $\theta_B(\phi)$ and the respective value of the fitted function $\theta_B^{\mathrm{FIT}}(\phi)$ can be introduced as

$$\Delta\theta_{\max} = \mathrm{MAX}\left[\left|\theta_B(\phi_i) - \theta_B^{\mathrm{FIT}}(\phi_i)\right|\right] \tag{7.11}$$

and a measure for the overall-error as

$$\delta(\theta) = \sqrt{\frac{1}{N}\sum_{i=1}^{N}\left[\theta_B(\phi_i) - \theta_B^{\mathrm{FIT}}(\phi_i)\right]^2} \tag{7.12}$$

where N denotes the number of rocking scans, i.e., $N = 41$ for the presented case.
At first glance, the measurement data shown in Fig. 7.6a seems to have only poor agreement with the shape of the analytical function shown in Fig. 7.3 but at the same time we have to acknowledge, that the Bragg angle θ_B varies in a very small range. Furthermore, we find three local minima at approximately $\phi = -120°, 0°$, and $120°$. Thus,

the fitting model might be improved by adding a cosine function in the form:

$$\theta_B^{c_{1,2}}(\phi, \omega_x, \omega_y, \theta_0) = 2\arctan\left[\frac{1}{h^2 - 2kh_x(\phi)}\left(2k\sqrt{h^2 - (h_x^0)^2 - (h_y^0)^2} \pm \sqrt{4k^2\left[h^2 - h_y^2(\phi)\right] - h^4}\right)\right] + \theta_0 + c_1\cos(3\phi - c_2). \tag{7.13}$$

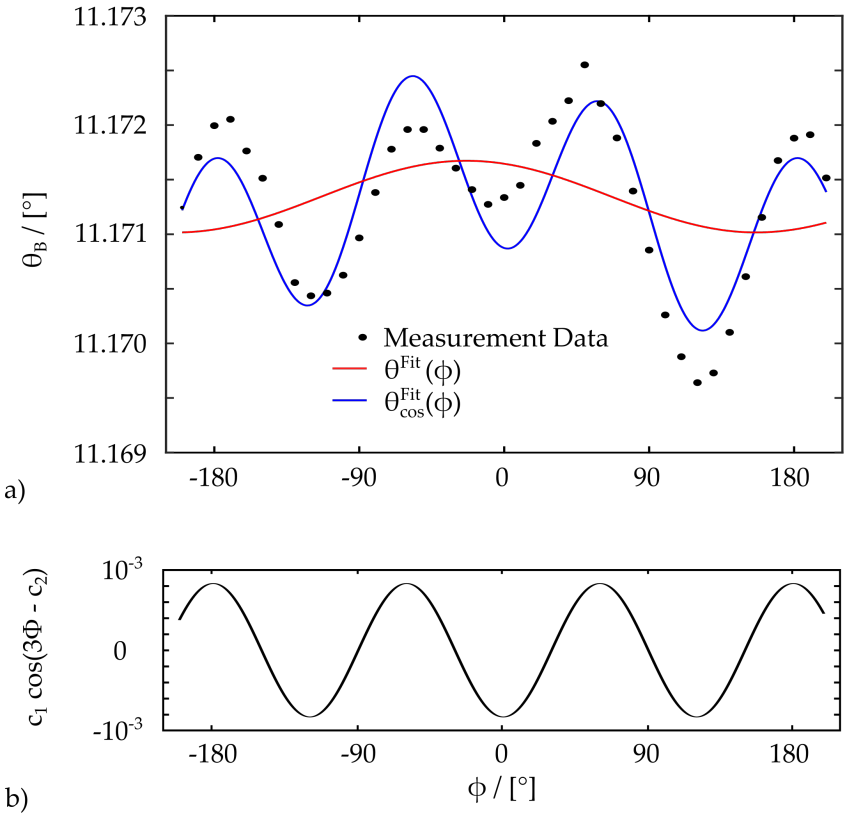

Figure 7.6: Results from the stability measurements at ID19, ESRF. In frame a) the data points are represented by black dots, while the red line shows the fit using the original function given in Eq. 7.7. The blue line shows the result based on the updated model given by Eq. 7.13. Frame b) shows the obtained cosine-function separately.

The result for this function is shown separately in 7.6b and improves the agreement of measurement and fitting model significantly (the best choice for $c_{1,2}$ turned out to be c_1 = -0.0008321° and c_2 = 3.153°). The explanation is given by the threefold symmetry of the parallel kinematics on top. As mentioned before, the SpaceFab Q-Motion is tripod-like: Three legs are mounted onto compiled stacks of piezo motors, carrying the top-plate. For any given orientation of these legs

with respect to the incoming beam direction $\boldsymbol{k}_0$ and therefore the inclination direction of the stack, the stability seems to vary (with three periods in 360°) and the SpaceFab seems to introduce a small additional tilt to the sample. The results are summarized in table 7.1.

	$\omega_x / 10^{-4\circ}$	$\omega_x / 10^{-4\circ}$	$\theta_0 / 10^{-4\circ}$	$\Delta\theta_{\max} / 10^{-4\circ}$	$\delta(\theta) / 10^{-4\circ}$
$\theta^{\text{FIT}}_{\cos}$	4.2	1.3	-24.8	6.5	3.5
θ^{FIT}	3.4	1.3	-24.2	11.1	6.8

Table 7.1: Results from the stability measurements at ID19, at the ESRF. $\theta^{\text{FIT}}_{\cos}$ refers to the fitting function that is incorporating the three-fold symmetry of the parallel kinematics via a cosine function. The second line, i.e. θ^{FIT}, shows the results for the original fit function for comparison.

Finally, the difference between measurement and fit function, i.e.,

$$\Delta\theta_B = \theta^{\text{exp}}_{B,i}(\phi_i) - \theta^{\text{FIT}}_B(\phi), \tag{7.14}$$

may be plotted over the respective ϕ-values to illustrate the performance of the instrument, see Fig. 7.7. Since the influence of the SpaceFab's three-fold symmetry can in principle be considered an instability, we also include the results for no additional cosine function used. This is also meaningful due to the fact, that compensation during a measurement is definitely possible via suitable script implementation, however, it remains questionable if this effort pays off. Incorporating the three-fold symmetry obviously leads to better results, almost by a factor of 2 in maximum deviation $\Delta\theta_{\max}$ and the overall error $\delta(\theta)$. However, the maximum deviation does hardly exceed $10^{-3\circ}$ even if there is no cosine function included in the fit function.

7.4.4 *Angular Resolution*

Next to the angular stability during rotation about the tomographic axis $\boldsymbol{\Phi}$ the angular resolution of the laminographic tilt axis $\boldsymbol{\Theta}$ is of major importance. This refers to the minimal step size the stage is able to move. For silicon, an incremental step size of $\theta_{i+1} - \theta_i \approx 2.5^{-10\circ}$ has proven to be sufficient for achieving suitable weak-beam conditions for projection acquisition. However, materials with considerably higher dislocation densities, like e.g., CdTe and in some cases GaAs, sometimes show lattice distortions that result in higher demands or even make it impossible to reach homogeneous weak-beam conditions over the whole FoV. These challenges can be handled by MARCI, which enables the computation of Virtual Weak-Beam (VWB)-projections, a technique that is currently in development, also see the short descrip-

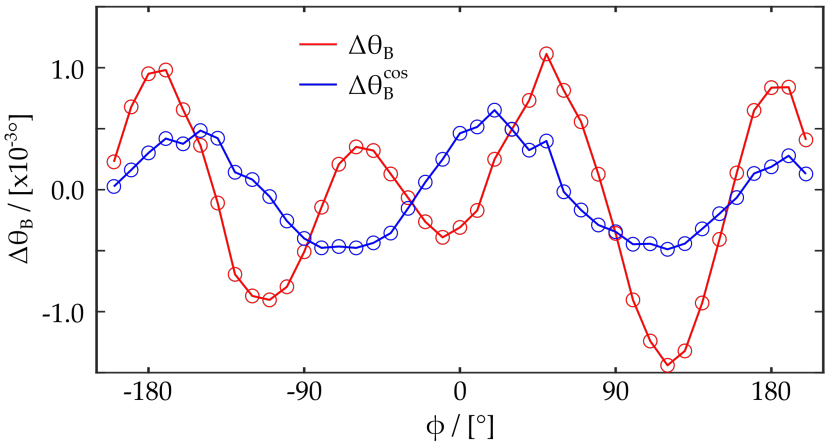

Figure 7.7: Deviation $\Delta\theta_B$ as defined in Eq. 7.14 for the two cases: (i) The red line shows the deviation at position ϕ for the original model, while the blue line includes the cosine function to take the SpaceFab's symmetry into account.

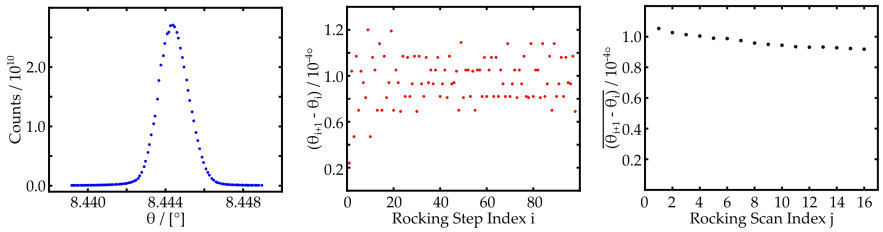

Figure 7.8: Measurement data acquired for a silicon sample in LTG at 25 keV, exploiting the $\overline{2}20$-reflex. The data was recorded at P23, Deutsches Elektronen Synchrotron (DESY) - PETRA III, Hamburg, Germany. a) Exemplary rocking scan of 100 steps in θ covering a range of approximately 0.01°. b) The step sizes $\theta_{i+1} - \theta_i$ during the scan shown in a). c) The mean step size $\overline{\theta_{i+1} - \theta_i}$ of 100 steps for 16 rocking scans at different view directions ϕ.

tion in Section 2.4. For this, and other applications, like regular RCI, high-resolution sampling of the rocking curve is required.

Fig. 7.8a shows a rocking scan measured with the X-ray diffraction imaging station (i.e., sample manipulator and base structure) in its final state. A silicon sample was scanned, exploiting the $\overline{2}20$-reflex at 25 keV, and the step size could be minimized down to 10^{-4}°. This has been the most precise sampling achieved with the instrument so far. In this regime the step size varies significantly as shown in Fig. 7.8b, which shows $\theta_{i+1} - \theta_i$ for a rocking scan encompassing 100 steps in θ, i.e., $i \in [0;99]$. However, the crucial aspect is sampling the rocking curves with steps as small as possible. Equidistant sampling is only of minor concern, if the exact motor positions corresponding to the recorded images are known, which is ensured by encoder read-out. Furthermore, Fig. 7.8c proves that the setup's performance is reliable

in this manner over several rocking scans with intermediate rotation about $\mathbf{\Phi}$.

7.5 SUMMARY AND CONCLUSION

Within the frame of this work a dedicated instrumentation for X-ray diffraction imaging techniques has been compiled, commissioned, and characterized. In its final state the minimal incremental step size of the goniometer, i.e., in θ, is roughly 0.0001°, which allows careful selection of suited weak-beam parameters $\Delta\theta$ and rocking scans with high angular resolution. The angular error is in a magnitude that allows for full rotation without losing Bragg condition. However, in the case of XDL, projection acquisition without intermediate rocking scans is not advisable, due to the high sensitivity of the image quality to the tilt angle θ. At least 5 to 10 rocking scans for re-alignment purposes are recommended during a 130° measurement interval to ensure high image quality. Although the close inspection of rocking scans is not part of this work, it is noteworthy, that a trend to perform even higher numbers of rocking scans during XDL-scans has been forming: Techniques like MARCI provide additional information and enable new ways of data processing, like VWB image calculation.
The sample manipulator system is relatively small (approximately $30 \times 30 \times 30$ cm^3) and the weight does not exceed 30 kg. Therefore, the sample stack is easily integrated into beamline infrastructure. A HP550 hexapod serves as an optional base structure. Due to the high number of degrees of freedom it provides, it is favorable, nevertheless, suited beamline equipment has also been utilized several times, also see Appendix E.
The whole system can be controlled via a dedicated control server that also offers the possibility to connect a CCD camera in order to easily control sample manipulation and image acquisition via one interface, see Fig. 7.9. This is advantageous because especially integrating self-owned stages into beamline control systems can cause many problems and is often time-consuming for several reasons (e.g., driver incompatibilities, IP-adress conflicts, etc.). In combination with dedicated motor controllers and control server the presented X-ray diffraction imaging station represents a *plug-and-play* solution, which is usually ready for operation within a few hours after arrival at the beamline.

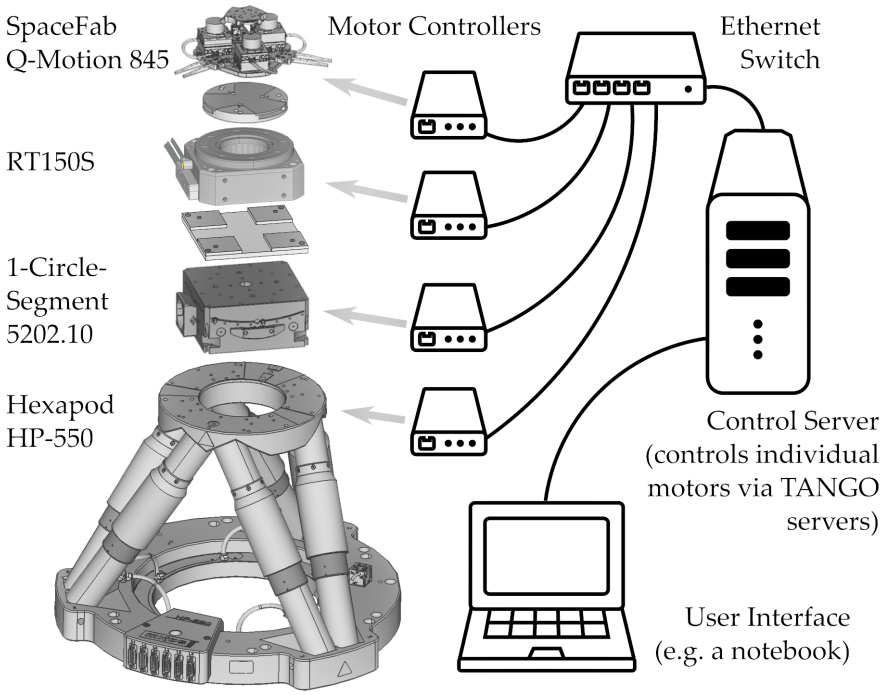

Figure 7.9: Technical drawing of the sample manipulator system including the (optional) base-structure, with schematical illustration of the controlling equipment. Sample manipulation and image acquisition are handled by the control server and easily controllable via one user interface, e.g., a conventional notebook.

8

INVESTIGATION OF SUITED RECONSTRUCTION TECHNIQUES

Optimizing the three-dimensional (3D) reconstruction procedure of tomographic and laminographic image data is an ongoing topic of research, for novel imaging techniques and applications as well as for well established 3D imaging methods. This ranges from medical imaging (e.g., by computed tomography) used among others in diagnosis for bone and vessel imaging [95] to electron tomography, e.g., to 3D-map materials approaching atomic scale resolution [26, 96]. In the case of electron tomography, often samples and sample holders limit the complete angular range of 180° to roughly 140° being accessible for image acquisition. Commonly, this is referred to as the 'missing wedge' and reduces the final quality of the 3D reconstruction image [97]. Obviously, this restriction is similar to the limited acquisition range of X-ray Diffraction Laminography (XDL) in Laue-transmission geometry (LTG), illustrated in more detail in Section 2.3. In addition, the number of projections to be recorded can either be limited by available measurement time or due to the specimen's sensitivity to radiation. This may also lower the image quality of the 3D result.
The wide range of challenges associated with handling this kind of projection data sets, whether they consist of X-ray topographs or are Transmission Electron Microscopy (TEM) based, motivates the investigation of different reconstruction algorithms in order to find robust techniques for the 3D reconstruction procedure. Therefore, the following chapter will focus on the reduction of the required number of projections, while maintaining a level of quality of the reconstruction image that allows a final segmentation by line tracing. We will summarize the main characteristics of XDL data sets, regarding the 3D structure under investigation as well as the specific properties of the topographic quasi projections that stem from the underlying contrast formation mechanism described in Chapter 5. Two algorithms will be tested on the characteristics of XDL projections individually and in combination - where it is feasible - and the respective performance will be compared to Filtered Backprojection (FBP), which is still widely utilized and in particular was utilized in the previous XDL studies in [2, 48].

8.1 MAIN CHARACTERISTICS OF TYPICAL XDL DATA

For the case of silicon, low dislocation densities embedded in a nearly perfect crystal are of interest (there may be point-defects present, but

no small angle grain boundaries or large sites of plastic deformation). This means we are handling sparse volumes of several mm^3 in size that contain arrangements of partially straight, line-like features. The desired result of the reconstruction can therefore be considered as binary: Either a certain point or voxel belongs to the perfect (here meaning dislocation-free) part of the crystal, resulting in a value of 0, or it is occupied by a dislocation line, i.e., the value of the voxel is 1. However, these properties may be similar to other application cases and especially they do not contradict the criteria for projections. Thus, in order to make a clear distinction of certain characteristics that will become clearer in the following, we label these as *regular characteristics*, also see Fig. 8.2.

As discussed in Chapter 5 we have to expect intensity fluctuations in the line contrast with changing view angle ϕ, except for dislocation line directions parallel to the selected reciprocal lattice vector: $\boldsymbol{l} \parallel \boldsymbol{h}_{hkl}$. This property of XDL data-sets violates the projection criteria since in the common sense of tomographic projections an object should not change from one view angle to another. Consequently, this will lead to inconsistencies that the utilized reconstruction technique will need to overcome. Since usually the image data is preprocessed by means of absorption correction with respect to the path lengths of the X-rays for every respective view direction, one could attempt to approach this feature performing a second correction according to the theoretical prediction of the intensity variation. However, the intensities behavior over ϕ is depending on the line direction $\boldsymbol{l}$ and the Burgers vector $\boldsymbol{b}$. This means a correction would require the clear separation of all individual segments in a complex arrangement, which would demand extensive effort. The most straight forward way would by itself require a high-quality reconstruction to begin with. We will also desist from binarizing the images to achieve similar contrast intensity for all dislocation segments. Inhomogeneities in the beam profile usually lead to regions of different contrast intensity in real measurement data. Furthermore, the previous reconstructions obtained by FBP indicate that the efforts of preprocessing related to this issue might prove to be unnecessary.

As a second specific characteristic we declare the position of the line contrast in the topographic images and its dependence on the view direction. Based on the theoretical framework presented in Chapter 5 we know that the volume containing the distorted crystal lattice that fulfills the Bragg-condition for $\theta = \theta_B + \Delta\theta$ does not only change its size but also circulates around the dislocation core with changing view angle ϕ. Consequently, image contrast created by strain in the vicinity of a dislocation core will indicate a different position of the respective feature in the volume from one projection to another. In the case of FBP this leads to a blurring of the line features in the reconstruction. However, it needs to be seen if other techniques treat

these inconsistencies in the localization of dislocation lines in a similar way or if the iterative comparison of intermediate steps with input data turns out inconclusive, finally leading the algorithm to fail.
Since the *intensity fluctuations* and the *contrast shift* both introduce a dependency on the view angle to the object function, consequently, the projection criteria is violated. Similar problems may occur in other 3D reconstruction problem, still these are important and very specific challenges regarding the case of XDL and they will therefore be labeled as *specific characteristics*. In the following, the focus will be put on the effects of the specific characteristics.

8.2 SELECTION OF RECONSTRUCTION TECHNIQUES

As mentioned above, so far only FBP has been used to obtain reconstructions by means of XDL. Still up until today the method is widely used in tomography and since previous XDL studies were rather an utilization of FBP and not an investigation of its performance, it will be included in the testing, also for comparison to make estimations on what to expect from the other techniques once they are applied to measurement data.
Secondly, the Simultaneous Iterative Reconstruction Technique (SIRT) [98] was selected to be tested. As a third candidate we investigate the Discrete Algebraic Reconstruction Technique (DART) [99, 100] which is a rather novel method designed to handle in particular discrete data sets with only few gray values. Especially but not only in electron tomography these two approaches are broadly utilized and adapted [101–105]. In the following, a brief overview over the basic concepts of the two methods will be given.

8.2.1 *Simultaneous Iterative Reconstruction Technique*

SIRT - proposed in [98] - follows the basic concepts described already in Section 2.1.2.2. However, implementations of SIRT do not change the cell values f_j with each projection, i.e., with each line in Eq. 2.12. These values rather remain unchanged during one iteration and are updated in the end according to the average of all calculated correction terms:

$$\begin{aligned}\Delta \boldsymbol{f}_j &= \frac{1}{M}\sum_{i=1}^{M} \Delta \boldsymbol{f}_j^i \\ &= \frac{1}{M}\sum_{i=1}^{M} \boldsymbol{f}_j^i - \boldsymbol{f}_j^{i-1} \\ &= \frac{1}{M}\sum_{i=1}^{M} \frac{\left(p_i - \boldsymbol{f}^{i-1}\cdot \boldsymbol{w}_i\right)}{\boldsymbol{w}_i \cdot \boldsymbol{w}_i} \boldsymbol{w}_{ij}. \end{aligned} \tag{8.1}$$

In the case of XDL this might be a suitable approach to handle the inconsistencies. Changing the result every time information from the next projection is available could result in a back and forth alteration of the image voxels $\boldsymbol{f}_j$, whereas averaging over all projections might yield a blurred approximation, hopefully with a clear localization of the dislocation feature at the position of highest overlap.

8.2.2 *Discrete Algebraic Reconstruction Trechnique*

A novel technique, that has been developed in the recent years, is the Discrete Algebraic Reconstruction Technique - or short: DART. Aiming to provide an elegant and robust solution for reconstruction problems with sets of only a small number of projections or projections from only a small angular range, DART makes use of *a priori* knowledge about the *materials* present in the reconstruction volume. In our case, we are of course not dealing with different *materials* to be represented by different gray values. However, as discussed above a *perfect* reconstruction would be a binary volume, in which a voxel either represents dislocation-free space or is *occupied* by a dislocation line. Since DART has also proven to handle noisy projection data particularly well, it seems like a technique suited for the XDL reconstruction problem. However, again the important question is how it is able to handle the inconsistencies present in XDL data sets.
In principle, DART relies on an Algebraic Reconstruction Method (ARM) as a subroutine. Here, SIRT is chosen for the same reasons given in section 8.2.1. DART starts with a regular ARM-reconstruction to which a segmentation via thresholding is applied to categorize the present materials and assign different gray values accordingly. As a next step, the volume is devided into fixed (F) and free (U) voxels. This can be achieved, e.g., by collecting all voxels that are neighbours to a voxel with a different gray value. In a binary image this would mean that the background voxels with value 0 as well as the voxels within the structure with value 1 are defined as fixed, while the boundary voxels are defined as free. The next ARM-reconstruction is then confined to the free voxels F, this vastly reduces the number of variables in the linear equation system 2.12 while the number of equations stays the same. Afterwards a stop criterion can be checked and the next DART iteration is performed if the criterion is not met. Before the next segmentation step, however, a smoothing is performed by gaussian blurring, which has shown to improve the overall result, since with limiting the free pixels the ARM will try to match noise in just this subset of pixels resulting in heavy fluctuations. This workflow is also schematically shown in Fig. 8.1. Note, that the final iteration always ends with an ARM-reconstruction, i.e., the result is not strictly discretized to the defined gray values, whether they are binary or more complex.

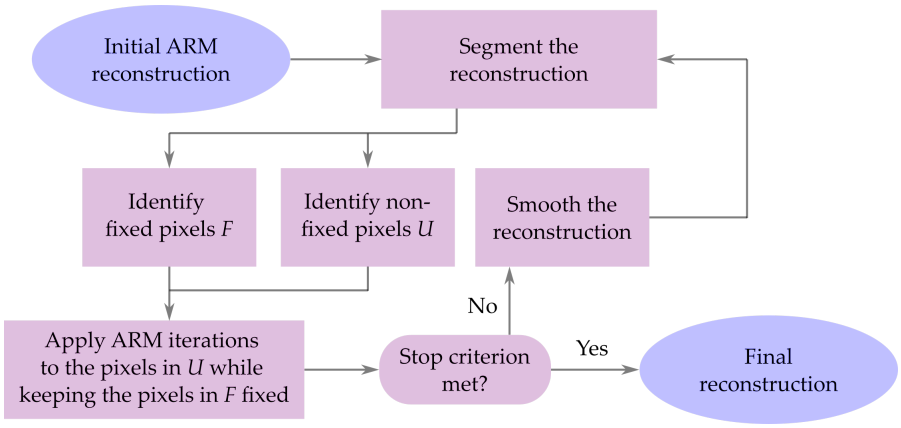

Figure 8.1: Schematic workflow of the discrete algebraic reconstruction Technique (DART).

The process may further be enhanced by adding a set of random voxels to the group of free voxels F. This may help to find inclusions in the volume that might otherwise be overlooked.
It is however noteworthy, that although DART seems very promising, it relies on the assumption that the object function is well-defined not only regarding its localization in the volume but also with respect to its gray levels. Due to the intensity fluctuations and the contrast shift in XDL projections this is not true for our application case. Thus, we may face problems created during the respective steps of a DART iteration, e.g., one could assume that defining a set of fixed pixels for a line-like feature whose position is travelling through the volume will eventually lead to the failure of the technique. This becomes even more likely when paying respect to the circumstance that not only position but also intensity varies from one projection to another. It is also noteworthy that in comparison to SIRT, DART in our application case is supposed to provide an almost binary image. This is achieved by defining the allowed gray values accordingly and the corresponding segmentations performed in every iteration. Eventually, the algorithm has to fit contradicting data points to binary values, which might lead to an outcome of lower quality compared to the application of FBP or SIRT.

8.3 RECONSTRUCTION OF SIMULATED DATA SETS

To determine the performance of the three techniques and how well they handle the inconsistencies, stemming from the topographic image formation, two separate approaches are proposed, this is also illustrated in Fig. 8.2: Firstly, the reconstruction techniques will be applied to projections simulated by means of the theoretical framework as presented in Chapter 6. This will result in volumes containing only one (or only few) dislocation(s), but therefore the projections contain both

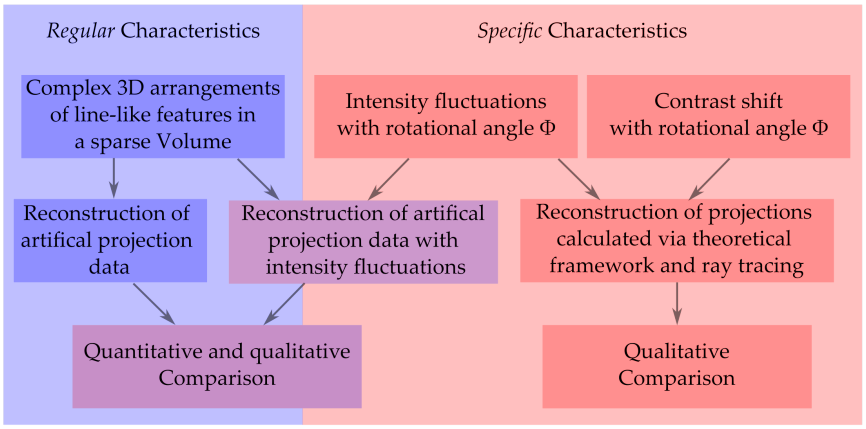

Figure 8.2: Schematic view showing the three major properties of XDL data sets, devided into *regular* and *specific* characteristics. While complex 3D structures with intensity fluctuations can also be evaluated quantitatively by comparing the initial to the reconstruction volume, we restrict the analysis of simulated projection (as presented in Chapter 6) data sets (incorporating both *specific* characteristics) to a qualitative comparison.

specific characteristics - namely intensity fluctuations and contrast shift. The results will be compared in a purely qualitative fashion. Secondly, an artificial volume containing an arrangement of line-like features represented in a binary fashion will be used for performance tests. Projections will be computed and artificial noise will be added in order to approach realistic conditions. Results from projections with and without intensity fluctuations will then be compared to the initial volume quantitatively and qualitatively.

This two-faceted approach is motivated by the fact that such a quantitative evaluation is simply not feasible, if the data contains a contrast shift. In a given volume the position of a dislocation is localized, while in the projections it is not. Consequently, introducing a contrast shift to a set of projections computed from an initial volume would yield a reconstruction volume, in which the dislocation lines are positioned differently as in the initial volume.

Another noteworthy point is that one could compare the projections used as input with a set computed from the reconstruction result. This would reduce computation times and is in fact done very often. However, both special characteristics make this approach unfeasible. The projections computed from the result would obviously not contain any inconsistensies, since they are based on the well-defined object function provided by the reconstruction volume (which is not view direction dependent anymore). Therefore, for the evaluation of reconstructions of line-like features with and without intensity fluctuations we will rely on a direct comparison of initial and reconstruction volume.

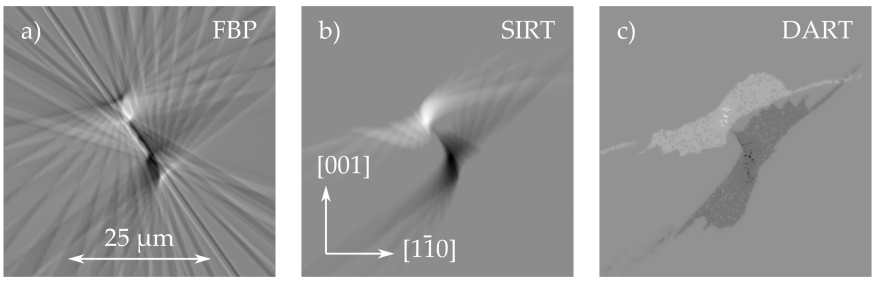

Figure 8.3: Exemplary slices (perpendicular to the rotation axis) of reconstructions of simulated projections (see Chapters 5 and 6) of a dislocation with line direction $\boldsymbol{l} = [10\bar{1}]$ and Burgers vector $\boldsymbol{b} = a/2[110]$ utilizing the $\overline{2}\overline{2}0$-reflex at an energy of 25 keV. The respective reconstruction techniques utilized are: a) FBP, b) SIRT, and c) DART with 4 DART iterations and 2 gray values, i.e. {0,1}. For every technique the sets of projections from the two acquisition interval were reconstructed individually and then merged according to the approach introduced in Section 6.2.

All reconstructions presented within this work have either been obtained by using *TOFU* for the application of FBP, a part of the *UFO*-framework [106], or by utilizing the *ASTRA Toolbox* for SIRT and DART based reconstructions [107, 108].

8.3.1 *Effects of Contrast Shift*

Based on the results in Chapter 6 the investigation starts with the reconstructions of two ensembles of projections, P_{I_1} and P_{I_2}, from two acquisition intervals in LTG. Each set of projections consists of 14 projections with view directions within a 130°-wedge, compare Chapter 6. The X-ray energy was set to $E_{\text{X-ray}} = 25$ keV resulting in a Bragg angle $\theta_B = 7.42°$ for the $\overline{2}\overline{2}0$-reflex of silicon. The Bragg deviation is $\Delta\theta = 0.002°$ and the diffraction interval is defined by $\delta = 0.0007°$. The dislocation line has a direction of $\boldsymbol{l} = [10\bar{1}]$ and the Burgers vector (BV) is $\boldsymbol{b} = a/2[110]$. Of course, this selection of parameters is intended to create a particularly high contrast shift. As shown in Fig. 6.5 this configuration of $\boldsymbol{l}$ and $\boldsymbol{b}$ leads to excitation relatively far from the dislocation core and thereby to strong inconsistencies in the data sets. In addition the weak-beam parameter is relatively small (but realistic, see Chapter 9) and thus results in excitation further away from the dislocation core.
Cross sections of the reconstruction volumes perpendicular to the rotation axis are shown in Fig. 8.3, again the dislocation core is positioned in the center of each slice. The FBP result in Frame 8.3a shows how the result is basically an overlap of backprojections of the projections. The ray-like artifacts indicate the view directions of the respective projections. They are clearly visible for only 14 projections per interval and

would decrease in visibility with an increasing number of projections n_{proj}. However, the darkest and brightest features indicating the dislocation positions obtained from the two intervals are clearly localized. Frame 8.3b was obtained using SIRT and we directly observe how the artifacts reduce drastically in comparison to FBP. Apart from some weak stripe-like features the image is very clean and the dislocation positions are shown by the crescent moon shaped dark and bright features. DART seems to run into problems facing the inconsistencies in the projection data. The features are more stretched out and contrast maxima are only given buy several black and bright dots (or pixels) and not as clearly visible as in the SIRT reconstruction. It is likely that the additional steps DART performs with every ARM reconstruction (here 4 equal to the number of DART iterations) simply do not converge with this level of inconsistencies in the input. However, it is noteworthy, that DART here only assumes two values, i.e., 1 and 0. In the end the final reconstruction is saved before and after segmentation via a final thresholding. What is shown here is the final reconstruction before thresholding, i.e., the data is not binary yet. Allowing more gray values might improve the result but an example with 5 gray values in Appendix F indicates only a neglectable effect. At same time this diminishes the suitability of DART regarding the anticipated binary result.
Drawing a first conclusion from these results, we find that SIRT provides the best reconstruction for the investigated parameter set. Apart from the quality of the reconstruction, SIRT is also easer to apply: While DART requires a set of input parameters which have to be carefully optimized for a given problem, SIRT only requires the number of iterations to perform and optionally allows for upper and lower constraints (e.g., no values below 0 in the reconstruction volume).

8.3.2 *Line Structures in Sparse Volumes*

The 3D structure we use in the following is binary and in its shape and distribution is based on a real dislocation arrangement captured by XDL, it was presented in [2, 48, 49]. Hereby, we ensure that the projection sets emulate realistic conditions regarding dislocation densities and crystal volume size. The volume under investigation is 1418 × 1418 × 1518 voxels large, which with an effective pixel size of 0.75 µm during the respective measurement corresponds to 1891 × 1891 × 2024 $\mu m^3 \approx 7.237\ mm^3$. A set of an arbitrary number (in the following denoted as n_{proj}) of projections will be computed and artificial noise will be added to each image. An example is given in Fig. 8.4 with a projection of the artificial structure in Frame 8.4a and the same projection with added noise in Frame 8.4b. Since, the BV-distribution within the original arrangement is known, we are able to modify each dislocation line segment (i.e., the straight parts of a dislocation line)

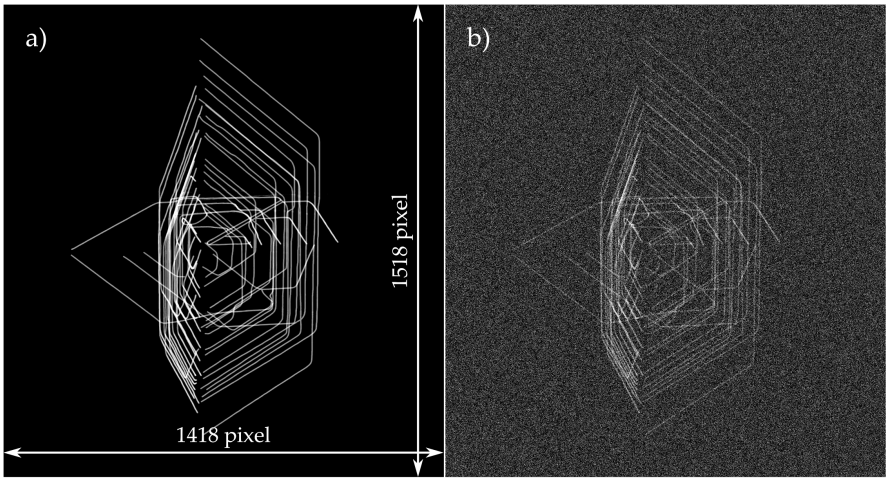

Figure 8.4: Exemplary projections from a simulated binary volume. The view direction is given by a 20°-rotation about a vertical axis starting from the surface normal of the virtual wafer volume, this axis is afterwards tilted by the laminographic-angle of 7.42° (corresponding to an X-ray energy of 25 keV and $\boldsymbol{h}_{hkl} = \boldsymbol{h}_{\overline{2}20}$ for silicon) towards the viewer. The projection is shown without noise in a) and with added artificial noise in b).

in each projection by its intensity fluctuation defined by the view angle ϕ, the line direction $\boldsymbol{l}$ and the BV $\boldsymbol{b}$. Essentially, this requires a segmentation by line tracing of the original volume, classifying all segments with a specific line direction and BV. Projections of these partial structures can than be multiplied with factors corresponding to the intensity profiles presented in Fig. 6.7. Applying this procedure to all partial volumes containing only dislocations with the same BV and line directions, one obtains the set of projections of the complete structure by simply summing up all projections with the same view angle.

The evaluation relies on a voxel-to-voxel comparison of initial and obtained reconstruction volume, as mentioned above. In order to account for the fact, that the initial volume is binary and the reconstruction volume in general is not, a thresholding method will be applied to binarize the obtained reconstruction. This can also be seen as a first automated segmentation step. The workflow is also illustrated in Fig. 8.5.

Regarding the procedure to binarize the reconstruction volume, nowadays, a variety of thresholding methods is available [109]. In the following, a *maximum entropy*-based thresholding technique was applied [110]. It is a widely used algorithm and yielded better results than e.g., the well-known *IsoData* method [111]. After the binarization of the result we compute the accumulated voxel error as

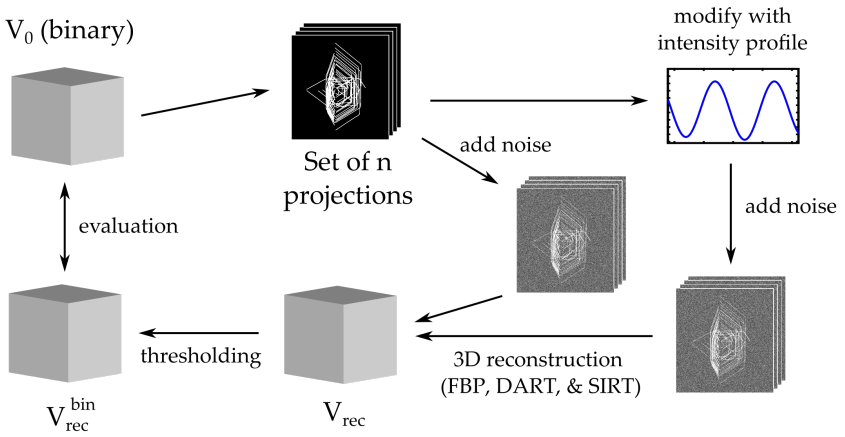

Figure 8.5: Illustration of the workflow to compare reconstructions obtained via different techniques for projection sets with and without intensity fluctuations.

$$\sigma = \sum_{i,j,k=1}^{N_i,N_j,N_k} \left| v_{ijk}^{\text{init}} - v_{ijk}^{\text{Rec}} \right| \tag{8.2}$$

with v_{ijk}^{init} and v_{ijk}^{Rec} denoting the values of the voxel at (ijk) in the initial original volume and the reconstruction volume, respectively.

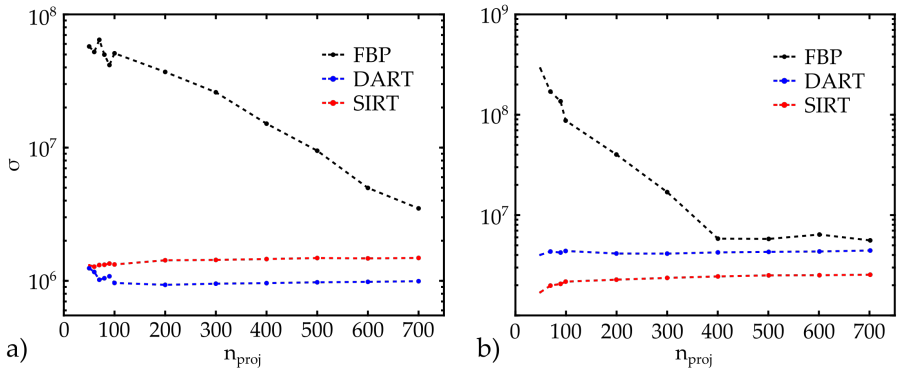

Figure 8.6: a) Accumulated voxel error σ over number of projections n_{proj} used for the reconstruction. The data points for FBP, DART, and SIRT in black, blue, and red, respectively, are connected by dashed lines to show the overall trend. Here, only noise was added to the projections. b) Same as in a) but now with intensity fluctuations introduced to the respective projection data sets. For the evaluation the volume was reduced to the relevant section containing the structure, yielding a size of 600 × 1200 × 1300 voxel = 936.0 × 10^6 voxel of which in the original volume 824385 voxel have value 1, i.e., represent a dislocation line.

The results shown in Fig. 8.6 show how FBP is the only technique that benefits from an increasing number of projections, while the

voxel error for SIRT and DART seems to hardly change when increasing the number of projections from 50 to 700. Frame 8.6a shows that for *regular* 3D reconstruction of noisy projections without any *special* XDL-features DART yields the best results for any number of projections. This was expected since the technique is optimized for this kind of reconstruction problem. SIRT also shows constant performance, although the error count is considerably higher (about 1.5 times the one of DART). If one now introduces inconsistencies in the form of intensity fluctuations to the data sets, the results change. In general higher deviations from the original volume are observed. And again the quality of the DART-reconstructions suffers in particular due to the object function now depending on the view direction. In this case, shown in Fig. 8.6b, SIRT seems to yield the best result, while for higher numbers of projections ($n_{\text{proj}} > 300$) FBP approaches the performance of DART. One also recognizes a slight increase in error counts for increasing n_{proj} in the SIRT-reconstructions. Looking at the respective reconstructions one finds, that this circumstance is due to an interplay of the reconstruction and the thresholding: With increasing n_{proj} the line features in the reconstruction become slightly larger and are not cropped as advantageously for the evaluation. Having a look at an exemplary slice in Fig. 8.7 one finds in Frames 8.7h and 8.7i that the quality improves significantly despite a higher error count. Fig. 8.7 also supports the other conclusions drawn from the results in Fig. 8.6:

- Frames 8.7b and 8.7c show how DART yields almost perfect reconstructions already for only $n_{proj} = 50$ projections, if the input data contains no inconsistencies. With the introduction of intensity fluctuations, however, the quality drastically decreases. It is also noteworthy that in comparison to SIRT DART provides an almost binary image. The reason for this are the segmentations performed in every iteration, but the attempting to fit contradicting data points to binary values eventually leads the algorithm to fail.

- SIRT on the other hand provides reconstructions of sufficient quality for 50 projections, too, see Frame 8.7d. But here the results improve noticeably with more input information as can be seen in Frame 8.7e. On the other hand, SIRT proves its resilience against inhomogeneities within the data set, compare Frames 8.7h and 8.7i with 8.7d and 8.7e, respectively.

- In addition, it is noteworthy that DART relies on a larger set of several parameters and adjustments improve the result also for the case where intensity fluctuations are included. However, a far more crucial challenge seems to be connected to the contrast shift, for more details see Section 8.3 and Appendix F.

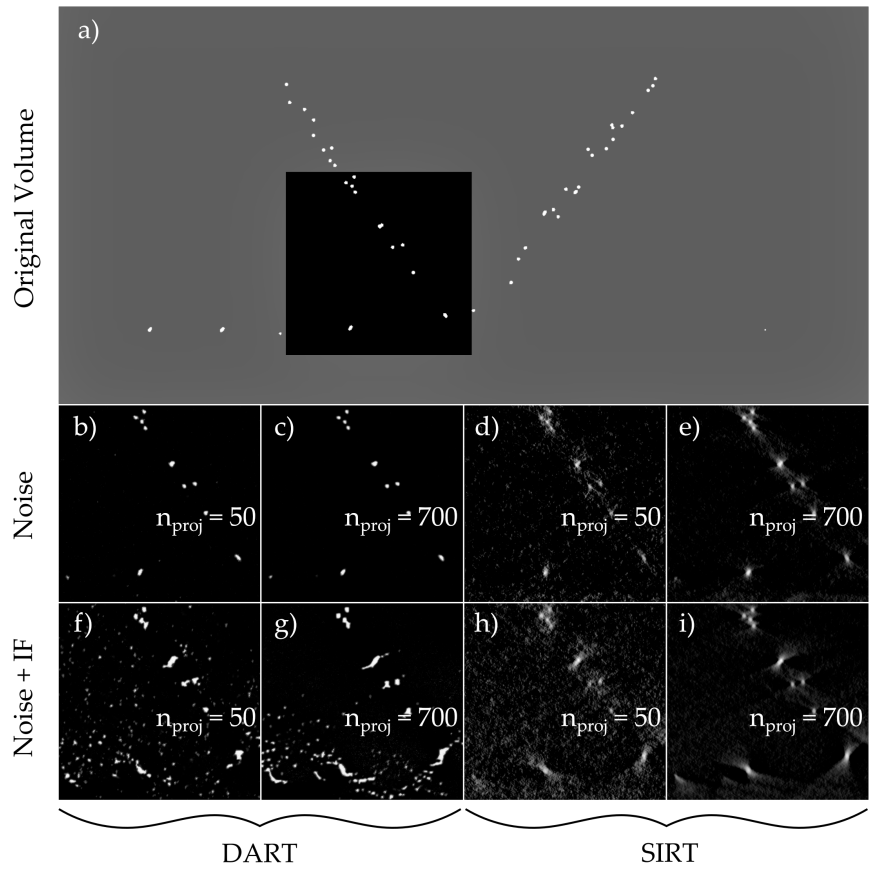

Figure 8.7: Exemplary slices from a) the original volume, showing the cross-section of the evaluated volume in its entire size; b) and c) and d) and e) DART- and SIRT-reconstructions for different numbers of projections with only noise added, respectively; f) and g) and h) and i) DART- and SIRT-reconstructions for different numbers of projections with noise and intensity fluctuations, respectively.

8.3.3 *Incorporation of A Priori Knowledge*

As mentioned before, algebraic reconstruction techniques easily enable the incorporation of *a priori* knowledge. This is done by adding a so called *mask* to the projection data input. A mask can be described as a simple binary pattern corresponding either to a projection or a slice from the reconstruction volume, defining the areas where features are present and cutting out all empty space, i.e., not allowing the algorithm to take empty voxels into account. Obviously, this can support the reconstruction technique and lead to better results. For most XDL data sets we know that the reconstruction volume is particularly sparse. The structure used for the analysis in Section 8.3.2, for example, only occupies 0.088 % of the investigated volume and it is based on real measurement data and thus represents a realistic dislocation arrangement in silicon. Therefore, this section will introduce a simple technique that provides suited masks for projection

data and the reconstruction volume of a given structure. As a first step, a thresholding value ρ needs to be selected for the projection data, allowing the computation of an *inverted* set of projections, meaning that every pixel in a projection with a value below the threshold is set to 1 and pixels with a value equal or above the threshold are set to zero. The goal is to assign 1 to a vast majority of pixels in a projection that do not indicate a part of a dislocation line. This set of inverted projections is then backprojected into the reconstruction volume, yielding a volume that has high-valued features in regions where the majority of projections imply empty space. If one now applies another thresholding procedure to the obtained volume with thresholding value ν, where every voxel above ν is set to zero and the values below ν to 1, respectively, this yields the volume mask M_{vol}. Experience has shown that in many cases, the parameters ρ and ν can quickly be selected in a way, that the mask result M_{vol} already represents not only a mask but a first medium quality reconstruction of the structure. Taking it one step further, one may now create a set of projection masks M_{proj} by simply computing projections based on M_{vol} and binarizing the result. Again this exploits a way of averaging over all projections, before the result is modified, in order to handle the inconsistencies in a reliable way. The computation times of this masking approach are very short in comparison to more complex techniques like SIRT or DART. This is due to the fact that the whole process is very similar to only one iteration of SIRT. Therefore, even a very careful search for a suited parameter set (ρ, ν) can be successfully completed in short amounts of time (approximately 5 to 20 minutes). Additionally, the choice of ρ and ν directly controls how much tolerance the scheme applies to fluctuating intensities and shifts of the dislocations lines from one projection to another. This convenient adjustability is the reason why the technique will here exemplarily be applied directly to real measurement data, skipping the step of testing procedures on artificial or simulated data sets.

A possible outcome of this masking technique, that will from now on be referred to as Empty Volume Backprojection (EVBP) is shown in Fig. 8.8. Note, that the artificial data used in the previous section is based on the measurement data used here. Therefore, the structure is identical and one may use the artificial volume in Frame 8.8e for a qualitative comparison with the obtained volume mask in Frame 8.8f. For this particular application the parameters ρ and ν were selected to yield very strict criteria. This ist already visible in the projection masks in Frames 8.8c and 8.8d, which almost look like line segmentations of the projections in 8.8a and 8.8b. This choice demonstrates how well some line features are captured in the volume mask 8.8f and how it may serve as an intermediate result when reconstructing a structure. However, careful comparison with Frame 8.8e shows that some features are lost, others appear in M_{vol} but not in the true

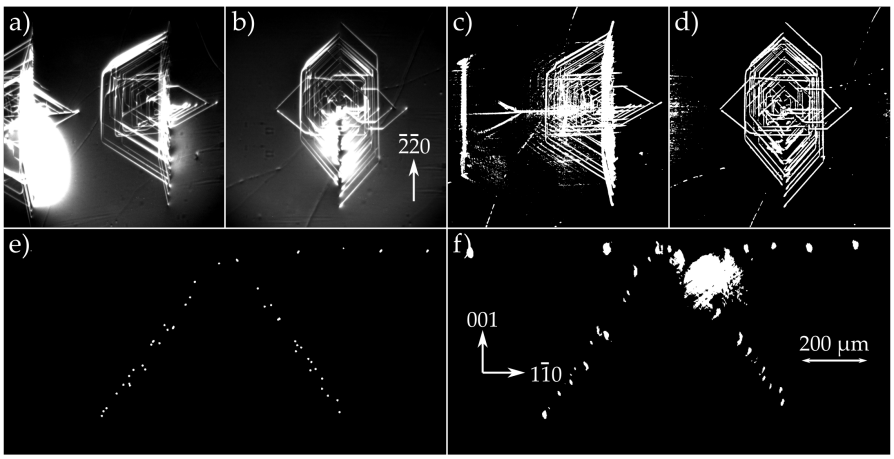

Figure 8.8: Exemplary masks for projection data and reconstruction volume. a) and b) Projections from different view directions taken from the measurement data the previously used artificial data is based on. c) and d) Binary projection masks corresponding to a) and b), respectively. e) Slice from the artificial volume, which may here serve to display the true structure for comparison. f) Slice from the obtained volume mask corresponding to e). Only 35 projections were used to compute the masks. In the measurement the $\overline{2}\overline{2}0$-reflex of silicon was used with an X-ray energy of 40 keV and a weak-beam parameter $\Delta\theta = 0.002°$. The projection data was absorption corrected and a band-pass filter was applied in the preprocessing. As preparation for the masking technique an intensity cut-off was performed to constraint values in the images to the interval [0;0.2] and the thresholding parameters were set to ρ =0.02 and ν =0.4.

structure. It goes to show that this approach has to be treated with caution: When computing masks to support a technique like SIRT it is always advisable to set ρ and ν rather generously, to allow tolerance space for inconsistencies and avoid cutting of certain features in the final reconstruction. Often times it is also advantageous to compute rather narrow masks and broaden the features by a few pixels (or voxels) afterwards.

8.4 SUMMARY AND DISCUSSION

Three different reconstruction techniques have been tested regarding the main characteristics of XDL data. Not surprisingly, Algebraic Reconstruction Techniques (ART) methods showed a significantly better performance for *regular* data sets, meaning projection ensembles that show no inconsistencies, especially when dealing with a small number of projections and a significant level of noise. This is a widely known fact as already mentioned before. More insightful are the tests that incorporate the *specific* properties of XDL projection ensembles, namely the view direction dependent intensity fluctuations of dislocation line

contrast, and the also view direction dependent localization of the diffracting crystal volume, here also referred to as contrast shift.
In the two cases of (i) only intensity fluctuations introduced to an arrangement of line features and (ii) intensity fluctuations and contrast shift in simulated projections of single dislocations the promising DART algorithm failed to produce superior results. Responsible are the DART-iterations, designed to fit (little) input information to a 3D volume in a consistent manner. This assumed consistency is not in par with the reality of XDL's contrast formation. In Appendix F it is shown that a reduction of the number of DART-iterations can improve the result for case (i). This is obvious, since less iterations effectively mean that DART approaches SIRT (if SIRT is selected as the employed ARM algorithm), and it is noteworthy that by careful parameter setting DART also for this case can produce better results than SIRT. The more crucial case is however represented by (ii), see Section 8.3.1 and in particular Fig. 8.3. In this case a straight forward attempt to utilize DART in a fashion more tolerant towards the specific characteristics of topographic projections is to allow more than two gray levels, i.e., not searching for a binary but a grayscale solution. However, increasing segmentation values from { 0.0 , 1.0 } to { 0.00 , 0.25 , 0.50 , 0.75 , 1.00 } does not improve the reconstruction significantly, also see Appendix F.
Another aspect to take into account is computational effort and simple applicability. While FBP offers fast computation and simple application, SIRT computations require more time and memory. Configuration allows setting constraints for the solution, the number of iterations and the incorporation of masking data for projections and reconstruction volume. DART also enables masking but requires a much higher number of input parameters. This makes straight forward utilization difficult, although automated routines have been developed to determine an optimal parameter set [112]. Naturally, computation times increase linearly with the number of DART-iterations, making reconstructions more time-consuming in comparison to SIRT.
Concluding, SIRT is the best suited reconstruction technique for the XDL reconstruction problem for two major reasons, showing its superiority to FBP and DART. Firstly, SIRT yields better results than FBP, especially for very small numbers of projections. Secondly, it handles inconsistencies in XDL data sets apparently far better than DART. Therefore, for the further investigations within this work, SIRT will be applied to all data sets if not explicitly declared otherwise. The content of the next chapter will concern the question how far the number of projections can be reduced regarding real measurement data, furthermore, support of SIRT by EVBP will be tested.
On a last note, it is important to stress, that EVBP not only as masking support but also as a single tool is extremely powerful and can provide reconstruction results of sufficient quality. Especially, closer inspection

of the backprojection volume before the segmentation step to obtain the volume mask M_{vol} is encouraged.

9 MINIMIZING THE NUMBER OF PROJECTIONS

In this chapter the Simultaneous Iterative Reconstruction Technique (SIRT) will be applied to measurement data with the support of Empty Volume Backprojection (EVBP). Here, the main objective is to reduce the numbers of projections used as input, while maintaining a sufficient quality of the reconstruction. The usual workflow after the recovering of the three-dimensional (3D) dislocation structure from projection images is to perform a segmentation by line tracing. This enables displaying the individual dislocations separately, isolating a certain Region of Interest (ROI), and displaying it from every desired view direction, and, furthermore, further analysis and characterization of the structure. Therefore, a *reconstruction of sufficient quality* here refers to a result that allows these respective processing steps.
At the time of writing, the structure already shown in in Fig. 8.8 represents the dislocation arrangement that has been studied, analyzed, and characterized to the highest degree. The sample "Cr_7" (a silicon wafer of approximately 700 µm thickness, with a surface normal of [001]) was indented with a Berkovich tip applying a load of 400 mN. Afterwards, the sample was annealed in a mirror furnace above the brittle-to-ductile transition temperature. The whole heating process was captured in two-dimensional (2D) topographs by X-ray White Beam Topography (XWBT) at the Topography Station of the Imaging Cluster at the Karlsruhe Institute of Technology (KIT) synchrotron light source. The X-ray Diffraction Laminography (XDL)-measurement was carried out at ID19 at the European Synchrotron Radiation Facility (ESRF). Further comprehensive measurements were performed on the sample revealing the Burgers vector (BV)-distribution (by XWBT again at the Topography Station of the Imaging Cluster at the KIT synchrotron light source) and correlating the dislocation half loops to surface features by circular polarized visible light differential interference contrast microscopy. The results have been published in [2, 48, 49], more information about the measurement is summarized in Appendix H. The 3D reconstruction was obtained by utilizing Filtered Backprojection (FBP) with 700 projections from I_1 as defined in Section 6.2 and will here serve as a guideline to judge the quality of the reconstruction provided by SIRT with fewer projections from the same angular acquisition range of 130°. The whole XDL workflow from data acquisition, over preprocessing of projections, creating masks via EVBP, and reconstructing the volume, to the final segmentation via line tracing is illustrated in Fig. 9.1. Note, that the preprocessing steps Fourier band-pass filtering - to emphasize features of certain size, e.g.

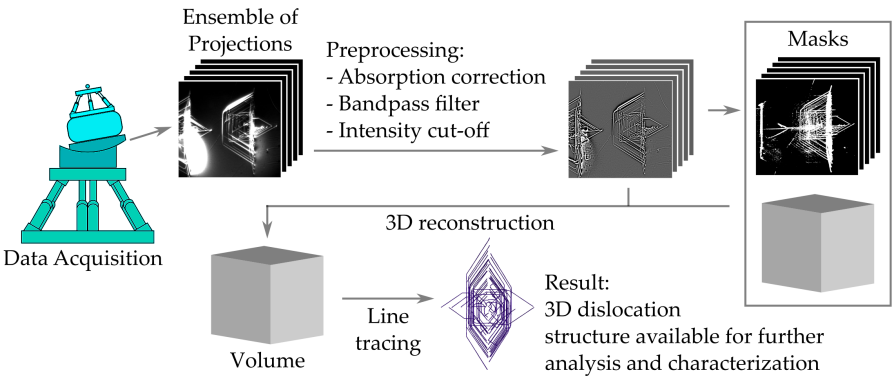

Figure 9.1: Workflow of XDL, from data acquisition to the final segmented 3D dislocation arrangement.

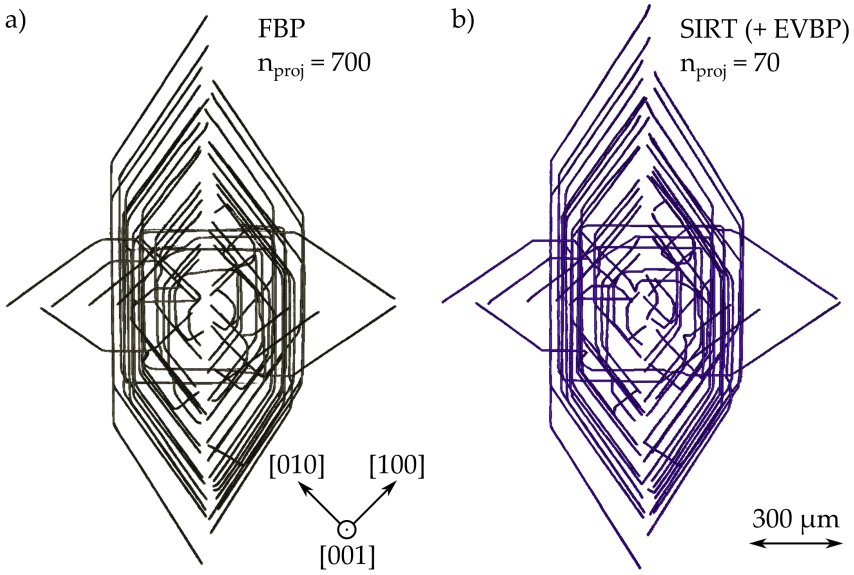

Figure 9.2: a) 3D rendering of the FBP reconstruction volume segmented by line-tracing. 700 projections from an acquisition interval of an angular range of 130° with the indent facing the detector (i.e. from interval I_1) were used as input. b) 3D rendering of the SIRT (supported by EVBP) reconstruction volume segmented by line-tracing. Here, every 10th projection from the whole data set was used, i.e. a total of 70 projections.

the line-width of dislocation line - and intensity cut-off - to achieve a more homogeneous intensity of different dislocations - are described in more detail in [49]. These two techniques are usually applied to all data sets, after a dark-field and the absorption correction.

9.1 COMPARING FBP AND SIRT RECONSTRUCTIONS

It is noteworthy, that manual segmentation by line tracing involves some degree of subjective interpretation. This, in combination with the

spatial resolution limit of 3 to 5 µm, is the reason why a quantitative analysis is not meaningful in this context and the focus is put on qualitative comparison. Comparing the two results, one finds that on first glance hardly any difference is noticeable, although the number of projections was reduced by exactly one order of magnitude, see Fig. 9.2. However, investigating and comparing the respective reconstruction volumes slice-by-slice reveals at least some minor differences, that are shown in Fig. 9.3. Two differences between the segmented dislocation arrangements each involve a pair of dislocations: In both cases the starting points of the dislocations agree, but the end points are switched: In the first case the two dislocations follow trajectories so close to one another for a few hundred µm that a clear separation is not possible anymore. In the second case the two segmented dislocation lines have different directions and seem to cross each other in the segmentation based on the SIRT reconstruction, while they just approach each other but never actually cross in the result obtained via FBP. (Note, that only the recovered lines seem to cross. The dislocation cores themselves may never approach each other closer than a few hundred atomic layers, but the strain fields can still overlap.)
Frame 9.3b shows four rather small dislocation line segments that were simply not traceable in the SIRT reconstruction and, therefore, are completely missing in the result. These segments are located closely to the initial damage site, i.e. the nano-indent. This region usually falls victim to contrast features of much higher intensity than the rest of the dislocation structure, making line segmentation in the vicinity (up to distances of 50 to 150 µm) of the indentation site particularly difficult.

9.2 DISCUSSION

Firstly, it is important to mention that due to the spatial resolution limit of XDL, it is simply not possible to determine the correct line paths of the dislocations shown in Fig. 9.3a. Unfortunately, both pairs of dislocations pair-wise share the same BV, otherwise drawing conclusions based on the BV-distribution would have been an option. One could make the argument, that the case of a crossing of the two dislocation lines in the SIRT-based segmentation (the dislocation pair shown at the bottom in Frame 9.3a) is more probable than the two dislocations approaching each other and changing directions once they are within a few µm distanced from one another. However, with only data from XDL and XWBT available, one has no way to be certain. Nevertheless, the similarity of the results and therefore the similarity of the level of quality of the reconstructions, is a very positive outcome, considering the fact that the number of used projections was reduced by a factor of 10. This is not intended to imply that an ensemble of 700 projections is necessary to successfully reconstruct the structure via FBP. The minimum amount of information has not been determined.

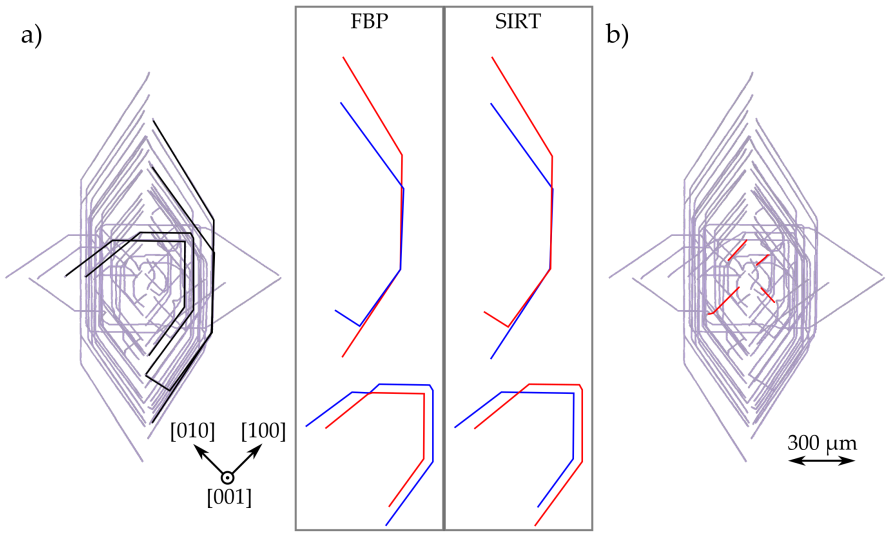

Figure 9.3: Differences between the line tracing segmentations performed on the FBP and SIRT reconstructions. a) The dislocation lines highlighted in black were traced differently in the two segmentations. In the frames schematic drawings show the paths of the respective dislocation lines more clearly, here colored in blue and red for easier visibility of the deviations. b) The segments in the middle of the arrangement highlighted in red could not be traced in the SIRT reconstruction.

However, 70 projections are not sufficient to reach a comparable result when using FBP and therefore with this first application of the EVBP-supported SIRT it has been confirmed, that the necessary amount of projections can be reduced drastically by incorporating *a priori* knowledge and employing a suited reconstruction algorithm. Eventually, this will enable more complex measurement campaigns (examples are given in Chapter 13 of this thesis) by significantly shortening the measurement duration required for a single XDL-scan.

10 THE CENTER OF ROTATION

When it comes to the application of tomography or laminography one important parameter for the reconstruction, which has not been considered yet is the position of the rotation axis in the respective projection images. The importance is obvious since a misplaced rotation axis will directly lead to artifacts. In particular, line-like features oriented parallel to the rotation axis would appear not as dots but as circular features in cross sections of the reconstruction volume perpendicular to the rotation axis. For most cases, this is a well investigated subject and methods to determine the rotation axis position - often referred to as the Center of Rotation (CoR) - from a given data set are well established, but also get improved up to this date for tomographic [113–115] and laminographic reconstructions [116].
Regarding regular tomography (i.e., $\theta = 0°$) these calibration techniques are often sinogram-based and can be classified into four categories: (i) center-of-sinogram methods, (ii) geometrical methods, (iii) iterative methods, and (iv) opposite-angle methods [117–120]. Center-of-sinogram methods exploit the fact, that features will flip on the other side of the rotation axis with a rotation of $\phi \rightarrow \phi + 180°$. The rotation axis then has to be positioned exactly between the features' positions in the respective projections. Geometrical methods allow for the line connecting the X-ray focus or source and the CoR not to be perpendicular to the detector plane. Iterative approaches are trial-and-error techniques. The CoR is altered and reconstructions are calculated until the image quality of the reconstruction reaches a certain abortion criterion. The opposite-angle method makes use of the X-ray passing the CoR being the only one projecting the same feature onto the same location of the detector for a rotation $\phi \rightarrow \phi + 180°$. However, with the generalization from tomography to laminography these approaches have to be modified. Furthermore, all these approaches except for the iterative methods generally assume a localized object function that does not change with the view direction. Obviously, this assumption is invalid for X-ray Diffraction Laminography (XDL): Not only do we have fluctuating intensity of the projected features with varying tomographic rotation angle ϕ, but also features change there position, as has been shown in Chapters 5 and 6.
Usually, the CoR should be determined during the alignment of the sample manipulator (discussed in Chapter 7) with a wire or a tip consisting of a highly absorbing material. Of course, the material has to be selected by taking into account the energy of the monochromatic X-ray beam and while energies of 20 to 40 keV (suitable for silicon

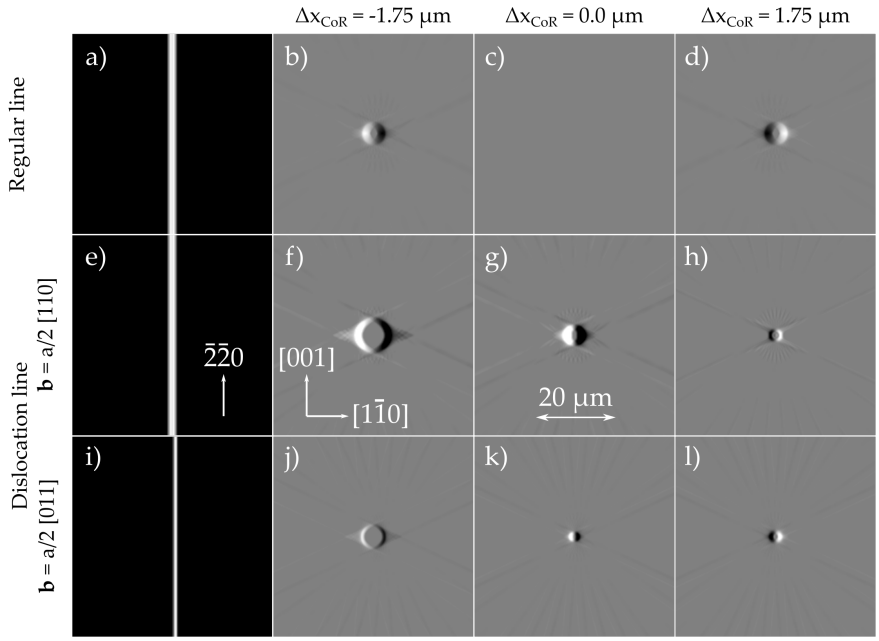

Figure 10.1: Comparison of reconstruction slices for a regular straight line feature and dislocations with two different Burgers vector (BV)-configurations. The CoR is altered to demonstrate the effect on the reconstruction image. The simulations regarding the dislocation lines have been executed with the same parameters used in Fig. 6.5.

samples) leave a wide range of possibilities, higher energies of about 60 (for GaAs) or even 120 (for CdTe) keV can make this determination challenging. However, we can never completely rule out changes in the position of the rotation axis during a measurement campaign, due to, e.g., instabilities in the setup or the base structure, detector re-positioning or exchange, or simply human failure.

Therefore, in the following approaches to determine the correct CoR for XDL data sets will be considered. These data sets at a minimum encompass an ensemble of projections and rocking scans taken within one acquisition interval without any additional knowledge about the CoR, but the assumption of a parallel orientation of the rotation axis $\mathbf{\Phi}$ and the detector columns is made. In order to illustrate the challenges related to XDL reconstructions arising from the topographic contrast formation, Fig. 10.1 shows exemplary projections and reconstruction slices of a regular straight, vertical line in Frames Fig. 10.1a-10.1d and the corresponding images for an equally positioned and oriented dislocation line with BV $\boldsymbol{b} = a/2[110]$ in Frames 10.1e-10.1h and $\boldsymbol{b} = a/2[011]$ in Frames 10.1i-10.1l. Since the data represents simulations, the exact CoR x^0_{CoR} is known (exactly in the center of the projections) and each column of reconstruction slices (i.e,. (i) Frames 10.1b, 10.1f, and 10.1j; (ii) Frames 10.1c, 10.1g, and 10.1k; (iii) Frames 10.1d, 10.1h, 10.1l) shows the outcome for a different CoR

$x_{\mathrm{CoR}} = x^0_{\mathrm{CoR}} + \Delta x_{\mathrm{CoR}}$. Taking a look at the regular line feature, showing no intensity fluctuations or contrast shift, the composed volume $V^{\mathrm{Rec}}_{\mathrm{Comp}}$ for a misplaced rotation axis, in Frames 10.1b and 10.1d, looks very similar compared to reconstructions of simulated projections, which inhabit specific XDL characteristics, if the CoR is set correctly, see Frame 10.1g. Note, that for the regular line feature the separate reconstructions corresponding to data from the acquisition intervals I_1 and I_2 should cancel each other out when merged in $V^{\mathrm{Rec}}_{\mathrm{Comp}}$ since $V^{\mathrm{Rec}}_{\mathrm{Comp}} = V^{\mathrm{Rec}}_{I_1} - V^{\mathrm{Rec}}_{I_2}$. Therefore, Frame 10.1c shows no features as it is to be expected. Furthermore, dislocation features reconstructed from data recorded in different intervals (i.e., dark and bright features) switch there respective positions with respect to the dislocation core located in the center of every slice, see Frames 10.1h and 10.1l. Drawing conclusions from the first simulations in Fig. 10.1, it is obvious that the inconsistensies in XDL data lead to reconstruction features that on first glance appear like artifacts arising from an incorrectly positioned rotation axis.

10.1 EFFECTS OF A MISPLACED ROTATION AXIS

Before presenting techniques to handle the challenges arising from the specific image formation process exploited by XDL, first a misplaced rotation axis at $x_{\mathrm{CoR}} = x^0_{\mathrm{CoR}} + \Delta x_{\mathrm{CoR}}$, with x^0_{CoR} denoting the correct position, will be considered. The calculations will be carried out for the easiest case of a dislocation line parallel to the rotation axis, i.e., $\boldsymbol{l} = [110]$. At the same time, the selection is again intended to maximize the effects of the contrast shift an therefore the BV $\boldsymbol{b} = a/2[110]$ - also parallel to the rotation axis - is selected. In order to enable an automated computation, that estimates the displacement of features in the reconstruction with respect to the actual position of the dislocation core for a large set of x_{CoR}-values, here a Center of Mass (CoM) approach is introduced: Within the separate reconstruction volumes V_{I_1} and V_{I_2} one calculates the CoM as

$$\boldsymbol{r}_{\mathrm{CoM}} = \frac{1}{c_\Sigma} \sum_{\substack{i=n_i,N_j \\ j=n_j}} c_{i,j} \boldsymbol{r}_{i,j}, \tag{10.1}$$

where $c_{i,j}$ denotes the value of the pixel (i,j) of the reconstruction slice and c_Σ denotes the count integrated over the Region of Interest (ROI). In this case the sum in Eq. 10.1 suggests a rectangular shape for the ROI, which of course can be customized. In particular, broad masks obtained by Empty Volume Backprojection (EVBP) can after some processing provide ROIs for the individual dislocation line features even in rather dense and complex dislocation arrangements, where a manual definition would be time consuming. For the reconstruction

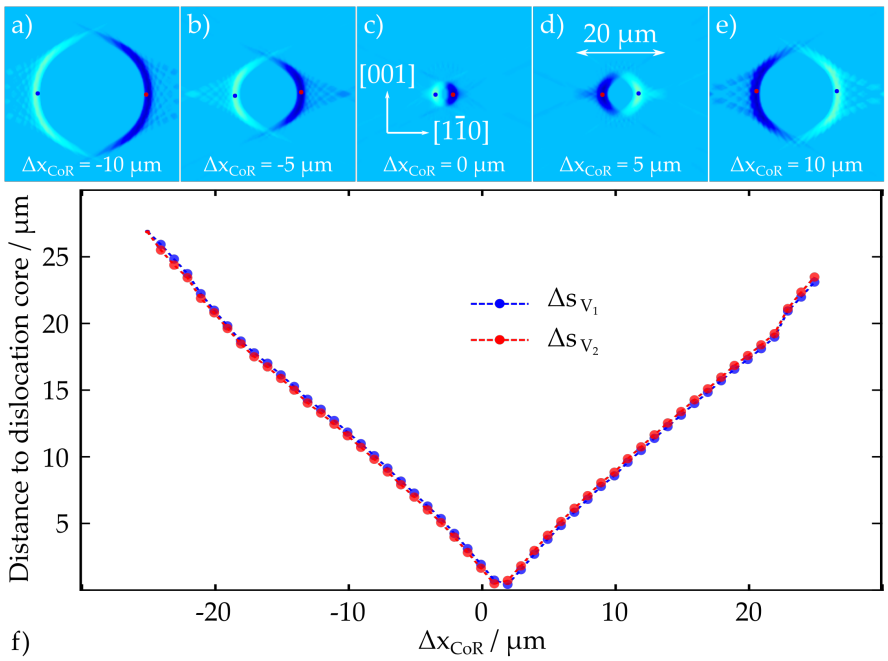

Figure 10.2: The effects of a displaced rotation axis for the case of XDL reconstructions on the basis of simulations. Frames a)-e): Corresponding reconstruction slices for different positions of the CoR. The calculated CoM is highlighted in blue and red in the features stemming from I_1 and I_2, respectively. f) Plot of the distance from CoMs of the features in V_{I_1} and V_{I_2} to the dislocation core in blue and red, respectively. The simulations were performed for an X-ray energy of 25 keV, with a Bragg deviation of $\Delta\theta = 0.002°$ and $\delta = 0.0007°$. Note, that here the misplacement parameter is denoted in µm, but when handling measurement data we will transition to a notation in pixels or columns of pixels. Also the simulation-based slices are here colored in blue for an easier distinction from measurement data (in grayscale).

of simulated data, simply finding the position of the maximum in the reconstruction feature and enclosing it by a simple geometrical shape would be a reasonable alternative.

In Fig. 10.2 the r_{CoM} is indicated with a blue or red dot for features originating from acquisition intervals I_1 (bright blue) and I_2 (dark blue), respectively, see Frames 10.2a-10.2e. The crescent moon shaped features extend further away from the dislocation core in the center of each frame with increasing absolute value of Δx_{CoR}. The second observation is, that the bright and dark features flip the sides at a certain value of Δx_{CoR}: In Frames 10.2a-10.2c the bright features (representing V_{I_1}) are located on the right of the dislocation core, while the dark features are positioned on the left. In Frames 10.2d and 10.2e it is the other way around. For the case presented in Fig. 10.2 the specific value of the *contrast flippening* is $\Delta x_{\mathrm{CoR}}^{\mathrm{Flip}} \approx 1.5$ µm, however, for a specific dislocation the exact value depends on a variety

of parameters, mainly on $\boldsymbol{l}$, $\boldsymbol{b}$, $\Delta\theta$. Of course, this is not surprising, but nevertheless, it raises the question how one could determine the right distribution of the respective features. This could become important for further investigating the relative position of features with respect to each other, e.g., in order to conclude on properties of the dislocations directly from XDL data sets. For example, the localization of such features with respect to the dislocation core is directly connected to the sign of the BV, see Section 5.4, meaning that bright and dark features would switch places if the BV-sign is inverted. Regarding the evaluation in Frame 10.2f, one finds that the minimum distance from reconstruction features to the dislocation core is not reached for the correct position of the rotation axis, but actually for a small shift, which is here resulting in $\Delta x_{\mathrm{CoR}} = 2$ µm with a minimal distance of $\Delta s_{V_1} = 1.7$ µm for the data from I_1 and a shift of $\Delta x_{\mathrm{CoR}} = 1$ µm with minimal distance of $\Delta s_{V_2} = 1.9$ µm for the data from I_2, respectively. This is explained by the features being shifted onto the position of the dislocation core for slight alterations of x_{CoR} in the right direction, which leads both dislocation line features to overlap. Apart from that, the error in localization follows a nearly linear dependence on Δx_{CoR}, with both reconstructions showing very similar behavior. This is also the case for a line direction not parallel but inclined with respect to the rotation axis $\boldsymbol{\Phi}$, which is in more detail discussed in Appendix D. Note, that in the here presented case the in-plane distance shown in the slices is equal to the true three-dimensional (3D) distance to the dislocation core, which changes if the line direction is inclined to the rotation axis.

10.2 APPROACHES TO DETERMINE THE CENTER OF ROTATION

In this section, two closely related approaches to estimate the correct position of the CoR will be presented. First, a scheme will be developed on how one can conclude on the correct distribution of the features originating from $V_{I_1}^{\mathrm{Rec}}$ and $V_{I_2}^{\mathrm{Rec}}$ in the compounded reconstruction volume $V_{\mathrm{comp}}^{\mathrm{Rec}}$. The second technique yields a direct approximation of the rotation axis' position exploiting the same properties of contrast in XDL projection data as the first one.

Fig. 10.3 illustrates the problem by means of measurement data: Although, the slices show features that appear more dotty and less smooth compared to simulations, one generally finds the same result with bright and dark features corresponding to information from the respective acquisition intervals, which evolve into crescent moon shapes if the CoR is increasingly deviating from its correct position. However, for now we can not know whether the distribution in Frame Fig. 10.3c or 10.3d is the correct one. Note, that in these two frames bright and dark features switch positions. Again the slices presented here show a region of the reconstruction volume where most of the

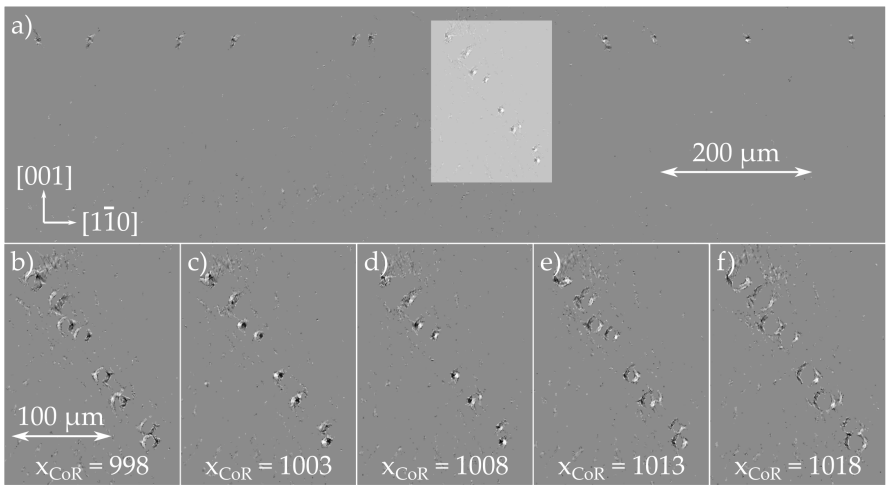

Figure 10.3: a) Reconstruction slice of a dislocation structure in the silicon sample A100_400_3. b)-f) the highlighted region in a) for different parameters x_{CoR}. The data was acquired at an energy of 25 keV, exploiting the $\bar{2}\bar{2}0$-reflex. Here a Bragg deviation of $\Delta\theta = 0.003^\circ$ was selected and both acquisition intervals were covered with 14 rocking scans (each consisting of 24 images) and 14 projections. More information about the sample and measurement is provided in Appendix H. The CoR is given in the figure in pixels with a total width of the projection images of 2004 pixels.

dislocation segments (in particular the segments shown in Frames 10.3b to 10.3f) follow a direction perpendicular to the slice plane, i.e., $\boldsymbol{l} = [110]$.

10.2.1 *Aligning Reconstruction Features*

As already mentioned above, one needs to exploit certain properties of the contrast formation mechanism utilized by XDL in order to determine the correct localization of the reconstruction features with respect to each other. In particular, the symmetry relation 5.47 is of major importance. A consequence of this property is, that a change in the sign of the weak-beam parameter $\Delta\theta$, i.e., transitioning from one flank of the rocking curve to the other, is equivalent to a change in the BV-sign and therefore, according to the quasi symmetry regarding the view direction $\boldsymbol{k_h}$ given in Eq. 5.49, similar to a rotation about $\boldsymbol{\Phi}$ by 180°. Obviously, the dislocation image will change its orientation according to the view direction, if $\boldsymbol{l} \nparallel \boldsymbol{\Phi} \parallel \boldsymbol{h}_{hkl}$, but the excited crystal region in the vicinity of the dislocation core is almost the same. This is presented on the basis of the local reflectivity R_δ in more detail in Appendix B.

If one now considers a dislocation line with $\boldsymbol{l} = [10\bar{1}]$ and an arbitrary BV resulting in a perfect dislocation, we can observe the flip in the projection image, when $\Delta\theta$ changes its sign. As already discussed

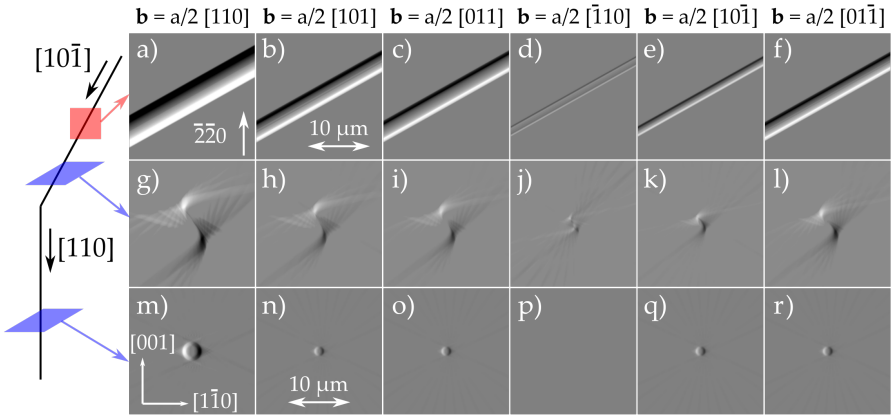

Figure 10.4: Projection images and cross sections for dislocations with different BVs. As illustrated by the sketch on the left the first row (Frames a) to f)) are simulated projection images with a line of direction $\boldsymbol{l} = [10\bar{1}]$, indicated by the red square at the $[10\bar{1}]$-segment. Frames g) to l) and Frames m) to r) show the corresponding reconstruction slices for the same line direction and $\boldsymbol{l} = [110]$, respectively, indicated by the corresponding blue parallelograms.

in Chapter 6 for perfect dislocations, we need to consider twelve BV-configurations, which pair-wise only differ in their sign. Therefore, we may divide the possible BVs into two groups:

- Group 1 G_1:

$$\boldsymbol{b} = \frac{a}{2}\{[110], [101], [011], [\bar{1}10], [10\bar{1}], [01\bar{1}]\} \text{ and} \tag{10.2}$$

- Group 2 G_2:

$$\boldsymbol{b} = \frac{a}{2}\{[\bar{1}\bar{1}0], [\bar{1}0\bar{1}], [0\bar{1}\bar{1}], [1\bar{1}0], [\bar{1}01], [0\bar{1}1]\} \tag{10.3}$$

with

$$G_1 = (-1) \times G_2. \tag{10.4}$$

Fig. 10.4 explains the motivation for this specific classification: Frames 10.4a to 10.4f show the result of subtracting a simulated projection image calculated with a Bragg deviation of $\Delta\theta = -0.003°$ from a projection obtained by setting $\Delta\theta = 0.003°$ while all other parameters remain unchanged. The images can be understood in a similar way as the slices of the compound volume $V_{\text{Comp}}^{\text{Rec}}$: The gray background represents values of zero, while the dark features show the projection image for $\Delta\theta$ = -0.003° and the bright features belong to $\Delta\theta =$

0.003°, respectively. Note, that for all BVs in group G_1 the dark dislocation line is located above its bright counterpart. Consequently, an inverted result would be obtained, if this procedure was performed for G_2. Investigating this change in the contrast localization was already proposed in [49] in order to identify the sign of a known BV (e.g., determined by X-ray White Beam Topography (XWBT)). Here, however, the *direction* of the flip is used to conclude on the correct appearance of features in the reconstruction. It is important to note, that while dark and bright features in the calculated projections in Frames 10.4a to 10.4f correspond to the transition $\Delta\theta \rightarrow -\Delta\theta$, dark and bright features in the reconstruction cross sections in Frames 10.4g to 10.4r correspond to features reconstructed from projection ensembles from different acquisition intervals, i.e., the transition $\phi \rightarrow \phi + 180°$. Furthermore, Fig. 10.4 shows reconstruction slices for $\boldsymbol{l} = [10\bar{1}]$ and $\boldsymbol{l} = [110]$. The reasoning for this is simple: The contrast flip in a projection is usually easier to spot for dislocation line direction not parallel or perpendicular to the rotation axis. On the other hand, aligning the reconstruction features in a region with such an inclined orientation of the dislocation line is less intuitive. Furthermore, the features for $\boldsymbol{l} = [110]$ and $\boldsymbol{b} \neq \pm a/2[110]$ are located much closer to each other, in many cases allowing for a better approximation of the correct CoR. With this knowledge one is now able to conclude on the correct positioning of reconstruction features stemming from data from different acquisition intervals simply by investigating images from rocking scans. As mentioned before in Chapter 7 these rocking scans are often necessary to ensure suited weak-beam conditions for projection acquisition in the whole interval range of 130°, but as demonstrated here also offer additional information about reconstruction parameters and thereby about dislocation properties.

Rocking scan data available from scans of the sample A100_400_3 now enables to compare data from the measurement to the simulated findings. Here, the convention is introduced that the result of the projection subtraction ΔP is always defined as the image obtained when subtracting the image recorded at smaller angle θ from the image acquired beyond θ_B, i.e.,

$$\Delta P_{i,j}(\phi) = P_{\theta_i}(\phi) - P_{\theta_i}(\phi) \text{ with } \theta_i > \theta_B > \theta_j. \tag{10.5}$$

This then yields the images shown in Frames 10.4b to 10.4e, while Frame 10.4a provides a projection image of the entire dislocation structure, where the investigated region is highlighted. Especially Frame 10.4b clearly shows that here the bright feature is located higher. Note, that Frame 10.4e shows darker features on top, however, the orientation of the dislocation line on the image has changed due to the rotation ($\phi = 56°$) and the frame is therefore not suited for a comparison to Fig. 10.4. The outcome is the opposite of the flip seen

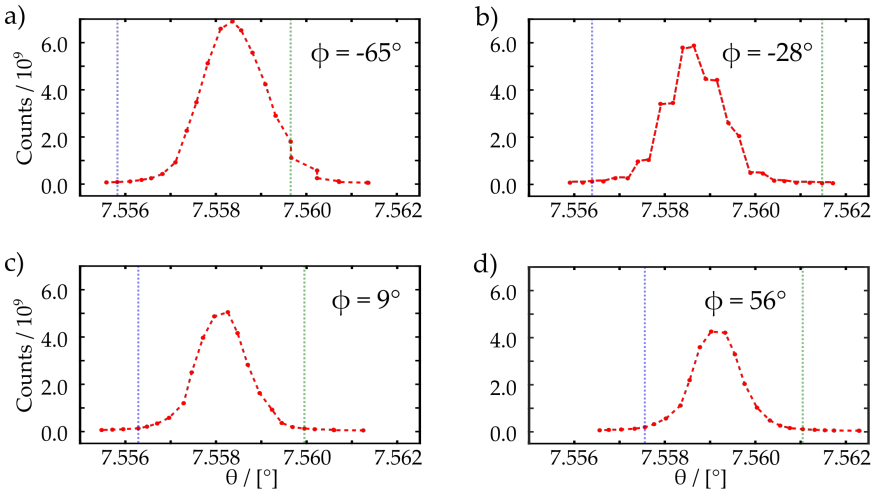

Figure 10.5: Number of counts integrated over the full image over angle θ during four rocking scans of the silicon sample A100_400_3. The measurement parameters are the same as given in the caption of Fig. 10.4. In each frame the green and blue dotted lines indicate the angular acquisition positions for the images that were then used to analyze the contrast flip.

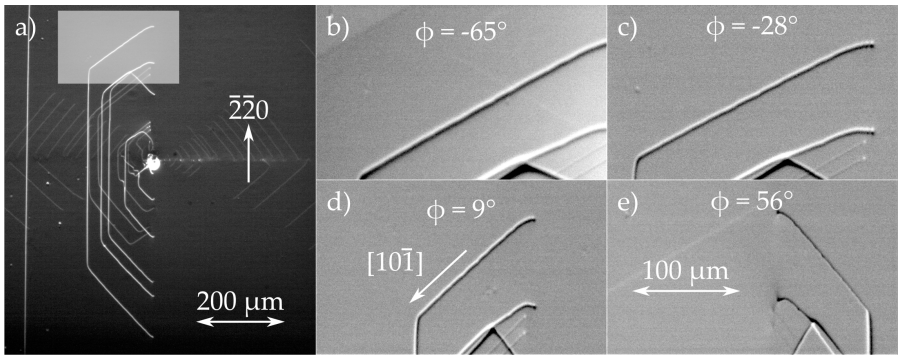

Figure 10.6: a) Projection image of the dislocation arrangement in the silicon sample A100_400_3. The area highlighted in gray was investigated regarding the contrast flip of the dislocation line. b)-e) Subtraction of the two images recorded at the indicated positions (green and blue lines in 10.5) from the four rocking scans corresponding to the data shown in Fig. 10.5.

in Fig. 10.4 and one may conclude that the involved BV belongs to group G_2. Consequently, the right distribution of the features in the reconstruction slices in this case is: dark features on the right side of the dislocation core, bright features on the left, which means that Frame 10.3d in Fig. with $x_{CoR} = 1008$ (here denoted in pixel columns from left to right) is the best estimate for the correct CoR-position.

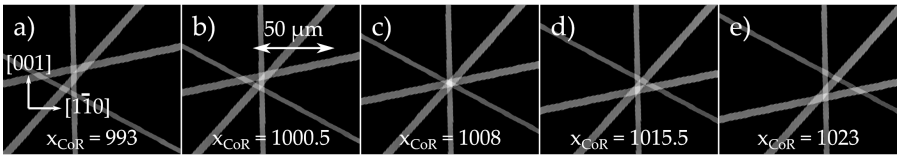

Figure 10.7: Slices of a volume obtained by reconstructing an estimate of the dislocation core in projection images. The CoR-position changes from one frame to another. Frame c) for $x_{\mathrm{CoR}} = 1008$ represents the best result, which is in agreement with the result of the minimization technique introduced in this section. Again the CoR is given in the figure in pixels with a total width of the projection images of 2004 pixels.

10.2.2 *Estimating the Dislocation Core*

Obviously, for the approach presented in the previous section, analyzing one rocking scan, e.g., the one corresponding to Fig. 10.5a and Frame 10.6b, would have been sufficient. However, utilizing several of these projection subtractions $\Delta P_{i,j}(\phi)$ acquired from different tomographic angles ϕ is necessary for the second approach. The basic idea is, that the dislocation core can be estimated by tracing the transition from the bright to the dark dislocation line. This can either be done by hand with a suited image processing software or by edge detection techniques (like, e.g., calculating a gradient image of $\Delta P_{i,j}(\phi)$). Since for the given data set extracting the dislocation core for four different view directions is sufficient it is unnecessary to employ elaborate techniques at this point. Extracting the transition lines manually and constraining the reconstruction volume to the region where the dislocation line is located, one then compares slices corresponding to different x_{CoR}-positions. A straight forward approach is to eliminate the straight stripes passing through the whole image and only hold on to the intersections of at least two stripes. This can easily be done either by thresholding or by optimizing the reconstruction (e.g., perform more Simultaneous Iterative Reconstruction Technique (SIRT)-iterations). A search for the frame with the minimum integrated count number then usually yields the best suited position of the CoR, in this case given by $x_{\mathrm{CoR}} = 1008$. Five slices calculated with different parameters x_{CoR} are shown in Fig. 10.7. Note, that for easier visibility here a line thickness of 2 to 3 pixels was selected for the line tracing of the dislocation core in the projections. This can be decreased in order to achieve higher precision.

10.3 DISCUSSION

In order to conduct a meaningful discussion about the findings of this chapter, one needs to acknowledge that successful reconstruction of XDL data sets is possible without applying the techniques presented

in the last sections or knowing the position of the rotation axis from sample manipulator alignment. This may be achieved by trial-and-error, sinogram based methods, mainly a simple center-of-sinogram approach due to its straight forward applicability, or the utilization of automated CoR determination tools.
However, especially sinogram based determination may lead to misplacements $\Delta x_{\mathrm{CoR}} \neq 0$ with respect to the physical rotation axis $\mathbf{\Phi}$, due to the contrast properties of XDL projections, resulting in resolution degradation of unknown quantity. Furthermore, a precise determination of the physical rotation axis $\mathbf{\Phi}$ is critical for estimations regarding the achieved spatial resolution. Therefore, approximating $\mathbf{\Phi}$ by reconstructing an estimate of the dislocation core improves reproducibility and accuracy of results, especially, if only data from one acquisition interval is incorporated. It is recommendable to perform the procedures for different line directions and in vertically different positions of the volume for higher accuracy and determining possible tilts between $\mathbf{\Phi}$ and the detector columns.
The true significance of the presented developments lies in the approach for the correct alignment of features from dislocations in the reconstruction volumes V_1^{Rec} and V_2^{Rec} with respect to each other. Not only can this technique be used to confirm a determined CoR, it also allows extracting signs of the BV in the dislocation arrangement. In particular, when dealing with complex structures like the one in sample Cr_7 (see Chapter 9), it is improbable that a BV sign determination is possible for every individual dislocation only from topographic images and their subtraction from one another. At least, the task would be time-consuming and cumbersome. By shifting the analysis from 2D topographic images to the 3D volume a successful extraction of every single BV-sign is much more convenient, therefore faster, and a lot more feasible. The underlying concept of a comprehensive investigation of topographic images and the corresponding reconstruction volumes $V_{1,2}^{\mathrm{Rec}}$ will be elaborated further in Chapter 12.

Concluding, it is strongly recommended to acquire projection ensembles from both acquisition intervals and at least a small number of intermediate rocking scans from suited view directions ϕ. The information this data contains about the CoR does not only give access to the signs of the BVs, it also provides an important base for comparison between simulations and measurement data, as demonstrated later in Section 11.3.

11 ACCESSING THE DISLOCATION CORE POSITION

The repetitive atomic displacement along the dislocation line is realized on length scales in the magnitude of the lattice constant a of the respective material, i.e., in the Å-regime (for silicon: $a = 5.43102$ Å $= 5.43102 \times 10^{-10}$ m). But as has been shown in [49] and in this work, the contrast utilized by X-ray Diffraction Laminography (XDL) is created by regions of the crystal volume in a distance to the dislocation core of much higher magnitude (several µm), resulting in an intrinsic resolution limit of the technique. However, state of the art methods employing lenses that are placed in the diffracted beam, referred to as X-ray dark-field microscopy, today reach spatial resolutions down to 200 nm - in this case defined by the dislocation line width in the image at half-widths at half-maximum [44]. It is stated, that there seems to be no fundamental physical reason prohibiting a substantial increase in spatial resolution of these approaches, especially with progress being made regarding the numerical apertures of multilayer Laue lenses [121] and the increase in brilliance (up to factors of 10 to 100 times) of radiation sources coming with the next generation of synchrotrons [122], one example being the European Synchrotron Radiation Facility (ESRF), which went back into operation after an upgrade in 2020, [123], [124].

The question arising is whether one considers strain in the crystal lattice in the vicinity of a dislocation as the object to be imaged or the dislocation core, whose position can only be estimated, since it is invisible to the exploited contrast mechanism. The obvious problem with the first perspective is that the determined position of a dislocation is then depending on a set of parameters (e.g., the weak-beam parameter $\Delta\theta$ and the view direction $\boldsymbol{k_h}$) and the Burgers vector (BV) of the respective dislocation (see the investigations in Chapter 6, especially Fig. 6.5). Therefore, while already projections from one acquisition interval indicate different positions for one and the same dislocation line, a second measurement (also from the same acquisition interval) with different parameters might again show deviating positions in the crystal volume. This is why the following considerations aim to develop an approach that allows estimating the dislocation core position more precisely, while at the same time eliminating dependencies on measurement parameters and dislocation properties. Furthermore, such an estimate could be considered as an enhancement of the spatial resolution of the resulting three-dimensional (3D) image.

It is noteworthy at this point, that in the case of XDL also the effective pixel size of the detector system is a limiting factor: So far, lenses have

not been incorporated, since the technique was originally developed to capture large-scale structures with extensions on the mm-scale. With a Field of View (FoV) of several mm^2 and volume sizes of several mm^3, the smallest effective pixel size during XDL-measurements was 0.36 µm. Maintaining this purpose, this approach aims for a spatial resolution of about 1 to 2 µm in comparison to the previously estimated 3 to 5 µm, [2, 48].

11.1 ESTIMATING THE POSITION OF THE DISLOCATION CORE

In order to obtain a more accurate approximation of the position of the dislocation core, i.e., the localization of the atomic displacement, a tool already utilized in the previous chapter represents a meaningful approach: By calculating the Center of Mass (CoM) of the respective reconstruction features stemming from the two projection ensembles acquired in the intervals I_1 and I_2 according to Eq. 10.1 one obtains two results in the vicinity of the dislocation core, denoted as $\boldsymbol{r}_{\mathrm{CoM}_i}$ with i = 1,2 (for the respective reconstruction volumes $V^{\mathrm{Rec}}_{i=1,2}$). If Eq. 5.49 can be regarded as a valid with only minor distortions, these would result in a quasi symmetry. A subsequent step to improve the estimation of the dislocation core is then to compute the mean position

$$\boldsymbol{r}_{\mathrm{CoM}} = \frac{\boldsymbol{r}_{\mathrm{CoM}_1} + \boldsymbol{r}_{\mathrm{CoM}_2}}{2}, \tag{11.1}$$

which can again be considered a CoM. Assigning the same weight to the two respective positions $\boldsymbol{r}_{\mathrm{CoM}_1}$ and $\boldsymbol{r}_{\mathrm{CoM}_2}$ is meaningful, since the two features might differ in their intensity because of inhomogeneities in the beam, due to the slight violation of the quasi symmetry, or due to entirely numerical reasons, arising during the 3D reconstruction. Consequently, it is here assumed that the differences in the voxel values of V^{Rec}_1 and V^{Rec}_2 should be neglected and the positions $\boldsymbol{r}_{\mathrm{CoM}_i}$ considered as equally credible.

11.1.1 *Influence of Dislocation Properties*

First, the approach is applied to volume slices obtained by reconstructing simulated data sets, here again restricting the consideration to line directions $\boldsymbol{l} = [10\bar{1}]$ and $\boldsymbol{l} = [110]$, as in Chapter 6. Since the selected pixel size of 0.25 µm used here is already on a level that hinders an investigation by eye, the distances from the respective CoMs to the dislocation core are also given in numbers in Tab. H.1.

As Fig. 11.1 already indicates the CoM-approach yields accurate estimations for the position of the dislocation core, regardless of which BV the dislocation has. (Note, that in the following, simulations will be colored in shades of blue for an easier distinction from measurement data. This is confirmed by the values for the distance $\Delta s_{\mathrm{CoM}_i}$ of the

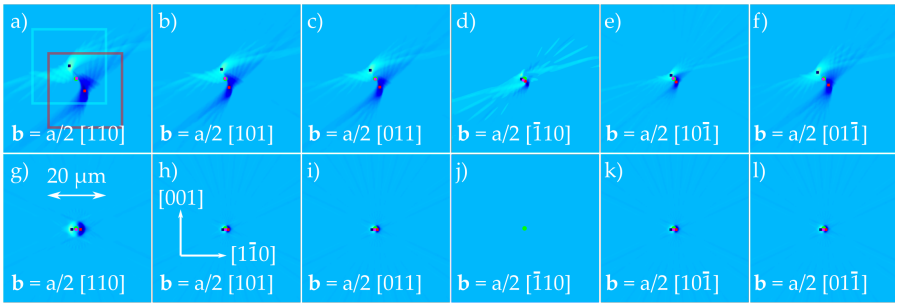

Figure 11.1: The CoM-approach applied to single reconstruction slices of simulated projection data sets with different BVs and line directions. BV and line direction configurations correspond to the ones presented in Fig. 6.5. The same parameters were used, i.e. $E = 25$ keV, $\Delta\theta = 0.002°$, and $\delta = 0.0007°$. The CoM positions for the reconstruction volumes V_1 and V_2 are pointed out in blue and red. The estimated position of the dislocation core is indicated by the pink dot, while the true position is marked by a green circle. In frame a) the selected Region of Interest (ROI)s are highlighted with light blue and red for respective reconstruction volumes.

$\boldsymbol{b}\,(\times 2/a)$	$[110]$	$[101]$	$[011]$	$[\bar{1}10]$	$[10\bar{1}]$	$[01\bar{1}]$
$\Delta s_{\mathrm{CoM}}\,/\,\mu\mathrm{m}$	0.21	0.13	0.07	0.53	0.11	0.05
$\Delta s_{\mathrm{CoM}_1}\,/\,\mu\mathrm{m}$	2.58	1.87	1.80	0.87	0.86	1.5
$\Delta s_{\mathrm{CoM}_2}\,/\,\mu\mathrm{m}$	2.35	1.67	1.67	0.39	0.63	1.43

Table 11.1: Distances $\Delta s_{\mathrm{CoM}_{(i)}}$ from the dislocation core to the positions $\boldsymbol{r}_{\mathrm{CoM}_{(i)}}$ of the CoMs of the features in the respective reconstruction volumes V_1^{Rec}, V_2^{Rec} and the mean position of the two. Here, for the case of a line direction $\boldsymbol{l} = [10\bar{1}]$ and the six relevant BVs. Note, that this is the shortest distance in 3D, not the in-plane distance.

$\boldsymbol{b}\,(\times 2/a)$	$[110]$	$[101]$	$[011]$	$[\bar{1}10]$	$[10\bar{1}]$	$[01\bar{1}]$
$\Delta s_{\mathrm{CoM}}\,/\,\mu\mathrm{m}$	0.18	0.21	0.21	-	0.21	0.21
$\Delta s_{\mathrm{CoM}_1}\,/\,\mu\mathrm{m}$	1.62	0.91	0.90	-	0.90	0.91
$\Delta s_{\mathrm{CoM}_2}\,/\,\mu\mathrm{m}$	1.36	0.62	0.63	-	0.63	0.62

Table 11.2: Distances $\Delta s_{\mathrm{CoM}_{(i)}}$ from the dislocation core to the positions $\boldsymbol{r}_{\mathrm{CoM}_{(i)}}$ of the CoMs of the features in the respective reconstruction volumes V_1, V_2 and the mean position of the two. Here, for the case of a line direction $\boldsymbol{l} = [110]$ and the six relevant BVs. Note, that here the shortest distance in 3D is equal to the in-plane distance.

respective CoM-positions $\boldsymbol{r}_{\mathrm{CoM}_i}$ to the dislocation core in Table H.1 and Table 11.2 for line directions $\boldsymbol{l} = [10\bar{1}]$ and $\boldsymbol{l} = [110]$, respectively. Note, that every value of Δs_{CoM} for the estimate of the core position is below 0.25 µm, which was the selected pixel size for these simulations.

This almost holds true for the in-plane distance, which visually is easier to grasp in Fig. 11.1, too: For $\boldsymbol{l} = [10\bar{1}]$ $\Delta s_{\mathrm{CoM}_{i=1,2}}$ reach values up to 5.1 µm, while the maximum value computed for Δs_{CoM} remains below 0.27 µm. For $\boldsymbol{l} = [110]$ the in-plane distance and the shortest 3D-distance are identical, of course. This is important in the sense, that in particular segmentation but also further analysis sometimes rely on a slice-by-slice investigation, and thereby, in some cases a precise estimation of the dislocation core position in single slices is much more important than the true distance in 3D.
Furthermore, the results indicate, that the quasi symmetry with respect to the view direction ϕ given in Eq. 5.49 (see Section 5.4 and Appendix B) is fulfilled to a degree that leads to a similar (quasi) symmetry of the positions $\boldsymbol{r}_{\mathrm{CoM}_i}$ with respect to the dislocation core. Regarding the overall concept presented here, this is a crucial conclusion.

11.1.2 *Center of Mass and Center of Rotation*

Although, in the previous chapter techniques were developed to determine the Center of Rotation (CoR) with a high level of precision and confidence, it is meaningful to analyze how resilient the CoM-approach is to deviations Δx_{CoR} from the correct position of the rotation axis x_{CoR}. This is due to the fact, that it sometimes turns out advantageous to misplace the rotation axis slightly ($\Delta x_{\mathrm{CoR}} < 3$ µm), in order to artificially converge the features from the two reconstruction volumes V_1^{Rec} and V_2^{Rec}. Experience has shown that this can help to improve visibility in the reconstruction slices and thereby simplify the line tracing segmentation, if the two volumes are summed up instead of subtracted (as it is done to obtain $V_{\mathrm{Comp}}^{\mathrm{Rec}}$). The simple explanation is that especially in dense arrangements, where dislocation lines are located only a few µm away from each other, certain parts and details might be captured better by projections from one acquisition interval than by the ones recorded in the opposing interval. We therefore, perform simulations with different settings of Δx_{CoR} and compute the mean distances $\overline{\Delta s}_{\mathrm{CoM}}$ over a set of reconstruction slices.

Frame 11.2a shows, that the CoM-approach is very stable regarding errors in the CoR. Even for significant deviations Δx_{CoR} one obtains results, that for the most part are still more accurate than reconstructions that rely on data from only one acquisition interval. The latter is shown in Frame 11.2b. In this case, there exists an almost linear relation between the misplacement of the CoR, Δx_{CoR}, and the distance $\Delta s_{\mathrm{CoM}_{i=1,2}}$ between the CoM positions $\boldsymbol{r}_{\mathrm{CoM}_i}$ of the features in the individual reconstructions and the dislocation core. One also finds, that for different configurations of $\boldsymbol{l}$ and $\boldsymbol{b}$ we find different settings for the CoR, that yield the best estimate for the position of the dislocation core. This is explained by the BV-dependent distribution: In the case of $\boldsymbol{l} = [10\bar{1}]$ and $\boldsymbol{b} = [110]$, see Fig. 11.1 Frame 11.1a, it will require

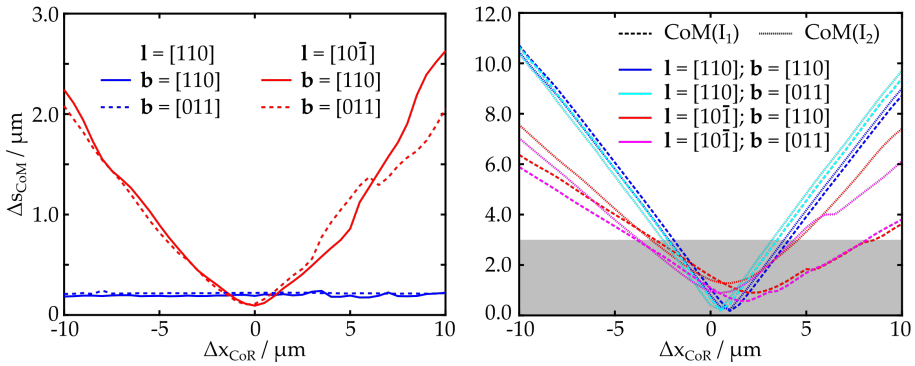

Figure 11.2: a) Mean distance $\overline{\Delta s}_{CoM}$ from the dislocation core to the CoM-position $\boldsymbol{r}_{CoM}$ for different line directions and BVs. b) Mean distance $\overline{\Delta s}_{CoM_{i=1,2}}$ from the dislocation core to the CoM-positions $\boldsymbol{r}_{CoM_{i=1,2}}$ of the respective reconstruction volumes V_1^{Rec} and V_2^{Rec} for different line directions and BVs. For comparison the y-axis range covered in a) has been indicated in gray. The simulations have been carried out for the parameters $E_{\text{X-ray}} = 25$ keV, $\Delta\theta = 0.002^\circ$, $\delta = 0.0007^\circ$, exploiting the $\overline{2}\overline{2}0$-reflex of silicon. The mean of the distances were calculated over 200 slices equally distributed around the center-slice in z- or 220-direction of the respective volumes.

a larger deviation in the CoR to shift the respective features onto the core position, than in other configurations.
Another important observation is that a misplaced CoR has a stronger effect on the CoM-estimate of the dislocation core position, if the line direction is inclined with respect to the rotation axis, i.e. $\boldsymbol{\Phi} \nparallel \boldsymbol{l} \not\perp \boldsymbol{\Phi}$. For this, two possible reasons have to considered: (i) The more extended reconstruction features, by introducing $\Delta x_{CoR} \neq 0$ µm get distorted in a way, leading to a less accurate result. Or (ii) the reason is the localization of the dislocation line: For the case of $\boldsymbol{l} = [110]$ the position of the dislocation core is coinciding with the CoR - and with the center of the reconstruction slices for that matter - in all of the 200 incorporated slices. This is not the case for $\boldsymbol{l} = [10\bar{1}]$, where the dislocation core crosses the rotation axis only in one slice (or depending on the computation between two slices). For the other slices, due to the inclination, the dislocation is not coinciding with the rotation axis. Although, one might intuitively tend to reason (i), the latter would have crucial implications for an intended shift of the CoR in order to ease line tracing: Imaging of dislocation lines further away from CoR would suffer in accuracy and the correct positioning of the rotation axis would become even more important. However, as it is shown in Appendix G this is not the case and the worse estimates for $\boldsymbol{\Phi} \nparallel \boldsymbol{l} \not\perp \boldsymbol{\Phi}$ are entirely stemming from the more complex reconstruction features. Concluding, the CoM-approach proves to be highly resilient to a misplaced rotation axis and, furthermore, provides an estimate of the

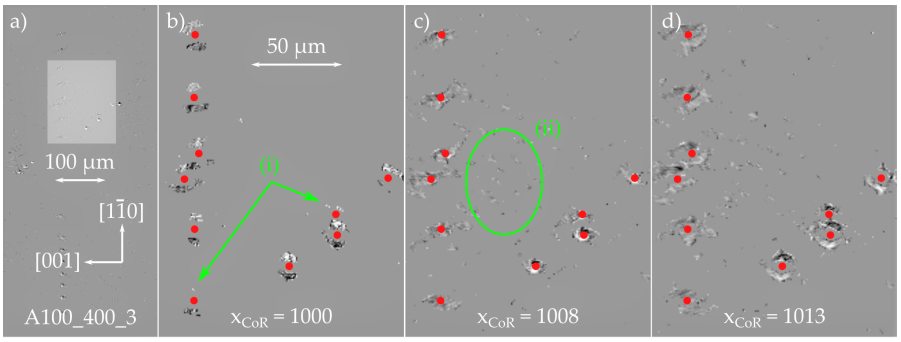

Figure 11.3: Slices of the 3D reconstruction volume comprising the dislocation structure in sample A100_400_3. a) Cross section of the entire crystal volume containing the dislocation structure. The area highlighted in bright gray is enlarged in the following frames. b) A reconstruction with a shift of the CoR of Δx_{CoR} = - 8 pxl = -5.76 µm with respect to the CoR determined in Chapter 10. Note, that here different parameters were used for the masking via Empty Volume Backprojection (EVBP), than in the frames c) and d). c) The CoR was set according to the findings in Chapter 10, i.e. Δx_{CoR} = 0 pxl= 0 µm. d) Here, we shifted the rotation axis in the other direction by Δx_{CoR} = 5 pxl = 3.6 µm. The position of the area shown in the slices is indicated by the gray parallelogram in Fig. 11.6, where the entire dislocation arrangement is shown. The reconstructions were obtained with the Simultaneous Iterative Reconstruction Technique (SIRT) supported by EVBP. The CoR is given in the figure in pixels with a total width of the projection images of 2004 pixels.

dislocation core position, which is not only more accurate than the respective reconstruction features in V_1^{Rec} and V_2^{Rec}, the estimate is also nearly independent of measurement parameters (also see Appendix G) and dislocation properties.

11.1.3 *An Exemplary Application*

Before continuing with the possible ways of implementing the CoM-approach, a first application to measurement data will be demonstrated. This will exemplarily show the possibilities to improve and manipulate reconstructions in order to achieve the best results. For this purpose, again the projections of the silicon sample A100_400_3 will be used, which were already introduced in the previous chapter: 14 Projections were recorded per acquisition interval at an energy of $E_{\text{X-ray}}$ = 25 keV, exploiting the $\overline{2}20$-reflex. The Bragg deviation was set to $\Delta\theta = 0.003°$ and the excitation interval is estimated by $\delta = 0.0007°$, according to the properties of the P23-beamline, Deutsches Elektronen Synchrotron (DESY) - Petra III, Hamburg, in Germany. More information about the sample and the measurement is given in Appendix H.

With a variation of the rotation axis position one again observes a flip in the features in Fig. 11.3: While Frames 11.3c and 11.3d show the correct distribution (here: bright below dark features), a shift of the CoR in the negative direction leads to the bright features being located above the dark features of one and the same dislocation. The red dots are indicating an estimate of the dislocation core position, that has simply been set by eye, but note: The red dots occupy the exact same positions in all three frames, their locations have not been altered from one frame to another. This can be considered a first demonstration of the CoM-approach's resilience to misplacements of the rotation axis. Furthermore, Fig. 11.3 shows how also a parameter variation of the EVBP-masking technique can help significantly to analyze data and track dislocation lines: While the slice in Frame 11.3b appears much cleaner, with almost no noise, disturbing features increase in the last two frames. They are highlighted in the green ellipse (ii) in Frame 11.3c. At the same time, some bright features are hardly visible in Frame 11.3b marked by (i). In Frames 11.3c and 11.3d, however, their visibility has improved significantly.

11.2 IMPLEMENTATION

Although, the simulations and their outcome presented in the previous section are very promising, applying the CoM approach to real dislocation structures is a challenging task: In simulated data sets reconstruction volumes that only contain features stemming from one single dislocation. Obviously, in this case determining the positions of the respective CoMs $\boldsymbol{r}_{\mathrm{CoM}_{i=1,2}}$ and subsequently calculating their mean position $\boldsymbol{r}_{\mathrm{CoM}}$ is easily automated. However, considering arrangements of dislocation that are more complex, e.g., the structure in sample Cr_7 shown in Chapter 9, quickly problems arise in regions of the reconstruction volume where features from several dislocations approach each other or even overlap. To some degree this can be approached by using several reconstructions with different settings of the CoR, but this does not solve the problem entirely. In this regard, here two approaches on how to handle more complex dislocation structures will be presented and the obtained results will be compared. First, a straight forward Mean of Segmented Lines (MSL)-approach will be introduced and, secondly, the Mean of Calculated Centers of Mass (MCC)-scheme, which opens possibilities to automate the line tracing to some degree, will be presented.

11.2.1 *Mean of Segmented Lines*

The first way to apply the CoM-technique to a data set, that captures a complex dislocation arrangement is straight forward: After the projection ensembles acquired in the intervals I_1 and I_2 have been

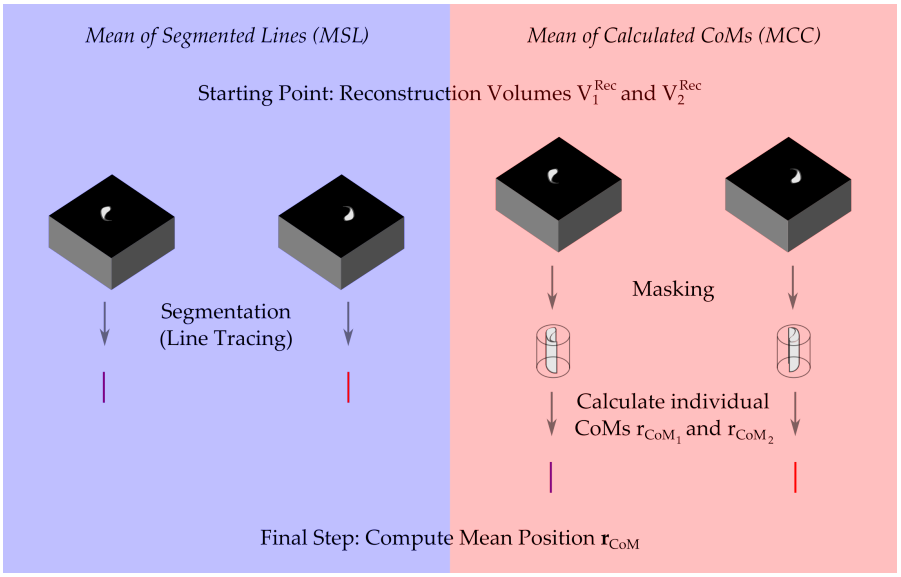

Figure 11.4: Schematic workflow of the two ways to implement the CoM-approach: left MSL; right MCC.

reconstructed separately to obtain V_1^{Rec} and V_1^{Rec} the segmentation via line tracing is carried out also separately in the two volumes. The two results can then easily be combined to yield the final result. This is simply done by calculating the mean positions $\boldsymbol{r}_{CoM}$ for every dislocation and slice. A schematic overview of the workflow is shown in Fig. 11.4 on the left.

The disadvantages of this approach are, firstly, that the line tracing has to be performed twice (once for V_1^{Rec} and once V_2^{Rec}, respectively), which effectively doubles the effort necessary for the segmentation. Secondly, a segmentation by line tracing in a slice-by-slice fashion is to some degree subjective. This concerns the exact position of the traced line in the perhaps blurred and slightly extended reconstruction feature as well as the individual paths of dislocations that cross or follow trajectories with only a few µm or less in between. A direct example for this subjectiveness has already been presented in Chapter 9, where two reconstructions and their respective segmentations (performed by two different people) yielded different paths for two pairs of dislocations, see Fig. 9.3. On the other hand, the MSL is easily performed, if the two projection ensembles each allow successful reconstruction and line tracing, which has to be regarded a criteria for the successful application of XDL to begin with, of course. Therefore, MSL can by default be considered as applicable.

Applying the MSL-approach to a rather simple structure in the silicon sample A100_400_3, which was already presented in Chapter 10, yields cross sections like the ones exemplarily shown in Fig. 11.5. In this case, for the CoR determined in the previous chapter, the features from the two reconstruction volumes are already located very close to each other, see Frame 11.5b. This is due to the line direction of most

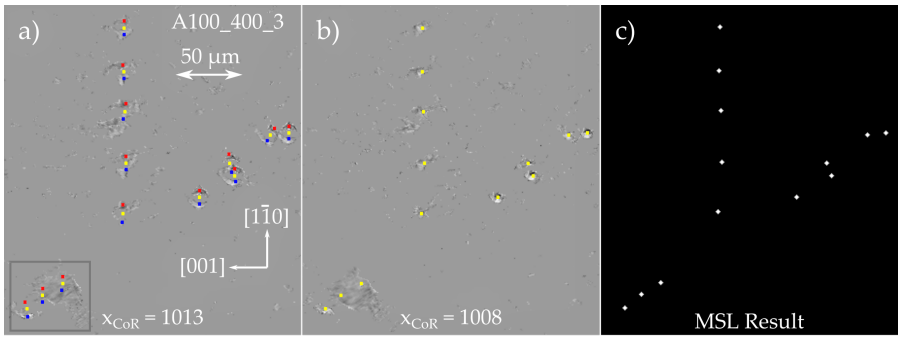

Figure 11.5: Reconstruction slices of a dislocation structure in the silicon sample A100_400_3 segmented with the MSL-Scheme. a) For better visibility a cross section of a reconstruction volume obtained by misplacing the rotation axis by $\Delta x_{CoR} = 5$ pxl $= 3.6$ µm. b) The corresponding reconstruction slice for $\Delta x_{CoR} = 0$ pxl $= 0.0$ µm. c) The final result obtained by MSL. In frames a) and b) the lines segmented from V_1^{Rec} are represented by the blue dots, the red dots mark the positions of the lines extracted from V_2^{Rec}. The green dots indicate the positions of the mean position or the CoM and correspond to the white dots in frame c). The CoR is given in the figure in pixels with a total width of the projection images of 2004 pixels.

visible segments ($\boldsymbol{l} = [110]$) but also due to the selection of $\Delta\theta = 0.003°$. Therefore, Fig. 11.5 also shows the application to a cross section where the CoR was misplaced by 3.6 µm for the purpose of better illustration of the technique (this is also the case for the illustration of the entire structure in Fig. 11.6, where the localization of the slices shown in Fig. 11.5 is indicated by the gray parallelogram). Note, that in the Frames 11.5a and 11.5b the green dots indicating the dislocation core position are located at exactly the same positions (this is also the case for the white dots in 11.5c, again indicating the resilience of the CoM-approach to misplacements of the rotation axis). However, for any further investigations the result obtained from a reconstruction volume which was calculated with $x_{CoR} = 1008$ pxl will be used, i.e., where $\Delta x_{Cor} = 0.0$ µm according to the findings in Chapter 10.

11.2.2 *Mean of Calculated Centers-of-Mass*

The second implementation, the MCC-scheme, allows for a segmentation of the CoM in semi-automated fashion. As a first step a mask, that enables isolating the features of the individual dislocation lines, needs to be applied to the volumes. In many cases, if the local dislocation density is not too high, i.e., if the dislocations are spatially separated by approximately 10 to 20 µm of dislocation-free crystal volume (in-plane, i.e., in the cross sections perpendicular to the rotation axis), the same mask can be used for V_1^{Rec} and V_2^{Rec}. This is of course to some degree also influenced by measurement parameters

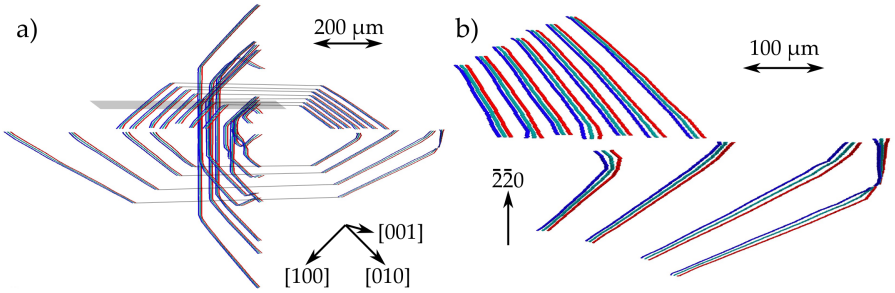

Figure 11.6: 2D-image of a 3D-rendering of the complete dislocation structure in silicon sample A100_400_3. Again the reconstructed dislocation lines stemming from V_1^{Rec} and V_2^{Rec} are colored in blue and red, respectively, while the CoM-position estimating the path of the dislocation core are colored in turquoise. a) The whole dislocation arrangement. The gray *slice* indicates the area shown in Fig. 11.3 and Fig. 11.5. b) Enlargement of the right hand-side of a). Note that here again reconstructions were obtained by misplacing the rotation axis by $\Delta x_{CoR} = 3.2$ µm for a better illustration of the CoM-approach. Also note, that the gray - almost horizontal - segments in frame a) could not be captured by XDL and had to be inserted artificially. This is due to the extinction rule, since they all have the BV $\boldsymbol{b} = \pm a/2[1\bar{1}0]$.

$\Delta\theta$ and δ as well as the line direction $\boldsymbol{l}$ and BV $\boldsymbol{b}$ of the respective dislocation segment. For dislocations that are located closer to one another, this approach is problematic, since overlapping features of different dislocations will falsify the calculation and eventually degrade the precision of the dislocation core position estimate. Therefore, the first exemplary demonstration of MCC will be restricted to the 26 selected line segments highlighted in Fig. 11.7.

A suited mask can be obtained by a rough segmentation of a regular volume mask obtained by EVBP. An exemplary cross section of such a mask volume is shown in Frame 11.8a. After the individual dislocation features have been isolated, $\boldsymbol{r}_{\mathrm{CoM}_i}$ are simply calculated for $i = 1, 2$ and every dislocation line feature. Afterwards, the mean position of two corresponding CoMs is determined. One then obtains slices like the cross section shown in Frame 11.8b, where the CoM-positions corresponding to the features in V_1^{Rec} and V_2^{Rec} are indicated in red and blue, respectively. The mean position, or the final CoM-position, which is the estimate for the position of the dislocation core is marked in green. Extracting these coordinates then yields the result, which can be binarized (as shown in Frame 11.8c) or indexed for further processing.

11.2.3 *Comparison of the two Implementations*

Previous to the general discussion of the CoM-approach, the two implementations presented in the previous two sections will be compared.

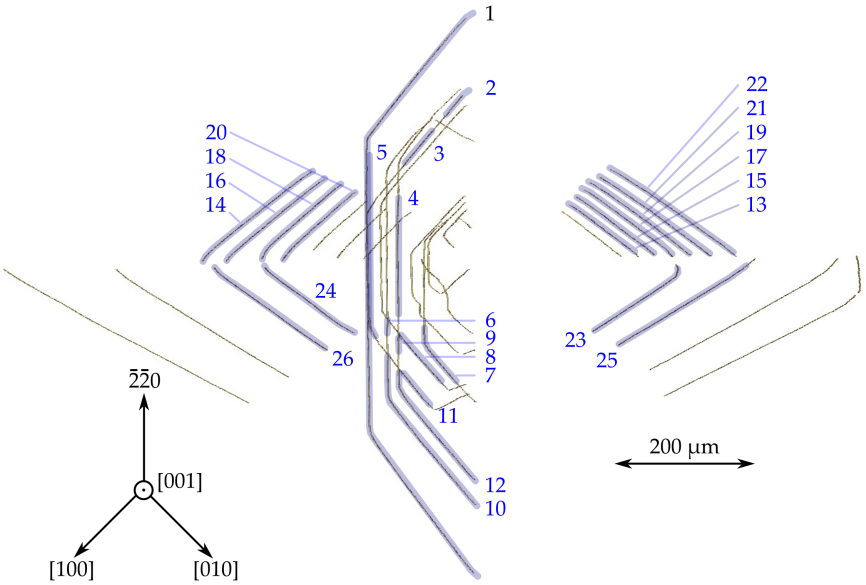

Figure 11.7: Two-dimensional (2D)-image of a 3D rendering of the dislocation structure in the silicon sample A100_400_3. The 26 segments highlighted in blue are well suited for applying the MCC-approach.

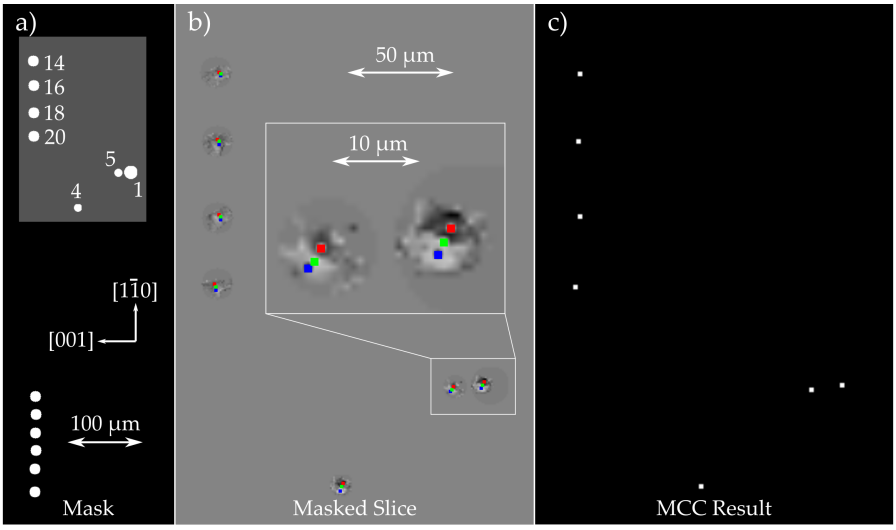

Figure 11.8: Exemplary cross sections of volumes corresponding to the several processing steps of MCC: a) Volume mask that enables isolation of individual dislocation line features for the calculations. b) Enlarged area highlighted in a): The mask was applied to slices obtained by a SIRT-reconstruction. The respective CoMs are indicated by blue and red dots, corresponding to features in V_1^{Rec} and V_2^{Rec}, respectively. The estimate of the dislocation core position, which is again shown solely as result in c) is here colored in green.

Since one simply does not know the exact position of the dislocation core in the reconstruction volumes obtained from measurement data,

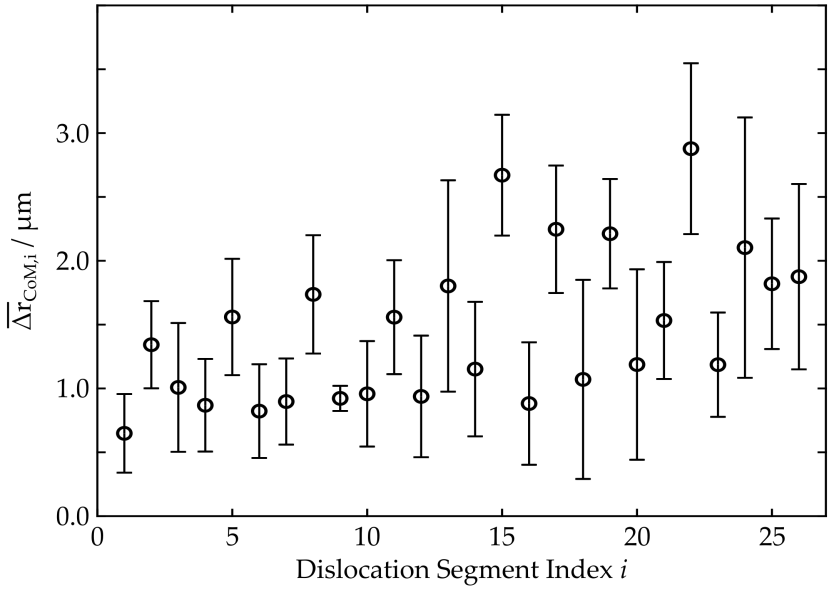

Figure 11.9: The mean deviation $\overline{\Delta r}_{CoM,i}$ for the 26 dislocation segments with indexes i shown in Fig. 11.7. The in-plane distances between the MCC- and the MSL-approach are calculated in slices j perpendicular to the rotation axis, afterwards the mean is calculated. The error bars indicate the standard deviation, also see Eq. 11.2 and 11.3.

one here has to rely on a quantitative comparison of the results from MSL and MCC. This is meaningful, because relying on simulations it is known that MCC yields estimates for the dislocations which are closer to the truth than a simple segmentation of features from either one of the two volumes V_1^{Rec} and V_2^{Rec} by up to 3 to 5 µm. Note, that this and the following values refer to the in-plane distance, i.e., the distance in the slice plane, which is perpendicular to the rotation axis, not to the shortest distance in 3D, which is plotted for different settings of the x_{CoR} in Fig. 11.2. Since MCC had to be restricted to the 26 line segments shown in Fig. 11.7, the mean difference compared to the MSL-results over all relevant slices is plotted over the segment index, the corresponding standard deviation are indicated by error bars:

$$\overline{\Delta r}_{CoM_i} = \frac{1}{n_z^i} \sum_{j=z_0^i}^{n_z^i} \left| \boldsymbol{r}_{CoM_{i,j},\perp}^{MCC} - \boldsymbol{r}_{CoM_{i,j},\perp}^{MSL} \right| \tag{11.2}$$

$$\sigma(\overline{\Delta r}_{CoM_i}) = \sqrt{\frac{1}{n_z^i - 1} \sum_{j=z_0^i}^{n_z^i} \left(\left| \boldsymbol{r}_{CoM_{i,j},\perp}^{MCC} - \boldsymbol{r}_{CoM_{i,j},\perp}^{MSL} \right| - \overline{\Delta r}_{CoM_i} \right)^2} \tag{11.3}$$

For the most part, as shown in Fig. 11.9, the difference between the two approaches is below 2 µm. For almost half of the line seg-

ments the estimates of the dislocation core position deviate only by 1 µm or less. The general trend of an increasing $\overline{\Delta r}_{\mathrm{CoM},i}$ with rising dislocation segment index i, can be understood by the dominating line direction: While the lower indices include large parts of segments with direction $\boldsymbol{l} = [110]$, the higher indexed lines are inclined with respect to the rotation axis, i.e., neither parallel nor perpendicular to $\boldsymbol{\Phi}$. Since the reconstruction features for those line directions are located further away from the core than it is the case for segments with $\boldsymbol{l} = [110]$, this results in higher mean deviations $\overline{\Delta r}_{\mathrm{CoM},i}$ and also higher standard deviations $\sigma(\overline{\Delta r}_{\mathrm{CoM}_i})$. Furthermore, one has to acknowledge that a computation via MCC is susceptible to errors, that can be avoided when performing a careful manual segmentation by tracing the lines in a slice-by-slice manner. An example can be seen in Frame 11.5a: In the bottom left corner, highlighted in a gray rectangle, three segmented lines are indicated by the colored dots. However, in this slice the features of the individual lines almost merge to one blurred area. Taking only this slice into account, it is hardly possible to identify three separate dislocations. While information from other slices and extrapolation reveals the three lines and enables a successful segmentation via MSL, this particular slice (among other similar slices) will distort the MCC result since the approach handles information from slices completely separately.
Concluding, both approaches yield results that differ only in a few pixels (in most cases only 2 to 3 pixels, i.e., 1 to 2 µm with the here present effective pixel size of 0.72 µm). Thus, the approaches already push the limitations in spatial resolution stemming from the detector system. While at this development stage, a manual segmentation in the fashion of MSL is strongly suggested, the prospect of an automated line extraction is highly attractive. Manual line tracing is time intensive and the effort doubles with the utilization of the CoM-approach in comparison to restricting the analysis to a projection ensemble from only one acquisition interval. Novel segmentation frameworks, like e.g., *Biomedisa* developed for segmentation of data from biomedical imaging [125], are tools that might turn out very useful also for tracing dislocation lines in reconstruction volumes captured by XDL. First test runs suggested this, however, it seems that further testing and adaptation of such techniques is necessary before they can be applied in a reliable and routinized fashion.

11.3 QUANTITATIVE TESTING

In order to draw a final conclusion regarding the CoM-approach, a last comparison of measurement-based results and simulations will be consulted. Therefore, Fig. 11.10 shows cross sections perpendicular to the rotation axis through the respective reconstruction volumes V_1^{Rec} and V_2^{Rec}. Note, that here the SIRT reconstruction was again supported

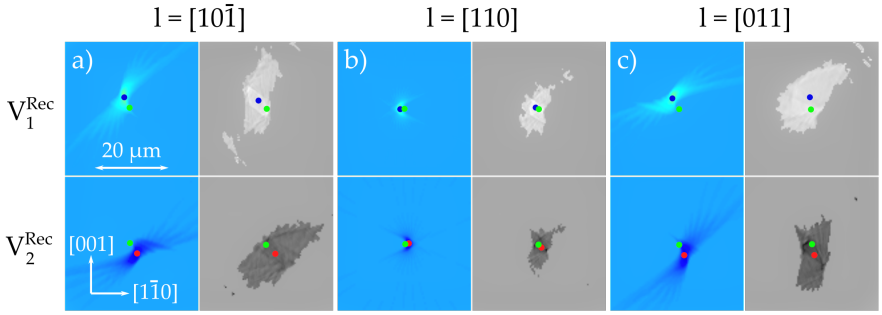

Figure 11.10: Selected reconstruction slices obtained from simulated and measurement data in comparison. The BV is $\boldsymbol{b} = a/2[\bar{1}\bar{1}0]$ in all cases. Cross sections from V_1^{Rec} are shown in the upper, slices from V_2^{Rec} in the lower row, respectively. The simulations are colored in blue while the corresponding slices from the measurement are grayscale images. Compared are reconstructions of dislocations with line directions a) $\boldsymbol{l} = [10\bar{1}]$, b) $\boldsymbol{l} = [110]$, and c) $\boldsymbol{l} = [011]$, covering the entire half loop structure. The measurement was executed exploiting the $\bar{2}\bar{2}0$-reflex of silicon, with an X-ray beam energy of $E_{X-ray} = 25$ keV. According to Appendix C the weak-beam parameter and the angular excitation interval were calculated as $\Delta\theta_{\mathrm{Sim}} = 0.0028°$ and $\delta_{\mathrm{Sim}} = 0.0009°$.

by EVBP, resulting in the sharp edges of the features in the measurement data.
Of special interest are the distances between the corresponding CoM positions $\boldsymbol{r}_{\mathrm{CoM},i=1,2}$, calculated for the individual volumes for measurement and simulation. They are given in Table 11.3 for the dislocation shown in 11.10 (line "A100_400_3 - $\boldsymbol{l}_1$") and for another dislocation with the same properties (line "A100_400_3 - $\boldsymbol{l}_2$"). Dislocations with the BV $\boldsymbol{b} = a/2[\bar{1}\bar{1}0]$ were selected, since this configuration yields the highest deviations from the dislocation core.

$\boldsymbol{l}$	$[10\bar{1}]$	$[110]$	$[011]$
A100_400_3 - $\boldsymbol{l}_1$	6.66 µm	1.58 µm	6.43 µm
A100_400_3 - $\boldsymbol{l}_2$	6.31 µm	0.79 µm	6.34 µm
Simulations	6.69 µm	1.60 µm	6.69 µm

Table 11.3: Distances between the CoMs calculated for the respective intervals, $|\boldsymbol{r}_{\mathrm{CoM},1} - \boldsymbol{r}_{\mathrm{CoM},2}|$ for two dislocations with $\boldsymbol{b} = a/2[\bar{1}\bar{1}0]$ in sample A100_400_3 and corresponding simulations. Line A100_400_3 - $\boldsymbol{l}_1$ corresponds to the exemplary cross sections in Fig. 11.10.

The results show a high level of agreement. Not only do the slices from simulations and measurements in Fig. 11.10 show similar shapes, but also the distances between the respective CoM positions corresponding to volumes V_1^{Rec} and V_2^{Rec} extracted from experimental data and noted in Tab. 11.3 are in close line with the simulations. This

could be achieved by calculating the effective Bragg deviation and the corresponding excitation interval as shown in Appendix C. Furthermore, the physical CoR was calculated according to Section 10.2.2 for positions in the image corresponding to the respective dislocation segments, revealing a tilt of approximately 0.2181° of the axis $\boldsymbol{\Phi}$ with respect to the detector columns. Usually, this could be neglected for a reconstruction, however, in the context of quantitative comparison between measurement and simulations it has been incorporated. Furthermore, the data shown here was recorded with an effective pixel size of 0.36 µm, which in combination with the detector optics yields a spatial resolution of 0.72 µm. This represents the finest resolution ever used for XDL projection acquisition and while processing data sets of mm^3-sized crystal volumes with this resolution is extensive and in many cases not necessary, it is meaningful to exhaust the possible limit for this particular evaluation.
However, it is important at this point to stress, that the here presented slices were picked at random, only ensuring that no artifacts are present, that could falsify the results. Although, the outcome attributes a high level of validity to the theoretical framework for the case of silicon, further more comprehensive studies would be required to confirm this. The value of 0.79 µm for the second [110]-segment with a simulation result of 1.60 µm already indicates that the localization of the CoMs calculated in this fashion might fluctuate significantly from slice to slice.

11.4 DISCUSSION

Although, the majority of results show good agreement between simulations and measurement, possible reasons for deviations are broadly scattered and maybe grouped into three categories:

- The assumptions the theoretical framework is based upon: In the considerations in Chapter 5 we assume isotropy of the material, which is of course only fulfilled to a certain degree. Silicon may show sufficient isotropic properties, but especially when considering compound semiconductors or crystals of non-cubic structure, this circumstance has to be carefully considered and revised. Furthermore, we use linear elasticity to describe the dislocation displacement field $\boldsymbol{u}(\boldsymbol{r})$. Another factor in this regard is the kinetic approximation of the diffraction mechanism.

- Secondly, simplifications have been introduced when implementing the contrast formation via the geometrical ray tracing approach: Here, straight parallel rays are assumed to model the diffracted X-ray signal. The diffracting volume does not change the ray direction. In this regard, estimates of the resulting uncertainty are given by equations 5.36 and 5.37 and in Appendix

A, although they are in most cases rather small (of the same magnitude as the effective pixel size). Additionally, the local reflectivity is defined as a binary property: A unit of the crystal volume either contributes as strongly as any other or not at all to the contrast formation on the detector plane.

- The last category is given by uncertainties during data acquisition. Here, the most crucial factor is the weak-beam parameter $\Delta\theta$. During an XDL-scan the Bragg peak and the corresponding angle θ_B is determined at several positions ϕ in one interval during projection recording. This is done by rocking scans, but since changing the illuminated crystal volume for this purpose is highly disadvantageous and endangers the success of the scanning procedure, the signal is distorted not only by dislocations in the FoV. Often times an indent-like damage on the sample is the origin of the dislocation structure. Therefore, the determined Bragg angle θ_B is not the Bragg angle of the undistorted crystal lattice and an additional shift $\Delta\theta_{\text{Dist}}$ to the laminographic angle as $(\theta = \theta_B + \Delta\theta_{\text{Dist}}) + \Delta\theta$ is introduced. This is neglected in corresponding simulations.

Despite these shortcomings, the approach presented in this chapter still represents a highly useful tool. Overall, predictions derived by the calculations are valid also for measurement data, although their numerical accuracy has to be considered with caution. The conclusion, that the mean- or CoM-position of corresponding line features from the respective reconstruction volumes is a better estimate of the position of the dislocation core, than a segmentation of only one reconstruction can provide, seems highly plausible. Furthermore, we nearly completely exclude influences dislocation properties (like line direction and BV) and measurement parameters (like weak-beam and diffraction interval parameters, $\Delta\theta$ and δ, respectively) have on the final estimate of the core position.
The presented data set from the silicon sample A100_400_3 was recorded with $\Delta\theta = 0.003°$. Based on experience, this can be considered as rather high: With a further increase in the weak-beam parameter, visibility of dislocation lines almost vanishes in noise. Consequently, the signal is created almost as close as possible to the dislocation core and still the application of the CoM-scheme improves the result, although it is here pushing the resolution limit of the employed detector system given by 1.44 µm in most cases presented here (especially for line directions $\boldsymbol{l} = \pm[110]$). Aiming for further refinements it may be necessary to decrease the effective pixel size and the resolution limit of the optics. One case with an effective pixel size of 0.36 µm and thus a resolution limit of 0.72 µm (with suitable detector optics) was presented. This resolution limit becomes meaningful, when applying the CoM approach.

Concluding on the basis of the preceding simulations, the agreement between simulations and measurement in Table 11.3 and assuming that the deviations between the two possible implementations of CoM-approach (apart from some outliners) plotted in Fig. 11.9 represent an average error of the technique, with the respective CoM positions being distributed randomly around the position of the dislocation core, the achieved spatial resolution should be estimated to about 1 to 2.5 µm (the limit of the detector system always serving as an absolute minimum).

For further studies it would be meaningful to start by conceptualizing measurements that allow an approximation of the distortion shift in the Bragg peak $\Delta\theta_{\mathrm{Dist}}$, e.g., by recording projections for different $\Delta\theta$ (also with different signs) and match them by investigating the resulting reconstructions. This can be simulated first by calculating projections for a specific Bragg deviation using an approach developed very recently, called Virtual Weak-Beam (VWB): Rocking scans are used for a pixel-wise fitting of the rocking curve, which then allows constructing an image on any angular position of the rocking curve by interpolation. Another possibility is to refine the simulations, e.g., by switching from a strictly binary local reflectivity to a scalar field or even allow ray trajectories not parallel to the original (virtual) ray.

12 TOWARDS BURGERS VECTOR DETERMINATION

For the comprehensive characterization of a dislocation arrangement another important aspect following the three-dimensional (3D) structure is the Burgers vector (BV) distribution. This refers to assigning the correct BV to every individual dislocation line in the arrangement. Regarding X-ray imaging the common approach to achieve this assignment is the recording of several topographic images of the same structure for different reflexes via X-ray White Beam Topography (XWBT). By comparing a set of X-ray topographs (often recorded on high resolution X-ray film), one may then conclude on the direction (not the sign) of the BV of a given dislocation [34, 49, 126], due to the extinction rule, see Section 5.5. As it has been shown in Chapter 10 and [49], the position of the line contrast in different frames during a rocking scan on opposite sides of the Bragg peak (i.e. $\theta_i < \theta_B < \theta_j$) then reveals the sign of the BV. This means, that with data from X-ray Diffraction Laminography (XDL) alone, we can only access the sign of the BVs, while up to this point the determination of their orientation requires an entirely different measurement setup and therefore turns out extensively time-consuming. Especially, aiming for quasi *in situ* studies in 3D with measurement schemes where a sample treatment is applied between several XDL-scans to obtain snap shots of the evolution of dislocation arrangements, this is hardly feasible. Determining the BV distribution for every single step would require XWBT measurements (involving several sample mountings and setup modifications) with every subsequent sample treatment.
This raises the question if it is possible to access also the orientation of a dislocation's BV directly from i) XDL projections, ii) data from intermediate rocking scans, or iii) the 3D reconstruction volumes (i.e. from the separately reconstructed volumes $V_{1,2}^{\mathrm{Rec}}$ or the compounded volume $V_{\mathrm{Comp}}^{\mathrm{Rec}}$). The following will present some approaches and discuss the related challenges with the aim to further extend the information made accessible by XDL.

12.1 TOPOGRAPHIC LINE CONTRAST

Referring to the considerations presented in Sections 5.5 and the corresponding simulations in Section 6.3 a nearby approach to determine the BV-orientation of a dislocation would be to investigate the intensity profile of the dislocation line over the tomographic rotation angle ϕ.

For easier readability Frame 12.1a again shows the intensity profile of different BVs for a perfect dislocation with line direction $\boldsymbol{l} = [10\bar{1}]$

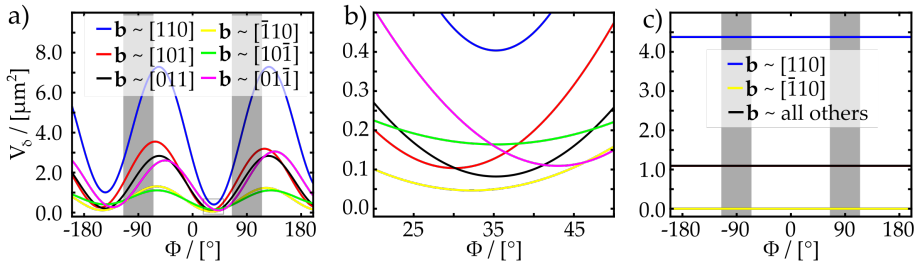

Figure 12.1: Excited volume per line length over tomographic rotation angle ϕ. a) All relevant BVs of a perfect dislocation with $\boldsymbol{l} = [10\bar{1}]$. b) Enlargement of the section containing the minima at positions $\phi \in [20°;50°]$. The same color-code as in a) has been used. c) Simulations for all relevant BVs of a perfect dislocation with $\boldsymbol{l} = [110]$. The calculations were performed for an energy of 25 keV for the $\overline{2}\overline{2}0$-reflex of silicon. The weak-beam parameter was set to $\Delta\theta = 0.002°$ and $\delta = 0.0007°$.

as in Fig. 6.7. Here, the gray bars indicate the angular sections that are not accessible for a laterally extended sample in Laue-transmission geometry (LTG). However, line intensity in the tomographic image is highly influenced by intensity fluctuations in the cross section of the incoming beam and therefore not easily comparable to simulations. This challenge can be overcome by specifically paying attention to the localization of intensity minima (or maxima for that matter), since they are located in a small (accessible) angular range. This means that in the vicinity of a minima the dislocation image does not move large distances in the image while rotating about $\boldsymbol{\Phi}$. In Frame 12.1b the minima between $\phi \in [20°;50°]$ are shown in more detail. Unfortunately, we find that according to the calculations three minima are found at the same angle positions, the values are noted down in Tab. 12.1.

$\boldsymbol{b} = a/2\times$	$[110]$	$[101]$	$[011]$	$[\bar{1}10]$	$[10\bar{1}]$	$[01\bar{1}]$
ϕ_{min}	35.3°	30.1°	35.3°	32.2°	35.3°	43.0°

Table 12.1: Positions ϕ_{min} of the intensity minima shown in frame b) of Fig. 12.1.

Furthermore, Frame 12.1c shows how the expected intensity is not changing if the line direction of the dislocation segment is $\boldsymbol{l} = [110]$, i.e., parallel to the selected reciprocal lattice vector and the rotation axis: $\boldsymbol{l} \parallel \boldsymbol{h}_{\overline{2}\overline{2}0} \parallel \boldsymbol{\Phi}$. While one obtains the strongest contrast for $\boldsymbol{b} = a/2[110]$, all other BVs yield the same intensity (or excited volume per line length V_δ, where often a linear connection is assumed as mentioned in Section 6.3 and [42, 47, 87]) except for $\boldsymbol{b} = a/2[\bar{1}10]$, which is invisible in agreement with the extinction rule. Although, this seems to provide sufficient criteria to determine the BV distribution of a dislocation, assuming a suited way to extract the line intensity

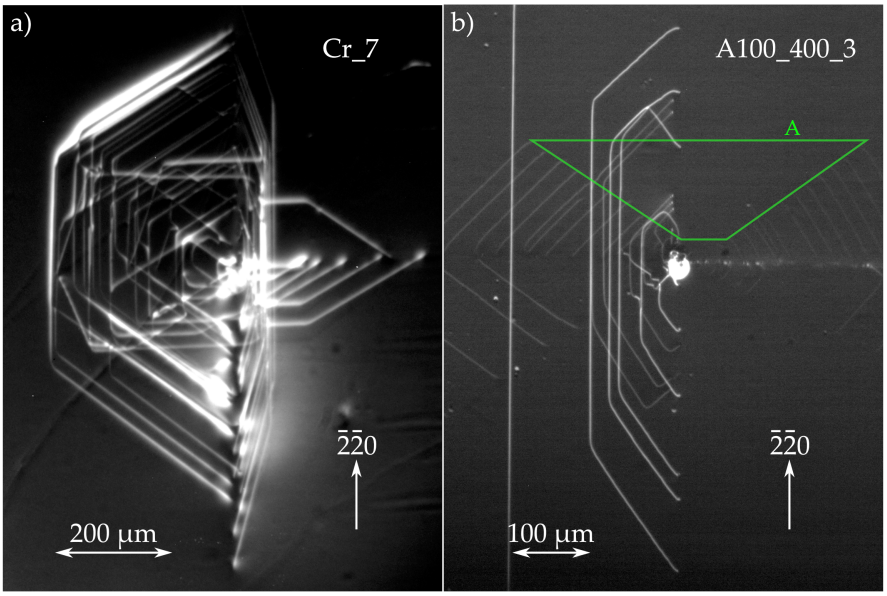

Figure 12.2: Exemplary projection data of two different samples, measured at two different beamlines: a) Sample Cr_7 at an energy of 40 keV with a weak-beam parameter of $\Delta\theta = 0.002°$, recorded at ID19 of the European Synchrotron Radiation Facility (ESRF), Grenoble, France. b) Sample A100_400_3 at an energy of 25 keV with a weak-beam parameter of $\Delta\theta = 0.003°$, recorded at P23 of the Deutsches Elektronen Synchrotron (DESY), Hamburg, Germany. The green trapezoid A frames non-visible segments with $\boldsymbol{l} = [\bar{1}10]$. More details on samples and measurements can be found in Appendix H.

normalized to the profile of the incoming X-ray beam is found, one faces another problem, when dealing with complex dislocation arrangements: The practicability of extracting the required information for every individual dislocation segment in a complex arrangement is highly unlikely. For several dislocations this will be impossible, especially for view directions, which are orientated parallel to preferred glide planes. To illustrate this, Fig. 12.2 shows two exemplary projections of structures in the samples Cr_7 and A100_400_3, which have already served as examples in the previous chapters.

While in Frame 12.2a the dislocations located on slip planes on the left of the center are clearly separable, the ones on the right of the center start to overlap more and more. In Frame 12.2b the view direction is slightly different: Here, the dislocations on the left of the center are located close to each other, judging from the viewer's perspective.

In summary, the feasibility of this approach is strongly connected to the complexity of the dislocation arrangement under investigation. While for structures comparable to the one present in the silicon sample A100_400_3 it might in fact be possible to extract sufficient

information about a majority of the present dislocations, this seems unlikely for structures of similar complexity as the arrangement in Cr_7. Here, it might only be possible to determine BVs of dislocations, that propagated far away from the evolution origin in the center of the structure. Nevertheless, it needs to be stressed that some information can be extracted in a straight forward manner: Looking closer at frame 12.2b one finds that the middle segments of the horizontal half loops, which should be located in the light green trapezoid A are completely invisible. This already allows to conclude that they are subject to the extinction rule and therefore $\boldsymbol{b} = \pm a/2[\bar{1}10]$.

12.2 RECONSTRUCTION FEATURES

In order to enable the extraction of information about the BV distribution also for complex dislocation arrangements like the one present in Cr_7, now another approach will be demonstrated. This is based on the fact, that according to the simulations in Chapter 6 different BVs result in a different localization of the reconstructed features even if the line direction remains unchanged, as is shown in Fig. 6.5. The advantage is, that investigations regarding features in the reconstructions should in general be possible, if the individual dislocation lines are resolvable and separable via XDL, since the resulting 3D image enables inspection from arbitrary view directions. Particularly, the analysis of cross sections perpendicular to the predominantly preferred line direction of dislocations (often parallel to the rotation axis $\boldsymbol{\Phi} \parallel \boldsymbol{h}_{\bar{2}\bar{2}0}$) proves to be very useful.

By careful investigation of cross sections as they are exemplarily shown in Fig. 12.3 we are able to find distinctive differences in the shape of features stemming from different dislocation lines, or in the relative positions of features in V_1^{Rec} and V_2^{Rec} originating from one and the same dislocation line. It also turns out, that varying the position of the rotation axis x_{CoR} can be useful for the investigation. In Frames 12.3b to 12.3f similar features are exemplarily circled in green, while another feature that shows slight differences is circled in red. Since these features all belong to dislocation segments with line direction $\boldsymbol{l} = [01\bar{1}]$ one may conclude, that they have different BVs. It is noteworthy, that this technique has to applied with caution: The features highlighted in yellow in Frame 12.3a seem to show a very unique behavior. In particular, bright and dark contrast features flip prior to all other features from all other visible dislocation lines, as can be seen in Frame 12.3f. This however does not indicate a different BV. The reason is rather that this is the only line in the shown slices that already changed to the line direction $\boldsymbol{l} = [110]$. To achieve a grouping of all dislocations in the volume an investigation of a large number of slices is necessary. However, eventually a categorization can be provided, that does not reveal the exact orientation of the

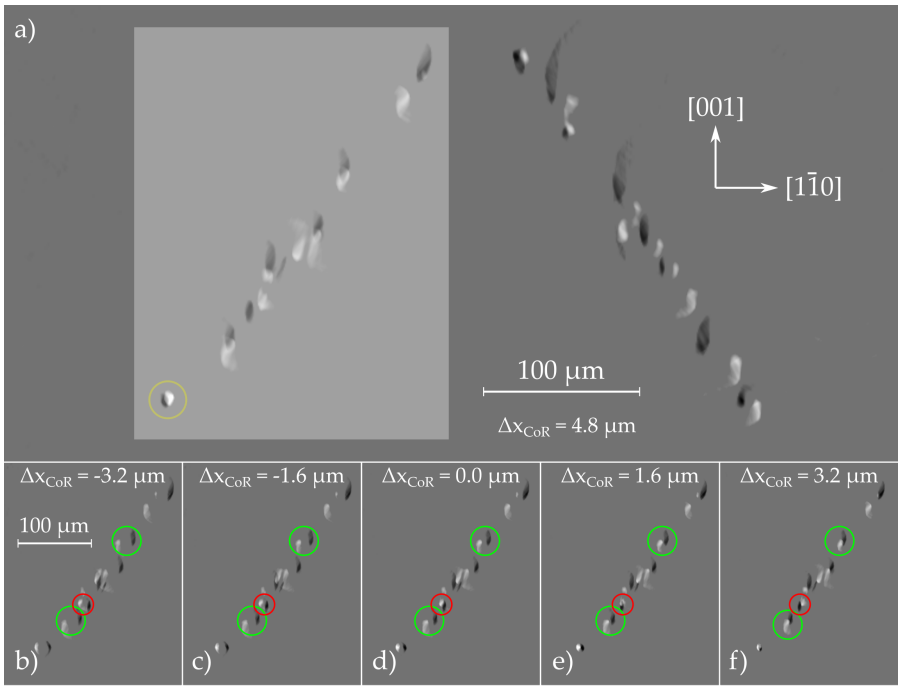

Figure 12.3: Cross sections perpendicular to the rotation axis $\mathbf{\Phi}$ of the dislocation arrangement in the silicon sample Cr_7. The reconstruction was obtained via Empty Volume Backprojection (EVBP) from projection ensembles (70 projections per acquisition interval) acquired at 40 keV with a weak-beam parameter of $\Delta\theta = 0.002°$, exploiting the $\overline{2}20$-reflex. Frames b)-f) show the highlighted area in frame a) for different settings of the Center of Rotation (CoR), in order to reveal the different distribution of reconstruction features corresponding to dislocations with a different BV. Examples are highlighted in colored circles (red and green).

individual BVs but at least which dislocations have the same BV. Fig. 12.4 shows the final result for the dislocation structure in Cr_7, which is in agreement with results from XWBT shown in [48, 49].

12.3 SUMMARY AND OUTLOOK

In this Chapter it was demonstrated how projection and rocking scan data in combination with 3D reconstruction images can be utilized to access the BV distribution in complex dislocation arrangements by relying only on XDL data.
Although, neither of the two approaches provides the whole information, a combination of the two techniques seems very promising and should be subject of further methodological developments. Assuming the BVs of a sufficient number of individual dislocations can be determined from contrast analysis in the projection images, this in combination with the grouping of reconstruction features might allow assigning the correct BV to every dislocation. Furthermore, the sign

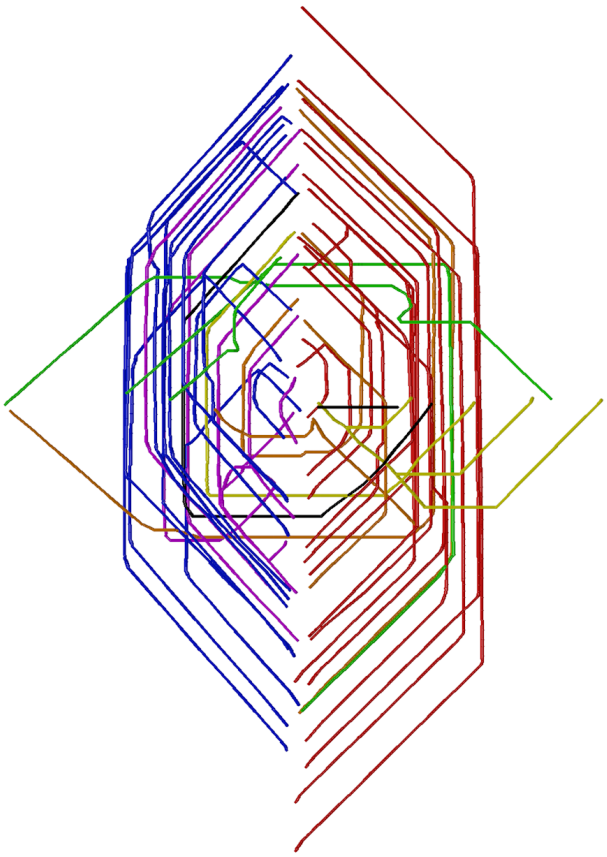

Figure 12.4: 2D-rendering of a 3D image of the dislocation arrangement in Cr_7. The reconstruction features in cross sections perpendicular to the rotation axis were analyzed and compared for different dislocations with the same line direction. The distinct differences in appearance allowed a categorization of dislocations corresponding to their respective BVs. While the orientation of the different BVs could not be determined, dislocations with identical BVs could be grouped together, providing an intermediate result.

could then be determined by analyzing the contrast flip in rocking scan data and the feature distribution in $V_{\mathrm{Comp}}^{\mathrm{Rec}}$, as shown in Chapter 10 and partially in [49].
Further investigations should also include determination of suited weak-beam parameter settings. In the here presented case of Cr_7 the Bragg deviation was set to $\Delta\theta = 0.002^\circ$. Comparison to other data sets gave the impression, that such weak-beam conditions (i.e. $\sim 0.002^\circ$) are more favorable for the analysis of reconstruction features than exciting regions of the volume particularly close to the dislocation core (i.e. with $\Delta\theta \sim 0.0030^\circ$ or 0.0035°). However, this has not been investigated in detail and thus could not be confirmed yet.

Part III

EXEMPLARY APPLICATIONS

13 QUASI 4D IMAGING OF DISLOCATIONS

As a first demonstration of the extended capabilities of X-ray Diffraction Laminography (XDL) enabled by the methodological developments conducted within this work, here an approach for the quasi four-dimensional (4D) imaging of dislocation - also referred to as quasi *in situ* three-dimensional (3D) imaging of dislocations - will be presented. In particular, the challenges that had to be overcome will be elaborated, especially in relation to this thesis.

13.1 CONCEPT AND CHALLENGES

Since acquisition of XDL projection sets was very time consuming, with sample alignment taking several hours and subsequent recording adding up to even days, a genuine *in situ* approach, which would also mean performing the complex sample manipulation in a heating environment, did not seem feasible. Therefore, a first approach to capture dislocation dynamics in a quasi 4D fashion was proposed. This is realized by a gradual sample treatment with intermediate XDL scans, to record snap shots of the emerging dislocation arrangement.

Fig. 13.1 illustrates this workflow for the special cases presented later: First, silicon samples are intentionally damaged by nano-indentation in order to emulate the introduction of scratches or microcracks by handling during typical processing steps. In semiconductor device fabrication the materials are often heated, e.g, during CMOS processing. This may lead to the nucleation of dislocations, evolving into complex structures and propagating into previously dislocation-free regions of the wafer far from the initial damage site (on mm and even cm scale). In the here presented case a mirror furnace is utilized to simulate these annealing treatments, more information can be found in [127–130]. Nevertheless, it is important to note, that the measurement scheme is of course not limited to heating; in principle, any form of sample treatment, which can be performed gradually with one processing step not taking longer than few hours and which does not introduce large scale damages ($\sim$ mm^2) to the sample surfaces (prohibiting X-ray topography with µm resolution), is applicable in a straight forward manner.
The challenges connected to this approach can be summarized as follows:

- The mirror furnace has to be carefully calibrated. In previous two-dimensional (2D) *in situ* studies the furnace was placed in the beam and the evolution of the dislocation arrangement could

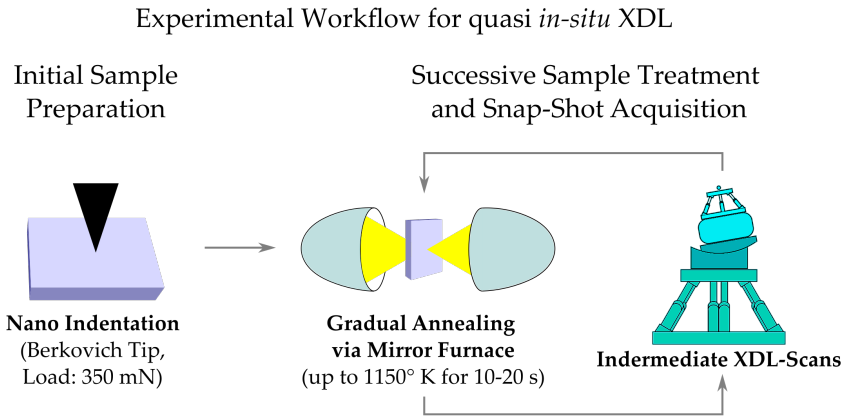

Figure 13.1: Sample preparation by means of nano-indentation and measurement scheme for the acquisition of quasi *in situ* XDL-data: a gradual heating treatment alternating with XDL scans.

be directly observed via X-ray White Beam Topography (XWBT). Due to the demands of XDL regarding monochromatic beam properties and stability, direct observation by, e.g., performing sample manipulation for XDL within the furnace, is not feasible. Therefore, the annealing has to be performed *blind* in a reproducible step-wise manner.

- Consequently, sample alignment for XDL has to be performed after every treatment step. Therefore, also this procedure requires reproducibility, which is achieved by dedicated sample holders and the utilization of the dedicated sample manipulator allowing the implementation of scripts for a semi-automated alignment, see Chapter 7.

- Scanning procedures had to be accelerated, to maximize the number of snap shots during the successive sample treatment, which results in a higher resolution of the dynamical processes. This was achieved by (i) reliable performance of the instrumentation - mainly the sample manipulator, and (ii) the reduction of the required number of projections.

Here, particularly the latter two bullet points are strongly related to the developments presented in this work, see Chapters 7, 8, and 9.

13.2 MEASUREMENTS AND RESULTS

In both presented cases the 20×20 mm^2 samples were cut from a 750 µm thick polished (both sides) wafer with a [001]-surface normal. Prior to the measurement the samples ware indented five times with a load of F = 350 mN and F = 300 mN, for the studies in Section 13.2.1 and in Section 13.2.2, respectively. During the annealing the samples

had to be heated above the brittle-to-ductile temperature for only a few seconds to provoke dislocation propagation. If heated longer, the evolution would have progressed to fast, degrading the resolution of the dynamics. Here, the temperatures reached were around 1150°K or 880°C and were only applied for durations of 10 to 20 s each cycle.

13.2.1 *Exemplary Quasi 4D Study*

In the first case, the initial damage sites, i.e. the indents, were arranged forming an *X*-pattern, also see Fig. 13.2. The measurements were conducted at ID19, at the European Synchrotron Radiation Facility (ESRF), Grenoble, France. The energy of the monochromatic X-ray beam (a 111 silicon Double Crystal Monochromator (DCM) was utilized) was set to $E_{\text{X-ray}} = 23.567$ keV, resulting in a Bragg angle of $\theta_B = 7.871°$ for the 220-reflex of silicon. For the different measurement steps the Bragg deviation was varied between 0.0025° and 0.003°.
Since it was one of the first measurements of its kind and alignment as well as positioning procedures during scans experienced a significant speed-up due to the introduction of the sample manipulator (described in Chapter 7), relatively high numbers of projections were recorded to ensure a successful reconstruction: 525 projections were recorded in interval I_1 with 15 intermediate rocking scans (encompassing 24 steps) and 105 projections were recorded in interval I_2 with only 3 intermediate rocking scans (also encompassing 24 steps), respectively. However, testing showed that 262 projections are sufficient for a successful 3D reconstruction (the actual minimum of required projections might be even lower).

Fig. 13.2 shows three subsequent snap shots of the emerging dislocation arrangements. The red arrow-like triangles indicate the sample treatment. Although, more than the three steps shown here have been performed, often times the annealing was too short to result in substantial development of the structure. It turned out, that the *blind* annealing was the most difficult aspect of the whole measurement campaign and was also defining the resolution limit for the dynamics. The BV distribution was determined in a separate experiment at the Topography Station of the Imaging Cluster at the Karlsruhe Institute of Technology (KIT) synchrotron light source in Eggenstein-Leopoldshafen, Germany. Since this was only possible for the final state, the intermediate steps had to be approximated. In this regard the developments in Chapter 12 could provide additional assurance and in the future even make XWBT-measurements obsolete.

13.2.2 *Dislocation-Dislocation Interaction*

In this example the indents were arranged in a horizontal line, i.e. along the $[1\bar{1}0]$ crystal direction of the sample. The gradual anneal-

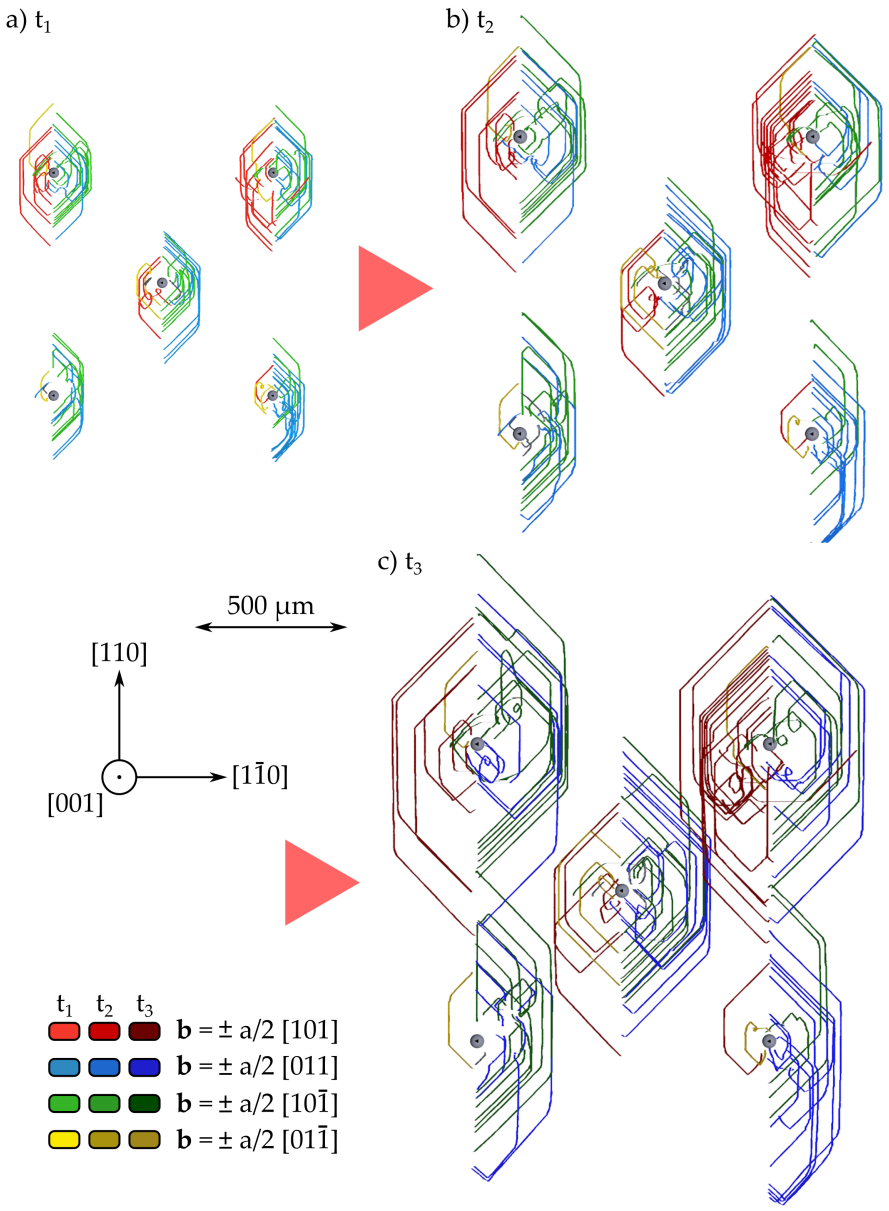

Figure 13.2: Three 3D snap shots of a dislocation arrangement emerging around five initial damage sites during a gradual annealing. The Burgers vector (BV)s determined by XWBT for the final state of the structures are shown in color-code, with colors changing from light to dark with the individual evolution steps. The arrow-like triangles indicate the intermediate sample treatments: An annealing above the brittle-to-ductile temperature to about 1150°K or 880°C for 10 s in the first and 20 s in the second heating sequence, respectively.

ing was applied in a similar fashion as in the previous case. The experiments were carried out at P23, Deutsches Elektronen Synchrotron (DESY) - PETRAIII, Hamburg, Germany. The energy of the monochromatic X-ray beam was set to 25 keV (again a silicon 111 DCM was utilized), which exploiting the 220-reflex of silicon resulted in a measured Bragg angle of $\theta_B = 7.56°$. For the 3D reconstruction 240 projections were acquired in one acquisition interval for each snap-shot with a Bragg deviation $\Delta\theta$ varying between 0.0025° and 0.003° for the respective scans.

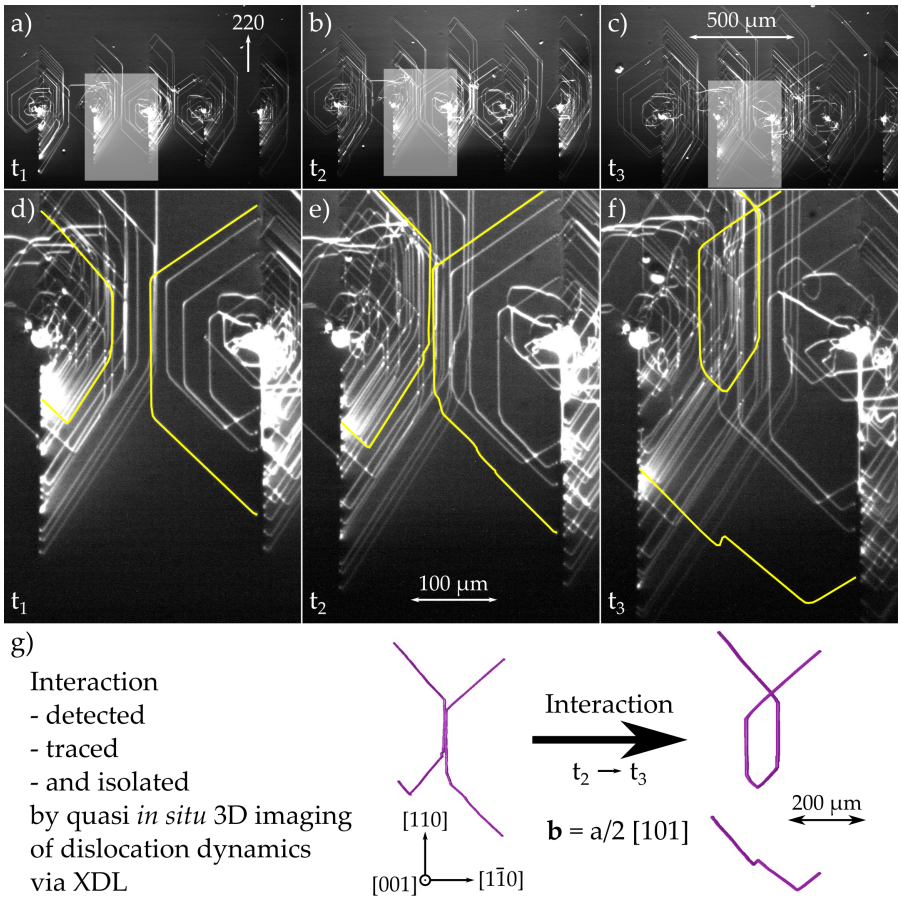

Figure 13.3: 2D weak-beam topographs (XDL projections) of three evolution steps of dislocation arrangement emerging around five initial damage sites during a gradual annealing. a)-c) show the complete FoV, while d)-f) show the areas highlighted in light gray for the respective snap-shots. g) The interacting dislocations highlighted in yellow in Frames d), e), and f) isolated from the 3D reconstructions obtained from projection ensembles corresponding to the evolution steps shown in a), b), and c). The BV was determined a $\boldsymbol{b} = \pm a/2[101]$. Note, that the color-code only serves visualization purposes here.

Fig. 13.3 shows XDL projections of the emerging dislocation structures from a view direction corresponding to typical X-ray topography measurement, i.e., the surface normal [001] of the sample lying in

the diffraction plane. Frames 13.3a to 13.3c show the whole captured Field of View (FoV), while Frames 13.3d to 13.3f show a Region of Interest (ROI) between two indents enlarged (highlighted in light gray in the corresponding frames). In the here presented quasi *in situ* study a dislocation-dislocation interaction was observed, the involved dislocations are highlighted in green. It is noteworthy, that this event would have been hard or even impossible to detect, if only the presented 2D data was available (corresponding to conventional X-ray topography). The 3D information made accessible by XDL provides certain confirmation of the interaction and allows isolating the involved segments for further analysis, as shown in Frame 13.3g, demonstrating the benefits of this quasi 4D imaging technique.

A more detailed analysis, relating the 3D data to the external thermal forces, can be found in [131] along with further information about the samples. The segmentation and BV-determination conducted in the frame of [131] and the permission for the adaption of Figures for this work is thankfully acknowledged and highly appreciated.

13.3 SUMMARY AND CONCLUSION

The quasi *in situ* capabilities of XDL, enabled by the substantial developments and improvements regarding data acquisition and processing achieved within this work, have successfully been demonstrated. Dislocation dynamics were captured in 3D in damaged silicon wafers, that underwent a gradual annealing. The dedicated instrumentation and the significant reduction of required projections represent the key milestones in this regard. Several measurement campaigns have been performed so far and the method is drawing more and more attention.

14 APPLICATION TO OTHER MATERIALS

This chapter will give a short summary of applications of X-ray Diffraction Laminography (XDL) to other materials apart from silicon. As already stated in Chapter 1, many observations indicated the three-dimensional (3D) nature of dislocations before 3D imaging was enabled. With the significance of elastic anisotropy especially the application of XDL to non-cubic structures could become relevant in the future. Nevertheless, the intention is rather to present feasibility and a short discussion of the challenges related to imaging dislocations in these materials, than a detailed discussion of the material properties and the defects present within them.

14.1 GALLIUM ARSENIDE

At the point of writing, two feasibility studies were conducted with Gallium arsenide samples, one with a liquid encapsulated Czochralski (LEC) grown wafer with a complex *intrinsic* dislocation network, i.e., defects stemming from the growth process, and a second on a vertical gradient freeze (VGF) grown wafer, that also experienced a heating treatment.

14.1.1 *GaAs grown by the Liquid Encapsulated Czochralski Method*

The example shown in FIg. 14.1 was the first feasibility study of XDL's application to GaAs. The measurement was performed at ID19, ESRF, Grenoble, France. A X-ray beam energy of 60 keV was selected, which - exploiting the 220-reflex - resulted in a Bragg angle of $\theta_B = 2.96°$, the Bragg deviation was set to $\Delta\theta = 0.0045°$ and the reconstruction was carried out utilizing 100 projections from one acquisition interval. Fig. 14.1 also shows an XWBT image of the 40 mm diameter wafer, the area highlighted in green was selected for the XDL feasibility study. In Frames 14.1b to 14.1e two-dimensional (2D) images of the 3D dislocation network from different view directions are shown. The spatial resolution achieved here is in the µm range while the detector resolution is given by 1.92 µm (two times the effective pixel size, since suited optics were used). This example shows the challenges especially related to data processing like segmentation and analysis, regarding more complex structures than the ones known from silicon, even if a sufficient spatial resolution is achieved. Since dislocation networks like this one, seemed too complex for a first *in situ* attempt, it was

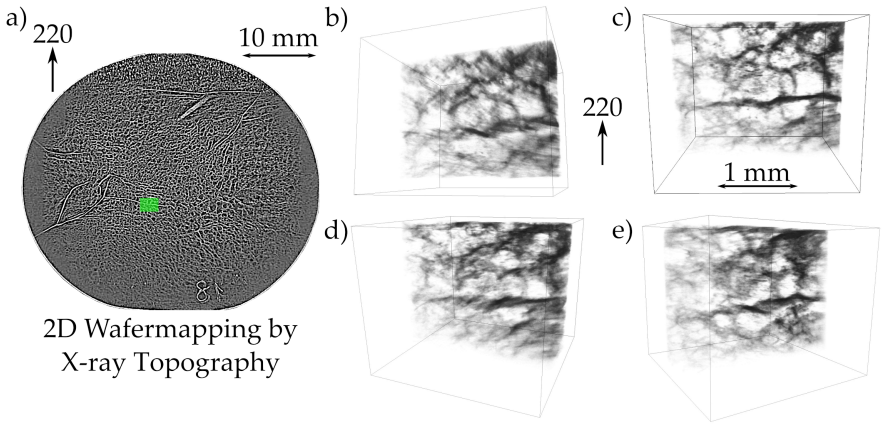

Figure 14.1: a) Mapping of the complete wafer, obtained by stitching several X-ray White Beam Topography (XWBT) images together, recorded at the Topography Station of the Imaging Cluster at the Karlsruhe Institute of Technology (KIT) synchrotron light source, Eggenstein-Leopoldshafen, Germany. The area highlighted in green was later scanned by XDL at ID19, European Synchrotron Radiation Facility (ESRF), Grenoble, France. b)-e) Images of the 3D volume from different view directions. The cellular structure of the dislocation network becomes especially visible in c).

decided to switch to VGF grown samples, which initially presented dislocation-free crystal volumes.

14.1.2 *GaAs grown by the Vertical Gradient Freeze Method*

XDL was applied successfully to a GaAs sample cut from a 100 mm diameter VGF grown wafer with a thickness varying between 625 and 650 µm.
Similar to the application in Chapter 13 the sample was indented with a Berkovich-tip with a load of 400 mN and subsequently annealed. The intermediate scans were performed at P07, Deutsches Elektronen Synchrotron (DESY) - Petra III, Hamburg, Germany. An energy of 65.5 keV was selected for the monochromatic beam, resulting in a Bragg angle of $\theta_B = 2.7141^\circ$ for the 220-reflection in Laue-transmission geometry (LTG) (with the surface normal being oriented along the [001] crystal direction). A weak-beam parameter of $\Delta\theta = 0.003^\circ$ allowed recording quasi projections with contrast properties enabling a 3D reconstruction. However, it turned out that not all three dislocation half loops were visible in the same topographic images. Surprisingly, their visibility was depending on the selected weak-beam condition, with certain half loops becoming visible for $\theta = \theta_B + \Delta\theta$ and others for $\theta = \theta_B - \Delta\theta$. This phenomenon has not been explained yet and is subject to further research. Eventually rocking scans had to be used to calculate projections containing all three dislocation half loops via Virtual Weak-Beam (VWB). Afterwards a Filtered Backprojection (FBP)

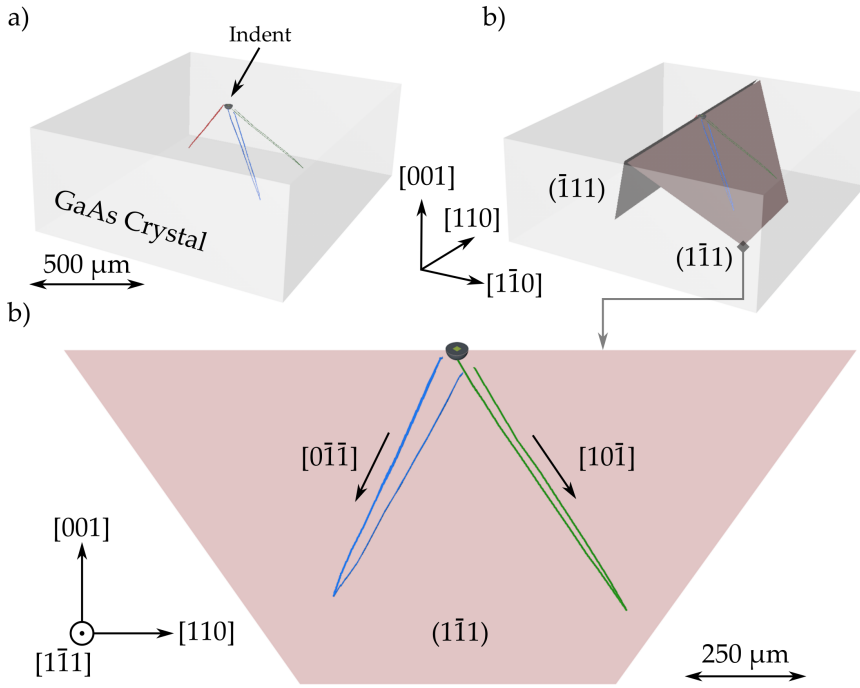

Figure 14.2: Inclined arm dislocations originating from a nano-indent (400 mN Load), extending into dislocation-free crystal areas, and approaching the opposite side of the wafer: a) Image of the segmented dislocations obtained from a 3D reconstruction. b) The corresponding glide planes in the wafer. Perpendicular view onto the $(1\bar{1}1)$ glide plane enabled by the 3D result: Two dislocations half loops are shown, each consisting of screw dislocation segments connected by a 60° segments (the Burgers vector (BV)s of the screw segments, therefore are $\pm a/2[011]$ and $\pm a/2[10\bar{1}]$ parallel to the line directions indicated in the illustration).

reconstruction was carried out, yielding the presented results.
Here, only one state of the dislocation structure is shown in Fig. 14.2, showing inclined arm dislocations evolving around an indent. A more detailed discussion is presented [131], correlating these results with findings from comprehensive XWBT studies, and concluding on extensions and modifications to the 3D dislocation model presented in [132] for materials crystallizing in the zinc-blende structure. Apart from the confirmation of the model, which was developed based on 2D topography data, this 3D result further allowed measuring distances in high precision, e.g., the distance between the screw segments close to the indent was found to be varying between 15 and 40 µm for the different half loops.

14.2 ALUMINUM NITRIDE

Although, AlN shows a non-cubic hexagonal wurtzite structure in this case it enabled a straight forward application without any significant alterations to the case of silicon. The presented data was recorded at P23, DESY - Petra III, Hamburg, Germany. The monochromatic X-ray beam energy was set to 22 keV, exploiting the $10\bar{1}0$-reflex in LTG this resulted in a measured Bragg angle of $\theta_B = 6.0°$. The Bragg deviation was again set to $\Delta\theta = 0.003°$.

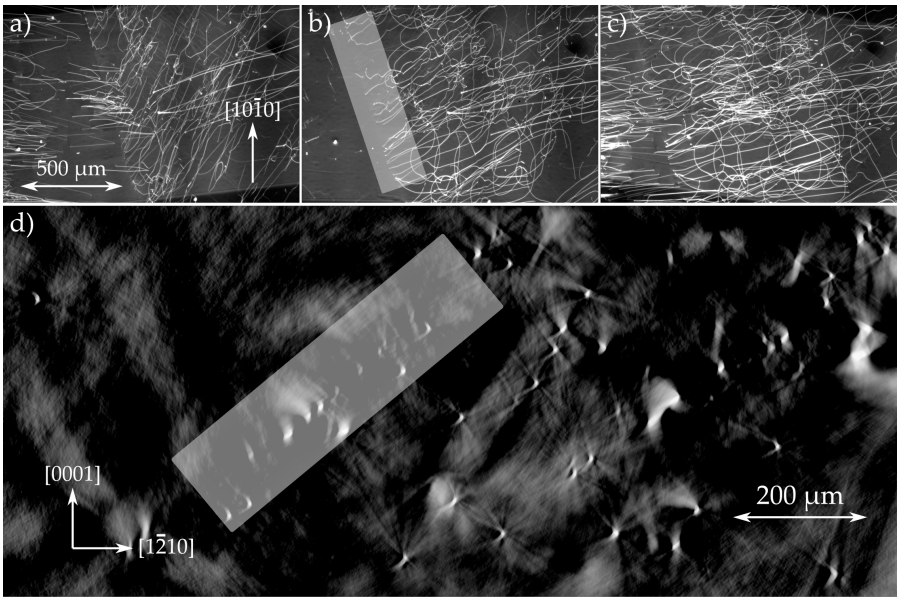

Figure 14.3: a)-c) Projections from different view directions. d) Exemplary slice from the reconstruction volume. The interface highlighted in b) is visible in the cross-section as well, also highlighted in light gray.

Despite the similar parameter set, as for the case of silicon, the here presented example highlights the advanced possibilities for investigations, that are enabled by a truly 3D image of the structure: While the straight line character of dislocation segments in silicon and their strict orientation on certain crystal planes and in certain crystal directions already allows a good impression of the 3D geometry of the arrangement also with only 2D topographs available, the arrangement captured in AlN is way more challenging to analyze. The topographic images from certain view directions already indicate the presence of an interface highlighted in gray in Frame 14.3b. However, its exact orientation and especially the orientation of dislocations in this plane is difficult (if not nearly impossible) to extract from 2D date alone. With performing a 3D reconstruction one is finally able to isolate a Region of Interest (ROI) of an arbitrary shape and localization from the volume and inspect it from arbitrary view directions. For example, a 3D box could be defined containing the interface in order to inspect it

from a perpendicular view. The extend of this ROI-box along the view direction can of course be adjusted as well, ranging from a view µm to approximately 1 mm (limited by the Field of View (FoV)), and thus encompassing exactly the desired regions of the crystal volume.
Exemplarily this is shown in Fig. 14.4: The interface has been isolated and while Frame 14.4a shows an almost perpendicular view onto the interface plane, the in-plane view in Frame 14.4c reveals that most dislocations are really located on a thin plane with some paths extending into the rest of the volume. Here, the Frames 14.4a, 14.4b, and 14.4c, show the interface from view directions ϕ_1, $\phi_2 = \phi_1 + 45°$, and $\phi_3 = \phi_1 + 90°$, this time perpendicular to the rotation axis defined during the measurement without a laminographic tilt θ. However, any view direction can be realized, it just turns out that these are convenient to illustrate the localization of the dislocations. The *box* that was defined around the interface, in this case has a thickness of approximately 144 µm and thus, all dislocations not localized within this box are not visible.

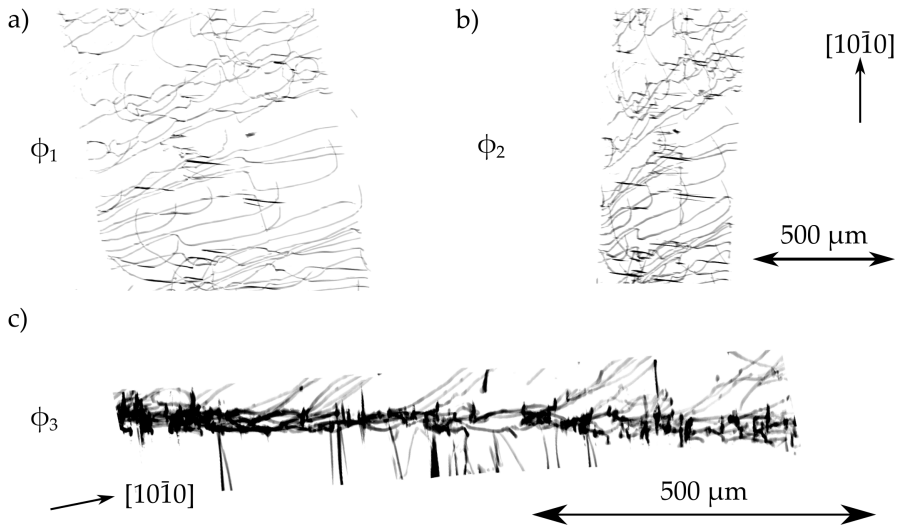

Figure 14.4: Interface isolated from remaining crystal volume by manipulating the 3D reconstruction volume. a) From an almost perpendicular view direction to the interface plane. b) Another view direction obtained by rotating about 45° about the physical rotation axis **Φ** defined during data acquisition. c) In-plane view of the interface, i.e. rotated by 90° with respect to a). Here, the view directions are truly perpendicular to **Φ** without a laminographic tilt θ, which is only possible via a reconstructed 3D image.

14.3 SILICON CARBIDE

XDL in its conventional application reaches its limits, when investigating structures that change there appearance radically with varying Bragg deviation $\Delta\theta$. This is illustrated at the example of a micropipe

in 4H-SiC. A micropipe refers to a screw dislocation with a large BV, this results in more strain and further special effects. In Fig. 14.5 each frame was recorded at a different laminographic tilt angle θ, i.e., with different weak-beam conditions. Due to the excitation of differently strained crystal volumes the mircopice appears as an almost straight, thin pipe in some images, but changes to a more complex structure when θ approaches the Bragg angle. In this feasibility study only 50 rocking scans in one acquisition interval were recorded, while projection acquisition was neglected completely. Materials with structures that show such a more complicated behavior (at least in comparison to Si, GaAs, and AlN) require more complicated approaches, like e.g. VWB computations, an approach that is currently under development. Other examples are CdTe, which often shows dislocation densities so high that certain regions of the FoV are tilted with respect to each other. This results in inhomogeneous contrast properties, making the direct acquisition of *quasi* projections for a 3D reconstruction unfeasible.

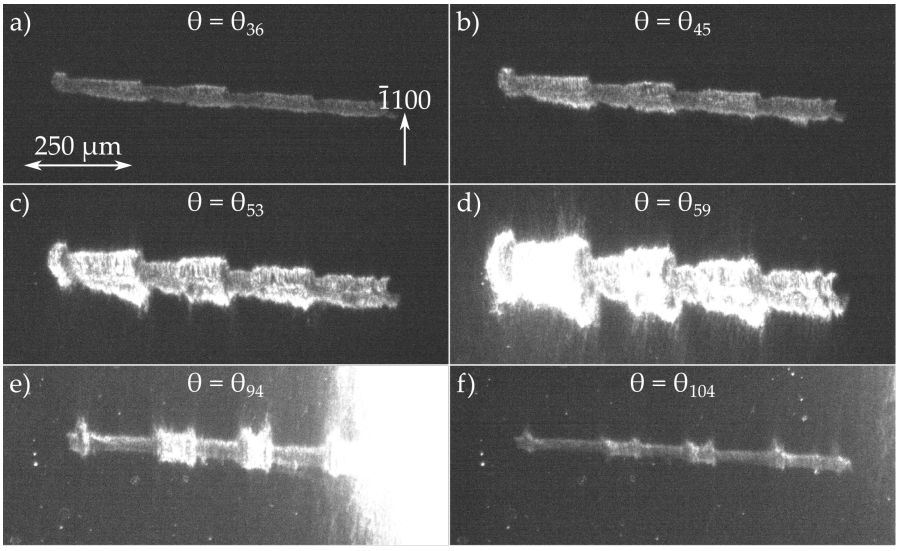

Figure 14.5: Micropipe in 4H-SiC. Frames a) to f) show how the appearance of the structure is highly depending on the selected Bragg deviation $\Delta\theta$.

The angles corresponding to the frames shown in Fig. 14.5 are given in Fig. 14.6 which also illustrates the sampling of a rocking curve from one view direction.
A more detailed discussion of 4H-SiC and the here presented date can be found in [133].

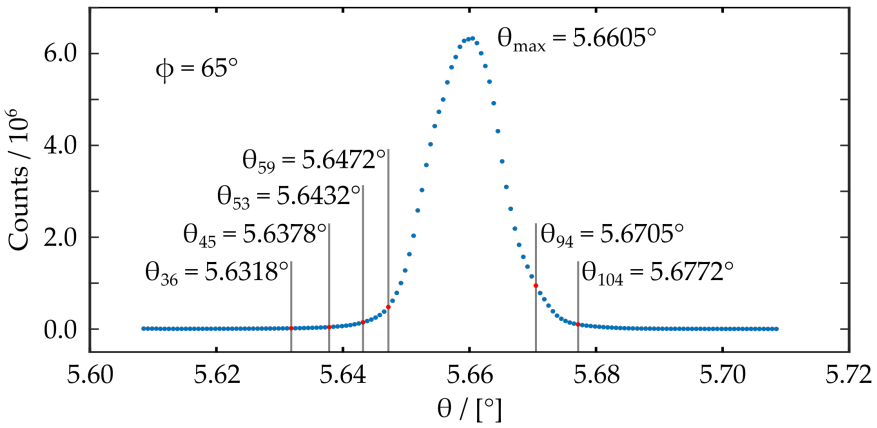

Figure 14.6: Plot of the rocking scan corresponding to the images in Fig. 14.5. The θ-positions corresponding to the frames in Fig. 14.5 are highlighted as well as the angular position of the Bragg peak $\theta_{\max} = \theta_B$.

15

SUMMARY AND CONCLUSION

This work has quantitatively investigated the imaging properties of X-ray Diffraction Laminography (XDL), in particular regarding the three-dimensional (3D) characterization of dislocation structures. By providing a deeper understanding of the interplay of the image formation mechanism and the 3D image reconstruction the methodology was refined, resulting in improved data processing and analysis. This also enabled the derivation of requirements for a dedicated instrumentation, which was then specified, commissioned and characterized. Finally, the progress accomplished in this work enabled the quasi *in situ* imaging of dislocation arrangements and their dynamics in 3D.
The extended capabilities of XDL were demonstrated by enabling the studies of thermally driven slip band formation in damaged silicon wafers and the investigation of dislocation arrangements in other materials.

Building on the basis laid out by [49] and in particular using the theoretical framework describing the contrast formation derived there, the presented work quickly supported embracing Laue-transmission geometry (LTG) as the favorable measurement geometry for the 3D imaging of dislocation structures in wafers. Considerations based on simulations have shown that limited angle laminography, enforced by the sample geometry, can be taken advantage of. Applying the 2 *interval measurement scheme* proposed in Chapter 6 with separate 3D reconstruction of two projection ensembles does not only prevent smearing of dislocation line features in the resulting 3D image, it also builds the foundation for additional techniques to enhance data processing.
Additionally, the obtained insight into the influence of measurement parameters provided by simulations allowed deriving suitable specifications for a dedicated instrumentation. In the frame of this work a mobile and flexible sample manipulator system has been compiled and characterized. The instrument fulfills the high demands in translational and angular space, enables semi-automated sample alignment, reliable execution of measurement schemes, and, furthermore, easy installation at different beamlines. The demonstrated successful operation of the setup during several measurement campaigns is a key milestone towards routine applicability of XDL and opening new routes for its recognition as a powerful imaging approach for defect characterization.
By reviewing the performance of different reconstruction techniques,

considering the particular characteristics of diffraction contrast, and developing new approaches to incorporate *a priori* knowledge, the 3D reconstruction procedure could be optimized significantly. With the utilization of the Simultaneous Iterative Reconstruction Technique (SIRT) and Empty Volume Backprojection (EVBP) the number of projections required for a successful reconstruction could be reduced by one order of magnitude while maintaining a quality of the result, that enables the tracing of individual dislocation lines. In combination with the sample manipulator a significant speedup was achieved, reducing the overall measurement duration (i.e. the time span from sample mounting to scan completion) by about 80 to 90%. With these accomplishments this work successfully enabled the quasi *in situ* 3D imaging of emerging dislocation structures, which was demonstrated at the example of the onset of slip band formation in silicon wafers driven by external thermal forces. Studies in [131] utilized XDL to confirm the 3D dislocation model for zinc-blende structures and extract quantitative information from dislocation structures in GaAs, while a feasibility study at AlN was successfully conducted.

Further developments based on the theoretical analysis of contrast formation and its effects on the 3D reconstructions allowed significant enhancements of XDL's methodology. With the presented techniques for the determination of the position of the physical Center of Rotation (CoR) it is now possible to conclude on the Burgers vector (BV) signs of individual dislocations from a 3D reconstruction image. This 3D approach avoids the cumbersome analysis of two-dimensional (2D) projection data and is even applicable in regions where several dislocation lines are located in close vicinity to each other (on the µm-scale). Motivated by the studies of the BV influence on the acquired dislocation image in XDL projections and then transitioning to analyzing the resulting features in the reconstruction volume, dislocations can now be classified according to their BV directly by information accessible via XDL. These are important steps towards a more comprehensive characterization of dislocation structures beyond their geometrical 3D arrangement, without the need for complementary X-ray White Beam Topography (XWBT) measurements, which in combination with XDL are not quasi *in situ* compatible.

Finally, the Center of Mass (CoM) approach for estimating the position of the dislocation core, developed within the frame of this thesis, enhances the spatial resolution of the 3D image to a level where it is almost competing with the image resolution of detector systems usually employed for XDL data acquisition. Not only could the resolution be enhanced from 3 to 5 µm to about 1 to 2.5 µm, furthermore, the dependence of dislocation positions in the 3D image on their BV, line direction and measurement parameters can be substantially reduced, which enables comparison and reproducibility of results.

Based on the presented findings, in the following, a short summary of guidelines established and successfully applied within this work will be given:

2 INTERVAL MEASUREMENT SCHEME It is highly advisable to exploit both accessible angular ranges (or the full 360° if possible) to acquire projections and rocking scans. This enables the application of techniques developed in this work to classify individual dislocations according to their BV's orientation and determining the BV-signs.

NUMBER OF PROJECTIONS The number of projections required for a successful 3D reconstruction strongly depends on the complexity of the arrangement. In general, 10 to a 100 projections should be sufficient if SIRT is applied with support of EVBP.

NUMBER OF ROCKING SCANS A minimum of 5 rocking scans should be performed in each acquisition interval. This will enable a sufficiently precise determination of the CoR.

CENTER OF MASS APPROACH For the spatial resolution to be enhanced via the CoM-approach, both acquisition intervals should be sampled with a number of projections (and a corresponding number of rocking scans) sufficient to perform successful separate reconstructions.

In conclusion, this work accomplished key milestones and significant progress in making XDL available for routine application. Enabled by improved data processing and the realization of a dedicated setup, the extended capabilities regarding the quasi *in situ* 3D imaging of dislocations have been demonstrated and were successfully applied in studies regarding the slip band formation in silicon, even capturing dislocation-dislocation interaction in 3D [131]. In the frame of [131] XDL has also been utilized for investigating the 3D arrangement of dislocations in GaAs and the applicability to AlN has successfully been showcased in a feasibility study.

In the future, with next generation synchrotrons reducing exposure times below 1 second, measurement procedures could be further enhanced. Delays of several seconds due to *step-wise* positioning between image acquisitions, e.g. during rocking scans, could be omitted by performing *continuous* scans, enabling extensive Multi-Azimuth Rocking Curve Imaging (MARCI) to be combined with XDL without significantly increasing scanning durations. This could extend the capabilities towards imaging considerably higher dislocation densities in other materials. In addition, the additional speed-up due to shorter exposure times regarding conventional XDL will enable a higher reso-

lution of the dynamical processes of defects, providing an even more detailed depiction, e.g., of dislocation emergence and propagation in 3D, and thereby contribute to a deeper understanding of such defects. This will support the development of techniques to control and maybe even avoid defect formation during growth or technical processing steps.

Part IV

APPENDIX

A

STRAIN AND LOCAL BRAGG VARIATION

To estimate the influence of strain $\Delta d/d$ on the local Bragg variation, one may use the representation of the displacement field $\boldsymbol{u}(\boldsymbol{r})$ given by Eq. 3.5 in the dislocation coordinate system. First the strain tensor is computed as

$$\epsilon_{ij}(\boldsymbol{r}) = \frac{1}{2}\left(\frac{\partial u_i(\boldsymbol{r})}{\partial x_j} + \frac{\partial u_j(\boldsymbol{r})}{\partial x_i}\right) \quad \text{with} \quad i,j \in \{1,2,3\}\,. \tag{A.1}$$

Since the displacement field $\boldsymbol{u}(\boldsymbol{r})$ is not depending on the z-component of $\boldsymbol{r}$ the strain tensor reduces to five independent elements:

$$\epsilon = \begin{pmatrix} \epsilon_{11} & \epsilon_{12} & \epsilon_{13} \\ \epsilon_{21} & \epsilon_{22} & \epsilon_{23} \\ \epsilon_{31} & \epsilon_{32} & \epsilon_{33} \end{pmatrix} = \begin{pmatrix} \frac{\partial u_1}{\partial x_1} & \frac{1}{2}\left(\frac{\partial u_1}{\partial x_2} + \frac{\partial u_2}{\partial x_1}\right) & \frac{1}{2}\frac{\partial u_3}{\partial x_1} \\ \frac{1}{2}\left(\frac{\partial u_2}{\partial x_1} + \frac{\partial u_1}{\partial x_2}\right) & \frac{\partial u_2}{\partial x_2} & \frac{1}{2}\frac{\partial u_3}{\partial x_2} \\ \frac{1}{2}\frac{\partial u_3}{\partial x_1} & \frac{1}{2}\frac{\partial u_3}{\partial x_2} & 0 \end{pmatrix} \tag{A.2}$$

with the individual elements given by

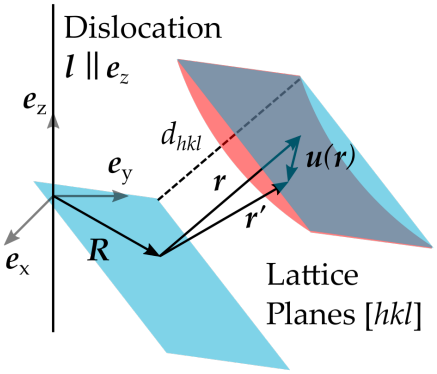

Figure A.1: Illustration of the displacement field in the vicinity of a dislocation distorting crystal lattice planes.

$$
\begin{aligned}
\epsilon_{11} &= \frac{b_e}{2\pi}\frac{x_2}{x_1^2+x_2^2}\left[\frac{x_2^2-x_1^2}{2(1-\nu)\left(x_1^2+x_2^2\right)}-1\right] \\
\epsilon_{12}=\epsilon_{21} &= \frac{b_e}{4\pi(1-\nu)}\frac{x_1}{\left(x_1^2+x_2^2\right)^2}\left[x_1^2-x_2^2\right] \\
\epsilon_{22} &= \frac{b_e}{4\pi}\frac{x_2}{\left(x_1^2+x_2^2\right)^2}\left[x_2^2-x_1^2\right] \\
\epsilon_{13}=\epsilon_{31} &= -\frac{b_s}{4\pi}\frac{x_2}{x_1^2+x_2^2} \\
\epsilon_{23}=\epsilon_{32} &= \frac{b_s}{4\pi}\frac{x_1}{x_1^2+x_2^2}.
\end{aligned} \tag{A.3}
$$

Since, the displacement field and its derivatives are independent of x_3, we now approximate the lattice tilts and the strain via

$$\omega_{x_1} = -\frac{\partial \boldsymbol{u}_3}{\partial x_1} = \epsilon_{31} \tag{A.4}$$

$$\omega_{x_2} = -\frac{\partial \boldsymbol{u}_3}{\partial x_2} = \epsilon_{32} \tag{A.5}$$

$$\frac{\Delta d}{d_{hkl}} = \hat{\boldsymbol{n}}_{hkl}^T \epsilon \hat{\boldsymbol{n}}_{hkl}, \tag{A.6}$$

where $\hat{\boldsymbol{n}}_{hkl}$ denotes the unit vector in the direction perpendicular to the lattice planes (hkl). To evaluate the strain tensor ϵ at position $\boldsymbol{R}$ we choose a representation in the dislocation coordinate system in cylindrical coordinates and due to the symmetry of the displacement field we select the z-component of $\boldsymbol{R}$ to be zero:

$$\boldsymbol{R} = \begin{pmatrix} x_1 \\ x_2 \\ 0 \end{pmatrix} = \begin{pmatrix} R\cos(\psi) \\ R\sin(\psi) \\ 0 \end{pmatrix} \tag{A.7}$$

To be able to directly compare the influence of tilt and strain we introduce the angular deviation resulting from the strain $\theta_{\Delta d/d}$ as

$$
\begin{aligned}
\theta_{\Delta d/d} &= \arcsin\left(\frac{\lambda}{2d_{hkl}}\right) - \arcsin\left(\frac{\lambda}{2d'}\right) \\
&= \arcsin\left(\frac{\lambda}{2d_{hkl}}\right) - \arcsin\left(\frac{\lambda}{2d_{hkl}(1-\Delta d/d)}\right)
\end{aligned}
$$

by using Bragg's Law in its most common form and the definition of $\Delta d/d = (d'-d)/d$.
Fig. A.2 shows the outcome for different dislocation parameters and different distances to the dislocation core R. We also see how the lattice tilt contribution vanishes for the cases of pure edge dislocations as it is expected. In the other cases, the lattice tilts clearly yield the dominating contribution except for some particular view directions ψ.

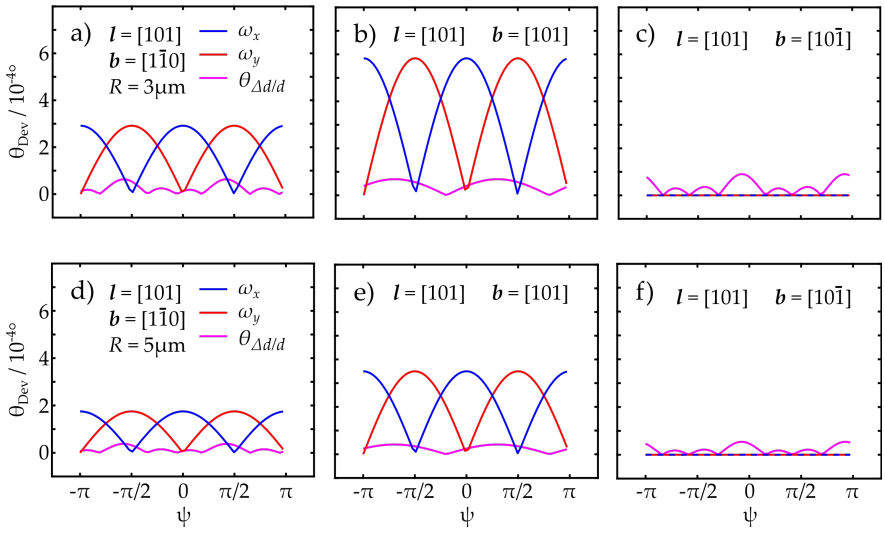

Figure A.2: a)-c) The local deviation of the Bragg angle θ_{Dev} is plotted over angle Ψ (see Chapter 5) for lattice tilts $\omega_{x,y}$ and strain $\Delta d/d$ in a distance of $R = 3$ µm to the dislocation core, for different line directions and BVs. d)-f) The same as above here distanced $R = 5$ µm from the dislocation core.

B

QUASI SYMMETRY

The easiest way to get an impression to which degree the quasi symmetry of the contrast formation regarding the view directions $\boldsymbol{k_h}(\Phi)$ and $\boldsymbol{k_h}(\Phi + 180°)$ is fulfilled, also see Eq. 5.49, we again investigate the binary maps of the local reflectivity R_δ. More precisely, we compare three sequences of maps for different view directions: i) a sequence of five binary maps calculated with a Bragg deviation of $\Delta\theta = 0.003°$; ii) a sequence of five binary maps from the same view directions but with $\Delta\theta = -0.003°$, which according to Eq. 5.47 is a true symmetry resulting from the assumptions used derive the theoretical framework, see Chapter 5; and iii) binary maps calculated again with $\Delta\theta = 0.003°$ but for tomographic angles $\Phi \to \Phi + 180°$, i.e., the *quasi opposing* view directions.

In Fig. B.1 every row of frames corresponds to one of the three cases i), ii), and iii). The tomographic rotation angle Φ is given in every frame, while the Bragg deviation for the whole row is only noted in the last frame. We see how Frames B.1g to k are direct transformations (rotation by 180° or point reflection with respect to the center) of the corresponding map in the first row. Analyzing Frames B.1l to p, especially in Frames B.1o and B.1p small deviations are visible. However, the general similarity between the second and third row is

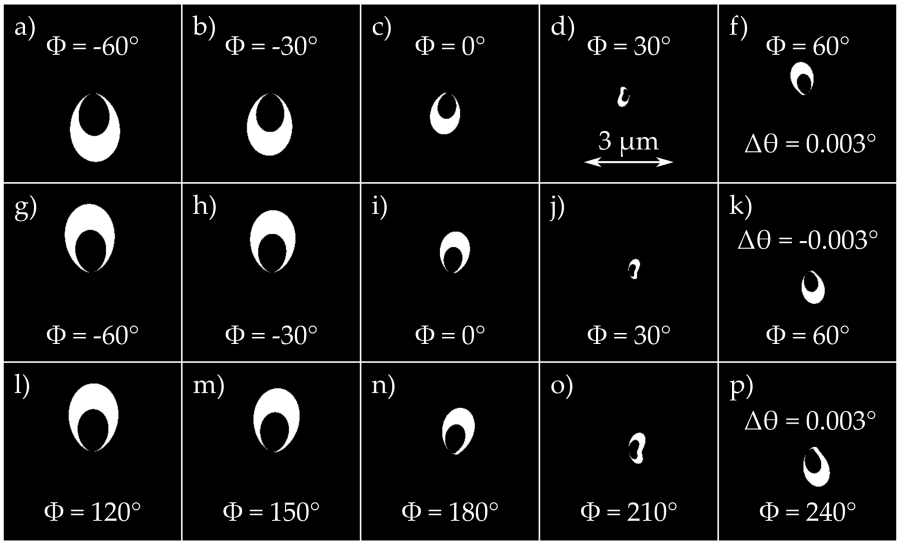

Figure B.1: Binary maps of the local reflectivity R_δ in order to compare the symmetry property with respect to $\boldsymbol{r} \to -\boldsymbol{r}$, $\boldsymbol{b} \to -\boldsymbol{b}$, or equivalently $\Delta\theta \to -\Delta\theta$, to the quasi symmetry regarding a rotation of 180° about $\boldsymbol{\Phi}$, which is only truly symmetric for $\theta = 0°$.

still striking and strongly suggests, that for typical laminographic tilt angles used during XDL measurements ($\theta < 10°$) the quasi symmetry property is valid to high degree.

C

X-RAY BEAM DIVERGENCE

Following [49] a way to calculate the specific parameters $\delta_{\text{min,max}}$, defining the angular excitation interval connected to the contrast formation, will be briefly described. This is especially of importance for the quantitative comparison of simulations and measurement data in Section 11.4.
Without going too much into detail, the important quantities for the calculation are as follows:

- σ - The size of the radiation source
- L - Source-to-sample distance
- θ_B^{mono} - Bragg angle of the crystal used for monochromatization of the X-ray beam
- w_D^{mono} - The Darwin width (FWHM) corresponding to θ_B^{mono}
- Δa - The distance to the beam center parallel to the diffraction plane
- θ_B - The Bragg angle of the sample
- w_D - The Darwin width (FWHM) corresponding to θ_B.

With this one may compute the effective weak-beam deviation as

$$\Delta\theta_{\text{eff}} = \Delta\theta + \Delta\left[\Delta\theta\right](\Delta a) \qquad \text{with:} \tag{C.1}$$

$$\Delta\left[\Delta\theta\right](\Delta a) \approx \left(1 - \frac{\tan\theta_B}{\tan\theta_B^{\text{mono}}}\right)\frac{\Delta a}{L}, \tag{C.2}$$

where $\Delta\left[\Delta\theta\right](\Delta a)$ describes a variation of the Bragg condition of the sample induced by the Double Crystal Monochromator (DCM). Note, that the calculation as here presented are only valid, if the orientation of the diffraction plane of the DCM is equal to the one of the sample.
The effective Darwin width of the sample w_D^{eff} is given by

$$w_D^{\text{eff}} = w_D + \Delta\alpha + \Delta\beta \qquad \text{with} \tag{C.3}$$

$$\Delta\alpha \approx \frac{\sigma}{L} \qquad \text{and} \tag{C.4}$$

$$\Delta\beta \approx \frac{\tan\theta_B}{\tan\theta_B^{\text{mono}}}\sqrt{2}w_D^{\text{mono}}, \tag{C.5}$$

where $\Delta\alpha$ denotes an estimate of the source divergence and $\Delta\beta$ describes an additional broadening of the sample's rocking curve again induced by the DCM. The term $\sqrt{2}w_D^{\text{mono}} = w_D^{\text{DCM}}$ here represents the Darwin width of the monochromator, i.e., the effective width of both crystals.
With this, it is now possible to estimate the important parameters

$$\delta_{\text{min}}(\Delta a) \approx \Delta\theta + \Delta\left[\Delta\theta\right](\Delta a) - \frac{w_D^{\text{eff}}}{2} \tag{C.6}$$

$$\delta_{\text{max}}(\Delta a) \approx \Delta\theta + \Delta\left[\Delta\theta\right](\Delta a) + \frac{w_D^{\text{eff}}}{2}. \tag{C.7}$$

For the properties of P23 at Deutsches Elektronen Synchrotron (DESY) Petra III, Hamburg, Germany, $\Delta\theta = 0.003^\circ$, and $\Delta a = 0.5$ mm, one finds the values $\delta_{\text{min}} = 0.0019^\circ$ and $\delta_{\text{max}} = 0.0037^\circ$. These correspond to the simulation parameters $\Delta\theta_{\text{sim}} = 0.0028^\circ$ and $\delta_{\text{sim}} = 0.0009^\circ$, which were used in the final comparison in Section 11.4. Strictly speaking, $\delta_{\text{min,max}}$ are of course linearly shifted with the distance of the center of the beam Δa parallel to the diffraction plane (i.e., vertically in all cases presented in this work). Whether an incorporation of this dependence into simulations is meaningful (most likely other assumptions and simplifications should be addressed first) is subject to further studies.

D

FEATURE-DISLOCATION LINE DISTANCE

Usually reconstruction volumes are handled in a slice-by-slice fashion to perform the line tracing segmentation. However, if the dislocation line is not parallel (and not perpendicular) to the rotation axis $\mathbf{\Phi}$ and thereby not perpendicular to the cross section of the volume, the distance between the reconstruction feature and a respective slice to the intersection of the slice with the invisible dislocation core might convey a distorted perception of the error or spatial resolution. Obviously, the shortest distance from the reconstruction feature to a dislocation line that is inclined with respect to the slice plane is not to be found in direction parallel to the slice but along a direction also inclined with respect to the cross section, see Fig. D.1.

The shortest distance between an infinitely long line and a point in 3D space is given by the well-known equation

$$d = \frac{|(\boldsymbol{x} - \boldsymbol{p}) \times \boldsymbol{l}|}{|\boldsymbol{l}|}, \tag{D.1}$$

where $\boldsymbol{x}$ is the position of the point, $\boldsymbol{p}$ is an arbitrary point on the line, and $\boldsymbol{l}$ defines the orientation of the line in space.
With this, we may now evaluate the position error in dependence on a misplacement of the CoR by Δx_{CoR} for the case of dislocation with e.g. line direction $\boldsymbol{l} = [10\bar{1}]$, as done for the case $\boldsymbol{l} = [110]$ in Section 10.1. We again set the BV to $\boldsymbol{b} = [110]$ in order to have an estimate for the *worst case* scenario, since this configuration yields the greatest expansion of the features into the crystal volume and away from the dislocation core.

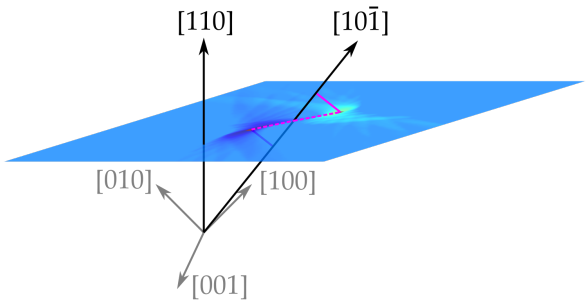

Figure D.1: Sketch of a volume slice perpendicular to the rotation axis $\mathbf{\Phi}$, here parallel to the crystal direction [110]. The dislocation line has the direction $\boldsymbol{l} = [10\bar{1}]$ and the shortest distance from reconstruction features in the respective reconstruction volumes V_{I_1} and V_{I_2} is highlighted in pink.

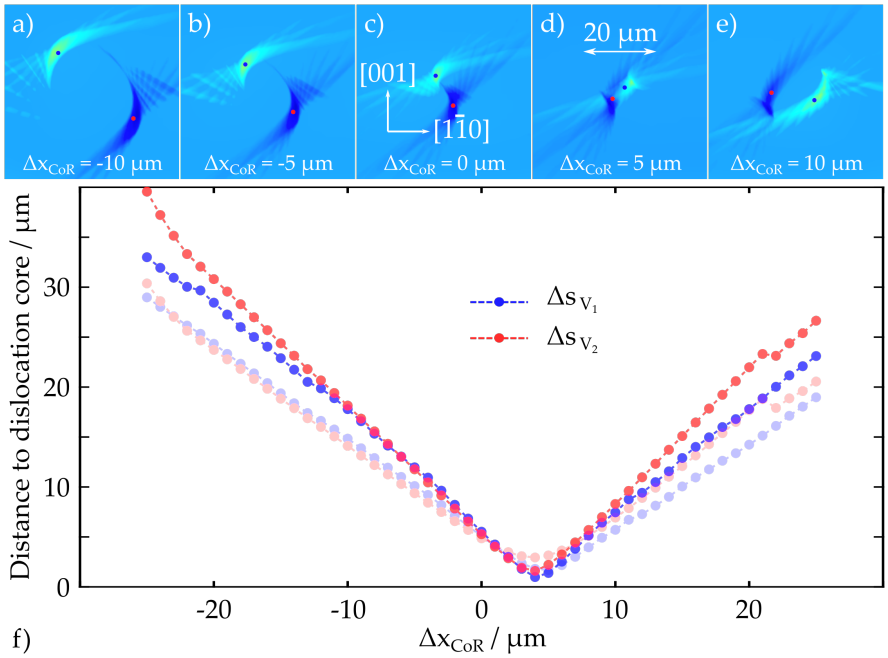

Figure D.2: Influence of a misplaced CoR on the distance between reconstruction features of a dislocation line to respective dislocation core. The line direction $\boldsymbol{l} = [10\bar{1}]$ and the BV was set to $\boldsymbol{b} = [110]$. For comparison, the transparent data points and lines correspond to the in-plane distance in the cross section.

E

SUPPLEMENT TO INSTRUMENTATION

SPECIFICATIONS

In the following, the most important specifications of the individual devices are summarized as provided by the manufacturers. The order will be from top to bottom.

SPACEFAB Q-MOTION 845 Regarding the parallel kinematics travel range in translational (x, y, z) and rotational space (ω_x, ω_y, ω_z) and the corresponding minimal step size are crucial for successful sample fine alignment (i.e. to achieve $\boldsymbol{h}_{hkl} \parallel \boldsymbol{\Phi}$). These are given in table E.1:

SpaceFab Q-Motion 845	x	y	z	ω_x	ω_y	ω_z
Range / [mm or °]	±7	±7	±5	±7	±7	±8
Min. Step / [nm or µrad]	6	6	20	0.9	0.9	0.9

Table E.1: Specifications of the SpaceFab Q-Motion 845

The weight of the device is 1.3 kg (2.6 kg with cables) and it has a load capacity of 10 or 5 N, depending on whether the base plate is orientated horizontally or arbitrarily, respectively.

RT150S The air-bearing rotary stage - representing $\boldsymbol{\Phi}$ - weighs 4.0 kg and has a maximum load capacity of 434 and 226 N. Important for maintaining suitable weak-beam conditions during data acquisition is especially the radial error of less than 100 nm measured on a spherical artifact 65 mm above the top plate of the axis.

1-CIRCLE SEGMENT 5202.10 The goniometer tilting the upper part of the sample manipulator towards the incoming X-ray beam to reach Bragg condition (i.e. rotation axis $\boldsymbol{\Theta}$) is a key device, where especially the angular resolution, i.e., the minimal step size, is important, since it is the motor responsible for rocking the sample in a step-wise manner during rocking scans. The minimal step size is indicated as $5 \times 10^{-5\circ}$ (which could not be realized) while the total travel range is $\pm 15.5^\circ$. The weight of the stage is 13 kg, while the load capacity is 1000 N.

HP 550 The optional base structure is here briefly summarized for the sake of completeness. The relevant degrees of freedom are the same as for the parallel kinematics:

HP550 (Base Structure)	x	y	z	ω_x	ω_y	ω_z
Range / [mm or °]	±50	±50	±50	±20	±20	±30
Min. Step / [µm or µrad]	0.5	0.5	0.5	10	10	10

Table E.2: Specifications of the HP 550

The weight of the device is 33 kg with a load capacity of 500 N assuming a horizontal orientation of the base plate.

In summary, the sample manipulator system weighs 19.6 kg (including cables of the parallel kinematics and excluding the optional base structure). In addition to the stability investigated in Chapter 7, Fig. 7.8 shows exemplary rocking scans and the corresponding step sizes, that were achieved in the final state of the instrument.

INTEGRATION INTO DIFFERENT BEAMLINE ENVIRONMENTS

The instrument has been integrated into several experimental environments at different beamlines within the last years, mainly at the European Synchrotron Radiation Facility (ESRF), Grenoble, France, and at DESY, Hamburg, Germany. Fig. E.1 shows photographs of the sample manipulator (in Fig. E.1d together with the optional base structure).

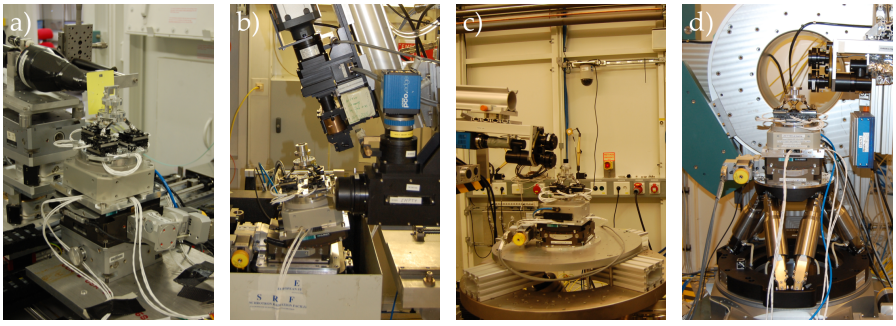

Figure E.1: Integration of the instrumentation at different beamlines: a) Mounted on a base structure provided by staff at ID15A, ESRF, Grenoble, France. b) Mounted on a medium resolution tomography table at ID19, ESRF, Grenoble, France. c) Mounted on a Hexapod (not the optional base structure) at P07, DESY, Hamburg, Germany. d) Sample Manipulator and HP550 mounted on the heavy-duty diffractometer at P23, DESY, Hamburg, Germany.

F

DART PERFORMANCE

In order to judge the Discrete Algebraic Reconstruction Technique (DART) performance correctly, here some additional results with different parameter settings are briefly discussed. As mentioned in Chapter 8 DART uses an Algebraic Reconstruction Method (ARM) as a sub-routine. This sub-routine can of course be selected according to the problem at hand, and consequently, for the XDL reconstruction problem SIRT was chosen for the same reasons that it is also investigated as an alternative of DART to begin with. This means, that with a reduction of DART iterations - i.e., the sequence of procedures illustrated in Fig. 8.1 - DART approaches SIRT.

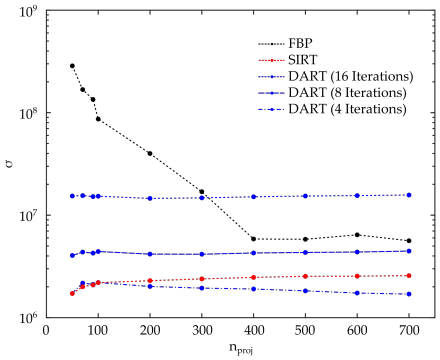

Figure F.1: Accumulated voxel error σ over number of projections used for the reconstruction n_{proj}. The data points for Filtered Backprojection (FBP), DART, and SIRT in black, blue, and red, respectively, are connected by dashed lines to show the overall-trend. Noise was added to the projection ensembles and intensity fluctuations were introduced according to Sections 6.3 and 8.3.2.

As can be seen in Fig. F.1 this is also verified by repeating the reconstruction tests on an artificial complex structure in a sparse volume with intensity fluctuations introduced to the line contrast in projections from different view angles ϕ. However, the investigations also show, that for only 4 DART iterations, the DART result shows fewer voxel errors σ than SIRT. Especially, if more than 200 projections are available as input. One needs to acknowledge, that even if inconsistencies are present in the input data, DART can be configured to yield better results. On the other hand, intensity fluctuations only present one of the two *specific characteristics* of XDL projection data, see Section 8.1. To continue adapting DART further to also the other specific property, the *contrast shift*, i.e., the varying localization of line contrast in the topographic projection images, DART could become

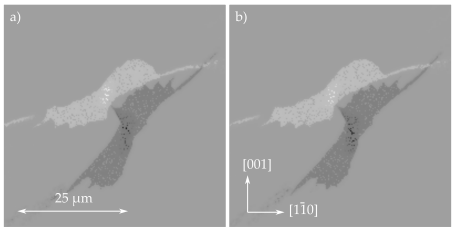

Figure F.2: Exemplary slices (perpendicular to the rotation axis) of reconstructions of simulated projections (see Chapters 5 and 6 of a dislocation with line direction $\boldsymbol{l} = [10\bar{1}]$ and Burgers vector $\boldsymbol{b} = a/2[110]$ utilizing the $\overline{2}20$-reflex at an energy of 25 keV. a) DART reconstruction allowing two gray levels $\{0.0, 1.0\}$. b) DART reconstruction allowing five gray levels $\{0.0, 0.25, 0.50, 0.75, 1.00\}$.

more efficient by introducing more than two gray values. This could allow the algorithm to handle the non-localized dislocation contrast in a more tolerant way, resulting in a slight blurring with maximum values in the reconstruction image indicating the most probable or an averaged position of the feature to be captured.

Allowing up to five gray values, i.e. $\{0.0, 0.25, 0.50, 0.75, 1.00\}$, should show improvements if this assumption is valid. However, in Fig. F.2 the reconstructions, one allowing only 2 values, F.2a, the other allowing 5, F.2b, of a single simulated dislocation line with both specific XDL characteristics are shown in comparison.
Concluding, changing the number of gray values has only a minor effect on the result, which means reducing the number of iterations is the most effective way to improve performance of DART, if inconsistencies are introduced to the input data. Since this effectively leads to DART becoming more and more similar to a regular SIRT approach, the extensive computational efforts and the time-consuming parameter calibration are not justified.

G

CENTER OF MASS: ADDITIONAL STUDIES

Here, a question from Section 11.1.2 is briefly addressed: A dislocation line with distances in the 100s of µm with respect to the CoR is reconstructed for several displacements Δs_{CoR} of the rotation axis. Furthermore, the influence of the weak-beam parameter settings $\Delta\theta$ on the deviation Δs_{CoM} between the computed mean position $\boldsymbol{r}_{\mathrm{CoM}}$ and the exact position of the dislocation core is shown.

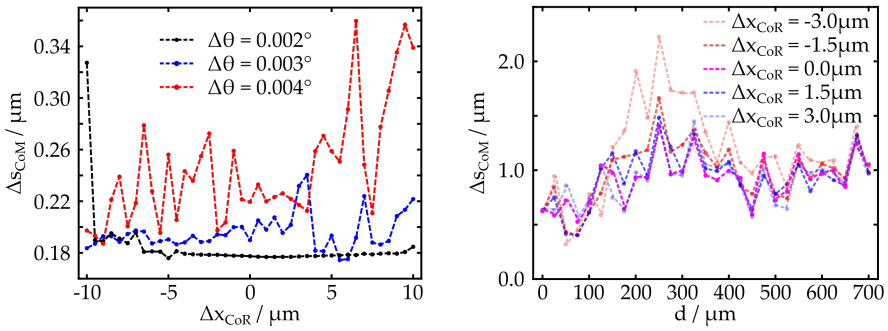

Figure G.1: a) Plot of the distance between CoM position $\boldsymbol{r}_{\mathrm{CoM}}$ and dislocation core for reconstructions of simulated projections for a dislocation with $\boldsymbol{l} = [110]$ and $\boldsymbol{b} = a/2[110]$ for different settings of the CoR. Different Bragg deviations $\Delta\theta$ are colour-coded. The pixel size in the simulation was set to 0.25 µm. b) The dislocation (with $\boldsymbol{l} = [110]$ and $\boldsymbol{b} = a/2[110]$) is shifted from the center of the volume by d. The distance from the CoM position $\boldsymbol{r}_{CoM}$ to the dislocation core is plotted over d. Here, due to the large values in d, the pixel size in the simulation was increased to 0.5 µm.

Frame G.1a shows that small deviations from the Bragg peak are favorable to improve the precision of the result for the case of dislocation with $\boldsymbol{l} = [110]$ and $\boldsymbol{b} = a/2[110]$. However, the deviations obtained for different values of $\Delta\theta$ are in the magnitude of the effective pixel size and, therefore, below the spatial resolution of the detector. Consequently, the selection of $\Delta\theta$ should not be influenced by this outcome, but rather rely on other factors, like overall image quality.
Frame G.1b shows the deviation Δs_{CoM} for a dislocation with the same line direction and BV as in Frame G.1a. Here, the dislocation line is re-located in a distance d to the CoR plotted on the x-axis. It is shown, that for small displacements of the rotation axis Δx_{CoR} there is no significant effect of the distance d to the physical CoR. Thus, the rotation axis may intentionally be displaced by a few µm in order to help with the visualization and segmentation of a given dislocation line.

H

SAMPLE AND MEASUREMENT DESCRIPTION

The sample A100_400_3 was cut from a 20 cm diameter double side polished silicon wafer (grown by the Czochralski method) with a [001] surface normal and a thickness of approximately 710 to 720 µm, see Fig. H.1. The sample was indented with a Berkovich tip 100 times arranged in an array, each indent with a Load of 400 mN. Afterwards, the sample was utilized for the commissioning of an induction heater, but dislocations were only generated at the upper left indent marked in red.

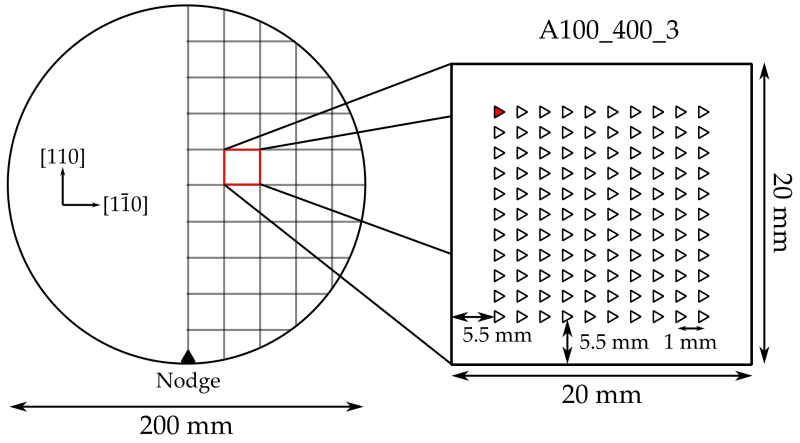

Figure H.1: Schematic Drawing of original wafer and sample A100_400_3. Dislocations extending significantly into the wafer were only created at the upper left indent marked in red.

During mounting, in order to position the Region of Interest (ROI) in the Pivot point (see Chapter 7), the sample had to be turned upside down, which resulted in the utilization of the $\overline{2}\overline{2}0$-reflex instead of 220. Since also the sample Cr_7 was measured in $\overline{2}\overline{2}0$ and these two samples are the most important for the here presented work, the simulations were also carried out for this specific reflex for the sake of unity.

In the following, the most important parameters of the measurements performed on samples A100_400_3 and Cr_7 will be summarized.

	A100_400_3	Cr_7
Geometry	LTG	LTG
Reflex *hkl*	$\overline{2}\overline{2}0$	$\overline{2}\overline{2}0$
Energy	25 keV	40 keV
Bragg angle θ_B	7.564°	4.67°
Weak-beam deviation $\Delta\theta$	0.003°	0.002°
Angular range	$2 \times 130°$	$2 \times 130°$
Number of projections	2×14	2×700
Exposure time	20 s	8 s
Number of rocking scans	2×14	2×35
Steps per rocking scans	24	33
Exposure time	3 s	1 s
δ_{min}	0.0019°	0.0019°
δ_{max}	0.0037°	0.0029°
Sample-detector distance D	$\approx$ 4.5 cm	$\approx$ 6 cm
Scintillator	8 µm LSO	13 µm GGG
Effective pixel size	0.36 µm	0.75 µm

Table H.1: Measurement parameters for: Scanning of A100_400_3 conducted at P23, DESY - PETRA III, Hamburg, Germany; and scanning of Cr_7 conducted at ID19, ESRF, Grenoble, France.

BIBLIOGRAPHY

[1] Roberto Fornari. *Single Crystals of Electronic Materials: Growth and Properties*. Woodhead Publishing, 2018.

[2] D Hänschke, L Helfen, V Altapova, A Danilewsky, and T Baumbach. "Three-dimensional imaging of dislocations by X-ray diffraction laminography." In: *Applied Physics Letters* 101.24 (2012), p. 244103.

[3] Klaus Schuegraf, Mathew C Abraham, Adam Brand, Mehul Naik, and Randhir Thakur. "Semiconductor logic technology innovation to achieve sub-10 nm manufacturing." In: *IEEE Journal of the Electron Devices Society* 1.3 (2013), pp. 66–75.

[4] BK Tanner, J Wittge, D Allen, MC Fossati, AN Danilwesky, P McNally, J Garagorri, MR Elizalde, and D Jacques. "Thermal slip sources at the extremity and bevel edge of silicon wafers." In: *Journal of Applied Crystallography* 44.3 (2011), pp. 489–494.

[5] JM Yi, YS Chu, TS Argunova, JZ Domagala, and JH Je. "X-ray diffractometry and topography of lattice plane curvature in thermally deformed Si wafer." In: *Journal of synchrotron radiation* 15.1 (2008), pp. 96–99.

[6] P Rudolph. "Dislocation cell structures in melt-grown semiconductor compound crystals." In: *Crystal Research and Technology: Journal of Experimental and Industrial Crystallography* 40.1-2 (2005), pp. 7–20.

[7] Michael Fiederle, Simon Procz, Elias Hamann, Alex Fauler, and Christer Fröjdh. "Overview of GaAs und CdTe pixel detectors using Medipix electronics." In: *Crystal Research and Technology* 55.9 (2020), p. 2000021.

[8] Elias Hamann, Thomas Koenig, Marcus Zuber, Angelica Cecilia, Anton Tyazhev, Oleg Tolbanov, Simon Procz, Alex Fauler, Tilo Baumbach, and Michael Fiederle. "Performance of a Medipix3RX spectroscopic pixel detector with a high resistivity gallium arsenide sensor." In: *IEEE transactions on medical imaging* 34.3 (2014), pp. 707–715.

[9] Elias Hamann, T Koenig, M Zuber, A Cecilia, A Tyazhev, O Tolbanov, S Procz, A Fauler, M Fiederle, and T Baumbach. "Investigation of GaAs: Cr Timepix assemblies under high flux irradiation." In: *Journal of Instrumentation* 10.01 (2015), p. C01047.

[10] Thomas Koenig, Julia Schulze, Marcus Zuber, Kristian Rink, Jochen Butzer, Elias Hamann, Angelica Cecilia, Andreas Zwerger, Alex Fauler, Michael Fiederle, et al. "Imaging properties of small-pixel spectroscopic x-ray detectors based on cadmium telluride sensors." In: *Physics in Medicine & Biology* 57.21 (2012), p. 6743.

[11] Marcus Zuber, Elias Hamann, Rafael Ballabriga, Michael Campbell, Michael Fiederle, Tilo Baumbach, and Thomas Koenig. "An investigation into the temporal stability of CdTe-based photon counting detectors during spectral micro-CT acquisitions." In: *Biomedical Physics & Engineering Express* 1.2 (2015), p. 025205.

[12] Rafael Dalmau, Jeffrey Britt, Baxter Moody, and Raoul Schlesser. "X-Ray Metrology of AlN Single Crystal Substrates." In: *ECS Transactions* 92.7 (2019), p. 113.

[13] Carsten Hartmann, Martin Albrecht, Jürgen Wollweber, Josephine Schuppang, Uta Juda, Christo Guguschev, Sebastian Golka, Andrea Dittmar, and Roberto Fornari. "SiC seed polarity-dependent bulk AlN growth under the influence of residual oxygen." In: *Journal of crystal growth* 344.1 (2012), pp. 19–26.

[14] Johannes Steiner, Melissa Roder, Binh Duong Nguyen, Stefan Sandfeld, Andreas Danilewsky, and Peter J Wellmann. "Analysis of the basal plane dislocation density and thermomechanical stress during 100 mm PVT growth of 4H-SiC." In: *Materials* 12.13 (2019), p. 2207.

[15] Peter Wellmann, Georg Neubauer, Lars Fahlbusch, Michael Salamon, and Norman Uhlmann. "Growth of SiC bulk crystals for application in power electronic devices–process design, 2D and 3D X-ray in situ visualization and advanced doping." In: *Crystal Research and Technology* 50.1 (2015), pp. 2–9.

[16] Peter J Wellmann. "Review of SiC crystal growth technology." In: *Semiconductor Science and Technology* 33.10 (2018), p. 103001.

[17] VG Kohn, TS Argunova, and Jung Ho Je. "Study of micropipe structure in SiC by x-ray phase contrast imaging." In: *Applied Physics Letters* 91.17 (2007), p. 171901.

[18] James Woodham Menter. "The direct study by electron microscopy of crystal lattices and their imperfections." In: *Proceedings of the Royal Society of London. Series A. Mathematical and Physical Sciences* 236.1204 (1956), pp. 119–135.

[19] PB Hirsch, RW Horne, and MJ Whelan. "LXVIII. Direct observations of the arrangement and motion of dislocations in aluminium." In: *Philosophical Magazine* 1.7 (1956), pp. 677–684.

[20] DJH Cockayne, ILF Ray, and MJ Whelan. "Investigations of dislocation strain fields using weak beams." In: *Philosophical Magazine* 20.168 (1969), pp. 1265–1270.

[21] Bengt Modéer. "Dislocation link length distributions studied by stereo electron microscopy." In: *Scripta Metallurgica* 8.10 (1974), pp. 1145–1152.

[22] GC Hua, N Otsuka, DC Grillo, Y Fan, J Han, MD Ringle, RL Gunshor, M Hovinen, and AV Nurmikko. "Microstructure study of a degraded pseudomorphic separate confinement heterostructure blue-green laser diode." In: *Applied physics letters* 65.11 (1994), pp. 1331–1333.

[23] P Hirsch, D Cockayne, John Spence, and M Whelan. "50 Years of TEM of dislocations: Past, present and future." In: *Philosophical Magazine* 86.29-31 (2006), pp. 4519–4528.

[24] JS Barnard, J Sharp, JR Tong, and PA Midgley. "High-resolution three-dimensional imaging of dislocations." In: *Science* 313.5785 (2006), pp. 319–319.

[25] Stephen J Pennycook and Peter D Nellist. *Scanning transmission electron microscopy: imaging and analysis*. Springer Science & Business Media, 2011.

[26] Chien-Chun Chen, Chun Zhu, Edward R White, Chin-Yi Chiu, MC Scott, BC Regan, Laurence D Marks, Yu Huang, and Jianwei Miao. "Three-dimensional imaging of dislocations in a nanoparticle at atomic resolution." In: *Nature* 496.7443 (2013), pp. 74–77.

[27] Chunyang Wang, Huichao Duan, Chunjin Chen, Peng Wu, Dongqing Qi, Hengqiang Ye, Hai-Jun Jin, Huolin L Xin, and Kui Du. "Three-Dimensional Atomic Structure of Grain Boundaries Resolved by Atomic-Resolution Electron Tomography." In: *Matter* (2020).

[28] Donghun Choi, Yangsi Ge, James S Harris, Joel Cagnon, and Susanne Stemmer. "Low surface roughness and threading dislocation density Ge growth on Si (0 0 1)." In: *Journal of Crystal Growth* 310.18 (2008), pp. 4273–4279.

[29] H Saka and G Nagaya. "Plan-view transmission electron microscopy observation of a crack tip in silicon." In: *Philosophical magazine letters* 72.4 (1995), pp. 251–255.

[30] David P Basile, Ron Boylan, Brian Baker, Kathy Hayes, and David Soza. "Fibxtem—Focussed ion beam milling for TEM sample preparation." In: *MRS Online Proceedings Library Archive* 254 (1991).

[31] Wolfgang Berg. "Über eine röntgenographische methode zur untersuchung von gitterstörungen an kristallen." In: *Naturwissenschaften* 19.19 (1931), pp. 391–396.

[32] AR Lang. "A method for the examination of crystal sections using penetrating characteristic X radiation." In: *Acta metallurgica* 5.7 (1957), pp. 358–364.

[33] AR Lang. "Studies of Individual Dislocations in Crystals by X-Ray Diffraction Microradiography." In: *Journal of Applied Physics* 30.11 (1959), pp. 1748–1755.

[34] T Tuomi, K Naukkarinen, and P Rabe. "Use of synchrotron radiation in X-ray diffraction topography." In: *physica status solidi (a)* 25.1 (1974), pp. 93–106.

[35] David Keith Bowen and Brian K Tanner. *High resolution X-ray diffractometry and topography*. CRC press, 1998.

[36] D Keith Bowen and Brian K Tanner. *X-ray metrology in semiconductor manufacturing*. CRC Press, 2018.

[37] S Kawado, S Iida, S Yamaguchi, S Kimura, Y Hirose, K Kajiwara, Y Chikaura, and M Umeno. "Synchrotron-radiation X-ray topography of surface strain in large-diameter silicon wafers." In: *Journal of synchrotron radiation* 9.3 (2002), pp. 166–168.

[38] D Lübbert, T Baumbach, J Härtwig, E Boller, and E Pernot. "μm-resolved high resolution X-ray diffraction imaging for semiconductor quality control." In: *Nuclear Instruments and Methods in Physics Research Section B: Beam Interactions with Materials and Atoms* 160.4 (2000), pp. 521–527.

[39] Daniel Lübbert. "Strain and lattice distortion in semiconductor structures: a synchrotron radiation study." In: *Ph. D. Thesis* (2000).

[40] Daniel Lübbert, Claudio Ferrari, Petr Mikulík, Petra Pernot, Lukas Helfen, Nicola Verdi, Dusan Korytár, and Tilo Baumbach. "Distribution and Burgers vectors of dislocations in semiconductor wafers investigated by rocking-curve imaging." In: *Journal of applied crystallography* 38.1 (2005), pp. 91–96.

[41] P Mikulik, D Lübbert, P Pernot, L Helfen, and T Baumbach. "Crystallite misorientation analysis in semiconductor wafers and ELO samples by rocking curve imaging." In: *Applied surface science* 253.1 (2006), pp. 188–193.

[42] JEA Miltat and DK Bowen. "On the widths of Dislocation images in X-ray Topography under Low-Absorption Conditions." In: *Journal of Applied Crystallography* 8.6 (1975), pp. 657–669.

[43] Hugh Simons, Anders Clemen Jakobsen, Sonja Rosenlund Ahl, Carsten Detlefs, and Henning Friis Poulsen. "Multiscale 3D characterization with dark-field x-ray microscopy." In: *Mrs Bulletin* 41.6 (2016), pp. 454–459.

[44] AC Jakobsen, H Simons, W Ludwig, C Yildirim, H Leemreize, L Porz, C Detlefs, and HF Poulsen. "Mapping of individual dislocations with dark-field X-ray microscopy." In: *Journal of Applied Crystallography* 52.1 (2019), pp. 122–132.

[45] AR Lang. "Direct observation of individual dislocations by X-ray diffraction." In: *Journal of Applied Physics* 29.3 (1958), pp. 597–598.

[46] David Allen, Jochen Wittge, Jennifer Stopford, Andreas Danilewsky, and Patrick McNally. "Three-dimensional X-ray diffraction imaging of process-induced dislocation loops in silicon." In: *Journal of Applied Crystallography* 44.3 (2011), pp. 526–531.

[47] W Ludwig, P Cloetens, J Härtwig, J Baruchel, B Hamelin, and P Bastie. "Three-dimensional imaging of crystal defects by topo-tomography'." In: *Journal of applied crystallography* 34.5 (2001), pp. 602–607.

[48] D Hänschke, A Danilewsky, L Helfen, E Hamann, and T Baumbach. "Correlated three-dimensional imaging of dislocations: Insights into the onset of thermal slip in semiconductor wafers." In: *Physical review letters* 119.21 (2017), p. 215504.

[49] D Hänschke. "Development and Correlative Application of X-ray Diffraction Laminpgraphy." PhD thesis. Karlsruhe Institute of Technology, 2015.

[50] Allan Macleod Cormack. "Representation of a function by its line integrals, with some radiological applications." In: *Journal of applied physics* 34.9 (1963), pp. 2722–2727.

[51] Allan Macleod Cormack. "Representation of a function by its line integrals, with some radiological applications. II." In: *Journal of Applied Physics* 35.10 (1964), pp. 2908–2913.

[52] GN Hounsfield. "A method and apparatus for examination of a body by radiation such as X-ray or gamma radiation. 1283915." In: (1972).

[53] SR Stock. "Recent advances in X-ray microtomography applied to materials." In: *International Materials Reviews* 53.3 (2008), pp. 129–181.

[54] Jens Als-Nielsen and Des McMorrow. *Elements of modern X-ray physics*. John Wiley & Sons, 2011.

[55] Johann Radon. "On the determination of functions from their integral values along certain manifolds." In: *IEEE transactions on medical imaging* 5.4 (1986), pp. 170–176.

[56] Avinash C Kak, Malcolm Slaney, and Ge Wang. *Principles of computerized tomographic imaging*. 2002.

[57] S Karczmarz. "Angenäherte Auflösung von Systemen linearer Gleichungen." In: *Bull. Int. Acad. Pol. Sic. Let., Cl. Sci. Math. Nat.* (1937), pp. 355–357.

[58] RS Ramakrishnam, SK Mullick, RKS Rathore, and R Subramanian. "Orthogonalization, Bernstein polynomials, and image restoration." In: *Applied optics* 18.4 (1979), pp. 464–468.

[59] WJ Palenstijn, KJ Batenburg, and J Sijbers. "Performance improvements for iterative electron tomography reconstruction using graphics processing units (GPUs)." In: *Journal of structural biology* 176.2 (2011), pp. 250–253.

[60] Daniel Castaño Diez, Hannes Mueller, and Achilleas S Frangakis. "Implementation and performance evaluation of reconstruction algorithms on graphics processors." In: *Journal of Structural Biology* 157.1 (2007), pp. 288–295.

[61] L Helfen, A Myagotin, Petr Mikulík, P Pernot, A Voropaev, M Elyyan, M Di Michiel, J Baruchel, and T Baumbach. "On the implementation of computed laminography using synchrotron radiation." In: *Review of Scientific Instruments* 82.6 (2011), p. 063702.

[62] L Helfen, T Baumbach, Petr Mikulík, D Kiel, P Pernot, P Cloetens, and J Baruchel. "High-resolution three-dimensional imaging of flat objects by synchrotron-radiation computed laminography." In: *Applied Physics Letters* 86.7 (2005), p. 071915.

[63] Anton Myagotin, Alexey Voropaev, Lukas Helfen, Daniel Hänschke, and Tilo Baumbach. "Efficient volume reconstruction for parallel-beam computed laminography by filtered backprojection on multi-core clusters." In: *IEEE Transactions on Image Processing* 22.12 (2013), pp. 5348–5361.

[64] L Helfen, F Xu, H Suhonen, L Urbanelli, P Cloetens, and T Baumbach. "Nano-laminography for three-dimensional high-resolution imaging of flat specimens." In: *Journal of Instrumentation* 8.05 (2013), p. C05006.

[65] Feng Xu, Lukas Helfen, Heikki Suhonen, Dan Elgrabli, Sam Bayat, Péter Reischig, Tilo Baumbach, and Peter Cloetens. "Correlative nanoscale 3D imaging of structure and composition in extended objects." In: *PLoS One* 7.11 (2012), e50124.

[66] Pengfei Yan, Jianming Zheng, Meng Gu, Jie Xiao, Ji-Guang Zhang, and Chong-Min Wang. "Intragranular cracking as a critical barrier for high-voltage usage of layer-structured cathode for lithium-ion batteries." In: *Nature communications* 8.1 (2017), pp. 1–9.

[67] FRN Nabarro. "Report of a Conference on the Strength of Solids." In: *The Physical Society, London* 75 (1948).

[68] AH Cottrell. "LX. The formation of immobile dislocations during slip." In: *The London, Edinburgh, and Dublin Philosophical Magazine and Journal of Science* 43.341 (1952), pp. 645–647.

[69] Derek Hull and David J Bacon. *Introduction to dislocations*. Vol. 37. Elsevier, 2011.

[70] Peter M Anderson, John P Hirth, and Jens Lothe. *Theory of dislocations*. Cambridge University Press, 2017.

[71] FC Frank. "LXXXIII. Crystal dislocations.—elementary concepts and definitions." In: *The London, Edinburgh, and Dublin Philosophical Magazine and Journal of Science* 42.331 (1951), pp. 809–819.

[72] Bruce Alexander Bilby, R Bullough, and Edwin Smith. "Continuous distributions of dislocations: a new application of the methods of non-Riemannian geometry." In: *Proceedings of the Royal Society of London. Series A. Mathematical and Physical Sciences* 231.1185 (1955), pp. 263–273.

[73] U Messerschmidt and M Bartsch. "Generation of dislocations during plastic deformation." In: *Materials chemistry and physics* 81.2-3 (2003), pp. 518–523.

[74] Max Born and Emil Wolf. *Principles of optics: electromagnetic theory of propagation, interference and diffraction of light*. Elsevier, 2013.

[75] André Authier. "Dynamical theory of X-ray diffraction." In: *International Tables for Crystallography* (2006), pp. 626–646.

[76] Ullrich Pietsch, Vaclav Holy, and Tilo Baumbach. *High-resolution X-ray scattering: from thin films to lateral nanostructures*. Springer Science & Business Media, 2004.

[77] Jürgen Härtwig. "Hierarchy of dynamical theories of x-ray diffraction for deformed and perfect crystals." In: *Journal of Physics D: Applied Physics* 34.10A (2001), A70.

[78] Satio Takagi. "Dynamical theory of diffraction applicable to crystals with any kind of small distortion." In: *Acta Crystallographica* 15.12 (1962), pp. 1311–1312.

[79] Heinrich Schlangenotto. "Dynamische Theorie der Röntgenbeugung für deformierte Kristalle." In: *Zeitschrift für Physik* 203.1 (1967), pp. 17–36.

[80] Satio Takagi. "A dynamical theory of diffraction for a distorted crystal." In: *Journal of the Physical Society of Japan* 26.5 (1969), pp. 1239–1253.

[81] Yves Epelboin. "Simulation of X-ray topographs." In: *Materials science and engineering* 73 (1985), pp. 1–43.

[82] CAM Carvalho and Y Epelboin. "Simulation of X-ray topographs: a new method to calculate the diffracted field." In: *Acta Crystallographica Section A: Foundations of Crystallography* 49.3 (1993), pp. 460–467.

[83] XR Huang, M Dudley, WM Vetter, W Huang, S Wang, and CH Carter Jr. "Direct evidence of micropipe-related pure superscrew dislocations in SiC." In: *Applied physics letters* 74.3 (1999), pp. 353–355.

[84] Yi Chen and Michael Dudley. "Direct determination of dislocation sense of closed-core threading screw dislocations using synchrotron white beam x-ray topography in 4 H silicon carbide." In: *Applied Physics Letters* 91.14 (2007), p. 141918.

[85] Balaji Raghothamachar, Yafei Liu, Hongyu Peng, Tuerxun Ailihumaer, Michael Dudley, F Shadi Shahedipour-Sandvik, Kenneth A Jones, Andrew Armstrong, Andrew A Allerman, Jung Han, et al. "X-ray topography characterization of gallium nitride substrates for power device development." In: *Journal of Crystal Growth* 544 (2020), p. 125709.

[86] A Authier, F Balibar, and Y Epelboin. "Theoretical and Experimental Study of Interbranch Scattering Observed near a Dislocation Line in X-Ray Topography." In: *physica status solidi (b)* 41.1 (1970), pp. 225–238.

[87] A Authier. *Advances in X-ray Analysis*. 1967.

[88] Lukas Helfen, Anton Myagotin, Alexander Rack, Petra Pernot, Petr Mikulík, Marco Di Michiel, and Tilo Baumbach. "Synchrotron-radiation computed laminography for high-resolution three-dimensional imaging of flat devices." In: *physica status solidi (a)* 204.8 (2007), pp. 2760–2765.

[89] Lukas Helfen, Thilo F Morgeneyer, Feng Xu, Mark N Mavrogordato, Ian Sinclair, Burkhard Schillinger, and Tilo Baumbach. "Synchrotron and neutron laminography for three-dimensional imaging of devices and flat material specimens." In: *International journal of materials research* 103.2 (2012), pp. 170–173.

[90] Pieter Verboven, Els Herremans, Lukas Helfen, Quang T Ho, Metadel Abera, Tilo Baumbach, Martine Wevers, and Bart M Nicolaï. "Synchrotron X-ray computed laminography of the three-dimensional anatomy of tomato leaves." In: *The plant journal* 81.1 (2015), pp. 169–182.

[91] Feng Xu, Lukas Helfen, Andrew J Moffat, Gregory Johnson, Ian Sinclair, and Tilo Baumbach. "Synchrotron radiation computed laminography for polymer composite failure studies." In: *Journal of synchrotron radiation* 17.2 (2010), pp. 222–226.

[92] Yang Shen, Thilo F Morgeneyer, Jérôme Garnier, Lucien Allais, Lukas Helfen, and Jérôme Crépin. "Three-dimensional quantitative in situ study of crack initiation and propagation in AA6061 aluminum alloy sheets via synchrotron laminography and finite-element simulations." In: *Acta Materialia* 61.7 (2013), pp. 2571–2582.

[93] Daniel Lübbert, Tilo Baumbach, Petr Mikulik, Petra Pernot, Lukas Helfen, Rolf Köhler, Thomas M Katona, Stacia Keller, and Steven P DenBaars. "Local wing tilt analysis of laterally overgrown GaN by x-ray rocking curve imaging." In: *Journal of Physics D: Applied Physics* 38.10A (2005), A50.

[94] TA Lafford, J Villanova, N Plassat, S Dubois, and D Camel. "Synchrotron X-ray imaging applied to solar photovoltaic silicon." In: *Journal of Physics: Conference Series*. Vol. 425. 19. IOP Publishing. 2013, p. 192019.

[95] Karl Wiesent, Karl Barth, Nassir Navab, Peter Durlak, Thomas Brunner, Oliver Schuetz, and Wolfgang Seissler. "Enhanced 3-D-reconstruction algorithm for C-arm systems suitable for interventional procedures." In: *IEEE transactions on medical imaging* 19.5 (2000), pp. 391–403.

[96] MC Scott, Chien-Chun Chen, Matthew Mecklenburg, Chun Zhu, Rui Xu, Peter Ercius, Ulrich Dahmen, BC Regan, and Jianwei Miao. "Electron tomography at 2.4-ångström resolution." In: *Nature* 483.7390 (2012), pp. 444–447.

[97] Noboru Kawase, Mitsuro Kato, Hideo Nishioka, and Hiroshi Jinnai. "Transmission electron microtomography without the "missing wedge" for quantitative structural analysis." In: *Ultramicroscopy* 107.1 (2007), pp. 8–15.

[98] Peter Gilbert. "Iterative methods for the three-dimensional reconstruction of an object from projections." In: *Journal of theoretical biology* 36.1 (1972), pp. 105–117.

[99] K Joost Batenburg, Jan Sijbers, Henning Friis Poulsen, and Erik Knudsen. "DART: a robust algorithm for fast reconstruction of three-dimensional grain maps." In: *Journal of Applied Crystallography* 43.6 (2010), pp. 1464–1473.

[100] Kees Joost Batenburg and Jan Sijbers. "DART: a practical reconstruction algorithm for discrete tomography." In: *IEEE Transactions on Image Processing* 20.9 (2011), pp. 2542–2553.

[101] Hamed Heidari Mezerji, Wouter Van den Broek, and Sara Bals. "A practical method to determine the effective resolution in incoherent experimental electron tomography." In: *Ultramicroscopy* 111.5 (2011), pp. 330–336.

[102] Hussein Banjak, Thomas Grenier, Thierry Epicier, Siddardha Koneti, Lucian Roiban, Anne-Sophie Gay, Isabelle Magnin, Françoise Peyrin, and Voichita Maxim. "Evaluation of noise and blur effects with SIRT-FISTA-TV reconstruction algorithm: Application to fast environmental transmission electron tomography." In: *Ultramicroscopy* 189 (2018), pp. 109–123.

[103] E Biermans, L Molina, KJ Batenburg, S Bals, and G Van Tendeloo. "Measuring porosity at the nanoscale by quantitative electron tomography." In: *Nano letters* 10.12 (2010), pp. 5014–5019.

[104] B Goris, Tom Roelandts, KJ Batenburg, H Heidari Mezerji, and S Bals. "Advanced reconstruction algorithms for electron tomography: from comparison to combination." In: *Ultramicroscopy* 127 (2013), pp. 40–47.

[105] Xiaodong Zhuge, Hiroshi Jinnai, Rafal E Dunin-Borkowski, Vadim Migunov, Sara Bals, Pegie Cool, Anton-Jan Bons, and Kees Joost Batenburg. "Automated discrete electron tomography–Towards routine high-fidelity reconstruction of nanomaterials." In: *Ultramicroscopy* 175 (2017), pp. 87–96.

[106] Matthias Vogelgesang, Tomas Farago, Thilo F Morgeneyer, Lukas Helfen, Tomy dos Santos Rolo, Anton Myagotin, and Tilo Baumbach. "Real-time image-content-based beamline control for smart 4D X-ray imaging." In: *Journal of synchrotron radiation* 23.5 (2016), pp. 1254–1263.

[107] Wim Van Aarle, Willem Jan Palenstijn, Jan De Beenhouwer, Thomas Altantzis, Sara Bals, K Joost Batenburg, and Jan Sijbers. "The ASTRA Toolbox: A platform for advanced algorithm development in electron tomography." In: *Ultramicroscopy* 157 (2015), pp. 35–47.

[108] Wim Van Aarle, Willem Jan Palenstijn, Jeroen Cant, Eline Janssens, Folkert Bleichrodt, Andrei Dabravolski, Jan De Beenhouwer, K Joost Batenburg, and Jan Sijbers. "Fast and flexible X-ray tomography using the ASTRA toolbox." In: *Optics express* 24.22 (2016), pp. 25129–25147.

[109] Mehmet Sezgin and Bülent Sankur. "Survey over image thresholding techniques and quantitative performance evaluation." In: *Journal of Electronic imaging* 13.1 (2004), pp. 146–166.

[110] Jagat Narain Kapur, Prasanna K Sahoo, and Andrew KC Wong. "A new method for gray-level picture thresholding using the entropy of the histogram." In: *Computer vision, graphics, and image processing* 29.3 (1985), pp. 273–285.

[111] TW Ridler, S Calvard, et al. "Picture thresholding using an iterative selection method." In: *IEEE trans syst Man Cybern* 8.8 (1978), pp. 630–632.

[112] Wim Van Aarle, Kees Joost Batenburg, and Jan Sijbers. "Automatic parameter estimation for the discrete algebraic reconstruction technique (DART)." In: *IEEE Transactions on Image Processing* 21.11 (2012), pp. 4608–4621.

[113] Nghia T Vo, Michael Drakopoulos, Robert C Atwood, and Christina Reinhard. "Reliable method for calculating the center of rotation in parallel-beam tomography." In: *Optics express* 22.16 (2014), pp. 19078–19086.

[114] Di Dong, Shouping Zhu, Chenghu Qin, Varsha Kumar, Jens V Stein, Stephan Oehler, Charalambos Savakis, Jie Tian, and Jorge Ripoll. "Automated recovery of the center of rotation in optical projection tomography in the presence of scattering." In: *IEEE journal of biomedical and health informatics* 17.1 (2012), pp. 198–204.

[115] Chang-Chieh Cheng, Yu-Tai Ching, Pai-Hung Ko, and Yeukuang Hwu. "Correction of center of rotation and projection angle in synchrotron X-ray computed tomography." In: *Scientific reports* 8.1 (2018), pp. 1–9.

[116] Min Yang, Zhongchuan Li, Lihong Liang, Xingdong Li, Wenli Liu, and Zhiguo Gui. "Automatic measurement of rotation center for laminography scanning system without dedicated phantoms." In: *Journal of Electronic Imaging* 23.5 (2014), p. 053018.

[117] Stephen G Azevedo, Daniel J Schneberk, J Patrick Fitch, and Harry E Martz. "Calculation of the rotational centers in computed tomography sinograms." In: *IEEE transactions on nuclear science* 37.4 (1990), pp. 1525–1540.

[118] Jianying Li, RJ Jaszczak, Huili Wang, KL Greer, and RE Coleman. "Determination of both mechanical and electronic shifts in cone beam SPECT." In: *Physics in Medicine & Biology* 38.6 (1993), p. 743.

[119] Antonio Brunetti and Francesco De Carlo. "A robust procedure for determination of center of rotation in tomography." In: *Developments in X-Ray Tomography IV*. Vol. 5535. International Society for Optics and Photonics. 2004, pp. 652–659.

[120] Tong Liu and Andrew Alexander Malcolm. "Comparison between four methods for central ray determination with wire phantoms in micro-computed-tomography systems." In: *Optical Engineering* 45.6 (2006), p. 066402.

[121] Andrew J Morgan, Mauro Prasciolu, Andrzej Andrejczuk, Jacek Krzywinski, Alke Meents, David Pennicard, Heinz Graafsma, Anton Barty, Richard J Bean, Miriam Barthelmess, et al. "High numerical aperture multilayer Laue lenses." In: *Scientific reports* 5.1 (2015), pp. 1–14.

[122] M Eriksson. "Special issue on Diffraction-Limited Storage Rings and New Science Opportunities Guest Editors: Mikael Eriksson and J. Friso van der Veen." In: *J. Synchrotron Rad* 21.Part 5 (2014), pp. 837–842.

[123] D Chenevier and A Joly. "ESRF: Inside the extremely brilliant source upgrade." In: *Synchrotron Radiation News* 31.1 (2018), pp. 32–35.

[124] D Chenevier, J McCarthy, and A Joly. "ESRF-EBS: Research and Innovation in the Time of COVID-19." In: *Synchrotron Radiation News* 34.1-3 (2021), pp. 18–20.

[125] Philipp D Lösel, Thomas van de Kamp, Alejandra Jayme, Alexey Ershov, Tomáš Faragó, Olaf Pichler, Nicholas Tan Jerome, Narendar Aadepu, Sabine Bremer, Suren A Chilingaryan, et al. "Introducing Biomedisa as an open-source online platform for biomedical image segmentation." In: *Nature communications* 11.1 (2020), pp. 1–14.

[126] JR Patel and PE Freeland. "Burgers vector of dislocations generated for dislocation velocity measurements in semiconductors." In: *Journal of Applied Physics* 41.7 (1970), pp. 2814–2817.

[127] A Eyer, R Nitsche, and H Zimmermann. "A double-ellipsoid mirror furnace for zone crystallization experiments in spacelab." In: *Journal of Crystal Growth* 47.2 (1979), pp. 219–229.

[128] AN Danilewsky, J Wittge, A Croell, D Allen, P McNally, P Vagovič, T dos Santos Rolo, Z Li, T Baumbach, E Gorostegui-Colinas, et al. "Dislocation dynamics and slip band formation in silicon: In-situ study by X-ray diffraction imaging." In: *Journal of crystal growth* 318.1 (2011), pp. 1157–1163.

[129] Andreas N Danilewsky. "X-Ray Topography—More than Nice Pictures." In: *Crystal Research and Technology* 55.9 (2020), p. 2000012.

[130] AN Danilewsky, J Wittge, A Hess, A Cröll, A Rack, D Allen, P McNally, T dos Santos Rolo, P Vagovič, T Baumbach, et al. "Real-time X-ray diffraction imaging for semiconductor wafer metrology and high temperature in situ experiments." In: *physica status solidi (a)* 208.11 (2011), pp. 2499–2504.

[131] M. P. Kabukcuoglu. "3D Investigation of Dislocation Development in Semiconductor Wafers by Means of X-Ray Diffraction Imaging." PhD thesis. Albert-Ludwigs-Universität, 2021.

[132] MR Surowiec and BK Tanner. "X-ray topographic investigation of microdeformation of InSb single crystals." In: *Philosophical Magazine A* 55.6 (1987), pp. 791–805.

[133] M. Roder. "Global defect distribution and their influence on the local real structure of 4H-SiC." PhD thesis. Albert-Ludwigs-Universität, 2021.

ACRONYMS

PVT	Physical Vapor Transport
XDL	X-ray Diffraction Laminography
XWBT	X-ray White Beam Topography
TEM	Transmission Electron Microscopy
FoV	Field of View
CT	Computerized Tomography
ART	Algebraic Reconstruction Techniques
BV	Burgers vector
FBP	Filtered Backprojection
BRG	Bragg-reflection geometry
LTG	Laue-transmission geometry
MARCI	Multi-Azimuth Rocking Curve Imaging
4D	four-dimensional
3D	three-dimensional
2D	two-dimensional
ND	N-dimensional
ROI	Region of Interest
RCI	Rocking Curve Imaging
ESRF	European Synchrotron Radiation Facility
DESY	Deutsches Elektronen Synchrotron
KIT	Karlsruhe Institute of Technology
DCM	Double Crystal Monochromator
SIRT	Simultaneous Iterative Reconstruction Technique
DART	Discrete Algebraic Reconstruction Technique
ARM	Algebraic Reconstruction Method
EVBP	Empty Volume Backprojection
CoR	Center of Rotation
CoM	Center of Mass
MSL	Mean of Segmented Lines
MCC	Mean of Calculated Centers of Mass
VWB	Virtual Weak-Beam

PUBLICATIONS

X-ray characterization of self-standing bent Si crystal plates for Large Hadron Collider beam extraction
R. Camattari, M. Romagnoni, L. Bandiera, E. Bagli, A. Mazzolari, A. Sytov, S. Haaga, M. Kabukcuoglu, **S. Bode**, D. Hänschke, and others
Journal of Applied Crystallography, 53.2 (2020): pp. 486-493

X-ray topo-tomography studies of linear dislocations in silicon single crystals
V. Asadchikov, A. Buzmakov, F. Chukhovskii, I. Dyachkova, D. Zolotov, A. Danilewsky, T. Baumbach, **S. Bode**, S. Haaga, D. Hänschke, and others
Journal of Applied Crystallography, 51.6 (2018): pp. 1616-1622

CONFERENCE CONTRIBUTIONS

Enabling Quasi 4D Imaging of Dislocation Dynamics in Semiconductor Wafers by X-Ray Diffraction Laminography
Poster, 14th Biennial Conference on High Resolution X-Ray Diffraction and Imaging (XTOP), 2018, Bari, Italy

Extension of X-Ray Diffraction Laminography towards 4D Imaging for the Investigation of Defect Dynamics in Crystalline Materials
Poster, 26th Annual Meeting of the German Crystallographic Society (DGK), 2018, Essen, Germany

Imaging the Dynamics and 3D Structure of Dislocation Arrangements in Semiconductor Wafers by Means of X-Ray Diffraction Laminography
Talk, 17th Conference on Defects-Recognition, Imaging and Physics in Semiconductors (DRIP XVII), 2017, Valladolid, Spain

LIST OF FIGURES

LIST OF TABLES

ACKNOWLEDGMENTS

I want to thank Prof. Tilo Baumbach for giving me the opportunity to work as a PhD student at the LAS and IPS and for supervising my dissertation. Our discussions opened up new perspectives and I am thankful for his continuous support and for him being the primary referee of my defense.

I want to thank Prof. Andreas Danilewksy for evaluating my PhD thesis and being the secondary referee of my defense. His support and comments regarding this work were very valuable, as well as the discussions during beamtimes and conferences.

Special thanks are directed to Daniel Hänschke for his impressive and motivating spirit. Working with him was highly educational in many ways, beamtimes together were exciting, sometimes adventurous, and always times to remember. I am grateful for his guidance, enthusiasm, expertise, and all his efforts. They were essential for this work.

I would like to thank Elias Hamann for his manifold support during my time as PhD student. A big thank you is directed to my fellow PhD students Merve Pinar Kabukcuoglu and Simon Haaga, who helped a lot to accomplish this work. Furthermore, I thank all partners involved in the the 3rd party project STROBOS-CODE. Financial support by the BMBF grant 05KK14VFA is gratefully appreciated.

Marcus Zuber and Tomas Farago are gratefully acknowledged for continuously supporting the realization of the X-ray diffraction imaging instrumentation with their expertise. Further thanks are directed to Angelica Cecilia, Thomas van de Kamp, and the whole imaging and scattering group of IPS.

The technical support by Stefan Uhlemann and IT-support by David Haas are also greatly appreciated. As well as the work of Daniel Gauder and staff of IBG-2 that contributed to this thesis. I would like to thank Lukas Helfen, Thomas Buslaps, and Dmitri Novikov for their help in planning and conducting beamtimes at the ESRF and DESY.

Schließlich möchte ich allen herzlich danken, die mich in diesem Lebensabschnitt begleitet haben, vor allem meinen Freunden, meinem Bruder Ruben Bode und meinen Eltern Gerhild Schneider-Bode und Georg Bode.